

**Multi-Scale Modeling and Rheological Approaches for  
Understanding the Structure-Property Relationships of  
Surfactant Solutions**

by  
Xueming Tang

A dissertation submitted in partial fulfillment  
of the requirements for the degree of  
Doctor of Philosophy  
(Chemical Engineering)  
in the University of Michigan  
2015

Doctoral Committee:

Professor Ronald G. Larson, Chair  
Professor Sharon C. Glotzer  
Professor Michael J. Solomon  
Associate Professor Katsuyo S. Thornton

© Xueming Tang 2015

---

All Rights Reserved



Dedicated to my two sons Zhonghao Max Yu and Zhongsheng Eric Yu, my husband Hai Yu, my sister Xuehui Tang, and my parents. Thank you for your love and support.

## Acknowledgements

First and foremost, I would like to express my sincere appreciation and gratitude to my advisor, Professor Ronald Larson, for his intellectual guidance and encouragement to my research, being very supportive to my two graduate internships and my personal life, and shaping me as a research scientist. Additionally, I appreciate him for his great patience in my writings.

I am very grateful to my collaborators at Procter and Gamble for funding, internships, and beneficial project meetings regularly. I would like to specifically thank Dr. Peter Koenig for five-year's collaboration with intuitive instructions and supports. I would like to thank Dr. Shawn McCoughnaghy for his trainings on experimental rheometry and industrial formulations, and insightful discussions. I wish to thank Dr. Mike Weavers for support and encouragement. I would like to thank Dr. David Eike for his intuitive discussions and collaborations. I wish to acknowledge Procter and Gamble modeling and simulation group lead by Dr. Bruce Murch for their support and helpful discussions during my internships.

I would like to thank Professor Mike Solomon, Professor Sharon Glotzer, and Professor Katsuyo Thornton for serving on my committee. Their excellent instructions make this research possible. I wish to thank Professor Mike Solomon for his precious

recommendation and career advice. I would like to show my appreciation to Professor Phillip Savage for his intelligent support and considerations.

I am thankful to all members of the Larson group, Zuowei Wang, Susan Duncan, Indranil Dalal, Xue Chen, Prateek Jia, Daniel Beltran, Shihu Wang, ShiYu, Priyanka Desai, Weizhong Zou, Kyle Huston, Fang Yuan, Lei Jiang, Jun Liu, Miqiu Kong, Ali Salehi, Wenjun Huang, Maziar Mohammadi, Abdulrazaq Adam, and Soroush Moghadam, for support and valuable group meeting discussions. I wish to thank Zuowei Wang and Indranil Dalal for their help at the beginning of my PhD study. I would like to thank Kyle Huston and undergraduate student Ashley Kiemen for working with me on an oil spill project. I am thankful to the collaboration with Weizhong Zou on wormlike micelle modeling.

Finally, I would like to thank my families for their endless support and love, which helped me to overcome difficulties during my graduate study.

This research was supported by National Science Foundation, Procter and Gamble Gift funding, and Golf of Mexico Research Initiative Funding.

## Table of Contents

Dedication .....	ii
Acknowledgements .....	iii
List of Tables .....	ix
List of Figures .....	xi
List of Appendices .....	xv
Abstract .....	xvi
Chapter 1 Introduction .....	1
1.1 Background .....	1
1.2 Dissertation Overview .....	8
1.3 References .....	10
Chapter 2 Molecular Dynamics Simulations of Sodium Dodecyl Sulfate Micelles in Water – the Effect of the Force Field.....	15
2.1 Introduction.....	15
2.2. Computational Models and Simulation Methods .....	24
2.2.1 Partial Charges .....	24
2.2.2 Force Field .....	25
2.2.2.1 GROMOS .....	25
2.2.2.2 CHARMM .....	27
2.2.2.3 OPLS-AA .....	28
2.2.2.4 OPLS-UA .....	30
2.2.3 Simulation Methods .....	31

2.3 Results and Discussion .....	33
2.3.1 Spherical Micelles Composed of 60 SDS in Small and Large Simulation Box Sizes .....	33
2.3.2 Micelle Composed of 100 Surfactants .....	41
2.3.2.1 Impact of Force Field on Micelle Structure .....	41
2.3.2.2 OPLS-AA-water-sodium models .....	45
2.3.3 Elongated Micelles Composed of 382 Surfactants .....	49
2.4 Conclusions .....	65
2.5 References .....	67
 Chapter 3 Molecular Dynamics Simulations of Structure Property Relationships of Tween 80 Surfactants in Water and at Interfaces .....	 76
3.1 Introduction .....	76
3.2. Computational Models and Simulation Methods .....	85
3.2.1 GROMOS53A6 <sub>OXY+D</sub> Force Field .....	85
3.2.2 Partial Charges and Topology .....	86
3.2.3 Five Representative Molecules in Tween 80 .....	90
3.2.4 MD Simulations .....	91
3.3 Results and Discussion .....	93
3.3.1 Micellar Composition Profiles of Isomers and Multitailed Surfactants .....	95
3.3.2 Interfacial Tensions of Tween 80-Coated Air—Water and Oil—Water Interfaces .....	101
3.4 Conclusions .....	112
3.5 References .....	113
 Chapter 4 Multi-Scale Modeling and Rheological Approaches Understanding the Structure-Property Relationships of Two-Modeled Body Washes, the Effect of Salt and Perfume Raw Materials (PRMs) .....	 118
4.1 Introduction .....	118
4.2. Theory for Predicting Micellar Microstructures .....	121
4.2.1 Packing Argument .....	121
4.2.2 Cates Model .....	122

4.2.2.1 Predicting Micellar Characteristic Times .....	123
4.2.2.2 Predicting Micellar Characteristic Lengths .....	126
4.2.3 Octanol/Water Partition Coefficient $\text{LogP}_{\text{ow}}$ .....	130
4.2.4 Dissipative Particle Dynamic (DPD) Simulations .....	131
4.3 Materials and Methods.....	133
4.3.1 Rheological Experimental Set Up.....	133
4.3.2 DPD Simulation Set Up and Analysis .....	137
4.4 Results and Discussion. I. Salt Effects .....	138
4.4.1 Salt Effects on Rheology Measurements .....	138
4.4.1.1 Salt Curves and Impact of ACCORD Addition .....	138
4.4.1.2 Frequency Sweeps .....	141
4.4.1.3 Cole-Cole Plots .....	143
4.4.1.4 Time-Temperature Superposition .....	145
4.4.2 Salt Effects on Micellar Lengths and Time Scales Obtained From the Cates Model .....	146
4.4.2.1 Micelle Characteristic Lengths and Times for BW-1EO at Different Temperatures .....	146
4.4.2.2 Comparison of Micellar Properties of BW-1EO and BW-3EO .....	151
4.4.3 Salt Effects on Rheological Properties and Surfactant Packing at Molecular Scale using DPD Modeling .....	152
4.5 Results and Discussion. II. PRM effects .....	155
4.5.1 PRM effects on Viscosity for BW-1EO Correlated With $\text{LogP}_{\text{ow}}$ .....	155
4.5.2 PRM Effects on Micellar Properties Based on the Cates Model	158
4.5.2.1 Comparison of the Effects of PRMs, Dipropylene Glycol, Linalool, Cumene, and Isopropyl Myristate on Rheological and Micellar Properties of BW-1EO .....	158
4.5.2.2 Effect of Linalool Rheology of BW-1EO and BW-3EO	159
4.5.3 PRM Effects on Surfactant Packing Using DPD Simulations.	163
4.5.3.1 Addition of Dipropylene Glycol, Linalool, Cumene, and Isopropyl Myristate to BW-1EO.....	163
4.5.3.2 Linalool Addition to BW-1EO and BW-3EO.....	168

4.6 Conclusions and Future Work .....	169
4.7 References .....	171
Chapter 5 Conclusions and Future work.....	177
5.1 Summary .....	177
5.2. Future Directions .....	181
Appendices.....	183

## List of Tables

Table 2.1. Partial charges of the SDS head group tested in this study.....	25
Table 2.2. Simulations carried out in this study and the resulting shapes of the micelles by the end of the run.....	33
Table 2.3. Simulations with mixed force field parameters from GROMOS45A3 and OPLS-UA with initially rodlike shaped micelles containing 382 SDS molecules in 2% NaCl, and resulting structures formed.....	55
Table 2.4. Cavity volume and solvent accessible surface area (SASA) per surfactant for 382 SDS surfactants in 2% NaCl estimated at the ends of simulations from two starting states using VolArea with probe radii of 2.0 Å for cavity volume and 1.4 Å for SASA calculations.....	64
Table 3.1. Properties of Two Stereoisomers, Two Additional Constitutional Isomers, and Two Component of Tween 80 with Two, and Three tails of Isolated Surfactants and of Spherical Micelles Composed of Those Isomers in Water.....	95
Table 4.1. Composition of ACCORD and each PRM's properties, including CAS number, IUPAC name, common name, chemical structure, octanol/water partition coefficient, molecular weight, and its weight percentage.....	136
Table 4.2. 15 PRMs added separately to BW-1EO at 15 mM. The corresponding values of $\log P_{ow}$ , the molecular structures, and resulting zero-shear viscosities (in Pas) are tabulated.....	157
Table A.1 Hydrophilic and total surface areas of SDS micelles at an aggregation number of 60.....	184
Table A.2 Intramolecular parameters of SDS in GROMOS45A31 and OPLS-UA force fields .....	185
Table A.3 Simulations with 382 surfactant molecules using different combinations of intramolecular parameters and the resulting micelle shape.....	185
Table A.4 Intermolecular parameters for two force fields.....	186
Table A.5 List of cross terms of the L-J parameters for sodium ion and oxygen tested in this study within the OPLS-AA force field .....	187



Table B.1 Main components of Corexit 9500 released by Nalco Holding Company..	193
Table B.2 Partial charges of tetramethyl sorbitan calculated using Gaussian 09, with density functional theory method at B3LYP/6-31G(d,p) level averaged over 27 conformational isomers.....	194
Table C.1 Coarse-grained DPD molecular mapping of surfactants and PRMs.....	197
Table C.2 DPD force field parameters, including bead densities, bond equilibrium distances and spring constants, and chi parameters.....	198

## List of Figures

Figure 2.1 Radial density distribution of tail groups, head groups, counter ions, and water about the micelle center of mass (COM) for a micelle composed of 60 SDS in a simulation box size of 12.65*12.65*12.65 nm <sup>3</sup> , for various force fields.....	35
Figure 2.2 RDF of sodium with respect to a). sulfur, and b). ionic oxygen atoms in the micelle head group for an SDS micelle with aggregation number 60....	39
Figure 2.3 Percentages of sodium ions within each RDF shell around ionic oxygens of the SDS head group in a box size of 12.65*12.65*12.65 nm <sup>3</sup> .....	40
Figure 2.4 Snapshots from simulations of micelle composed of 100 SDS at 0.8 M....	42
Figure 2.5 RDF of sulfur to sulfur atoms at 0.8 M at an aggregation number of 60 and 100.....	44
Figure 2.6 Number of water molecules within 0.35 nm of Na <sup>+</sup> plotted against inner peak height of RDF of sodium to ionic oxygens in SDS head group for different Na <sup>+</sup> /water models within OPLS-AA.....	47
Figure 2.7 Evolution of initially elongated SDS micelles and bicelles with an aggregation number of 382 at 0.26 M concentration and 2% NaCl.....	52
Figure 2.8 Comparison of distribution of gradient of the percentage of sodium ions with respect to the nearest a). sulfur atom and b). ionic oxygen atoms, for an aggregate of 382 SDS molecules.....	57
Figure 2.9 Ratios of principal radii of gyration for aggregation number 382 SDS in 2% salt.....	61
Figure 3.1 Canonical structure of Tween 80 molecule with X, Y, and Z head groups (green), W headgroup (purple) containing x, y, z, and w number of ethylene oxide (EO) units respectively, and tail (blue).....	80
Figure 3.2 Five different Tween 80 molecules are chosen in this work.....	83
Figure 3.3 Tetramethyl sorbitan used in quantum mechanical calculations.....	88
Figure 3.4 Snapshots of initial (top) and final (bottom) states of air—water and oil—water interfaces in simulations with isomer 666-2-1S.....	93

Figure 3.5 Comparison of properties of three constitutional isomers and three components of Tween 80 with one, two, and three tails.....	97
Figure 3.6 RDFs of oxygens of the W headgroup of isomer 222-14-1S, numbered starting from the attachment point to the THF ring and increasing outward.....	99
Figure 3.7 Dependence of interfacial tensions at oil–water interfaces on surfactant surface coverage for surfactants 555-5-1S and 555-5-3S.....	102
Figure 3.8 Comparison of interfacial tensions of five Tween 80 molecules at the air–water and oil–water interfaces.....	106
Figure 3.9 Comparison of properties of three constitutional isomers of Tween 80 surfactant at the air–water and oil–water interfaces.....	107
Figure 3.10 Comparison of properties of three components of Tween 80 with one, two, and three tails at the air–water and oil–water interfaces.....	109
Figure 3.11 Surfactant density profiles at oil–water interfaces averaged over the axis that is perpendicular to the plane and averaged over time.....	111
Figure 4.1 Weight distribution of number of ethylene oxide (EO) groups for SLE1nS in BW-1EO and SLE3nS in BW 3EO.....	135
Figure 4.2 Snapshot of an equilibrated periodic wormlike micelle.....	137
Figure 4.3 Salt curves for 11% and 9.5% formulations containing 1% ACCORD (solid lines) and without ACCORD (dashed lines): diamonds - 11% BW-1EO formulation, triangles - 11% BW-3EO formulation, and circles - 9.5% BW-3EO formulation.....	139
Figure 4.4 Storage and loss moduli for BW-1EO (a, b) and BW-3EO (a', b') at different salt weight percentages, given in the legends.....	143
Figure 4.5 Cole-Cole plots and normalized Cole-Cole plots for BW-1EO and BW-3EO.....	145
Figure 4.6 Master curves of frequency dependent moduli obtained by time-temperature superposition (TTS) at salt concentrations of 0.50% (a), 1.00% (b), and 2.00% (c) NaCl for BW-1EO.....	146
Figure 4.7 Viscosity (a) vs. salt concentration at 20.0, 22.0, 23.5, and 25.0°C, and the computed micellar characteristic lengths and times, including average micelle length (b), reptation time (c), micellar entanglement length (d) breakage time (e), and plateau modulus (f) of BW-1EOs.....	148
Figure 4.8 Boltzmann behavior of average micelle length vs. 1/T at various salt concentrations and Scission/branch formation free energy, viscosity activation energy, and terminal relaxation time activation energy from Arrhenius laws converge at high salt concentrations for BW-1EO.....	150

Figure 4.9 Comparison of average micelle length (filled symbols) (a) and scission energy (opened symbols) (b) for BW-1EO (diamonds) and formular BW-3EO (triangles).....	152
Figure 4.10 Bead number density distribution of head, tail, and water within a shell at the radial distance with respect to the core of the cylindrical micelles a) for solutions containing 11% BW-1EO at salt concentrations spanning the peak of the salt curve; b) for 11.0% BW-1EO at 0.70% NaCl and 11.0% BW-3EO at 2.13% NaCl, which have the same experimental viscosity of 11.0 Pas; and c) for BW-1EO solutions of three different surfactant concentrations at 0.7% NaCl. d) Surfactant packing distance defined as the ratio of the micelle spine length to the number of surfactants in the micelle in all of the above systems.....	153
Figure 4.11 Viscosities of BW-1EO on addition of 15 PRMs at 15 mM plotted against logPow, of the PRM.....	156
Figure 4.12 Dependence of viscosity on concentration of dipropylene glycol (DPG), cumene, linalool, and isopropyl myristate (IPM) in BW-1EO containing ACCORD and average micelle length vs. PRM concentration, computed from the Cates model.....	158
Figure 4.13 (a) Loss and storage modulus vs. frequency, (b) Cole-Cole plot, and (c) normalized Cole-Cole plot at various linalool concentrations in BW-1EO; and the same in BW-3EO are presented in a'), b') and c').....	161
Figure 4.14 Plot of $\tan\delta$ vs. ratio of breakage time to reptation time squared at various temperatures and concentrations of linalool in BW-3EO.....	162
Figure 4.15 Plot of zero shear viscosity and surfactant packing distances for BW-1EO upon addition of 15 mM dipropylene glycol (DPG), cumene, linalool, and isopropyl myristate (IPM) vs. their logPow.....	164
Figure 4.16 Bead number count of tail, head, water and an additional PRM, namely a). DPG, b). linalool, c). cumene, and d). IPM within a shell of 1.3 nm width at a radial distance with respect to the core of the cylindrical micelles...	165
Figure 4.17 Comparison of the bead number count within a shell at a radial distance from the center of a periodic cylindrical micelle of BW-3EO containing 1% ACCORD in the presence and in the absence of 15 mM linalool.....	168
Figure 5.1. Developing the structure-property relationship of surfactant formulations using multi-scale modeling and experimental techniques.....	178
Figure A.1 Hydration number for methylene hydrocarbons of SDS micelle in the small box estimated as the average number of water oxygens within 0.35 nm of the center of mass of the corresponding methylene. Carbon number 1 represents the alpha carbon and 12 the terminal methyl carbon.....	184

Figure A.2 (a) RDF of sodium to ionic oxygens in SDS head group in a simulation of box of size 5*5*5 nm <sup>3</sup> with a micelle having an aggregation number of 60 and different Na+/water models and Aqvist5 sodium ion within OPLS-AA .....	187
Figure A.3 a). RDF of sodium to ionic oxygens and b). sodium to water oxygens in SDS head group in a simulation of box of size 6*6*6 nm <sup>3</sup> with a micelle having an aggregation number of 100 and Aqvist5 Na+/different water model within OPLS-AA.....	188
Figure A.4 Square root of principal radii of gyration vs. time for preassembled rod-like micelles (a-f) and preassembled bicelles (a'-f') of 382 SDS molecules in 2% NaCl for six force fields.....	189
Figure A.5 RDF of sodium with respect to ionic oxygen atoms in the micelle head group for an SDS micelle with aggregation number 60 using GROMOS53A6 and GROMOS54A8 force fields.....	190
Figure B.1 RDF distributions of tail, W head, X, Y, Z head, and water for a micelle of Tween 80 composed of 60 surfactants using (a) the GROMOS53A6 force field, and (b) the GROMOS53A6 <sub>OXY+D</sub> force field.....	194
Figure B.2 Comparison of radial distribution functions (RDFs) of various atom groups of Tween 80 isomer 555-5-1S with respect to the micelle center of mass (COM) from two independent runs, as shown by solid and dashed lines.	195
Figure B.3 Comparison of micelle properties of two epimers of Tween 80: (a) Radial distribution functions (RDFs) of different groups with respect to the micelle center of mass (COM); (b) The distributions of single-surfactant Rg values for surfactants within the micelle.....	195
Figure B.4 Densities of water, head, tail, and oil atoms of isomer 555-5-1S, at (a) an air—water interface, averaged over both 40 to 50 ns (solid lines) and 90 to 100 ns (dashed lines) after the start of the simulation; and at (b) an oil—water interface, averaged over both 100 to 120 ns (solid lines) and 220 to 240 ns (dashed lines).....	196
Figure B.5 Comparison of oleate tail order parameters of (a) three one-tailed structure isomers of Tween 80 and (b) one, two, and three-tail Tween 80 molecules.....	196

## **List of Appendices**

<b>Appendix A:</b> Supplementary Information for Chapter 2.....	183
A.6 References.....	190
<b>Appendix B:</b> Supplementary Information for Chapter 3.....	192
<b>Appendix C:</b> Supplementary Information for Chapter 4.....	197

## **Abstract**

In this work, we applied multi-scale modeling and rheological measurements to understand the structure-property relationships of surfactant solutions. We used molecular dynamics (MD) and dissipative particle dynamics (DPD) simulations to address behavior extending from the molecular level to the micellar mesoscale, the Cates model to bridge the micellar mesoscale to macroscale rheological behavior, and rheometry to measure rheological behavior and compare it to predictions of the Cates model.

Starting with a simple surfactant, sodium dodecyl sulfate, we compared force field effects on micellar properties at various aggregation numbers by MD simulations. We found the parameters that control the shape of large micelles were the Lennard-Jones parameters of  $\text{Na}^+$  and ionic oxygen atoms, as well as the water model, which controls hydration of  $\text{Na}^+$  in the presence of surfactants. These parameters control the degree of binding of  $\text{Na}^+$  to ionic oxygens and head group packing, and resulted in different micellar shapes.

We also studied structure-property relationships of a commercial surfactant mixture, polyoxyethylene (PEO) sorbitan oleates, which contains multiple species and were

represented as five “typical” structures varying the lengths of EO head groups and the number of tails using MD simulations. We found structures with more than one tail, and with shorter EO head group that attaches the tail to the sorbitan ring, pack more efficiently within micelles and at interfaces. This efficient packing leads to lower interfacial tensions at air–water and oil–water interfaces at the same surfactant interfacial density.

Finally to assess the behavior of complex body washes containing cylindrical micelles, we studied the effects of salts (NaCl) and perfume raw materials (PRMs) by combining results from rheology, the micellar Cates model, and DPD modeling. We determined the relationship between viscosity and average micelle length, and elasticity and micellar characteristic time. Salts modify viscoelasticities of body washes by condensing  $\text{Na}^+$  near micellar surface, changing surfactant head groups packing, and maintaining the cross-section radius constant. PRMs modify viscoelasticities of body washes by partitioning into the micelles according to their octanol/water partition coefficients and chemical structures, adjusting surfactant packing at head and/or tail regions, and possibly changing the cross-section radius.



# Chapter 1

## Introduction

### 1.1 Background

Surfactants are amphiphilic molecules that contain hydrophilic head(s) and hydrophobic tail(s). In water at concentrations above the first critical micelle concentration (1<sup>st</sup> CMC), dispersed surfactants aggregate into spheroidal micelles. Correspondingly, a fairly abrupt change in solution properties, including interfacial tension and electronic conductivity, occurs and this is used to determine the concentration of the 1<sup>st</sup> CMC.<sup>1</sup> The 1<sup>st</sup> CMC was also predicted by molecular-thermodynamic theories considering the free energy of micellization as the summation of the hydrophobic effects, the entropic effect, the steric repulsions of surfactant head groups, and possible static and/or electrostatic repulsions in solutions containing ionic surfactants.<sup>2-4</sup> As the concentration of surfactant increases, a second abrupt property change of solutions appears, namely the 2<sup>nd</sup> CMC. For sodium dodecyl sulfate (SDS) it is defined as the transition concentration where the majority of the micelles are changed from the spheroidal micelles to short rodlike micelles.<sup>5,6</sup> As surfactant concentration increases further, the micelles can grow uniaxially to form cylindrical micelles having circular or elliptical cross sections,<sup>7-9</sup> or biaxially to form

bicelles,<sup>10,11</sup> or possibly micellar rings.<sup>12,13</sup> At higher surfactant concentrations, entangled worms, vesicles, hexagon, or higher ordered phases are formed.<sup>10,14–18</sup>

The shapes of the surfactant aggregates depend on concentrations and species of surfactants and cosurfactants, salts, and other molecules if exist, and temperature and pressure of solutions.<sup>16,19,20</sup> Under stress or change of the environment, these microstructures within the complex fluid rearrange and could form new structures. For example, addition of salts to surfactant solutions containing ionic surfactants lowers the free energy of micellizations, lowers the CMCs, and promotes longer micelles or higher ordered phases by reducing the electrostatic repulsions between the surfactant head groups. The surfactant packing structures at the molecular scale determines the properties of the solutions at the continuum scale, and in practical applications. Surfactants have been widely used in consumer products including detergents, health and personal care products, and foodstuffs, and in industrial applications including oil recovery and drug delivery industries.<sup>19,21–24</sup>

The properties of surfactant formulations, including rheology and interfacial tensions and others, are tested frequently in practical applications. However, the connection between surfactant packing structures and the corresponding properties, namely the structure-property relationships, comparing with its practical applications, has been developed slowly. This is due to the complexity of industrial surfactant formulations and the challenge of quantifying surfactant microstructures at the molecular scale. Currently, one of the best approaches to quantify the effect of molecular structure of surfactants on micellar properties is molecular modeling.

With the exponential increase of the computational powers and tremendous algorithmic improvements, molecular modeling, including molecular dynamics (MD) simulations and dissipative particle dynamics (DPD) simulations, has been developed rapidly. These simulations provide a unique resolution of structural details down to the molecular scale. At the all-atom (AA) level, MD simulations of surfactant solutions containing up to millions of atoms and time scales of hundreds of ns are carried out.<sup>25</sup> The simulations can be accelerated, especially for surfactants with long hydrocarbon tails, by grouping each carbon with its bonded hydrogen atoms into a pseudo or united-atom (UA) and applying a larger time step size, without sacrificing atomistic details significantly.<sup>26</sup> At this UA-level, micelle structures and interfacial tensions of aliphatic surfactants can be computed accurately. Application to solutions containing aromatic surfactants needs to be carried out cautiously due to the observation of the inaccurate intermolecular interactions between aromatic compounds relative to experimental results.<sup>27</sup> For investigations of hydrodynamic behavior and rheological properties of cylindrical micelles in an accurate and efficient matter, the simulations can be further accelerated using DPD simulations by lumping three to five heavy atoms into one quasi-particle or bead and using a soft repulsive potential.<sup>28,29</sup>

The accuracy of the molecular simulations is determined by the degree of validations of the force field parameters against the physical-chemical properties measured experimentally. Two standard approaches to optimize force field parameters, including reproducing the structural information and/or reproducing the thermodynamics, have been applied to the four popular empirical force fields, CHARMM-AA, OPLS-AA,

AMBER-AA, and GROMOS-UA.<sup>30-37</sup> Validation of structural information, including liquid density, liquid volume, pair distribution functions (RDF) of atoms, and/or critical temperatures, were carried out at the earlier generations of force fields due to the low computational cost, followed by the validation of thermodynamics, including enthalpy of vaporizations, hydration free energy, and other potential energies at higher computational cost against experimental measurements.<sup>38</sup> Recently, validation of the vicinal diether functions based on quantum mechanical calculations of conformational populations against experimental measurements enables the MD simulations of polymers or surfactants containing polyethylene oxide groups be accurate.<sup>39,40</sup>

Prior to the development of force fields, water models were optimized by structural validation of density, RDF of oxygen-oxygen ( $g_{OO}$ ),  $g_{OH}$  and  $g_{HH}$ , and dimerization energy against experimental data. The three-sites models of SPC, SPC/E and TIP3P water models, the four-sites TIP4P, and the five sites TIP5P water model, original or modified were tested.<sup>41-43</sup> All models reproduce the density and potential functions of water to the experimental measurements well.<sup>42</sup> While the complex water model, TIP5P, computes the second peak of  $g_{OO}$ , more accurately than others at higher computational cost.<sup>38</sup> Polarizable force fields can model water accurately, for example, on the dipole moments, but is inhibitive expensive for applications.

The successful parameterization of water supports the development of empirical force fields. By adopting one available water model with or without modification and introducing protein, nucleic acids, lipids, and/or surfactants into water, the force field parameters of the organic species and of intermolecular interactions between the organics

and water are optimized to experimental structural and thermodynamic data. Generally, in CHARMM-AA force field a modified TIP3P water model is used, in OPLS-AA the TIP4P water model is used, OPLS-UA and SPC or TIP3P water model is used, in AMBER-AA the TIP3P water model is used, and in GROMOS-UA the SPC water model is used. The force field potential function in AMBER force field is represented as the following equation:

$$V(x) = \sum_{bonds} K_i(l_i - l_{i,0})^2 + \sum_{angles} K_i(\theta_i - \theta_{i,0})^2 + \sum_{torsions} \sum_n \frac{V_n}{2} [1 + \cos(n\omega - \gamma)] \\ + \sum_{i=1}^{N-1} \sum_{j=i+1}^N f_{ij} \left\{ \epsilon_{ij} \left[ \left( \frac{r_{0ij}}{r_{ij}} \right)^{12} - 2 \left( \frac{r_{0ij}}{r_{ij}} \right)^6 \right] + \frac{q_i q_j}{4\pi\epsilon_0 r_{ij}} \right\}$$

Here the equilibrium bond distance  $r_{0ij} = 2^{\frac{1}{6}}\sigma$ . The first three terms represents the intramolecular bonded interactions, including harmonic bond potentials, harmonic angle potentials, and dihedral potentials. The last term represents the non-bonded interactions, including the 6-12 form of Lennard-Jones (L-J) and the columbic interactions. The combination rule to generate parameters of the inter- and intramolecular interaction uses the geometric average of the two with a fudge factor. The functional form, combination rule, and the fudge factor are force field dependent. While in GROMOS force field all parameters, including the intra and intermolecular interactions, are listed explicitly. Interchange parameters between force fields need to be cautious and consistent with its default units. Furthermore, it is important to use the water model that was originally designed for optimization of that force field parameters otherwise the structural and thermodynamic properties could be changed. Similarly, ion model should be adopted

only if the water model in the force field is consistent with the water model used to parameterize that ion. In addition, performing MD simulations within the range of temperature and pressure is important since the parameters, when optimized, are within a certain range.

Parameterization of the most widely used surfactant, SDS, was firstly carried out more than two decades ago.<sup>44</sup> Due to the limitation of the computational power then, Klein carried out a MD simulation of one spheroidal micelle at a size of 42 solvated into 1901 water models for 182 ps at a UA level. The parameters were based on quantum mechanical calculations since there is no available force field parameter for SDS then. Later MacKerell carried out simulation of SDS micelle at a size of 60 solvated into 4398 water for 120 ps use CHARMM22 force field at an AA level.<sup>32</sup> As the computational power increases, a decade later after the first MD simulation, a milestone study of properties of SDS micelles composed of 60 SDS was performed by Bruce et al.<sup>45</sup> for 5 ns using AMBER-UA force field parameters developed in Berkowitz's group.<sup>46</sup> The validation method of SDS force field parameter used by comparing the RDF of sulfur atom to sodium ions ( $g_{S-Na}$ ) within a spherical micelle at a size of 60 in a small simulation box, and the radius of gyration ( $R_g$ ) of SDS tail, have been used even since then,<sup>47,48</sup> even though the computational power has been improved tremendously in the decade.

The shape of a micelle composed of 60 SDS will be more or less an ellipsoidal due to the geometric constrains. The sulfur atom, which is shielded under the three connected ionic oxygen, has limited access from contacting the sodium ions and is less sensitive to changes in the environment. Therefore, both validation methods are less sensitive to the

force field parameters. Furthermore, all the simulations used small simulation boxes to reduce the computational demand by simulating less water, while neglected the fact that the shape and size of the micelles are concentration dependent. Even at the lowest SDS concentration of 0.4 M in former studies, the majority of the micelles within the systems are rodlike micelles or longer wormlike micelles since the concentration of SDS is far above the 2<sup>nd</sup> CMC of 0.069 M.<sup>5,49</sup> More stringent methods of force field validation that connect to the physical-chemical properties, including the shape of the micelles at its corresponding concentrations, are computational feasible but have not been applied yet. Locating force field parameters of one or two that determine the shape of the micelles, can provide useful information for surfactant force field parameterization as well.

The increase of computational power enables simulations of much complex surfactants with larger sizes. In practical applications, many surfactants are mixtures of several similar structures instead of one component. For convenience and limited by the computational resources, researches used one averaged species as a representative structure in MD simulations, neglecting the fact that different structures could result in very different properties. Take polyethylene sorbitan oleate (Tween 80) as an example, former MD simulations of Tween 80 at UA or AA level only carried out one molecule using the averaged structure.<sup>50,51</sup> With increasing computational power and the improved accuracy of force field parameters, it is time to investigate more possible structures of commercial surfactants from synthetic point of view and study the structure-property relationships of the surfactants. Understanding how the packing of surfactants with certain structure lead to superior properties of interest can build the structure-property

relationships and predict properties of surfactants. Tuning the synthesis of surfactants to the increasing fractions of the superior properties can improve the efficiency of the surfactant products.

Furthermore, industrial surfactant formulations, for example, body washes, are complex mixtures of several species of surfactants, salts, and perfume raw materials (PRMs) in order to meet consumer's demands and take the advantages superior properties of mixed surfactants than single species. These surfactant formulations are complex fluids having microstructures. The properties of those formulations are determined by the microstructures of surfactants at a molecular scale. Due to the complexity of the formulation and the challenges of quantifying the microstructures experimentally, empirical formulations are mainly used without understanding the structure-property relationships of body washes. How to connect those surfactant-packing structures at a molecular scale to the viscoelastic properties of the body washes at a continuum scale has not been addressed so far. The DPD models with significant improvements,<sup>29,52,53</sup> together with micellar scale models<sup>54,55</sup> and rheological measurements, can provide possible solution to solve this multi-scale problems and develop the structure-property relationship models.

## **1.2 Dissertation Overview**

To address the three issues in surfactant modeling and applications, we carried out the following three projects starting from a simple surfactant, SDS solution using MD simulations, to larger surfactant mixtures, Tween 80, containing relevant structures, and to complex body wash formulations containing several species of surfactants, salts, and



PRMs using modeling and rheological techniques. Based on results from SDS simulations, we chose GROMOS force field using the SPC water model for Tween 80 simulations considering the accuracy and efficiency. Specially:

I. Force field effects on SDS micelles in water using MD simulations:

- a. Identified key force field parameters determine the shape of large micelles: cylinders vs. bicelles;
- b. Developed a more stringent standard for force field validation.

II. Developed five model molecules to represent Tween 80 commercial mixtures and study the structure-property relationships of Tween 80 in water and at interfaces:

- a. Represented surfactant packing structures within micelles using the RDF distribution of surfactants;
- b. Represented surfactant packing structures at interfaces by the density profiles at interfaces.

III. Connected the surfactant packing structures at the molecular scale and micellar scale, to viscoelastic properties at continuum scale upon addition of salts and PRMs to body washes using rheometry, micellar modeling, and DPD simulations:

- a. Determined viscoelastic properties changes upon the addition of salts and the corresponding structure changes at the molecular scale and micellar scale;
- b. Determined viscoelastic properties changes upon the addition of PRMs and the corresponding structure changes at the molecular scale and micellar scale relevant to its  $\log P_{ow}$  and chemical structures.

### 1.3 References:

- (1) Preston, W. C. Some Correlating Principles of Detergent Action. *J. Phys. Colloid Chem.* **1948**, *52*, 84–97.
- (2) Puvvada, S.; Blankschtein, D. Molecular-thermodynamic Approach to Predict Micellization, Phase Behavior and Phase Separation of Micellar Solutions. I. Application to Nonionic Surfactants. *J. Chem. Phys.* **1990**, *92*, 3710–3724.
- (3) Puvvada, S.; Blankschtein, D. An Analytical Expression for the Free Energy of Micellization. *J. Phys. Chem.* **1992**, *96*, 7830–7832.
- (4) Srinivasan, V.; Blankschtein, D. Effect of Counterion Binding on Micellar Solution Behavior: 1. Molecular - Thermodynamic Theory of Micellization of Ionic Surfactants. *Langmuir* **2003**, *19*, 9932–9945.
- (5) Kodama, M.; Kubota, Y.; Miura, M. The Second CMC of the Aqueous Solution of Sodium Dodecyl Sulfate. III. Light-Scattering. *Bull. Chem. Soc. Jpn.* **1972**, *45*, 2953–2955.
- (6) Yasunaga, T.; Oguri, H.; Miura, M. Acoustic Study on the Kinetics for the Dissociation-Recombination Reaction between Micelle and Counterion in Sodium Dodecyl Sulfate Solution. *J. Colloid Interface Sci.* **1967**, *23*, 352–357.
- (7) Bergstro, M.; Pedersen, J. S. A Small-Angle Neutron Scattering ( SANS ) Study of Tablet-Shaped and Ribbonlike Micelles Formed from Mixtures of an Anionic and a Cationic Surfactant. *J. Phys. Chem. B* **1999**, *103*, 8502–8513.
- (8) Bergstro, M.; Pedersen, J. S. Small-Angle Neutron Scattering ( SANS ) Study of Aggregates Formed from Aqueous Mixtures of Sodium Dodecyl Sulfate ( SDS ) and Dodecyltrimethylammonium Bromide ( DTAB ). *Langmuir* **1998**, *7463*, 3754–3761.
- (9) Bergstro, M.; Pedersen, J. S. Formation of Tablet-Shaped and Ribbonlike Micelles in Mixtures of an Anionic and a Cationic Surfactant. *Langmuir* **1999**, *15*, 2250–2253.
- (10) Gabriel, N. E.; Roberts, M. F. Spontaneous Formation of Stable Unilamellar Vesicles. *Biochemistry* **1984**, *23*, 4011–4015.

- (11) Sanders, C. R.; Hare, B. J.; Howard, K. P.; Prestegard, J. H. Magnetically-Oriented Phospholipid Micelles as a Tool for the Study of Membrane-Associated Molecules. *Prog. Nucl. Magn. Reson. Spectrosc.* **1994**, *26*, 421–444.
- (12) In, M.; Aguerre-Chariol, O.; Zana, R. Closed-Looped Micelles in Surfactant Tetramer Solutions. *J. Phys. Chem. B* **1999**, *103*, 7747–7750.
- (13) Bernheim-Groswasser, A.; Zana, R.; Talmon, Y. Sphere-to-Cylinder Transition in Aqueous Micellar Solution of a Dimeric (Gemini) Surfactant. *J. Phys. Chem. B* **2000**, *104*, 4005–4009.
- (14) Imae, T.; Kamiya, R.; Ikeda, S. Formation of Spherical and Rod-like Micelles of Cetyltrimethylammonium Bromide in Aqueous NaBr Solutions. *J. Colloid Interface Sci.* **1985**, *108*, 215–225.
- (15) Diat, O.; Roux, D. Preparation of Monodisperse Multilayer Vesicles of Controlled Size and High Encapsulation Ratio. *J. Phys. II* **1993**, *3*, 9–14.
- (16) Kekicheff, P.; Grabielle-Madellmont, C.; Ollivon, M. Phase Diagram of Sodium Dodecyl Sulfate-Water System : I A Calorimetric Study. *J. Colloid Interface Sci.* **1989**, *131*, 112–132.
- (17) Kekicheff, P. Phase Diagram of Sodium Dodecyl Sulfate-Water System 2. Complementary Isoplethal and Isothermal Phase Studies. *J. Colloid Interface Sci.* **1989**, *131*, 133–152.
- (18) Cates, M. E. Nonlinear Viscoelasticity of Wormlike Micelles ( and Other Reversibly Breakable Polymers ). *Journal Phys. Chem.* **1990**, *94*, 371–375.
- (19) Larson, R. G. *The Structure and Rheology of Complex Fluids*; Oxford University Press, New York, USA, 1999; pp. 551–593.
- (20) Zana, R.; Kaler, E. W. *Giant Micelles: Properties and Applications*; v140 ed.; CRC Press: Surfactant Science Series, 2007.
- (21) Rhein, L. D. .; Schlossman, M.; O'Lenick, A.; Somasundaran, P. . *Surfactants in Personal Care Products and Decorative Cosmetics*; Third.; CRC Press: Surfactant Science Series, 2006; Vol. 40.
- (22) Kralova, I.; Sjoblom, J. Surfactants Used in Food Industry : A Review. *J. Dispers. Sci. Technol.* **2009**, *30*, 1363–1383.

- (23) Maitland, G. . Oil and Gas Production. *Curr. Opin. Colloid Interface Sci.* **2000**, *5*, 301–311.
- (24) Lawrence, M. J. Surfactant Systems: Their Use in Drug Delivery. *Chem. Soc. Rev.* **1994**.
- (25) Zhao, G.; Perilla, J. R.; Yufenyuy, E. L.; Meng, X.; Chen, B.; Ning, J.; Ahn, J.; Gronenborn, A. M.; Schulten, K.; Aiken, C.; et al. Mature HIV-1 Capsid Structure by Cryo-Electron Microscopy and All-Atom Molecular Dynamics. *Nature* **2013**, *497*, 643–646.
- (26) Dunfield, L. G.; Burgess, A. W.; Scheraga, H. A. Energy Parameters in Polypeptides . 8 . Empirical Potential Energy Algorithm for the Conformational Analysis of Large Molecules. *J. Phys. Chem.* **1978**, *82*, 2609–2616.
- (27) MacKerell Jr., A. D. Empirical Force Fields for Biological Macromolecules: Overview and Issues. *J. Comput. Chem.* **2004**, *25*, 1584–1604.
- (28) Espanol, P.; Warren, P.; Road, M.; Sunlight, P.; East, Q. R. Statistical Mechanics of Dissipative Particle Dynamics. *EPL Europhysics Lett.* **1995**, *30*, 191–196.
- (29) Groot, R. D.; Warren, P. B. Dissipative Particle Dynamics: Bridging the Gap between Atomistic and Mesoscopic Simulation. *J. Chem. Phys.* **1997**, *107*, 4423–4435.
- (30) Jorgensen, W. L.; Maxwell, D. S.; Tirado-Rives, J. Development and Testing of the OPLS All-Atom Force Field on Conformational Energetics and Properties of Organic Liquids. *J. Chem. Soc.* **1996**, *118*, 11225–11236.
- (31) Kaminski, G.; Duffy, E. M.; Matsui, T.; Jorgensen, W. L. Free Energies of Hydration and Pure Liquid Properties of Hydrocarbons from the OPLS All-Atom Model. *J. Phys. Chem.* **1994**, *98*, 13077–13082.
- (32) MacKerell Jr., A. D. Molecular Dynamics Simulation Analysis of a Sodium Dodecyl Sulfate Micelle in Aqueous Solution : Decreased Fluidity of the Micelle Hydrocarbon Interior. *J. Phys. Chem.* **1995**, *99*, 1846–1855.
- (33) Berendsen, H. J. C.; Postma, J. P. M.; van Gunsteren, W. F.; Hermans, J. Intermolecular Forces. In *edited by B. Pullman (Reidel, Dordrecht)*; 1981; pp. 331–338.
- (34) Cornell, W. D.; Cieplak, P.; Bayly, C. I.; Gould, I. R.; Merz, K. M.; Ferguson, D. M.; Spellmeyer, D. C.; Fox, T.; Caldwell, J. W.; Kollman, P. a. A Second

Generation Force Field for the Simulation of Proteins, Nucleic Acids, and Organic Molecules. *J. Am. Chem. Soc.* **1995**, *117*, 5179–5197.

- (35) Schuler, L. D.; Daura, X.; van Gunsteren, W. F. An Improved GROMOS96 Force Field for Aliphatic Hydrocarbons in the Condensed Condensed Phase. *J. Comput. Chem.* **2001**, *22*, 1205–1218.
- (36) Poger, D.; Gunsteren, W. F. V. A. N.; Mark, A. E. A New Force Field for Simulating Phosphatidylcholine Bilayers. *J. Comput. Chem.* **2010**, *31*, 1117–1125.
- (37) Martin, M. G. Comparison of the AMBER, CHARMM, COMPASS, GROMOS, OPLS, TraPPE and UFF Force Fields for Prediction of Vapor–liquid Coexistence Curves and Liquid Densities. *Fluid Phase Equilib.* **2006**, *248*, 50–55.
- (38) Jorgensen, W. L.; Tirado-Rives, J. Potential Energy Functions for Atomic-Level Simulations of Water and Organic and Biomolecular Systems. *Proc. Natl. Acad. Sci. U. S. A.* **2005**, *102*, 6665–6670.
- (39) Fuchs, P. F. J.; Hansen, H. S.; Hünenberger, P. H.; Horta, B. A. C. A GROMOS Parameter Set for Vicinal Diether Functions : Properties of Polyethyleneoxide and Polyethyleneglycol. *J. Chem. Theory Comput.* **2012**, *8*, 3943–3963.
- (40) Pastor, R. W.; MacKerell Jr., A. D. Development of the CHARMM Force Field for Lipids. *J. Phys. Chem. Lett.* **2011**, *2*, 1526–1532.
- (41) Mark, P.; Nilsson, L. Structure and Dynamics of the TIP3P, SPC, and SPC/E Water Models at 298 K. *J. Phys. Chem. A* **2001**, *105*, 9954–9960.
- (42) Jorgensen, W. L.; Chandrasekhar, J.; Madura, J. D.; Impey, R. W.; Klein, M. L. Comparison of Simple Potential Functions for Simulating Liquid Water. *J. Chem. Phys.* **1983**, *79*, 926–936.
- (43) Vega, C.; de Miguel, E. Surface Tension of the Most Popular Models of Water by Using the Test-Area Simulation Method. *J. Chem. Phys.* **2007**, *126*, 154707.
- (44) Shelley, J.; Watanabe, K.; Klein, M. L. Simulation of a Sodium Dodecylsulfate Micelle in Aqueous Solution. *Int. J. Quantum Chem. Quantum Biol. Symp.* **1990**, *38*, 103–117.
- (45) Bruce, C. D.; Berkowitz, M. L.; Perera, L.; Forbes, M. D. E. Molecular Dynamics Simulation of Sodium Dodecyl Sulfate Micelle in Water : Micellar Structural Characteristics and Counterion Distribution. *J. Phys. Chem. B* **2002**, *106*, 3788–3793.

- (46) Schweighofer, K. J.; Essmann, U.; Berkowitz, M. Simulation of Sodium Dodecyl Sulfate at the Water-Vapor and Water-Carbon Tetrachloride Interfaces at Low Surface Coverage. *J. Phys. Chem. B* **1997**, *101*, 3793–3799.
- (47) Shang, B. Z.; Wang, Z.; Larson, R. G. Molecular Dynamics Simulation of Interactions between a Sodium Dodecyl Sulfate Micelle and a Poly ( Ethylene Oxide ) Polymer. **2008**, 2888–2900.
- (48) Shang, B. Z.; Wang, Z.; Larson, R. G. Molecular Dynamics Simulation of Interactions between a Sodium Dodecyl Sulfate Micelle and a Poly(Ethylene Oxide) Polymer. *J. Phys. Chem. B* **2008**, *112*, 2888–2900.
- (49) Ma, C.; Li, G.; Xu, Y.; Wang, H.; Ye, X. Determination of the First and Second CMCs of Surfactants by Adsorptive Voltammetry. *Colloids Surfaces A Physicochem. Eng. Asp.* **1998**, *143*, 89–94.
- (50) Konkell, J. T.; Myerson, A. S. Empirical Molecular Modeling of Suspension Stabilisation with Polysorbate 80. *Mol. Simul.* **2008**, *34*, 1353–1357.
- (51) Raith, K.; Schmelzer, C. E. H.; Neubert, R. H. H. Towards a Molecular Characterization of Pharmaceutical Excipients: Mass Spectrometric Studies of Ethoxylated Surfactants. *Int. J. Pharm.* **2006**, *319*, 1–12.
- (52) Travis, K. P.; Bankhead, M.; Good, K.; Owens, S. L. New Parametrization Method for Dissipative Particle Dynamics. *J. Chem. Phys.* **2007**, *127*, 014109–1 – 12.
- (53) Liyana-arachchi, T. P.; Jamadagni, S. N.; Eike, D.; Koenig, P. H.; Siepman, J. I.; Liquid – Liquid Equilibria for Soft-Repulsive Particles : Improved Equation of State and Methodology for Representing Molecules of Different Sizes and Chemistry in Dissipative Particle Dynamics Liquid – Liquid Equilibria for Soft-Repulsive Particles : Imp. *J. Chem. Phys.* **2015**, *142*, 044902–1 – 13.
- (54) Cates, M. E.; Candau, S. J. Statics and Dynamics of Worm-like Surfactant Micelles. *J. Phys. Condens. Matter* **1990**, *2*, 6869–6892.
- (55) Larson, R. G. The Lengths of Thread-like Micelles Inferred from Rheology. *J. Rheol.* **2012**, *56*, 1363–1374.

## Chapter 2

### Molecular Dynamics Simulations of Sodium Dodecyl Sulfate Micelles in Water – the Effect of the Force Field

The work in Chapter 2 has been published as: X. Tang, P. Koenig, and R. G. Larson  
Molecular Dynamics Simulations of SDS Micelles in Water – the Effect of the Force  
Field. *J. Phys. Chem. B*, 118 (2014) 3864-3880.

#### 2.1. Introduction

Sodium dodecyl sulfate (SDS) is perhaps the most widely studied anionic surfactant, and is used in both fundamental scientific studies and industrial products, such as detergents and body washes. For SDS in water without salt at 25 °C, the first critical micelle concentration (CMC), at which fairly abrupt changes in solution properties occur, is 0.008 M<sup>56-59</sup> and the average aggregation number near this concentration is around 60.<sup>60-62</sup> The first CMC can be measured by various techniques including electrical conductivity, surface tension, light scattering,<sup>6,62</sup> as well as small-angle X-ray scattering (SAXS)<sup>57</sup> and small-angle neutron scattering (SANS).<sup>59,63</sup> At the first CMC, spherical and/or ellipsoidal micelles with a distribution of aggregation numbers are formed,<sup>60,61,64,65</sup> but the solution rheology remains Newtonian.

As the concentration of SDS passes through the “second CMC”, which is about 0.069 M in water, a more subtle transition than that at the first CMC is observed (usually as a small change in slope of a property plotted versus concentration) by light scattering, conductivity, viscosity, velocity of sound, fluorescence probes, cyclic voltammetry, adsorptive voltammetry and polarography,<sup>5,6,49,66</sup> and anisotropy of micelle properties emerges, along with higher micelle aggregation numbers. The second CMC is typically associated with the growth of elongated micelles, which become rodlike or threadlike as the concentration continues to increase.

Small-angle neutron scattering (SANS) shows a possible elliptical cross-section rather than circular cross-section for rodlike micelles.<sup>64,65</sup> Viscoelastic rheology is typically observed beyond the second CMC when threadlike micelles are formed. As the concentration of SDS is raised further to 36% by weight, or 1.250 M, Kekicheff and coworkers have found higher-order phases, such as hexagonal and lamellar phases coexisting with isotropic cubic phases.<sup>16</sup> Once lamellar phases are formed, the solutions phase separate.

The phase behavior and micellar structure are also sensitive to temperature, and type and concentration of any co-surfactant, counterions and added salts.<sup>16,17,59,61,67,68</sup> Hammouda recently studied the effects of surfactant concentration, temperature, and salt concentration on SDS micelle structure using SANS.<sup>65</sup> An oblate ellipsoidal structure was inferred and the micelle size was observed to increase, as expected, with a decrease in temperature, an increase in the NaCl concentration or an increase in the surfactant concentration.<sup>65</sup> (However, Vass et al.<sup>69</sup> show that some scattering data can be equally



well fit by monodisperse prolate ellipsoids or slightly polydisperse oblate ellipsoids.) With increasing salt, at 1% SDS and 21° C, Hammouda reports that the micelles became increasing oblate, with a long axis reaching 6.5 nm diameter at 0.5 M salt, and the short dimension remaining at around 3 nm thickness. In many industrial applications, surfactant solutions are deployed at concentrations above the second CMC and below that of the lamellar phase; at such concentrations of industrial relevance, viscoelastic properties are important.

In recent years, the properties of SDS solutions have been studied extensively by molecular dynamics (MD) simulations. MD simulations provide a unique resolution of structural details down to the Angstrom scale. With increasing computational power, all-atom (AA) MD simulations of surfactant solutions containing up to millions of atoms and time scales of hundreds of ns have been carried out.<sup>25</sup> Atomistic MD simulations can be accelerated, especially for surfactants with long hydrocarbon tails, by grouping each carbon with its bonded hydrogen atoms into a pseudo or united-atom (UA) and applying a larger time step size.<sup>26</sup> MD UA simulations usually speed up the simulations 3-4 fold compared with AA simulations, without sacrificing atomistic details significantly. Simulations of SDS micelles in water have been studied using the four popular empirical force fields, namely CHARMM, OPLS, AMBER, and GROMOS, and some additional specialized force fields. Both NVT and NPT ensembles, with either initially randomly distributed SDS molecules, or initially prepackaged spherical micelles, have been employed.

In pioneering work, Shelley, Watanabe and Klein<sup>44</sup> carried out UA MD simulations of a preassembled SDS micelle using partial charges of the SDS head group atoms obtained from the semi-empirical quantum mechanical “Austin Model 1”,<sup>70</sup> and basing intermolecular and intramolecular parameters of the SDS head group on X-ray diffraction data and hydration energy.<sup>71,72</sup> These partial charges and other optimized parameters were adopted in later SDS simulations using OPLS, AMBER, and GROMOS force fields.<sup>48,73–76</sup> MacKerell<sup>32</sup> carried out an AA MD simulation of a preassembled SDS micelle using the CHARMM force field with different partial charges, and intermolecular and intramolecular parameters. These partial charges and optimized parameters were adopted in later SDS simulations using the CHARMM force field.<sup>77,78</sup> The simulations of Shelley et al. and of MacKerell were performed in a small box (corresponding to a high SDS concentration) and the simulation times were too short for equilibration of counterion positions due to computational limitations.<sup>32,45,79</sup>

A milestone study of properties of SDS micelles composed of 60 SDS was performed in 2002 by Bruce et al.<sup>45</sup> in a box size corresponding to a concentration of 0.4 M for 5 ns using AMBER-UA force field parameters from Berkowitz’s group.<sup>46</sup> They found that a stable distribution of counterions and an equilibrated, slightly nonspherical, micelle shape were reached after only 1 ns of simulation. Structural properties, including the radius of gyration, shape eccentricity, solvent accessible surface area, dry hydrocarbon core, dihedral angle distribution, and micelle diffusivity were evaluated. In a follow-up study by Bruce et al.,<sup>79</sup> the effects of counterions on SDS micelle properties and diffusivity of water near the micelle surfaces were studied extensively using the same force field. The

structural stability of SDS micelles with aggregation number ranging up to 121 was also studied using a CHARMM-AA force field with 8488 water molecules for up to 4.5 ns.<sup>77,78,80</sup>

A long, 21 ns simulation for a preassembled SDS micelle composed of 60 surfactants was performed by Palazzesi et al. at 0.2 M using a general AMBER force field (GAFF) in 2011.<sup>81</sup> They observed a roughly prolate SDS micelle with eccentricity of 0.15. This result is consistent with recent SANS and SAXS studies that show nonspherical shapes of cesium dodecyl sulfate micelles.<sup>69</sup> Here the eccentricity is defined as  $1 - I_{\min}/I_{\text{ave}}$ , where  $I_{\min}$  is the smallest of the three moments of inertia along the principal axes of the micelle, and  $I_{\text{ave}}$  is the moment of inertia averaged over the three axes.

The use of UA beads to represent carbon atoms with their bonded hydrogens was first implemented more than 30 years ago.<sup>26</sup> It has been applied to the most commonly used empirical force fields (i.e., CHARMM, OPLS, AMBER, and GROMOS) and used also in specialized UA force fields.<sup>82-84</sup> However, use of united atoms has been found to lead to inaccuracy in intermolecular interactions between aromatic compounds relative to experimental results.<sup>27</sup> By a “specialized” UA force field we mean one developed for a specific chemical system and used only within a small group of researchers; such force fields will not be discussed here. The more widely used CHARMM-UA, AMBER-UA and OPLS-UA force fields were last updated at least ten years ago and have not been significantly improved on since.<sup>31,85</sup> An exception is the GROMOS force field available only in UA form which has been updated several times since its introduction.<sup>35,86-88</sup> Parameterization of the GROMOS force field is based on reproducing the pure liquid

density, heat of vaporization, as well as free enthalpy of hydration, and apolar solvation for a variety of compounds. Instead of applying simple geometric combination rules for Lennard-Jones (L-J) potentials of all pairs of interacting atoms, up to three sets of L-J potential parameters are available for each atom from which one is chosen based on polar and ionic interactions between the two atoms. Therefore, in GROMOS there are up to nine possible combination values of force field parameters for each pair of atoms. In addition, pair potentials between the first and the fourth atoms connected through three covalent bonds - i.e., the 1-4 L-J potentials – involve usage of specialized L-J parameters, which were optimized separately instead of using simple combination rules as in all other UA force fields. These specialized steps insure the accuracy of the force field at a UA level when coarse-grained nonpolar hydrogen is collapsed into the bead for the connected carbon. However, this special treatment means that introducing a new atom type into GROMOS becomes more challenging because it may involve parameterizing multiple 1-4 L-J parameter sets, one set for the interaction of the new atom with each other atom type. Several efforts have been made to simulate SDS using the GROMOS force field by choosing the closest atom type available for each SDS atom to avoid additional parameter optimizations for any atom types in SDS that are missing in the GROMOS force field set.<sup>48,76,89,90</sup> Specifically, to avoid developing a series of 1-4 L-J force field parameters for the ionic oxygens in the sulfate head group of SDS, the ionic oxygens have been replaced by either carboxyl oxygens by Sammalkorpi et al.<sup>76</sup> or by two carbonyl oxygens and a hydroxyl oxygen by Shang et al.<sup>48</sup> The carboxyl, carbonyl and hydroxyl oxygen force field parameters are already available in GROMOS.<sup>48,76,89,90</sup> Since the intramolecular

potential for the head group is not available in the standard GROMOS force field considered in this study, this potential was generated using the corresponding carboxyl (in Sammalkorpi et al.)<sup>29</sup> or carbonyl (which in Shang et al.<sup>48</sup> was used for *intramolecular* potentials of all bonds involving the ionic oxygens, including the oxygen whose *intermolecular* interactions was represented by a hydroxyl oxygen). With these simple replacements within GROMOS, agreement with experimental results and with other simulations was obtained in simulations of a SDS micelle with 60 surfactants at 0.4 M for 5 ns.<sup>48,89</sup> A GROMOS force field also enabled simulation of self-assembly of spherical micelles of SDS surfactants in water from a solution containing up to 400 SDS within a 200 ns time scale.<sup>76</sup> At the end of the 200 ns simulation, an aggregation number of 70 was observed at a concentration of 1.0 M SDS, and an aggregation number of 60 at a concentration of 0.4 M,<sup>76</sup> which are lower aggregation numbers than observed experimentally at these concentrations. In a coarse-grained simulation extending up to 5  $\mu$ s, an aggregation number of 113 was observed at a concentration of 1 M in a box containing 1000 SDS.<sup>91</sup> The simulated aggregation number using the coarse-grained force field is significantly lower than the experimental value at these high concentrations, which suggests that even coarse-grained simulations might not reach equilibrium within 5  $\mu$ s.

In summary, simulations of small-*preassembled* spherical SDS micelles in solutions have been carried out using four popular force fields and results are consistent with experimental measurements. Achieving equilibrated self-assembly of SDS micelles at even the coarse-grained level is still prohibitively expensive, however, due to the long

simulation times needed to reach equilibrium. Thus, to date, most MD simulations of SDS micelles in aqueous solutions at the atomistic UA and AA levels have focused on preassembled spherical micelles composed of 60 SDS in boxes so small that the surfactant concentrations in these boxes were higher than the second CMC, where micelles with aggregation number higher than 60 are the dominant species in solution. To our knowledge, to date no simulations have addressed the effect of box size on micelle properties of the same aggregation number, which could be significant since box size might affect the counterion distribution around an SDS micelle. Nor have elongated micelles composed of more than 121 surfactant molecules been simulated. In addition, comparisons of SDS micelle structures obtained from different force fields have not yet been carried out.

It is particularly important to assess the ability of different force fields to simulate accurately the structures of surfactant aggregates other than simple spherical micelles, since simulating spherical micelles may not be a very sensitive test of the force field. The dimensionless Israelachvili “packing parameter,”  $p = V/l_c a_0$  controls micelle shape, where  $a_0$  is the area occupied by the hydrophilic head on the micelle surface.<sup>92</sup> The length  $l_c$  of the surfactant tail and the tail volume  $V$  already to a large extent control the size, shape, and structure of a micelle whose aggregation number is only large enough to allow spherical micelles to form (as is the case for an aggregation number of 60 for SDS). With increasing aggregation number,  $a_0$  must either decrease or the spherical shape must give way to some other shape, and this transition and the micelle shape at higher

aggregation number could be more sensitive to the force field than is the structure of a simple spherical micelle.

In addition, since some of the most widely applied industrial surfactant solutions contain primarily elongated micelles, it would be of interest to simulate such SDS micelles at a concentration above the second CMC and with enough surfactant molecules to form large micelles. Finally, there has not yet been a comprehensive comparison of the structures of SDS aggregates, either spherical or elongated, obtained using different force fields. We therefore here will compare such SDS micelles, simulated using three versions of GROMOS (UA),<sup>48,86,87</sup> as well as OPLS-UA,<sup>31,93</sup> CHARMM36 (AA),<sup>40</sup> and OPLS-AA<sup>30</sup> force fields. The sodium ion and chloride in the GROMOS53A6 force field has been re-parameterized in the GROMOS54A7<sup>94</sup> force field, and these values were used in the GROMOS54A8<sup>95</sup> force field as well. The parameters for all the atoms used in our SDS simulations are the same in GROMOS54A7 as they are in GROMOS54A8, but the sodium ion parameters differ somewhat from those in GROMOS53A6. We therefore tested the new sodium ions in the GROMOS54A8 force field in simulations with a SDS micelle of aggregation number 60, and found only a slight difference in the Na-O RDF obtained using GROMOS53A6 (Fig. A.5). As described below, all of these force fields, except for CHARMM36, need special adaptations to allow simulation of the sulfate head group of SDS, while CHARMM36 already contains parameters for the sulfate atoms in the standard force field parameter set. We will also consider alternative L-J parameter sets for sodium ions. We will present results for spheroidal micelles of aggregation numbers of 60 and 100 in different boxes sizes to mimic concentrations of 0.800 M and

0.050 M in water. We will also simulate a periodic threadlike micelle composed of 300 SDS molecules and a finite-length rodlike micelle or a bicelle composed of 382 surfactants in water and in 2% NaCl. The rest of the article is structured as follows: Section 2.2 lists the computational models and simulation methods; Section 2.3 contains the results; and Section 2.4 summarizes the conclusions.

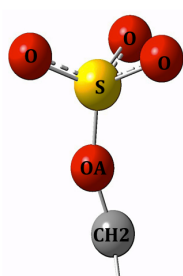
## **2.2. Computational Models and Simulation Methods**

### **2.2.1 Partial Charges**

Three sets of partial charges, listed in Table 2.1, were investigated. The partial charges of the SDS head group given in the second column, from Shelley et al., will be tested in simulations using all the force fields considered here except the CHARMM36 and GROMOS53A6OXY force fields. The standard partial charges used in the CHARMM36 force field are given in the third column, while the fourth column lists partial charges suggested recently by the GROMOS developers<sup>96</sup> and used here with the GROMOS53A6OXY force field.<sup>87</sup> We cannot cover all the force field parameters used for SDS, but limit ourselves to the updated popular force fields available for use in the GROMACS simulation engine, namely GROMOS, CHARMM-AA, OPLS-AA and OPLS-UA. The AMBER-AA force field is not tested against SDS micelle simulations since no updated general AMBER force field (GAFF) or AMBER12 lipid force field parameter set is available in GROMACS.



**Table 2.1.** Partial charges of the SDS head group tested in this study.



Charge sets	M. Klein (1990)	CHARMM	GROMOS Developer
O	-0.654	-0.650	-0.635
S	1.284	1.330	1.000
OA	-0.459	-0.280	-0.360
CH <sub>2</sub>	0.137	-0.100	0.265

In Table 2.1, “O” represents the ionic oxygen; “OA” represents the ester oxygen; and “CH<sub>2</sub>” represents the alpha carbon attached to the ester oxygen and its bonded hydrogens. The charge of this “CH<sub>2</sub>” is the net charge of the alpha carbon and connected hydrogens for all-atom CHARMM and OPLS force fields, and is the charge on the united CH<sub>2</sub> bead of a carbon in the GROMOS and OPLS-UA force fields.

## 2.2.2 Force Fields

We consider six different force fields, three of them different versions of GROMOS, as well as CHARMM36, OPLS-AA, and OPLS-UA, as described below.

### 2.2.2.1 GROMOS

The GROMOS43A1 force field has been successfully applied to simulations of proteins.<sup>97</sup> GROMOS45A3, on the other hand, was developed to study lipids with long alkane chains and/or branches, by reproducing pure alkane liquid density and heat of vaporization at room temperature and pressure.<sup>35</sup> Several SDS micelle simulation studies have successfully applied the GROMOS45A3 force field.<sup>48,89,98</sup> To address accurately solvation effects and partition coefficients for molecules of different polarities, the newer GROMOS53A6 force field was developed to reproduce the free enthalpies of hydration in SPC water and the apolar solvation for a series of compounds.<sup>86</sup> GROMOS53A6OXY

refined further the GROMOS53A6 force field parameters for oxygen-containing compounds to optimize the predictions of their liquid density, enthalpy of vaporization, and solvation properties.<sup>87</sup> Because of the impact of head group oxygen parameters on SDS micelle properties, we include GROMOS53A6OXY in this study although it is not available as part of the standard GROMACS simulation engine. In short, we consider three versions of the GROMOS force field: GROMOS45A3,<sup>48</sup> GROMOS53A6, and GROMOS53A6OXY using SPC water model. Two sets of partial charges for SDS head groups are tested. One is adopted from Shelley et al.<sup>21</sup> and is applied here to GROMOS45A3 and GROMOS53A6 force fields, and the other (“GROMOS Developer”) was selected based on analogies to existing GROMOS force field parameters and we apply it to the GROMOS53A6OXY force field. Thus, three different combinations of GROMOS force field parameter sets and partial charge sets are tested here.

The UA coordinate file for SDS was generated using Materials Studio (MS), followed by hydrogen removal. The topology file was generated using the topology auto generator ProDRG server.<sup>99</sup> The partial charges and torsional parameters of the generated topology file were adjusted manually.<sup>100</sup> The Ryckaert-Bellemans (R-B) potential was adopted for the dihedral parameters of the hydrocarbon tail of SDS.<sup>101</sup> The three sets of GROMOS force field parameters described above are tested. For the GROMOS45A3 force field, Shang et al.<sup>48</sup> represented the three ionic oxygen atoms in the head group of SDS by two carbonyl oxygen atoms and one hydroxyl oxygen atom<sup>48</sup> for inter-molecular parameters, and three carbonyl oxygen atoms for intra-molecular parameters. We follow that approach here for our implementation of the GROMOS45A3 force field. For the other

two GROMOS force field/partial charge sets, each of the three ionic oxygen atoms in the head group are represented as carboxyl oxygens, and the bonded parameters for the SDS head group are taken from Berkowitz's group,<sup>46,102</sup> which they, in turn, obtained from Shelley et al.,<sup>21</sup> who were guided by x-ray studies.<sup>46,102</sup>

### **2.2.2.2 CHARMM**

The CHARMM22 force field is an AA force field developed for studying proteins in condensed phases while retaining compatibility with earlier published nucleic acid and lipid CHARMM-AA parameters.<sup>103</sup> The addition of a 1-3 L-J Urey-Bradley potential for the pair angle bending potentials between the first and the third atoms connected through two covalent bonds allowed optimization of the vibrational spectra. The intermolecular and bonded parameters were optimized based on experimental spectroscopy measurements of geometrics and vibrational spectra, as well as on quantum mechanical calculations of torsional energy surfaces. The intermolecular or nonbonded parameters, mainly partial charges, were then optimized for solvent density, model compound heats and free energies of vaporization, solvation, and structural geometries with a modified TIP3P water.<sup>103</sup> 1-4 L-J interaction and 1-4 electrostatic interaction parameters were parameterized explicitly instead of using a simple scaling rule. The CHARMM force field parameterized many of the commonly studied biological molecules in one compatible force field and therefore has been widely applied. Systematic refinement of CHARMM22 resulted in CHARMM27, which improved the alkane L-J parameters, torsional parameters, and the partial atomic charges of the phosphate lipids.<sup>104</sup> The

recently updated CHARMM36<sup>40,105</sup> force field led to improvement in two important properties of lipid bilayers over CHARMM27: CHARMM36 gives a zero surface tension at the experimental bilayer lipid density and matches the NMR (nuclear magnetic resonance) signature splitting of the deuterium order parameters in the glycerol and upper-chain (head-head-group) carbons. The differences between CHARMM36 and CHARMM27 parameters relevant to SDS are in the L-J parameters of the ester oxygen, and the dihedral functions of the aliphatic tails of SDS. The coordinate file of the AA SDS for our work was generated using Materials Studio. The topology file for SDS was generated automatically using the SwissParam server<sup>106</sup> with modifications of the aliphatic dihedral parameters. Partial charges and L-J interaction parameters were also adjusted to match the available CHARMM27 and CHARMM36 SDS parameters. Here, we used the CHARMM36 force field. A modified TIP3P water model, as given in the CHARMM folder of the GROMACS engine, was used in all simulations.

### **2.2.2.3 OPLS-AA**

The OPLS-AA force field optimizes liquid densities and heats of vaporization for various common organic liquids, in addition to fitting rotational energy profiles based on *ab initio* calculations. The bond stretching and angle bending parameters were mostly adopted from the AMBER-AA force field.<sup>30</sup> The intramolecular and intermolecular parameters of the head group of SDS are not included in the standard OPLS-AA force field and were therefore adopted from Berkowitz's group.<sup>46,102</sup> The rest of the parameters were the standard OPLS-AA ones. All L-J cross interactions were calculated according to

the normal OPLS mixing rule. A thorough study of the effect of seven different sodium ion models on SDS micelle properties within the OPLS-AA force field will be described in what follows. These sodium ion parameters were either optimized recently, or are available in the GROMACS simulation engine, as options within the OPLS-AA force field.

Topology files were generated automatically from the AA pdb file of SDS using Topogen.pl written by Lemkul.<sup>107</sup> The hydrocarbon tail parameters were adopted from the force field file using the R-B potential.<sup>101</sup> The two sodium ion force fields available<sup>108,109</sup> using a TIP4P water model in the GROMACS OPLS-AA folder were parameterized at least 25 years ago. Therefore, five additional recently parameterized sodium ion models from Dang,<sup>110</sup> Joung and Cheatham,<sup>111</sup> and Jensen and Jorgensen<sup>112</sup> are also tested in what follows. The parameterization of ions involves optimization of the thermodynamic properties of ion pairs in a specific water model, the radial distribution describing the ion-water structure, or both. Since the sodium ions models studied here were parameterized with different water models, for each sodium ion model considered, we used the corresponding water model for which that sodium model was originally developed. In addition, the effects of the water model will also be tested using ion models from Jorgensen and coworkers<sup>108</sup> and from Aqvist<sup>109</sup> to understand water-model effects on micelle properties.

#### 2.2.2.4 OPLS-UA

Developed in 1988, the OPLS-UA or OPLS/AMBER force field optimizes liquid densities and heats of vaporization for a variety of organic liquids and is compatible with TIP4P, TIP3P, and SPC water models.<sup>113</sup> The coordinate file of UA SDS was generated here using Materials Studio followed by hydrogen removal. The topology file was generated using the topology auto generator ProDRG server<sup>99</sup> and modified manually. Bond stretch, torsion, and L-J parameters of the ester oxygen and alpha carbon in the SDS head group were adopted from transferable potentials for the phase equilibria–united atom (TraPPE-UA) force field<sup>93</sup> as developed by Pierre Verstraete from Procter and Gamble. While other L-J cross interactions were calculated from the normal mixing rule, the L-J interaction parameters of the ester oxygen with the water oxygen were adopted from Shang et al.<sup>48</sup> The remaining parameters of the SDS head group were adopted from the work of Berkowitz’s group,<sup>46,102</sup> and are the same as those used in the OPLS-AA force field described above. Also adopting parameters for SDS tail groups from the newly parameterized TraPPE-UA force field could further improve the behavior of SDS micelle simulations, but this was not done here. The head group parameters (except for those of the ester oxygen and alpha carbon) were drawn from an AMBER UA force field. The SPC water model is used with this force field.

### 2.2.3 Simulation Methods

Preassembled micelles, either spherical, short rodlike, periodic cylindrical micelles, or disklike bicelles, were generated using PACKMOL software.<sup>114,115</sup> Energy minimization was performed before and after the addition of water and counterions or salts to keep the maximum force on any atom below  $1000 \text{ kJ mol}^{-1} \text{ nm}^{-2}$ . Then, water and ions were distributed randomly outside of these micelles within the simulation box. Table 2.2 lists details of simulations performed in this study and the shape of the micelle at the end of the simulations. The surfactants were studied at three concentrations: 0.05 M in a box size of  $12.65 \times 12.65 \times 12.65 \text{ nm}^3$  at an aggregation number of 60, and a box size of  $15.5 \times 15.5 \times 15.5 \text{ nm}^3$  at an aggregation number of 100, which is between the first and the second CMC, where spherical or ellipsoidal micelles are the dominant species; 0.80 M in a box size of  $5 \times 5 \times 5 \text{ nm}^3$  at an aggregation number of 60, and a box size of  $6 \times 6 \times 6 \text{ nm}^3$  at an aggregation number of 100, which is between the second CMC and liquid crystalline SDS concentration, where micelles of higher aggregation number are dominant; and 0.26 M in box sizes of  $11 \times 11 \times 16$  at an aggregation number of 300, and  $11 \times 11 \times 20 \text{ nm}^3$  at an aggregation number of 382, which is above the second CMC, below the liquid crystalline phase, and close to the concentration of surfactants in consumer products. At a surfactant concentration of 0.26 M, either only sodium counter ions or these counter ions plus 2% by weight sodium chloride were added to study the effect of salt on micelle shapes. For the other concentrations, only sodium counter ions were added, with no additional salt. Initially spherical micelles were preassembled at aggregation numbers of 60 and 100.

Periodic cylindrical micelles were preassembled at an aggregation number of 300. Short rodlike micelles were preassembled at an aggregation number of 382.

The GROMACS simulation engine was used for all the simulations. Temperature control was accomplished using the velocity-rescaling weak-coupling method. Pressure control was applied using the Berendsen weak-coupling method either isotropically or semi-isotropically, at 300 K ( $\tau_T$ ) and 1 bar ( $\tau_P$ ), where  $\tau_T$  and  $\tau_P$  are the duration of update steps or time constants, taken to be 0.1 ps and 1.0 ps respectively, for temperature and pressure.

A cutoff scheme was used for short-range nonbonded interactions according to the force field recommendation values respectively, and long-range electrostatic interactions were computed using the Particle Mesh Ewald technique. A time step of 2 fs was used for AA force field simulations, and of 5 fs for UA force fields. The neighbor list was updated every ten time steps. Bond lengths were constrained using LINCS. Bonds containing hydrogen were constrained using SHAKE. And the water geometry was constrained using SETTLE. Before the production MD run, position-restraint runs of duration 200 ps were employed by harmonically restraining the head group atoms with a force constant of  $1000 \text{ kJ mol}^{-1} \text{ nm}^{-2}$  to allow the relaxation of water and to reach desired temperature and pressure gradually. The production MD run lasted for 20 ns if using AA force fields, and 30 ns if using UA force fields. Trajectories after 10 ns were used for small micelles of 60 and 100 SDS analyses, and trajectories of the last 5 ns were used for micelles of 382 SDS analysis, during which the potential energy and radius of gyration remained stable.



**Table 2.2.** Simulations carried out in this study and the resulting shapes of the micelles by the end of the run.

Initial Shape of micelles	ForceField and Water model		GROMOS-UA/ SPC			OPLS-UA /SPC	CHARMM36 /TIP3P	OPLS-AA /TIP4P
			45A3	53A6	53A6OXY			
	Partial Charges		Shelley et. al. <sup>44</sup>	Shelley et. al. <sup>44</sup>	GROMOS Developer	Shelley et. al. <sup>44</sup>	CHARMM <sup>32</sup>	Shelley et. al. <sup>44</sup>
SPH	60 SDS	0%NaCl	ELL	ELL	ELL	ELL	ELL	ELL
	100 SDS	0%NaCl	BICELLE	ELL	ELL	ELL	ELL	BICELLE
INF CYL	300 SDS 0.26M	0%NaCl	INF RIB	3 ELLs	3 ELLs	3 ELLs	ROD	INF RIB
		2%NaCl	INF RIB	INF CYL	INF CYL	ROD	ROD	INF RIB
ROD	382 SDS 0.26M	0%NaCl	BICELLE	4SPHs	ROD	3 SPHs	2 RODs	BICELLE
		2%NaCl	BICELLE	ROD	ROD	ROD	RODs	BICELLE
BICELLE	382 SDS 0.26M	2%NaCl	BICELLE	2RODs	ROD	ROD	BICELLE	BICELLE

Initial structures of surfactants were preassembled SDS micelles. ELL: ellipsoidal shape; BICELLE: similar to bilayer structure but with a much smaller aggregation number; RIB: finite Ribbon-like structure or bilayer structure in an elongated shape; INF: infinite length; ROD: finite cylindrical micelle with two end caps; INF CYL: infinite cylindrical shape. “1SPH and 1ROD” one spherical micelle and one rodlike micelle.

## 2.3. Results and Discussion

### 2.3.1 Spherical Micelles Composed of 60 SDS in Small and Large Simulation Box

#### Sizes

As mentioned above, although SDS micelles have a distribution of aggregation numbers whose average increases with SDS concentration, to save computation time, in typical simulations a single micelle with small aggregation number of 60 is simulated in a small periodic box corresponding to a concentration above the 2<sup>nd</sup> CMC (which is at 0.069 M). In this study, we compare micelle properties at two different simulation box sizes that correspond to concentrations of 0.80 M and 0.05 M, which are above and below the 2<sup>nd</sup> CMC, respectively, for multiple popular force field parameter sets. Specifically, we compare radial density distribution functions (RDF's) of head groups, tail groups of

SDS, counterions, and water about the micelle center of mass (COM), radii of gyration ( $R_g$ 's) of SDS and carbon tails,  $R_g$  of sulfur atoms about the micelle COM, RDF's of sodium ions to ionic oxygens of SDS head groups, solvent-accessible surface areas (SASA's), and the hydration numbers of the tail carbons.

In general, we find that after equilibration, there are greater differences in micelle properties resulting from different force fields than from the differences in simulation box sizes. But even many of the differences resulting from different force fields are not large for micelles of aggregation number 60. As shown in Figure 1, at 0.05 M, the RDFs of the SDS tail groups are nearly the same for the different force fields. The differences in peak position are less than 0.5 Å. The height and width of the peaks are only slightly different. No significant differences are observed when using the same force field but different simulation box sizes (figure not shown). The low density region for the tail groups near the center of mass suggests a vacancy in the micelle center.<sup>80</sup> This structure of the SDS micelle is consistent with the Hayter and Penfold's three shell model<sup>116</sup> and a dry hydrocarbon core. The first shell is composed of hydrophobic paraffin core without water wetting; the second shell is composed of mainly hydrophobic tails and a small amount of water and sodium ions; and the third shell is composed mainly of hydrophilic heads with a significant amount of "bound" water, sodium counterions, and a small amount of protruding tails. A slightly stronger binding of sodium ions to the micelle is observed for the GROMOS45A3 and OPLS-AA force fields, as shown by the insert in Figure 1. Since sodium ions screen the electrostatic repulsion between the head groups and modify the packing parameters, different micellar properties might be expected for the above two

force fields, compared to the others, and this expectation is realized for larger micelles, as discussed in detail later.

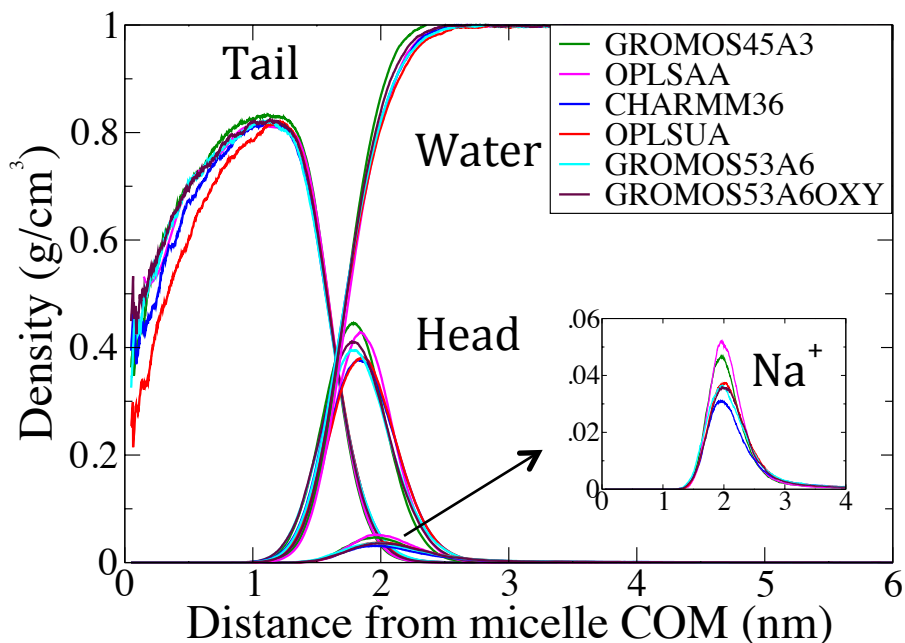


**Figure 2.1** Radial density distribution of tail groups, head groups, counter ions, and water about the micelle center of mass (COM) for a micelle composed of 60 SDS in a simulation box size of  $12.65 \times 12.65 \times 12.65 \text{ nm}^3$ , for various force fields. The order of the listed force fields in the legend is based on the binding strength of sodium ions to the ionic oxygen as shown in Figure 2.3b, with highest strengths at the top.

Micellar sizes can be quantified by radius estimates from experiments and simulations. Experimentally, the radius of the SDS micelle hydrocarbon core was found by small-angle X-ray scattering (SAXS) to be 1.52 nm for 0.18 M in water at  $22^\circ\text{C}$ <sup>60</sup>, and a similar value was obtained by fitting small-angle neutron scattering (SANS) data<sup>61</sup> for 0.1 M SDS in aqueous solution at  $25^\circ\text{C}$ . In SANS experiments, the measured radius is considered to be equal to the radius of the hydrocarbon core because the scattering length

density of sulfate head groups and D<sub>2</sub>O water are equal to within experimental error.<sup>63</sup> The corresponding micelle aggregation numbers are approximated from the measured micelle size and model-fitting of micelle shapes. The micellar hydrodynamic radius R<sub>h</sub> measured by Quasielastic Light Scattering Spectroscopy, is 2.2nm for 0.069 M SDS in 0.15 M NaCl at a temperature of 25°C<sup>59</sup>. Here R<sub>h</sub> was estimated as an average over all aggregation numbers and orientations of the somewhat ellipsoidal micelle,<sup>59</sup> and includes water molecules and counter ions bound to the surface of the micelle. In MD simulations, the radius of the whole micelle R can be determined from the average radius of gyration of the micelle, assuming an approximately uniform mass distribution within the micelle, if the polydispersity P in micelle aggregation number is known, using  $R_g^2 = \frac{3}{5} R^2 \left[ \frac{1+10P^2+15P^4}{1+3P^2} \right]$ .<sup>63</sup> In our study using the six force fields, using the computed R<sub>g</sub> and the above formula, the radii R range from 1.97 to 2.04 nm among the different force fields, if we take the polydispersity P to be 10% (0.1), and from 1.81 to 1.87 nm if we assume a polydispersity of 20%. The radius R can also simply be taken as the RMS distances of the sulfur atoms from the micelle COM<sup>45</sup> and it is in the range from 1.89 to 1.98 nm for the different force fields. Within the same force field, the difference in radii inferred from these two measurements is within 0.1 nm at a polydispersity of 10-20% and is negligible. The hydrodynamic radius R<sub>h</sub> can be related to R using the method of Bruce et al.<sup>45</sup> to incorporate the bound water near the micellar surface. The difference between simulations and scattering experiments<sup>60,61</sup> in the radii of gyration is less than 0.1nm. For all force fields, the radius of gyration R<sub>g</sub> or equivalently radius R in the smaller box is

less than 0.02 nm smaller than in the bigger box. All the measurements using different force fields agree with experimental measurements to within 0.1 nm. The prolatenesses<sup>117</sup> of micelles for different force fields are all less than 0.2 (but greater than zero) and the asphericities<sup>117</sup> are less than 0.3. Thus, all force fields produced micelles of slightly prolate shape with radii that match the experimental values.

The hydrophobicity of a micelle surface can be evaluated using the solvent-accessible surface area (SASA). In brief, a probe of spherical “water” molecule of radius 1.4 Å is rolled over the rough potential energy surface of the micelle to measure the hydrophobic, hydrophilic, and total surface areas of the micelle. The SASA values of the SDS micelles vary more significantly from one force field to the next than do the various radii. The hydrophilic percentage does not seem to correlate with the size of the micelle or the total SASA. There are no significant differences in the percentages of the hydrophilic surface area for the two box sizes.

Interactions between the sodium counterion and the SDS head group are believed to be critical to packing parameters and therefore to the shape of the micelle. The interaction can be studied using the RDF between sodium and sulfur, and between sodium and ionic oxygens in SDS. As shown in Figure 2.2, for each force field there are two large, distinct peaks within the first 1 nm, corresponding to the first two sodium shells. The heights and positions of these differ greatly among the force fields. From the first peak in both figures, we find that distances between sodium and sulfur or ionic oxygen are shortest for the GROMOS45A3 force field (with the adaptations for the sulfate head group, as described in Section 2.2.1 above), followed by the CHARMM force field, which has a

significantly smaller peak. For the OPLS-AA force field (using the head group parameters described in Section 2.2.3), the distance between the sodium and either sulfur or ionic oxygens is greater than for the CHARMM force field, but the height of the peak for OPLS-AA is considerably greater than for CHARMM36. The distance is greater and the peak is smaller for OPLS-UA, and no apparent first peak is observed at all for all the GROMOS force fields except for GROMOS45A3. A better resolution of peaks is found in the sodium-to-ionic oxygen RDF's than in those for sodium to sulfur. This may be due to the spatial arrangement of the SDS head group in which the sulfur atom is buried under the three ionic oxygens. To quantify more accurately the ion distributions within the two shells of sodium near micelle surface, we integrated the shell volume under each peak as described in the caption to Figure 2.3. As shown in Figure 2.3, the total fraction of sodium ions within the first two shells of the sodium-to-ionic oxygen RDF is roughly comparable for all force fields but is smallest for the CHARMM force field. The relative numbers of sodium ions in the first versus the second shell are comparable for GROMOS45A3, OPLS-AA, CHARMM, and OPLS-UA, with OPLS-AA having the highest proportion within the first shell, followed by GROMOS45A3. However, for GROMOS53A6 and GROMOS53A6OXY, 90% of the first two shell's sodium ions are concentrated in the second shell with little penetration into the first shell. There are no significant differences in the RDF's for Na-S or Na-O between the GROMOS53A6 and GROMOS53A6OXY force fields. Different sets of partial charges were used for these two force fields (Klein's for GROMOS53A6 and GROMOS Developer for GROMOS53A6OXY), and these differences in partial charges (shown in Table 2.1)

evidently have little effect on the RDF's. Up to 81% of the sodium ions are condensed at the surface of the micelle in the smaller simulation boxes, while in the larger simulation box, no more than 70% condense. While condensation of sodium ions may be critical to micelle shape at higher surfactant concentration, to our knowledge this is difficult to determine experimentally, especially within a distance of 0.35 nm of the micelle surface.

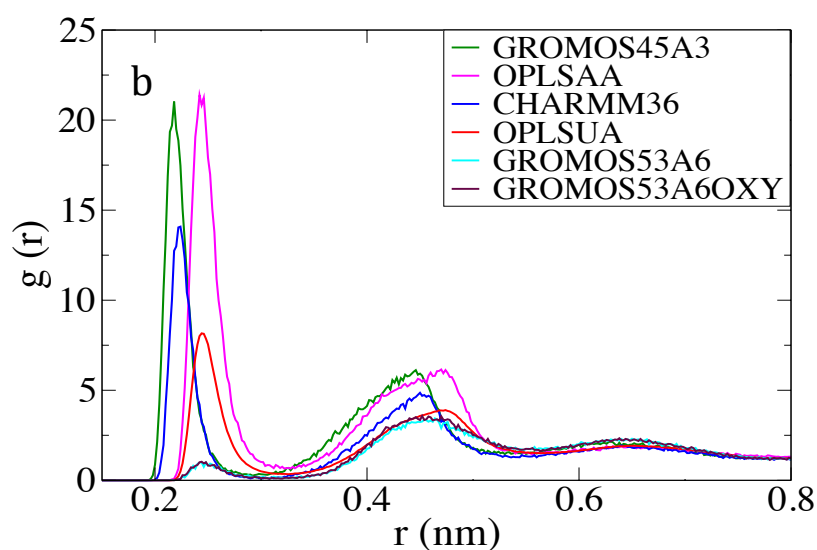
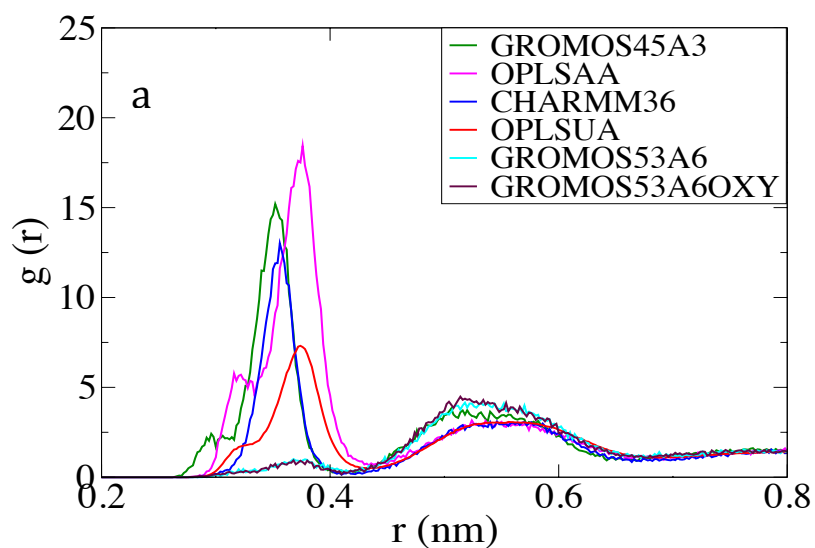


**Figure 2.2** RDF of sodium with respect to a). sulfur, and b). ionic oxygen atoms in the micelle head group for an SDS micelle with aggregation number 60.

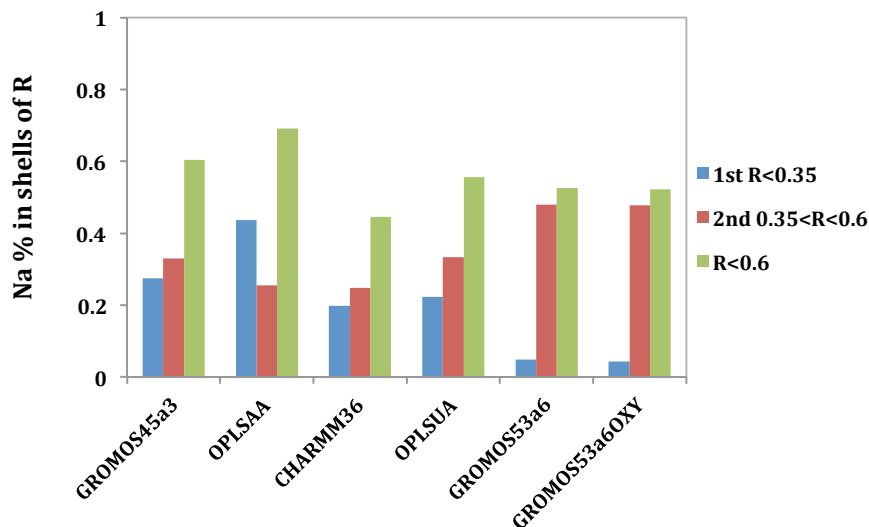


**Figure 2.3** Percentages of sodium ions within each RDF shell around ionic oxygens of the SDS head group in a box size of  $12.65 \times 12.65 \times 12.65 \text{ nm}^3$ . The boundaries of each shell are chosen to be 0 nm and 0.35 nm for the inner shell, and 0.35 nm and 0.6 nm for the outer shell. These are based on distances near the two minima of the sodium to oxygen RDF.

To sum up this section, we investigated micelles composed of 60 SDS molecules for two different periodic box sizes using six different force fields and three different sets of partial charges, and compared the results with available simulations from the literature and with experimental results. We find little effect of box size; it appears that a micelle composed of 60 SDS can be studied in a small box, even though it corresponds to a concentration above the range where such small micelles are found experimentally. All the force fields accurately capture many of the micelle properties, including  $R_g$ , and RDF



of head or tail groups relative to micelle COM. SASA and hydration numbers are slightly different for different force fields but still roughly compatible. The functions most sensitive to the force field are the RDF of sodium to ionic oxygen, and of sodium to sulfur, especially the distribution of sodium within the two shells surrounding the ionic oxygens. This difference does not much affect micellar shape for small micelles, but we will see that it has a profound impact on micelle shape and shape transitions for larger micelles that are prevalent at high concentration. Thus, *the computationally cheapest way to detect force field differences that are important at high aggregation number is to examine the sodium-to-oxygen RDF of a micelle of aggregation number 60.*

### **2.3.2 Micelle Composed of 100 Surfactants**

At an aggregation number of 60, the final shapes of the micelle do not differ, even though the RDF distributions of sodium and ionic oxygens are different. We next consider a micelle composed of an intermediate aggregation number of 100 to investigate the effect of force field on micelle properties.

#### **2.3.2.1 Impact of Force Field on Micelle Structure**

To see if the effects of the force field on SDS micelle properties at an aggregation number higher than 60 but still lower than the number enough to generate a rodlike micelle, we simulated a SDS micelle composed of 100 molecules in box sizes of  $6*6*6$  nm<sup>3</sup> and  $15*15*15$  nm<sup>3</sup>, corresponding to concentrations of 0.80 M and 0.05 M, respectively. At the end of the simulations, for GROMOS45A3 and OPLS-AA force

fields, which are the force fields that produced the highest first peaks in the sodium-to-ionic-oxygen RDF for micelles of aggregation number 60, Figure 2.4 shows that on micelle of aggregation number 100, a two-dimensional “crystal” patch of head groups is formed (upper row) with an oxygen-to-sodium ratio of 4 to 1. The micelle for these two force fields remains nearly spherical, with prolateness parameter between -0.05 and 0.05, but with tail groups somewhat ordered (as indicated in the right two images on the lower row of Fig. 2.4). A more or less prolate shape with prolateness less than 0.2 without the crystal patch is formed for the rest of the force fields.

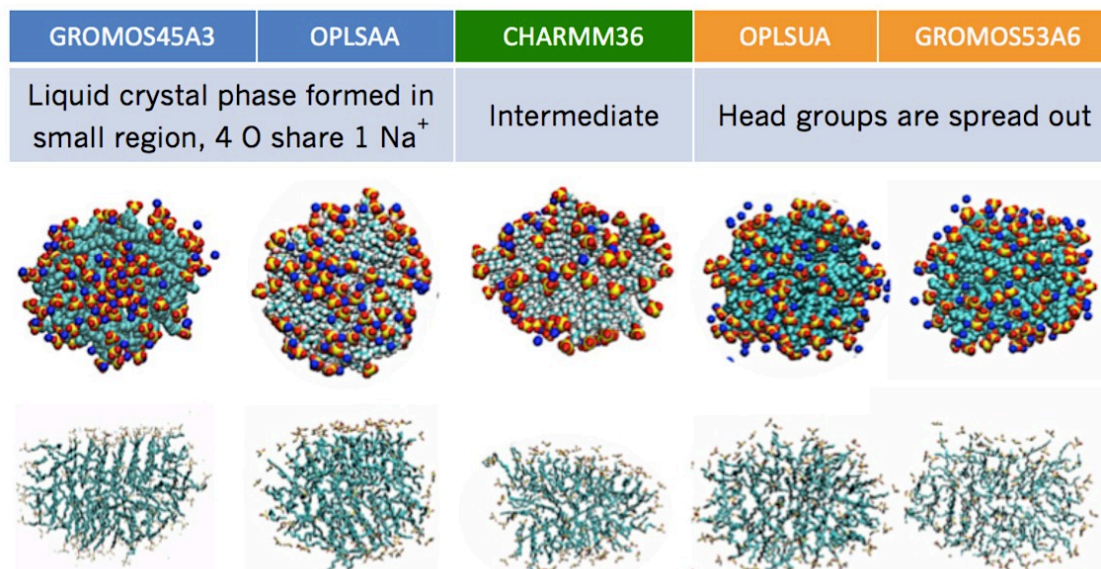


**Figure 2.4** Snapshots from simulations of micelle composed of 100 SDS at 0.8 M. Upper row: VDW sphere representation of atoms. Yellow: sulfur atom; red: ionic oxygen; blue: sodium ions within 0.6 nm of micelle; cyan, white, or blue: hydrocarbons and ester oxygen. Lower row: stick representation of bonds at a united-atom level. Cyan: hydrocarbons; brown: sulfate. The results are arranged from left to right in order of decreasing height of inner sodium/ionic oxygen peak.

The RDF's of sodium to sulfur and sodium to ionic oxygens are similar to those at an aggregation number of 60 and are not shown here. As shown in Figure 2.5, the RDF's of sulfur atoms with each other (S-S) show peaks at 0.5 nm for GROMOS45A3 and OPLS-AA force fields at an aggregation number of 100. No such "inner peak" at distances at 0.5 nm is observed at an aggregation number of 60 even with the same parameters and concentration. The S-S RDF is similar for aggregation numbers of 60 and 100 for the other force fields. The emerging inner peak of the S-S RDF reflects a smaller sulfate surface area that results from stronger screening of electrostatic repulsion of the head groups produced by sodium ions condensed near the micelle surface. There are many more sodium ions condensed within the first layer within 0.35 nm of the micelle surface when using OPLS-AA and GROMOS45A3, even though fewer ions in the second layer within 0.6 nm of the surface are present than for the other force fields and the total sodium ions within 0.6 nm of micelle surface are similar among all six force fields. It is evidently the higher concentration of sodium ions within the first layer of the sodium-to-ionic-oxygen RDF that screens the electrostatic repulsion between the ionic oxygens efficiently and decreases the head group surface area further. Correspondingly, the micelle has a smaller head group surface area, a closer peak in the S-S RDF, and smaller total SASA for the OPLS-AA and GROMOS45A3 force fields. At an aggregation number of 60, the same ion distribution patterns are observed; sodium ions condense at the micelle surface within 0.35 nm of the first layer for OPLS-AA and GROMOS45A3 force fields. However, no unusual "crystal" structures are formed at an aggregation number of 60, apparently due to geometric constraints.

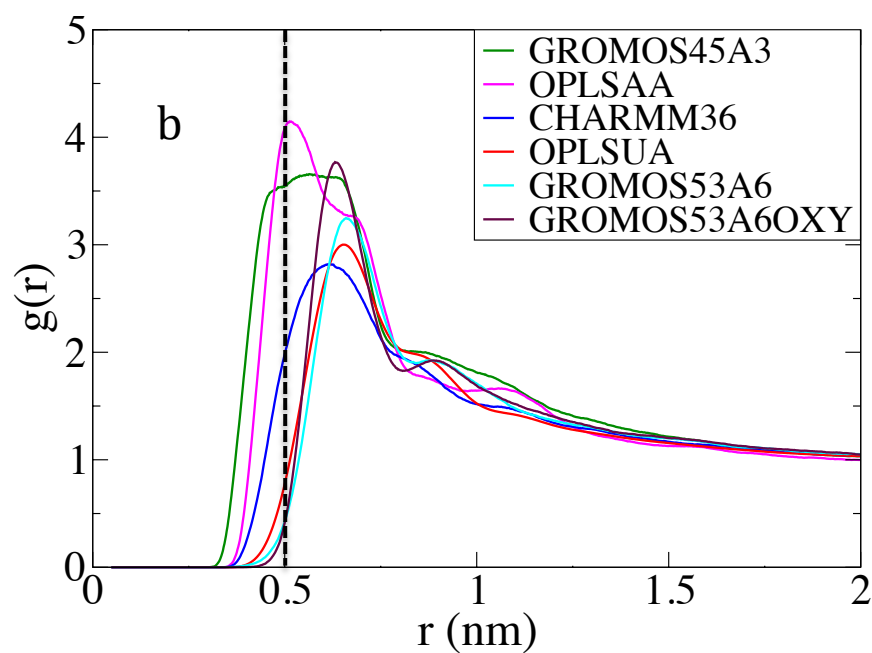
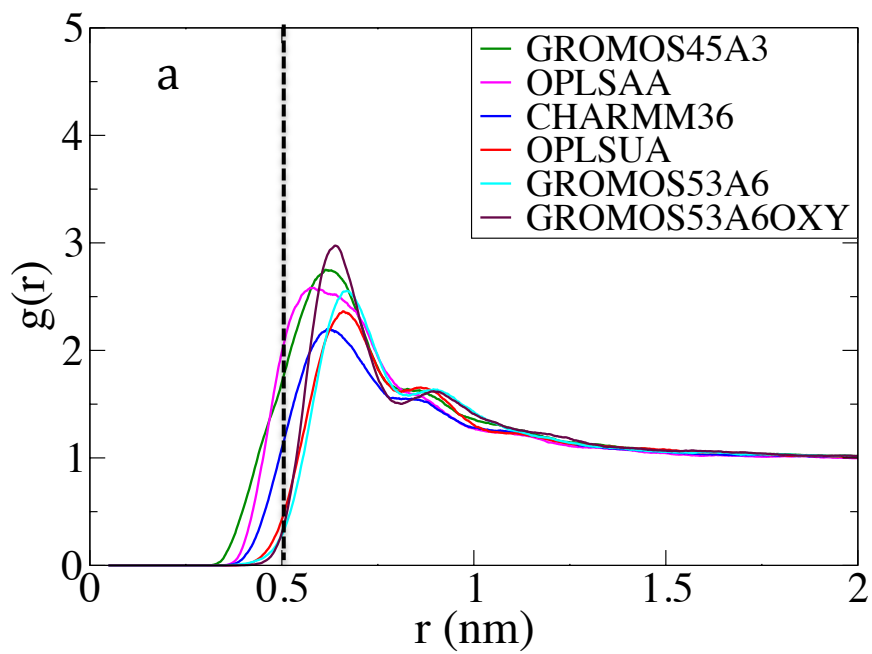


**Figure 2.5** RDF of sulfur to sulfur atoms at 0.8 M at an aggregation number of a). 60; b).

100.

The clustering of head groups for an aggregation number of 100 also results in ordering of the tails, which suggests the formation of a crystalline/gel phase. Although the tail ordering in the micelle for GROMOS45A3 and OPLS-AA at a concentration of 0.80 M and temperature of 300K possibly falls in the regime where a liquid crystalline phase might form,<sup>16,65</sup> we observe the same tail crystallization phenomenon and bicelle formation for large aggregation numbers of 382 surfactants at 0.26 M for GROMOS45A3 and OPLS-AA, as described shortly. The presence of the tail crystallization at a low SDS concentration of 0.26 M in the latter simulations suggests that this head group and tail crystallization is an artifact resulting from the force field parameters and is not representative of the true behavior of SDS surfactants under these conditions<sup>118</sup>.

### **2.3.2.2 OPLS-AA-water-sodium models**

For the OPLS-AA force field, there are two parameter sets for sodium ions available in GROMACS. One of the default sodium ion parameter sets was developed by Aqvist in 1990<sup>109</sup> and was used in his simulations, and another was parameterized by Jorgenson and coworkers in 1984.<sup>108</sup> Parameterization of metal ions usually is based on experimental ion hydration free energy in dilute solutions and/or radial distribution of water and/or water ions around the metal ion for the given water model. The sodium ion parameterization by Aqvist was based on the hydration free energy of sodium using a SPC water model, while the sodium ion parameterization by Jorgensen and coworkers was based on the radial distribution of the water oxygens about the ion with TIP4P water. Since the accuracy of the optimized radial distribution of sodium and oxygen was limited by the computational

power available in 1984, in 2006 Jensen and Jorgensen re-parameterized the sodium ion based on both hydration free energy and the radial distribution of water using a TIP4P water model.<sup>112</sup> This new sodium ion parameterization using TIP4P water has not yet been updated in the GROMACS simulation engine. Recently, Joung and Cheatham<sup>111</sup> and Dang<sup>110</sup> parameterized sodium ions using different water models based on experimental hydration free energy and the radial distribution of water around the sodium ions. In addition, the lattice energy and lattice constant of the sodium chloride crystals were also optimized in Joung and Cheatham's ion model. Here, the different water models used in ion parameterization, namely SPC, SPC/E, TIP3P, TIP4P<sub>EW</sub><sup>111</sup> and TIP4P are compared. All these water models are fixed point-charge models but otherwise differ in many respects. For example, TIP4P is a four-site model and the rest are all three-site models. The L-J parameters, bond lengths and angle parameters are all different for the various models. The resulting water physical properties including density and dipole moment are all different. To evaluate the effect of the water model, we simulate a pre-package micelle composed of 60 in a box size of 5\*5\*5 and 100 SDS molecules in a box of size 6\*6\*6 nm<sup>3</sup> using the OPLS-AA force field and sodium ions with the water model used to parameterize the sodium.<sup>27,38</sup>

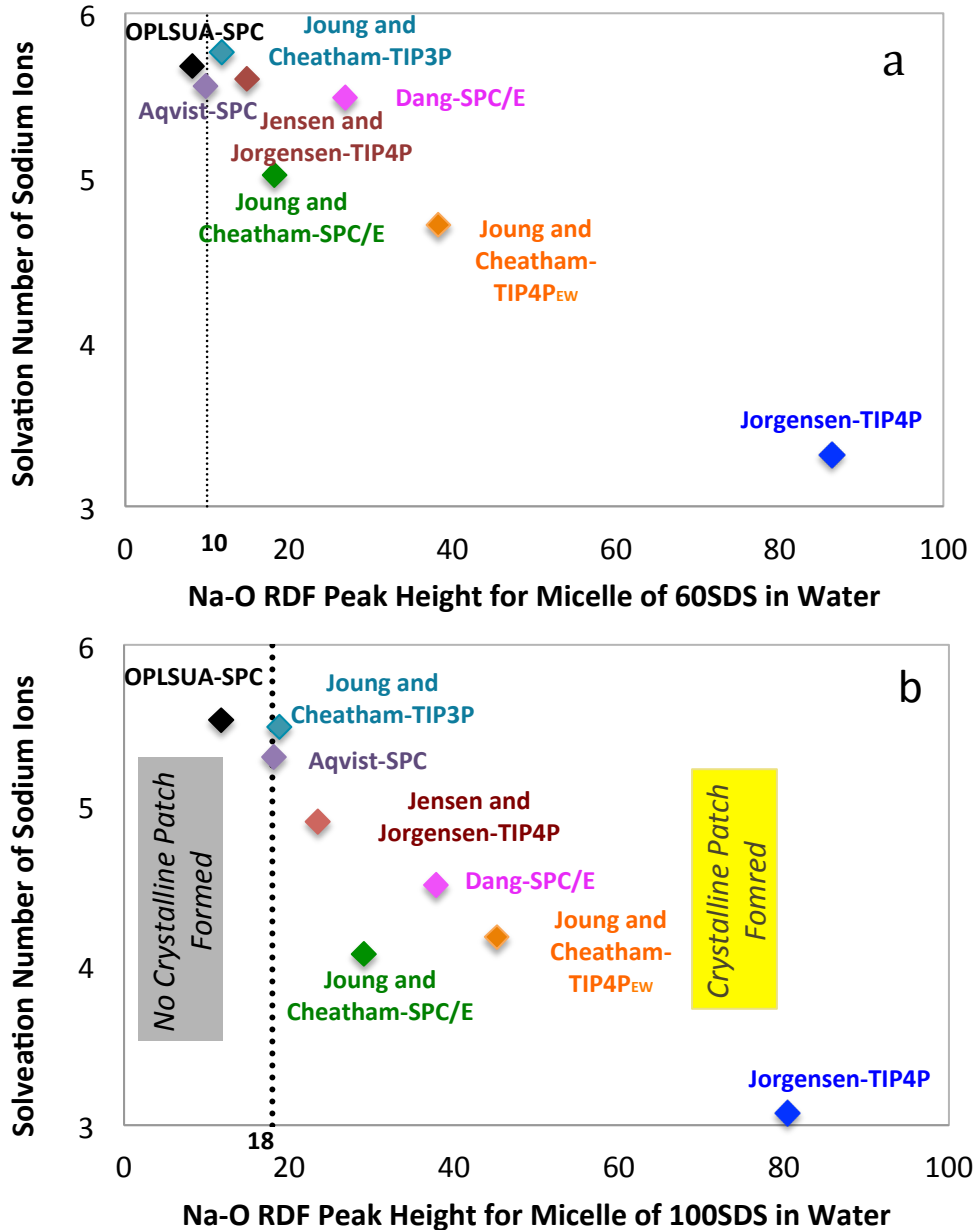


**Figure 2.6** Number of water molecules within 0.35 nm of  $\text{Na}^+$  plotted against inner peak height of RDF of sodium to ionic oxygens in SDS head group for different  $\text{Na}^+$ /water models within OPLS-AA. a). for a box of size  $5 \times 5 \times 5 \text{ nm}^3$  with a micelle having an aggregation number of 60; b). for a box of size  $6 \times 6 \times 6 \text{ nm}^3$  with a micelle having an aggregation number of 100. TIP4P<sub>EW</sub> is a modified TIP4P water model.<sup>111</sup> The dashed

lines separate the models on the right that produced bicelles in simulations of aggregates containing 382 surfactants, from those on the left, that did not.

In Figure 2.6 we plot the solvation number of the sodium ions, which we take to be the number of water molecules whose center is within 0.35 nm of the center of mass of the sodium ion vs. the height of the nearest Na-O RDF peak for a micelle having an aggregation number of 60 (Fig. 2.6a) and 100 (Fig. 2.6b) using different Na<sup>+</sup>/Water models within OPLS-AA. As the height of the Na-O RDF increases, we see a decrease in the solvation number at aggregation numbers of both 60 and 100. The values of the L-J  $\sigma$  cross terms for sodium with ionic oxygen roughly set the equilibrium distances between sodium and ionic oxygen, and therefore set the peak position in the RDF of sodium ion around ionic oxygen (Fig. A.2). The peak height itself cannot be correlated simply to the magnitude of the  $\epsilon$  L-J cross term, however, as it depends on a number of factors. The sodium solvation numbers in salt water in the absence of the SDS are around 5.5 for both Aqvist/SPC and Jorgensen/TIP4P, as expected since without the competition with the head-group oxygens the sodium will be fully hydrated by water regardless of the forcefield. But when a SDS micelle is present, this solvation number decreases to 3 for the Jorgensen/TIP4P parameters, but remains at 5.5 for the Aqvist/SPC parameters because of the competition with the head-group oxygens for binding to the sodium ions. Using each of two different sodium ion models in GROMACS but different water models, the number of waters binding to sodium ions in the presence of the SDS micelle increases in the order: TIP4P, SPC/E, SPC, TIP3P. Thus, TIP3P water binds sodium the most strongly, since it continues to be highly solvated in the presence of ionic oxygens in



the SDS head. The RDF's for sodium binding to head group ionic oxygens and water oxygens for all four water models are given in Figure A.3. Thus, the water model influences the number of waters binding to the sodium ions, and together with the L-J potential of the sodium ions, determines the number of hydrated sodium ions condensed to the surface of the micelle, the Na-O RDF peak height, and the morphology of the micelle. It is thus important to choose the right water model for simulations of surfactant and ions.

As will be discussed in the next section, at higher aggregation number (382), micelles can be either rodlike micelles or bicelles. Their shape correlates with the peak height of the Na-O RDF at an aggregation numbers of 60 or 100. For the water and sodium models considered in this section, Na-O RDF peak heights greater than or equal to that obtained using the Aqvist sodium ion with SPC water, or the Joung and Cheatham sodium ion with TIP3P water model, result in bicelles. For an aggregation number of 60, this corresponds to a Na-O RDF peak height of around 10 (as shown in Fig. 2.6a and Fig. A.2), while for an aggregation number of 100, the critical peak height above which bicelle form is around 18 (as shown in Fig. 2.6b). These simple correlations, if robust, could be used to quickly assess the realism of force fields for SDS, and possibly for other surfactants as well.

### **2.3.3 Elongated Micelles Composed of 382 Surfactants**

Although of great interest, elongated micelles of SDS have **not** before been simulated at the atomistic level owing to the computational cost of simulating systems large enough to

contain them. Here, taking advantage of advances in computer speed, we study preassembled SDS micelles composed of 382 SDS molecules at a concentration of 0.26 M in water or in 2% sodium chloride. Experiments show that SDS micelles under these conditions are, in fact, elongated. All simulations were carried out for 20 ns when using AA force fields, and 30 ns when using UA force fields except the simulation starting as a bicelle using CHARMM36 was extended to 40 ns and that using OPLS-UA was extended to 60 ns. The six force fields that we studied for spherical micelles composed of 60 or 100 SDS are again compared for both initially elongated micelles and initially disklike bicelles composed of 382 SDS surfactants. While we cannot equilibrate a micelle size distribution in the short time and small boxes that we use, we here seek to determine if elongated micelles of aggregation number 382 are stable against breakup, and to transformation of structure or shape over runs of duration of 20-30 ns. The effects of initial condition and time after the beginning of the simulation can be determined by comparison of simulation results between two starting states (i.e., initially elongated and initially disklike).

Interestingly, while different force fields produced similar shapes and structures for micelles with aggregation numbers 60 and 100, for an aggregation number of 382, the final aggregate structures attained within the limited simulation time are dependent on force field. In the presence of 2% NaCl, a bicelle with ordered tails is formed with GROMOS45a3 and OPLS-AA force fields when starting from either a rodlike or a disklike bicelle shape. Here, whenever we use the term “bicelle,” we mean an aggregate with two flat parallel surfaces, and ordered tails, similar to a piece of a bilayer, as shown

in Figure 2.7. The overall shape at the end of the simulation need not be disklike or even oblate, but could be prolate, or tablet shaped, as is the case for the bicelle in Figure 2.7. The head groups of the bicelle are typically denser on the flat surfaces than on the edges of the bicelle, which expose the tails to water, since head group coverage is relatively sparse. For the CHARMM36 force field, an elongated micelle is formed when starting with a rodlike micelle, and, when starting from a disklike bicelle, the bicelle structure rearranges slowly towards a more cylindrical shape with disordered tails. After 20 ns, the tails still retained order, however, and so the simulation was extended to 40 ns, by which time the tails had become disordered. For the other three force fields, a final elongated micelle with disordered tails forms in the presence of 2% NaCl starting either from a rodlike micelle or from a disklike bicelle within 30 ns. We choose two UA force fields for more detailed comparison, namely GROMOS45A3 and OPLS-UA (with head group parameters discussed above), the former forming a bicelle and the latter a rodlike micelle shape, from either starting condition, as shown in Figure 2.7. In experiments, ordered, non-rodlike structures in water were only observed at concentrations of 1.25 M or higher in experiments,<sup>16</sup> and so bicelles with ordered tails are probably artificial in simulations at 0.26 M. In particular, a viscous, clear solution is observed for SDS at a concentration of 0.26 M SDS in 2% NaCl, which is a concentration above the sphere-to-rod transition for SDS in aqueous solutions.<sup>57</sup> We therefore believe that the elongated rodlike micelle obtained using the OPLS-UA force field, rather than the bicelle, observed with our version of the GROMOS45A3 force field, represents the true SDS behavior at 0.26 M SDS in 2% NaCl. The simulation starting as a bicelle for the OPLS-UA force field was

extended to 60 ns to study bending and straightening of the cylindrical micelle that had formed from the bicelle within the first 30 ns of the simulation.

It is important for parameter optimization to determine which parameter values of the GROMOS45A3 force field lead to a bicelle structure instead of the elongated shape seen with the OPLS-UA force field. We therefore here systematically study the effects of force field parameters on the shape of the micelle.

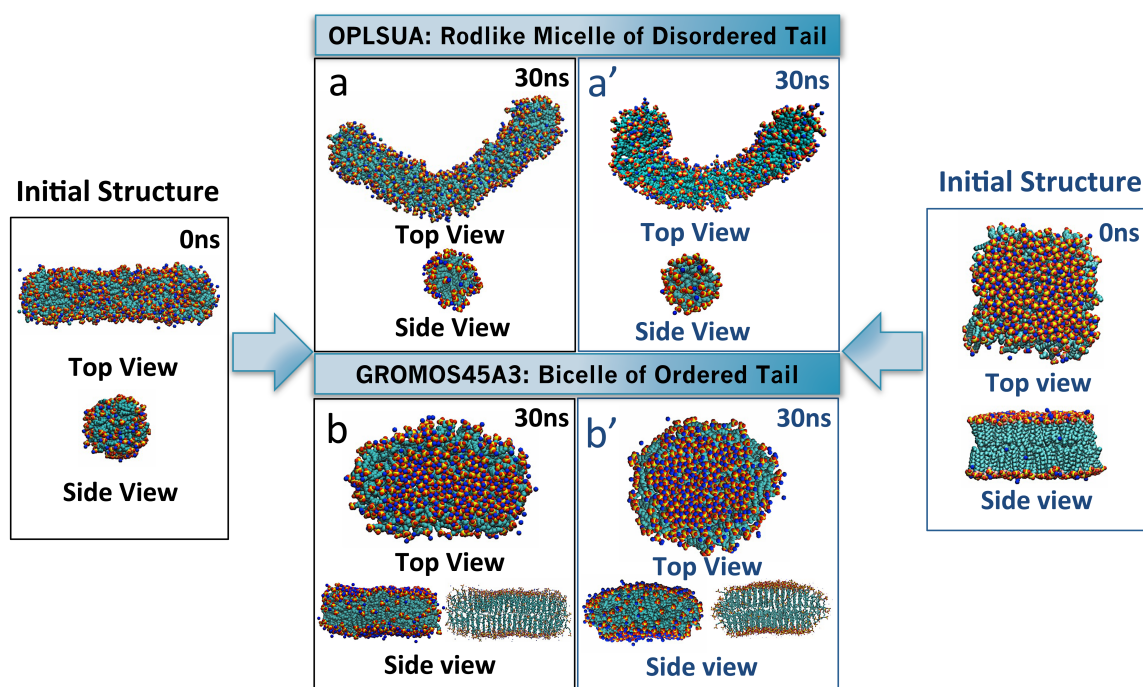


**Figure 2.7** Evolution of initially elongated SDS micelles and bicelles with aggregation number of 382 at 0.26 M concentration and 2% NaCl. Final structure after 30 ns for a). OPLS-UA force field for an initial rodlike micelle; a'). OPLS-UA of an initial bicelle; b). GROMOS45A3 for an initial rodlike micelle; b'). GROMOS45A3 for an initial bicelle. The side views for bicelle final structures show tails in both spherical-bead and stick-figure formats, the latter clearly showing the tail ordering.

While all parameters differ somewhat between the GROMOS45A3 and OPLS-UA force fields used here, we first examine the effect of the intramolecular parameters. The intramolecular parameters of the sulfate head group in GROMOS45A3 were parameterized to the tetrahedral structure with corresponding bond length.<sup>48</sup> The intramolecular parameters of the sulfate group in OPLS-UA were taken from Berkowitz's group.<sup>46,102</sup> Here, we determine which parameters affect micelle shape by systematically replacing the harmonic bond parameters, angle parameters, or/and dihedral parameters of OPLS-UA with the corresponding GROMOS45A3 force field parameters. The purpose of mixing force field parameters is not to optimize the force field parameters, but to determine which parameter(s) produced the different micelle shapes. Table 2.2 lists the various combinations of simulation force field parameters we tested to determine their effects on the micelle shape, listed in the final column.

We find that as long as we retain the GROMOS45A3 *intermolecular* parameters, then replacing some or all of the *intramolecular* parameters by OPLS-UA values does not change the micelle shape that results at the end of the simulations. Only switching the intermolecular parameters from GROMOS45A3 to OPLS-UA is able to switch the final micelle structure from a micelle to an elongated rod. Therefore, as expected, the intramolecular parameters are not the source of the difference in micelle shapes of SDS with its short alkyl tail.

Therefore, we next focus on the effects of individual intermolecular parameters. These include both the L-J potentials and the Coulomb potentials from the partial charges of the atoms and ions. Here, there were no differences in the partial charges used within the two

force fields, GROMOS45A3 and OPLS-UA. However, the L-J potentials of SDS and of ions differ greatly between the two force fields. We group the parameters as 1) head group parameters including those for the sulfate and the alpha carbon, 2) tail group parameters, including those for the hydrocarbon tail atoms except the alpha carbon, and 3) ion parameters, especially for the sodium ions that are described by different L-J parameters in the two force fields.

We start with the OPLS-UA force field parameters and replace some of the parameters systematically with those of the GROMOS45A3 force field, to determine the effect of each. First, when we replace the L-J potentials of the head, tail, and ion groups by GROMOS45A3 parameters one group at a time, we find that the resulting micelle shapes remain rodlike, as shown in the top rows of Table 2.3. We then replace two of the three L-J groups simultaneously. Interestingly, replacing both the head and tail group L-J parameters by GROMOS45A3 parameters does not result in a bicelle. However, replacing the L-J parameters for *both* sodium ions and the head groups by GROMOS45A3 parameters (with sulfate group parameters defined by Shang et al.<sup>48</sup>), we find that a bicelle is formed. We then further discriminate among the SDS head group parameters by changing only the L-J parameters of the sulfate group and not the alpha carbon; this change is labeled “SO4,” and finally we change the L-J parameters of only the three ionic oxygens of the sulfate group, without changing either the ester oxygen or the sulfur; this change is labeled “O3.” In all these cases, the result is a bicelle. While Table 2.3 shows results for 2% salt, bicelles also result when 0% salt is present for the same three force fields only. For all other force fields, the final state remains that of a

rodlike micelle at 2% salt, while at 0% salt, some of the rods broke up into two or more ellipsoidal micelles by the end of the simulation, but did not form bicelles. Thus, the pair of L-J parameters for the sodium ion and the ionic oxygens of the SDS head group control the final micellar state. This result is consistent with recent findings for phospholipid bilayers by Bhatnagar et al., that the interactions between sp<sup>2</sup> hybridized oxygens and sodium ion strongly affected the bilayer area per lipid.<sup>119</sup> When the parameters of the sodium ion and of the ionic oxygens are taken from the GROMOS45A3 force field, bicelles are formed; while when they are taken from the OPLS-UA force field, the initially elongated micellar shape is retained at 2% salt, which is the shape most consistent with experimental observations. The stronger attraction between ionic oxygens and sodium ions resulting from the GROMOS45A3 force field parameters produces a stronger interaction between the ionic oxygens of SDS and the sodium ions. This evidently favors an incorrect bilayer structure.

**Table 2.3.** Simulations with mixed force field parameters from GROMOS45A3 and OPLS-UA with initially rodlike shaped micelles containing 382 SDS molecules in 2% NaCl, and resulting structures formed. See text for explanation.

Intermolecular parameters L-J			Equilibrium Micellar Structures
SDS head	SDS tail	Na <sup>+</sup> , Cl <sup>-</sup>	
<i>OPLS-UA</i>	<i>OPLS-UA</i>	<i>OPLS-UA</i>	<i>Rod</i>
<b>GROMOS45A3</b>	<b>OPLS-UA</b>	<b>OPLS-UA</b>	<b>Rod</b>
<b>OPLS-UA</b>	<b>GROMOS45A3</b>	<b>OPLS-UA</b>	<b>Rod</b>
<b>OPLS-UA</b>	<b>OPLS-UA</b>	<b>GROMOS45A3</b>	<b>Rod</b>
<b>GROMOS45A3</b>	<b>GROMOS45A3</b>	<b>OPLS-UA</b>	<b>Rod</b>
<b>OPLS-UA</b>	<b>GROMOS45A3</b>	<b>GROMOS45A3</b>	<b>Rod</b>
<b>GROMOS45A3</b>	<b>OPLS-UA</b>	<b>GROMOS45A3</b>	<b>Bicelle</b>
<b>GROMOS45A3 SO4</b>	<b>OPLS-UA</b>	<b>GROMOS45A3</b>	<b>Bicelle</b>
<b>GROMOS45A3 O3</b>	<b>OPLS-UA</b>	<b>GROMOS45A3</b>	<b>Bicelle</b>

The interaction between the head group of SDS and sodium is studied in more detail by plotting the distribution of the sodium ions relative to the sulfur atoms and ionic oxygen atoms along the surface of the aggregate. Since the aggregate is not spherical, rather than use a radial distribution function, we compute the percentage of all sodium ions that are within a given distance of any sulfur atom or ionic oxygen on the micelle. To express this in a manner analogous to a radial distribution, we differentiate this percentage with respect to the distance, and plot the result as a function of distance from the nearest sulfur or ionic oxygen. Two starting states, namely initially rodlike and initially disklike bicellar were carried out. As shown in Figure 2.8, the distributions of sodium ions around the sulfur (Figure 2.8a) or around the ionic oxygens (Figure 2.8b) obtained within 30 ns from the two starting states reach the same equilibrium distribution when using OPLS-UA force field, and nearly the same distribution when using the GROMOS45 force field. Although the total number of ions condensed at the surface of the SDS micelle is comparable, namely 38% for OPLS-UA and 45% (initially rodlike) or 47% (initial bicellar) for GROMOS45A3, the broader and stronger first peak of the sodium to sulfur or to ionic oxygens shows the stronger interaction obtained from the GROMOS45A3 parameters than from the OPLS-UA parameters. The smaller  $\sigma$  values and higher  $\epsilon$  values in GROMOS45A3 mean a closer and stronger interaction between ions and the SDS head groups and more sodium ions condensed onto the SDS surface at the location of the first RDF peak of the micelle with aggregation number 382. The more condensed, tighter, binding sodium ions screen the repulsive electrostatic interaction between the head groups of SDS, resulting in a smaller surface area for the SDS head group. This favors a



higher Israelachvili packing parameter.<sup>92</sup> Stronger binding of sodium to the micelle is also observed at an aggregation number 60 as shown in Figure 2.1 and Figure 2.2 when using GROMOS45A3 force field parameters. This has little effect on small aggregates of size 60 and 100, which retain an ellipsoidal shape regardless of this change in head-group packing, but for larger micelles, this change produces bicellar structures.

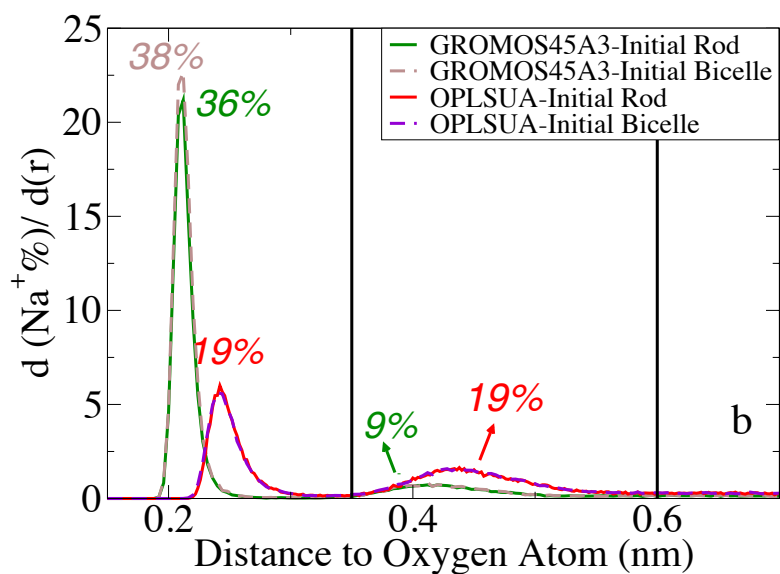
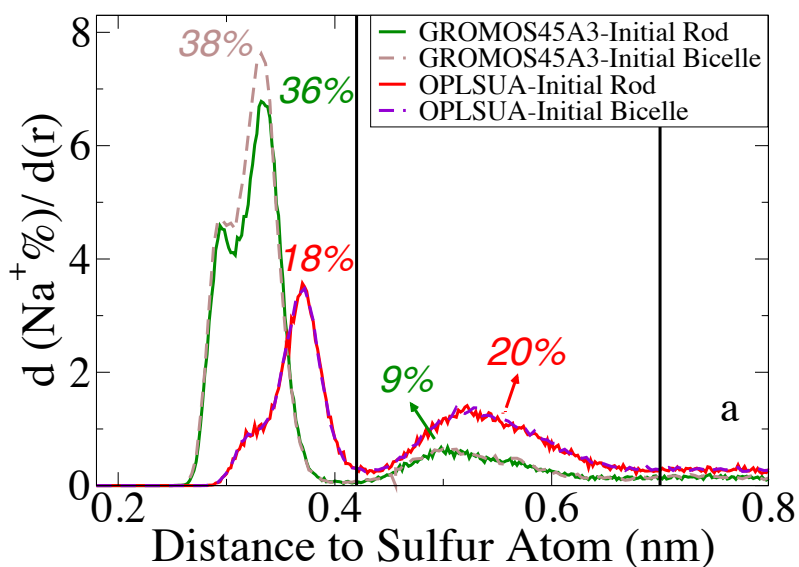


**Figure 2.8** Comparison of distribution of gradient of the percentage of sodium ions with respect to the nearest a). sulfur atom and b). ionic oxygen atoms, for an aggregate of 382 SDS molecules, for OPLS-UA preassembled as a rod (red), preassembled as a bicelle (purple) and GROMOS45A3 preassembled as a rod (green) and preassembled as a bicelle (brown). The percentages of Na<sup>+</sup> in each of the two peaks are given.

The dependence of micelle shape on initial condition can be measured by ratios of the principle radii of gyration of the micelle. These are obtained from the time-average components of the diagonalized radius of gyration tensor, that is, by the principal moments of inertia  $Rg_{11}^2$ ,  $Rg_{22}^2$ , and  $Rg_{33}^2$ , where at each instant in time these components are ordered such that  $Rg_{11} > Rg_{22} > Rg_{33}$ .<sup>120</sup> Figure 2.9 plots the final values of the ratios  $Rg_{11}/Rg_{22}$  and  $Rg_{22}/Rg_{33}$  for each of the two starting states (where for open symbols, the micelle started as a bicelle, while for closed symbols, it started as a cylinder) and each of the six force fields. For notational convenience, in Points on the black dashed lines have the “ellipsoidal volumes” given. The “ellipsoidal volumes” are given by  $4\pi\sqrt{3}Rg_{11}Rg_{22}Rg_{33}$ <sup>121</sup> which is the volume they would have if they were ellipsoids with the given ratios of  $Rg_{11}/Rg_{22}$  and  $Rg_{22}/Rg_{33}$  and with  $Rg_{33}=1.0$  nm, which is close to the value obtained in all cases from the simulations. Larger values of the “ellipsoidal volumes” are obtained for the elongated micelles than for the bicelles. As can be seen, the best convergence within the 30 ns runs is obtained for the OPLS-UA and GROMOS53A6OXY force field, with poorer convergence for the others. Although the final overall shapes (after 20 or 30 ns) of the micelles did not converge, both

GROMOS45A3 and OPLS-AA produced final structures with ordered tails, regardless of the starting state. For these two force fields, the initially oblate disklike bicelle shape remained disklike, while the initial cylindrical shape with disordered tails formed elongated tablet-like bicelles with ordered tails. The force fields OPLS-UA, GROMOS53A6, and GROMOS53A6OXY all formed elongated, or prolate, micelles with disordered tails at long times, although the aspect ratios for the two initial conditions did not converge. The two starting states for CHARMM36 did not converge within 20 ns; the initially rodlike micelle with disordered tails remained cylindrical with disordered tails (Fig. 2.9 filled blue triangle), while the initially disklike micelle with ordered tails retained some degree of order in the tails (Fig. 2.9 lower open blue triangle). But after 40 ns (Fig. 2.9, higher open blue triangle), the initially ordered tails in the bicellar starting state had become disordered, and the aggregate shape had become elongated, and its aspect ratio was not too far from that of the micelle that had started as a cylinder and had been aged for 20 ns. This is shown by the near convergence of the positions of the open and closed blue triangles in Figure 2.9. The intermediate behavior of the simulations with CHARMM36 is consistent with the behavior seen in small micelles, where the peaks of the Na-O and S-S RDFs for CHARMM36 are intermediate between those for the bicelle-forming GROMOS45A3 and OPLS-AA force fields, and those for the rodlike-micelle-forming GROMOS53A6, GROMOS53A6OXY, and OPLS-UA force fields.

The two starting states for OPLS-UA both converged to rodlike micelles, although the ratios of principal radii of gyration fluctuate as the micelle bends and unbends. To illustrate the extent of the bending fluctuations and its effect on the  $R_g$  ratios, the multiple

small open diamonds show a series of 30 pairs of ratios of principal radii of gyration over the extended period 30 to 60 ns for the OPLS-UA force field. When the micelle is bent,  $R_{g_{11}}$  is reduced and  $R_{g_{22}}$  increased, relative to their values for a straight cylinder. Correspondingly the ratio of  $R_{g_{11}}/R_{g_{22}}$  is reduced and  $R_{g_{22}}/R_{g_{33}}$  is increased, and the ratios of principal radii of gyration have values in the lower right corner of Fig 2.9. When the micelle is straight,  $R_{g_{11}}$  is larger and  $R_{g_{22}}$  smaller, and the principal radii of gyration move to the upper left corner of Fig. 2.9. These fluctuations are too slow to average out over the duration of even a 60 ns simulation, and so we make no attempt to obtain average values of the ratios of radii of gyration. Three depictions of the fluctuating shape of the cylindrical micelle for the OPLS-UA force field are shown in Fig. 2.9.

We note that ellipsoidal volumes of bent micelles are higher than those of straight micelles. We note also that the fluctuations in aggregate shape observed in the simulations are much smaller in magnitude for the micelles obtained using the GROMOS45A3 and OPLS-AA force fields, which form bicelles with ordered tails, than for micelles obtained with the other force fields. Also, the failure of the bicelle-forming shapes to converge is not surprising – the bicelles have ordered tails, which make them rigid and solid-like, and hence slow to change overall shape.

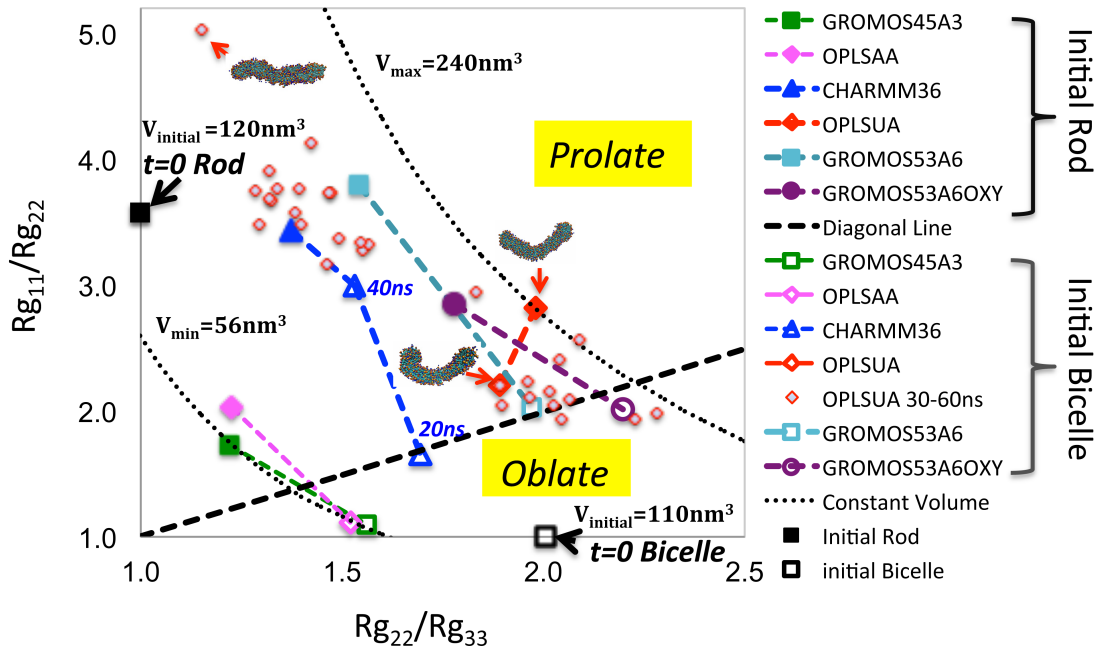


**Figure 2.9** Ratios of principal radii of gyration for aggregation number 382 SDS in 2% salt. Closed symbols are for simulations starting as rodlike micelles; open symbols are for those starting as bicelles; the many small open diamonds are from results taken at time spacings of 1 ns over the interval 30 to 60 ns for simulations starting with a bicelle using OPLS-UA. The dashed lines connecting pairs of same-colored points show how the final state for a given force field depends on the initial state.  $R_{g_{11}}$ ,  $R_{g_{22}}$ , and  $R_{g_{33}}$  are the ordered square roots of the averaged principal components of the radius of gyration tensor, with  $R_{g_{11}} > R_{g_{22}} > R_{g_{33}}$ . Black dotted lines have constant ellipsoidal volumes estimated by  $4\pi\sqrt{3}R_{g_{11}}R_{g_{22}}R_{g_{33}}$  assuming  $R_{g_{33}}$  is 1.0 nm.<sup>121</sup> Initial volumes designated by “t=0” are taken as the volume of a rod or disk whose dimensions match those of the starting shapes. The diagonal black dashed line separates oblate and prolate shapes. Images are depicted of cylindrical micelles corresponding to three different points for the OPLS-UA force field.

To analyze the packing of molecules within the micelle structures, we added hydrogen atoms to the four UA model structures using Gaussian09<sup>122</sup> software, and we then used

VolArea software<sup>123</sup> to estimate the volume occupied by surfactant atoms in the micelle, solvent accessible surface areas (SASA), and the volume of the cavities between atoms. Using the experimental van der Waals radius for each atom of the surfactant and the positions of those atoms from the simulations (which for united atom simulations were augmented by the added hydrogens), we found that the surfactant atomic volumes within the micelles are approximately 0.43 nm<sup>3</sup> per surfactant molecule, independent of the force field and of the shape of the aggregate. The cavity volumes, estimated by adding up volumes of cavities outside of the van der Waals radii of neighboring spheres, using VolArea software with a “cavity probe radius” of 2 Å (see ref. 85 for details), are given in Table 2.4. The SASA<sup>124</sup> are estimated by rolling a probe sphere of radius 1.4 Å over the surface of the micelles and the summed contact areas are shown as well. As can be seen, the cavity volumes, which are around 0.023 to 0.048 nm<sup>3</sup> per surfactant, are less than 12% of the volume occupied by the molecules of the micelle, which is 0.43 nm<sup>3</sup> per surfactant. The choice of probe radius of 2.0 Å means that only cavities within 2.0 Å of the atom centers can be counted, and, and not spaces further away than 2.0 Å from all atoms. Note that the cavity volume for rodlike micelles obtained using OPLS-UA, GROMOS53A6, and GROMOS53A6OXY are almost the same, regardless of the starting states, and are approximately twice those of the bicelles obtained using GROMOS45A3 and OPLS-AA, which are also insensitive to the starting state. The significantly smaller cavity volume of the bicelles relative to the cylinders is consistent with the observed decrease of the solvent accessible surface area per surfactant. The identical atomic volumes and small cavity volumes show that the molecular packing densities vary by

around 5% between cylindrical micelles and bicelles. The “ellipsoidal volumes,” however, differ by up to a factor of four, as shown in Fig. 2.9. The reason is that an ellipsoid is a poor match to the actual geometries. The cylindrical micelles, for example, bend considerably, as shown in Fig. 2.9, thus sweeping out a much larger ellipsoidal volume than does a straight cylinder or ellipsoid. Very long cylindrical micelles have random walk configurations, whose ellipsoidal volumes can be orders of magnitude larger than the volume actually occupied by the micellar material. However, the ellipsoidal volume per surfactant in the micelle can be important for estimating the micellar aggregation numbers using neutron scattering methods.

The convergence of cavity volumes from two very different starting states, together with convergence of SASA (Table 2.4), and Na-O and Na-S RDFs (Fig. 2.8), all suggest that local equilibrium of micelle tail and head group packing is reached within 20 ns for AA models and 30 ns for UA models (except in the case of the CHARMM36 force field for which 40 ns is needed), even though the overall shapes of the aggregates are not converged. The slow change in structures obtained from the two starting states when using CHARMM36, indicates that this force field does not provide as strong a preference for either local packing as is the case for the other force fields, for which local packing converges more quickly.

**Table 2.4.** Cavity volume and solvent accessible surface area (SASA) per surfactant for 382 SDS surfactants in 2% NaCl estimated at the ends of simulations from two starting states using VolArea<sup>123</sup> with probe radii of 2.0 Å for cavity volume and 1.4 Å for SASA calculations. Hydrogen atoms were reconstructed using Gaussian09<sup>122</sup> for UA models. Data from simulations starting as a bicelle using CHARMM36 are given at 20 ns (before arrow) and 40 ns (after arrow). Data from simulations starting as a bicelle using OPLS-UA are the same at 30 ns and 60 ns.

Force Fields	Cavity*100/Surfactant (nm <sup>3</sup> )		SASA/Surfactant (nm <sup>2</sup> )	
	Initial Rod	Initial Bicelle	Initial Rod	Initial Bicelle
GROMOS45A3	2.4	2.3	0.8	0.8
OPLSAA	2.8	2.6	0.9	0.9
CHARMM36	4.2	3.4→4.2	1.5	1.2→1.4
OPLSUA	4.7	4.7	1.6	1.7
GROMOS53A6	4.4	4.5	1.4	1.5
GROMOS53A6OXY	4.1	4.2	1.4	1.4

The hydration numbers (data not shown) are not dependent on aggregation number for CHARMM, OPLS-UA, GROMOS53A6, and GROMOS53A6OXY force fields for micelles at aggregation numbers of 60, 100, and 382. For these force fields, no bicelle is formed at an aggregation number of 382. When using GROMOS45A3 and OPLS-AA, however, the hydration number decreases more than 20% as the aggregation number increases from 60 to 382, as bicelles form with close-packed head groups and ordered tail groups, at the highest aggregation number.



## 2.4. Conclusions

The interaction between sodium counter ions and ionic oxygens in SDS head groups determine the head group surface area of SDS and the resulting equilibrium micellar structure in MD simulations. This interaction depends on two factors: one is the L-J parameters of sodium ions and ionic oxygen; and another is the number of waters binding to sodium ions in the presence of the micelle, which increases in the order: TIP4P, SPC/E, SPC, and TIP3P when using the same ion model. Stronger L-J interactions between sodium and ionic oxygen, or weaker binding of water to sodium, both allow sodium to more strongly bind with ionic oxygens. The radial distribution function (RDF) of sodium to ionic oxygen can be used as a quantitative metric by taking the number of sodium ions within 0.35 nm of the oxygen to be the first shell and between 0.35 to 0.60nm to be the second shell of the oxygens at the micelle surface. The number of sodium ions within the first shell, rather than the total number of sodium ions condensed within the first two shells, determines the structure of large micelles. The differences in the numbers of sodium ions condensed within the first shell of the micelle surface do not result in different micellar shapes or overall structure at small aggregation number of 60 due to geometric constraints. However, these differences begin to have significant effects on micelle structure at aggregation numbers of 100 or higher. The larger number of sodium ions condensed within the first shell when using GROMOS45A3 (with head group parameters from Shang et al<sup>48</sup>.) and OPLS-AA force fields results in crystal-like patches of condensed sodium ions and partial ordering of tails in micelles of aggregation number 100, and in disklike or slab-like bicelles with ordered tails at aggregation

numbers of 380 or so. Tighter binding of sodium ions to micelle surfaces screen the electrostatic repulsion more effectively, and result in a smaller SDS surface area and higher Israelachvili packing parameter, leading to bicelle formation in large aggregates. At an aggregation number of 60, SDS force field parameters have little effect on the micelle radius of gyration, solvent accessible surface area, or radial distributions of head, tail, or water with respect to the center of mass of the micelle. More effective validation of SDS parameters can be done by evaluating the RDF of sodium to ionic oxygen for small micelles of aggregation number 60, or by examining tail ordering and RDFs of sulfur to sulfur at an aggregation number of 100 or higher. Simulations using GROMOS45A3 and OPLS-AA force fields at higher aggregation number resulted in bicelles with ordered tails, which appear to be inconsistent with experimental observations. This suggests that those force field parameters are inaccurate. Simulations using CHARMM, OPLS-UA, GROMOS53A6, and GROMOS53A6OXY yield rodlike micelles, which are consistent with experimental observations, suggesting that parameters for these force fields are accurate enough. Comparing with simulation results with experimental scattering results for SDS micelles and comparing free energies of hydration of SDS head groups for different force fields could further validate the parameters or optimize them.

## 2.5 References

- (1) Evans, H. C. 117. Alkyl Sulphate. Part I. Critical Micelle Concentration of the Sodium Salts. *J. Chem. Soc.* **1956**, 579–586.
- (2) Reiss-Husson, F.; Luzzati, V. The Structure of the Micellar Solutions of Some Amphiphilic Compounds in Pure Water as Determined by Absolute Small-Angle X-Ray Scattering Techniques. *J. Phys. Chem.* **1964**, *68*, 3504–3511.
- (3) Mukerjee, P.; Mysels, K. *Critical Micelle Concentrations of Aqueous Surfactant Systems*; NSRDS-NBS.; US. Government Printing Office: Washington D.C., 1971; pp. 1–21.
- (4) Mazer, N. A.; Benedek, G. B.; Carey, M. C. An Investigation of the Micellar Phase of Sodium Dodecyl Sulfate in Aqueous Sodium Chloride Solutions Using Quasielastic Light Scattering Spectroscopy. *J. Phys. Chem.* **1976**, *80*, 1075–1085.
- (5) Itri, R.; Amaral, L. Q. Distance Distribution Function of Sodium Dodecyl Sulfate Micelles by X-Ray Scattering. *J. Phys. Chem.* **1991**, *95*, 423–427.
- (6) Bezzobotnov, V. Y.; Borbely, S.; Cser, L.; Farago, B.; Gladkih, I. A.; Ostanevich, Y. M.; Vass, S. Temperature and Concentration Dependence of Properties of Sodium Dodecyl Sulfate Micelles Determined from Small-Angle Neutron Scattering Experiments. *J. Phys. Chem.* **1988**, *92*, 5138–5143.
- (7) Bales, B. L.; Messina, L.; Vidal, A.; Peric, M.; Nascimento, O. R. Precision Relative Aggregation Number Determinations of SDS Micelles Using a Spin Probe. A Model of Micelle Surface Hydration. *J. Phys. Chem. B* **1998**, *102*, 10347–10358.
- (8) Yasunaga, T.; Oguri, H.; Miura, M. Acoustic Study on the Kinetics for the Dissociation-Recombination Reaction between Micelle and Counterion in Sodium Dodecyl Sulfate Solution. *J. Colloid Interface Sci.* **1967**, *23*, 352–357.
- (9) Bendedouch, D.; Chen, S.-H.; Koehler, W. C. Structure of Ionic Micelles From Small Angle Neutron Scattering. *J. Phys. Chem.* **1983**, *87*, 153–159.
- (10) Bergstrom, M.; Pedersen, J. S. Structure of Pure SDS and DTAB Micelles in Brine Determined by Small-Angle Neutron Scattering ( SANS ). *Phys. Chem. Chem. Phys.* **1999**, *1*, 4437–4446.

- (11) Hammouda, B. Temperature Effect on the Nanostructure of SDS Micelles in Water. *J. Res. Natl. Inst. Stand. Technol.* **2013**, *118*, 151–167.
- (12) Kodama, M.; Kubota, Y.; Miura, M. The Second CMC of the Aqueous Solution of Sodium Dodecyl Sulfate. III. Light-Scattering. *Bull. Chem. Soc. Jpn.* **1972**, *45*, 2953–2955.
- (13) Ma, C.; Li, G.; Xu, Y.; Wang, H.; Ye, X. Determination of the First and Second CMCs of Surfactants by Adsorptive Voltammetry. *Colloids Surfaces A Physicochem. Eng. Asp.* **1998**, *143*, 89–94.
- (14) Shi, Y.; Luo, H. Q.; Li, N. B. Determination of the Critical Premicelle Concentration, First Critical Micelle Concentration and Second Critical Micelle Concentration of Surfactants by Resonance Rayleigh Scattering Method without Any Probe. *Spectrochim. Acta Part A Mol. Biomol. Spectrosc.* **2011**, *78*, 1403–1407.
- (15) Kekicheff, P.; Grabielle-Madelmont, C.; Ollivon, M. Phase Diagram of Sodium Dodecyl Sulfate-Water System : I A Calorimetric Study. *J. Colloid Interface Sci.* **1989**, *131*, 112–132.
- (16) Kekicheff, P. Phase Diagram of Sodium Dodecyl Sulfate-Water System 2. Complementary Isoplethal and Isothermal Phase Studies. *J. Colloid Interface Sci.* **1989**, *131*, 133–152.
- (17) Missel, P. J.; Mazer, N. A.; Benedek, G. B.; Young, C. Y.; Carey, M. C. Thermodynamic Analysis of the Growth of Sodium Dodecyl Sulfate Micelles. *J. Phys. Chem.* **1980**, *84*, 1044–1057.
- (18) Missel, P. J.; Mazer, N. A.; Carey, M. C.; Benedek, G. B. Influence of Alkali-Metal Counterion Identity on the Sphere-to-Rod Transition in Alkyl Sulfate Micelles. *J. Phys. Chem.* **1989**, *93*, 8354–8366.
- (19) Vass, S.; Pedersen, J. S.; Plestil, J.; Laggner, P.; Rétfalvi, E.; Varga, I.; Gilányi, T. Ambiguity in Determining the Shape of Alkali Alkyl Sulfate Micelles from Small-Angle Scattering Data. *Langmuir* **2008**, *24*, 408–417.
- (20) Zhao, G.; Perilla, J. R.; Yufenyuy, E. L.; Meng, X.; Chen, B.; Ning, J.; Ahn, J.; Gronenborn, A. M.; Schulten, K.; Aiken, C.; et al. Mature HIV-1 Capsid Structure by Cryo-Electron Microscopy and All-Atom Molecular Dynamics. *Nature* **2013**, *497*, 643–646.

- (21) Dunfield, L. G.; Burgess, A. W.; Scheraga, H. A. Energy Parameters in Polypeptides . 8 . Empirical Potential Energy Algorithm for the Conformational Analysis of Large Molecules. *J. Phys. Chem.* **1978**, *82*, 2609–2616.
- (22) Shelley, J.; Watanabe, K.; Klein, M. L. Simulation of a Sodium Dodecylsulfate Micelle in Aqueous Solution. *Int. J. Quantum Chem. Quantum Biol. Symp.* **1990**, *38*, 103–117.
- (23) Dewar, M. S.; Zoebisch, E. G.; Healy, E. F.; Stewart, J. P. AM1 : A New General Purpose Quantum Mechanical Molecular Model '. *J. Am. Chem. Soc.* **1985**, *107*, 3902–3909.
- (24) Jarvis, J. A. J. Crystal Structure of Potassium Ethyl Sulphate. *Acta Crystallogr.* **1953**, *6*, 327–330.
- (25) Jorgensen, W. L. Intermolecular Potential Functions and Monte Carlo Simulations for Liquid Sulfur Compounds. *J. Phys. Chem.* **1986**, *90*, 6379–6388.
- (26) Bresme, F.; Farauo, J. Computer Simulation Studies of Newton Black Films. *Langmuir* **2004**, *20*, 5127–5137.
- (27) Bresme, F.; Chacon, E.; Martinez, H.; Tarazona, P. Adhesive Transitions in Newton Black Films: A Computer Simulation Study. *J. Chem. Phys.* **2011**, *134*, 214701–1–214701–214712.
- (28) Bresme, F.; Artacho, E. Electronic Structure Computations of Newton Black Films. *J. Mater. Chem.* **2010**, *20*, 10351–10358.
- (29) Shang, B. Z.; Wang, Z.; Larson, R. G. Molecular Dynamics Simulation of Interactions between a Sodium Dodecyl Sulfate Micelle and a Poly(ethylene Oxide) Polymer. *J. Phys. Chem. B* **2008**, *112*, 2888–2900.
- (30) Sammalkorpi, M.; Karttunen, M.; Haataja, M. Structural Properties of Ionic Detergent Aggregates: A Large-Scale Molecular Dynamics Study of Sodium Dodecyl Sulfate. *J. Phys. Chem. B* **2007**, *111*, 11722–11733.
- (31) MacKerell Jr., A. D. Molecular Dynamics Simulation Analysis of a Sodium Dodecyl Sulfate Micelle in Aqueous Solution : Decreased Fluidity of the Micelle Hydrocarbon Interior. *J. Phys. Chem.* **1995**, *99*, 1846–1855.
- (32) Yoshii, N.; Okazaki, S. A Molecular Dynamics Study of Surface Structure of Spherical SDS Micelles. *Chem. Phys. Lett.* **2006**, *426*, 66–70.

- (33) Yoshii, N.; Okazaki, S. A Molecular Dynamics Study of Structure and Dynamics of Surfactant Molecules in SDS Spherical Micelle. *Condens. Matter Phys.* **2007**, *10*, 573–578.
- (34) Bruce, C. D.; Berkowitz, M. L.; Perera, L.; Forbes, M. D. E. Molecular Dynamics Simulation of Sodium Dodecyl Sulfate Micelle in Water : Micellar Structural Characteristics and Counterion Distribution. *J. Phys. Chem. B* **2002**, *106*, 3788–3793.
- (35) Bruce, C. D.; Senapati, S.; Berkowitz, M. L.; Perera, L.; Forbes, M. D. E. Molecular Dynamics Simulations of Sodium Dodecyl Sulfate Micelle in Water : The Behavior of Water. *J. Phys. Chem. B* **2002**, *106*, 10902–10907.
- (36) Schweighofer, K. J.; Essmann, U.; Berkowitz, M. Simulation of Sodium Dodecyl Sulfate at the Water-Vapor and Water-Carbon Tetrachloride Interfaces at Low Surface Coverage. *J. Phys. Chem. B* **1997**, *101*, 3793–3799.
- (37) Yoshii, N.; Okazaki, S. A Molecular Dynamics Study of Structural Stability of Spherical SDS Micelle as a Function of Its Size. *Chem. Phys. Lett.* **2006**, *425*, 58–61.
- (38) Palazzesi, F.; Calvaresi, M.; Zerbetto, F. A Molecular Dynamics Investigation of Structure and Dynamics of SDS and SDBS Micelles. *Soft Matter* **2011**, *7*, 9148–9156.
- (39) Gao, J.; Ge, W.; Hu, G.; Li, J. From Homogeneous Dispersion to Micelles—a Molecular Dynamics Simulation on the Compromise of the Hydrophilic and Hydrophobic Effects of Sodium Dodecyl Sulfate in Aqueous Solution. *Langmuir* **2005**, *21*, 5223–5229.
- (40) Gao, J.; Ren, Y.; Ge, W. Molecular Dynamics Simulation of Effect of Salt on the Compromise of Hydrophilic and Hydrophobic Interactions in Sodium Dodecyl Sulfate Micelle Solutions. *Chinese J. Chem. Eng.* **2009**, *17*, 654–660.
- (41) Cheng, T.; Chen, Q.; Li, F.; Sun, H. Classic Force Field for Predicting Surface Tension and Interfacial Properties of Sodium Dodecyl Sulfate. *J. Phys. Chem. B* **2010**, *114*, 13736–13744.
- (42) MacKerell Jr., A. D. Empirical Force Fields for Biological Macromolecules: Overview and Issues. *J. Comput. Chem.* **2004**, *25*, 1584–1604.

- (43) Kaminski, G.; Duffy, E. M.; Matsui, T.; Jorgensen, W. L. Free Energies of Hydration and Pure Liquid Properties of Hydrocarbons from the OPLS All-Atom Model. *J. Phys. Chem.* **1994**, *98*, 13077–13082.
- (44) Weiner, S. J.; Kollman, P. A.; Nguyen, D. T.; Case, D. A. An All Atom Force Field for Simulations of Proteins and Nucleic Acids. *J. Comput. Chem.* **1986**, *7*, 230–252.
- (45) Schuler, L. D.; Daura, X.; van Gunsteren, W. F. An Improved GROMOS96 Force Field for Aliphatic Hydrocarbons in the Condensed Condensed Phase. *J. Comput. Chem.* **2001**, *22*, 1205–1218.
- (46) Oostenbrink, C.; Villa, A.; Mark, A. E.; van Gunsteren, W. F. A Biomolecular Force Field Based on the Free Enthalpy of Hydration and Solvation: The GROMOS Force-Field Parameter Sets 53A5 and 53A6. *J. Comput. Chem.* **2004**, *25*, 1656–1676.
- (47) Horta, B. A. C.; Fuchs, P. F. J.; van Gunsteren, W. F.; Hunenberger, P. H. New Interaction Parameters for Oxygen Compounds in the GROMOS Force Field : Improved Pure-Liquid and Solvation Properties for Alcohols, Ethers, Aldehydes, Ketones, Carboxylic Acids, and Esters. *J. Chem. Theory Comput.* **2011**, *7*, 1016–1031.
- (48) Kunz, A.-P. E.; Allison, J. R.; Geerke, D. P.; Horta, B. A. C.; Hunenberger, P. H.; Riniker, S.; Schmid, N.; van Gunsteren, W. F. New Functionalities in the GROMOS Biomolecular Simulation Software. *J. Comput. Chem.* **2012**, *33*, 340–353.
- (49) Shang, B. Z.; Wang, Z.; Larson, R. G. Effect of Headgroup Size, Charge, and Solvent Structure on Polymer-Micelle Interactions, Studied by Molecular Dynamics Simulations. *J. Phys. Chem. B* **2009**, *113*, 15170–15180.
- (50) Sammalkorpi, M.; Sanders, S.; Panagiotopoulos, A. Z.; Karttunen, M.; Haataja, M. Simulations of Micellization of Sodium Hexyl Sulfate. *J. Phys. Chem. B* **2011**, *115*, 1403–1410.
- (51) LeBard, D. N.; Levine, B. G.; Mertmann, P.; Barr, S. A.; Jusufi, A.; Sanders, S.; Klein, M. L.; Panagiotopoulos, A. Z. Self-Assembly of Coarse-Grained Ionic Surfactants Accelerated by Graphics Processing Units. *Soft Matter* **2012**, *8*, 2385–2397.

- (52) Israelachvili, J. N.; Mitchell, D. J.; Ninham, B. W. Theory of Self-Assembly of Hydrocarbon Amphiphiles into Micelles and Bilayers. *J. Chem. Soc. Faraday Trans. 2 Mol. Chem. Phys.* **1975**, *72*, 1525–1568.
- (53) Stubbs, J. M.; Potoff, J. J.; Siepmann, J. I. Transferable Potentials for Phase Equilibria. 6. United-Atom Description for Ethers, Glycols, Ketones, and Aldehydes. *J. Phys. Chem. B* **2004**, *108*, 17596–17605.
- (54) Pastor, R. W.; MacKerell Jr., A. D. Development of the CHARMM Force Field for Lipids. *J. Phys. Chem. Lett.* **2011**, *2*, 1526–1532.
- (55) Jorgensen, W. L.; Maxwell, D. S.; Tirado-Rives, J. Development and Testing of the OPLS All-Atom Force Field on Conformational Energetics and Properties of Organic Liquids. *J. Chem. Soc.* **1996**, *118*, 11225–11236.
- (56) Huang, W.; Lin, Z.; Gunsteren, W. F. Van. Validation of the GROMOS 54A7 Force Field with Respect to  $\alpha$ -Peptide Folding. *J. Chem. Theory Comput.* **2011**, *7*, 1237–1243.
- (57) Reif, M. M.; Winger, M.; Oostenbrink, C. Testing of the GROMOS Force-Field Parameter Set 54A8: Structural Properties of Electrolyte Solutions, Lipid Bilayers, and Proteins. *J. Chem. Theory Comput.* **2013**, *9*, 1247–1264.
- (58) Jozica D. GROMOS Developer. Private Communication, 2013.
- (59) Scott, W. R. P.; Hunenberger, P. H.; Tironi, I. G.; Mark, A. E.; Billeter, S. R.; Fennen, J.; Torda, A. E.; Huber, T.; Kruger, P.; van Gunsteren, W. F. The GROMOS Biomolecular Simulation Program Package. *J. Phys. Chem. A* **1999**, *103*, 3596–3607.
- (60) Yan, H.; Cui, P.; Liu, C.-B.; Yuan, S.-L. Molecular Dynamics Simulation of Pyrene Solubilized in a Sodium Dodecyl Sulfate Micelle. *Langmuir* **2012**, *28*, 4931–4938.
- (61) Schüttelkopf, A. W.; van Aalten, D. M. F. PRODRG: A Tool for High-Throughput Crystallography of Protein-Ligand Complexes. *Acta Crystallogr. D. Biol. Crystallogr.* **2004**, *D60*, 1355–1363.
- (62) Lemkul, J. A.; Allen, W. J.; Bevan, D. R. Practical Considerations for Building GROMOS-Compatible Small-Molecule Topologies. *J. Chem. Inf. Model.* **2010**, *50*, 2221–2235.



- (63) Ryckaert, J.-P.; Bellemans, A. Molecular Dynamics of Liquid Alkanes. *Faraday Discuss. Chem. Soc.* **1978**, *66*, 95–106.
- (64) Dominguez, H.; Berkowitz, M. L. Computer Simulations of Sodium Dodecyl Sulfate at Liquid/Liquid and Liquid/Vapor Interfaces. *J. Phys. Chem. B* **2000**, *104*, 5302–5308.
- (65) MacKerell Jr., A. D.; Bashford, D.; Bellott, M.; Dunbrack Jr., R. L.; Evanseck, J. D.; Field, M. J.; Fischer, S.; Gao, J.; Guo, H.; Ha, S.; et al. All-Atom Empirical Potential for Molecular Modeling and Dynamics Studies of Proteins †. *J. Phys. Chem. B* **1998**, *102*, 3586–3616.
- (66) Feller, S. E.; MacKerell Jr., A. D. An Improved Empirical Potential Energy Function for Molecular Simulations of Phospholipids. *J. Phys. Chem. B* **2000**, *104*, 7510–7515.
- (67) Klauda, J. B.; Venable, R. M.; Freites, J. A.; O'Connor, J. W.; Tobias, D. J.; Mondragon-Ramirez, C.; Vorobyov, I.; MacKerell Jr., A. D.; Pastor, R. W. Update of the CHARMM All-Atom Additive Force Field for Lipids: Validation on Six Lipid Types. *J. Phys. Chem. B* **2010**, *114*, 7830–7843.
- (68) Zoete, V.; Cuendet, M. A.; Grosdidier, A.; Michielin, O. SwissParam : A Fast Force Field Generation Tool for Small Organic Molecules. *J. Comput. Chem.* **2011**, *32*, 2359–2368.
- (69) Programs Written by GROMACS Users: Other Software;  
[http://www.gromacs.org/Downloads/User\\_contributions/Other\\_software\\_topolgen-1.1.tgz](http://www.gromacs.org/Downloads/User_contributions/Other_software_topolgen-1.1.tgz) (accessed December 19, 2013).  
[http://www.gromacs.org/Downloads/User\\_contributions/Other\\_software](http://www.gromacs.org/Downloads/User_contributions/Other_software).
- (70) Chandrasekhar, J.; Spellmeyer, D. C.; Jorgensen, W. L. Energy Component Analysis for Dilute Aqueous Solutions of Li<sup>+</sup>, Na<sup>+</sup>, F<sup>-</sup>, and Cl<sup>-</sup> Ions. *J. Am. Chem. Soc.* **1984**, *106*, 903–910.
- (71) Aqvist, J. Ion-Water Interaction Potentials Derived From Free Energy Perturbation Simulations. *J. Phys. Chem.* **1990**, *94*, 8021–8024.
- (72) Dang, L. X. Mechanism and Thermodynamics of Ion Selectivity in Aqueous Solutions of 18-Crown-6 Ether : A Molecular Dynamics Study. *J. Am. Chem. Soc.* **1995**, *117*, 6954–6960.

- (73) Joung, I. S.; Cheatham, T. E. Determination of Alkali and Halide Monovalent Ion Parameters for Use in Explicitly Solvated Biomolecular Simulations. *J. Phys. Chem. B* **2008**, *112*, 9020–9041.
- (74) Jensen, K. P.; Jorgensen, W. L. Halide, Ammonium, and Alkali Metal Ion Parameters for Modeling Aqueous Solutions. *J. Chem. Theory Comput.* **2006**, *2*, 1499–1509.
- (75) Jorgensen, W. L.; Tirado-Rives, J. The OPLS Potential Functions for Proteins. Energy Minimizations for Crystals of Cyclic Peptides and Crambin. *J. Am. Chem. Soc.* **1988**, *110*, 1657–1671.
- (76) Martínez, L.; Andrade, R.; Birgin, E. G.; Martínez, J. M. Software News and Update Packmol : A Package for Building Initial Configurations. *J. Comput. Chem.* **2009**, *30*, 2157–2164.
- (77) Martinez, J. M.; Martinez, L. Packing Optimization for Automated Generation of Complex System ' S Initial Configurations for Molecular Dynamics and Docking. *J. Comput. Chem.* **2003**, *24*, 819–825.
- (78) Hayter, J. B.; Penfold, J. Self-Consistent Structural and Dynamic Study of Concentrated Micelle Solutions. *J. Chem. Soc. Faraday Trans. 1* **1981**, *77*, 1851–1863.
- (79) Rawdon, E. J.; Kern, J. C.; Piatek, M.; Plunkett, P.; Stasiak, A.; Millett, K. C. Effect of Knotting on the Shape of Polymers. *Macromolecules* **2008**, *41*, 8281–8287.
- (80) Garrido, N. M.; Queimada, A. J.; Jorge, M.; Macedo, E. A.; Economou, I. G. 1-Octanol / Water Partition Coefficients of N -Alkanes from Molecular Simulations of Absolute Solvation Free. *J. Chem. Theory Comput.* **2009**, *5*, 2436–2446.
- (81) Jorgensen, W. L.; Tirado-Rives, J. Potential Energy Functions for Atomic-Level Simulations of Water and Organic and Biomolecular Systems. *Proc. Natl. Acad. Sci. U. S. A.* **2005**, *102*, 6665–6670.
- (82) Bhatnagar, N.; Kamath, G.; Potoff, J. J. Biomolecular Simulations with the Transferable Potentials for Phase Equilibria: Extension to Phospholipids. *J. Phys. Chem. B* **2013**, *117*, 9910–9921.
- (83) Theodorou, D. N.; Suter, U. W. Shape of Unperturbed Linear Polymers: Polypropylene. *Macromolecules* **1985**, *18*, 1206–1214.

- (84) Hadizadeh, S.; Linhananta, A.; Plotkin, S. S. Improved Measures for the Shape of a Disordered Polymer To Test a Mean-Field Theory of Collapse. *Macromolecules* **2011**, *44*, 6182–6197.
- (85) Frisch, M. J.; Trucks, G. W.; Schlegel, H. B.; Scuseria, G. E.; Robb, M. A.; Cheeseman, J. R.; Scalmani, G.; Barone, V.; Mennucci, B.; G. A. Petersson, et, A. Gaussian 09, Revision D.01, 2009, Gaussian, Inc., Wallingford CT,.
- (86) Ribeiro, J. V; Tamames, J. a C.; Cerqueira, N. M. F. S. a; Fernandes, P. a; Ramos, M. J. Volarea - a Bioinformatics Tool to Calculate the Surface Area and the Volume of Molecular Systems. *Chem. Biol. Drug Des.* **2013**, *82*, 743–755.
- (87) Futamura, N.; Aluru, S.; Ranjan, D.; Hariharan, B. Efficient Parallel Algorithms for Solvent Accessible Surface Area of Proteins. *IEEE Trans. Parallel Distrib. Syst.* **2002**, *13*, 544–555.

## Chapter 3

### Molecular Dynamics Simulations of Structure Property Relationships of Tween 80 Surfactants in Water and at Interfaces

The work in Chapter 3 has been published as: X. Tang, K. J. Huston, and R. G. Larson, Molecular Dynamics Simulations of Structure-Property Relationships of Tween 80 Surfactants in Water and at Interfaces. *J.Phys.Chem.B*, 118 (2014), 12907-18.

#### 3.1. Introduction

In 2010, the Deepwater Horizon oil spill led to the release of approximately 4.9 million barrels of Mississippi Canyon Block 252 (MC 252) crude oil into the Gulf of Mexico.<sup>125,126</sup> To protect the coastline and marine environments, roughly 1.84 million gallons of chemical dispersants (e.g. Corexit 9500) were sprayed into the gulf, of which 1.07 million gallons went onto the sea surface and 0.77 million gallons went under the sea into the oil plume.<sup>126</sup> Generally, chemical dispersants accelerate natural dispersal processes that involve formation of dispersible droplets through turbulence in the water column or wave energy at the surface, followed by ingestion by microorganisms. However, there is a lack of scientific study of the detailed mechanisms of dispersant activity, in part due to the complexity of the industrial dispersant formulations. Also, the role of individual components of dispersant mixtures on dispersing efficiency has not

been understood in any detail. Recently, however, increasing computational power has enabled atomistic molecular dynamics (MD) simulations to be carried out for systems containing up to millions of atoms over time scales of hundreds of nanoseconds.<sup>76</sup> MD simulations provide a unique resolution of structural details down to the angstrom scale, and reveal dynamics and possible kinetics of various molecular processes relevant to dispersion of oil in water. This motivates us to use atomistic MD simulations to study dispersant micelle properties and dispersant behavior at air—water and oil—water interfaces.

Corexit 9500 contains a mixture of nonionic (48 wt%) and anionic (35 wt%) surfactants, as well as solvents,<sup>127</sup> as listed in Table B.1.<sup>128,129</sup> The composition is designed, among other things, to ensure that stable emulsions are formed of oil droplets dispersed in water, rather than the reverse. Cationic surfactants are usually not considered due to the toxicity of quaternary ammonium salts (the most common commercial type of cationic surfactant) to many organisms. Because solvents reduce the viscosity of the final dispersant mixture, solvents aid in spraying or otherwise deploying the dispersant, and facilitate its penetration and mixing into the oil slick.<sup>127,129</sup> Developed by ExxonMobil and sold to Nalco Holding Company, the dispersant Corexit 9500 contains as one of its main surfactants Tween 80, or polysorbate 80 (polyoxyethylene sorbitan oleates). Tween 80 is a nonionic surfactant with four hydrophilic head groups in its canonical structure (although the commercial mixture likely contains many species that are missing some head groups). Other surface-active components of Corexit 9500 include an ionic surfactant, namely dioctyl sodium sulfosuccinate (DOSS), also known as “Aerosol OT”

(AOT), and co-nonionic surfactants Span 80 (sorbitan monooleate) and Tween 85 (polyoxyethylene sorbitan trioleate). Also contained in Corexit 9500 are solvents such as polyethylene glycol, butoxypolypropylene glycol, and hydrotreated oil. Each of the sorbitan-derived species is an industrial mixture containing thousands of chemically distinct compounds. In addition, the effectiveness of the dispersant depends on the type of oil and its extent of weathering,<sup>127,130</sup> the salinity,<sup>131</sup> the sea state,<sup>127</sup> and the temperature<sup>132</sup> of the seawater as well. MC 252, in particular, is a light sweet or light low sulfur content oil.<sup>133</sup> After evaporation of most of the volatile organic compounds within the first 24–48 h of the oil spill, the remaining weathered oil contained a carbon number range from C15 to C44 with C20 being the most abundant species.<sup>133</sup>

Ideally, one would like to study how the dispersant components behave cooperatively during the process of oil dispersal. However, it is worth studying each surface-active component in isolation from the others before attempting to understand the synergistic effects of two or more species. Reichert et al.<sup>134</sup> developed a simplified experimental model for an oil—brine—dispersant system that uses Tween 80 as a representative for Corexit 9500, squalane (i.e., 2,6,10,15,19,23-hexamethyltetracosane,  $C_{30}H_{62}$ ) for MC 252 crude oil, and a model seawater<sup>135</sup> composed of sodium sulfate (35 mM), sodium chloride (430 mM), and magnesium chloride (50 mM). Adsorption of AOT et al. was found to be inhibited to oil—water interfaces containing preadsorbed Tween 80.<sup>136,137</sup> Earlier, Blondina et al.<sup>131</sup> showed that the effect of salinity on Corexit 9500 is moderate compared with Corexit 9527, and Reichert et al.<sup>134</sup> showed that there is little effect of salinity on the stability and interfacial tension of Tween 80. Therefore, in our work, we further simplify

Reichert's oil—brine—dispersant model by simulating a mixture of Tween 80, squalane, and water in the absence of salts.

The major surfactant component Tween 80 has been widely used not only as a dispersant but also as an emulsifier, a lubricant, and an excipient as well.<sup>138</sup> The critical micelle concentration (CMC) of Tween 80 in water has been reported to lie in the range 0.010–0.015 mM at 25 °C.<sup>132,139–142</sup> The CMC for the Tween series decreases with increasing numbers of alkyl carbon atoms in the hydrophobic tail, and increases with increasing numbers of oxyethylene (OE) monomers in the head groups.<sup>132</sup> At concentrations above the CMC, Tween 80 self-aggregates into micelles. The average aggregation number for micelles of Tween 80 obtained using fluorescence probes in solutions containing phosphate buffers at 298 K was estimated by Glenn et al. to be 22 at 40 mM,<sup>140</sup> while Haque et al. and Tummino and Gafni estimated it to be 124 at 100 mM<sup>143</sup> and 133 at 15 mM,<sup>142</sup> respectively. Mahajan et al. used small-angle neutron scattering (SANS), and assumed an ellipsoidal micelle shape, to obtain an unusually high aggregation number of 350 at 23 mM,<sup>141</sup> while de Campo et al. obtained an estimate of 60 using SANS at ~160 mM or 20% volume fraction.<sup>139</sup> The wide variation in reported micelle aggregation numbers for commercial Tween 80 may be related to its chemical heterogeneity, including its distribution of ethoxylated headgroup sizes,<sup>144</sup> and perhaps there is batch-to-batch variability in its composition. In this study, an aggregation number of 60 is chosen, since this value is in the midrange of values reported in experiments,<sup>139</sup> has been chosen in a previous simulation,<sup>20</sup> and is reported in chemical company literature as well.<sup>146</sup> In addition, a fixed aggregation number is chosen for structure

property comparison among five components of Tween 80. A radius of gyration ( $R_g$ ) value of 2.74 nm for a Tween 80 micelle of the canonical structure and an  $R_g$  value of 1.55 nm for the tail groups of this Tween 80 micelle at an aggregation number of 60 are obtained from our simulations reported below. These results are consistent with the most recent SANS study of a Tween 80 micelle which gave an  $R_g$  value of 2.7 nm for the whole micelle and an  $R_g$  value of 1.5 nm for the tail groups, and with the dynamic light scattering measurement in the same study assuming a polydispersity of 20% in micelle aggregation number for the solution.<sup>63,147</sup>

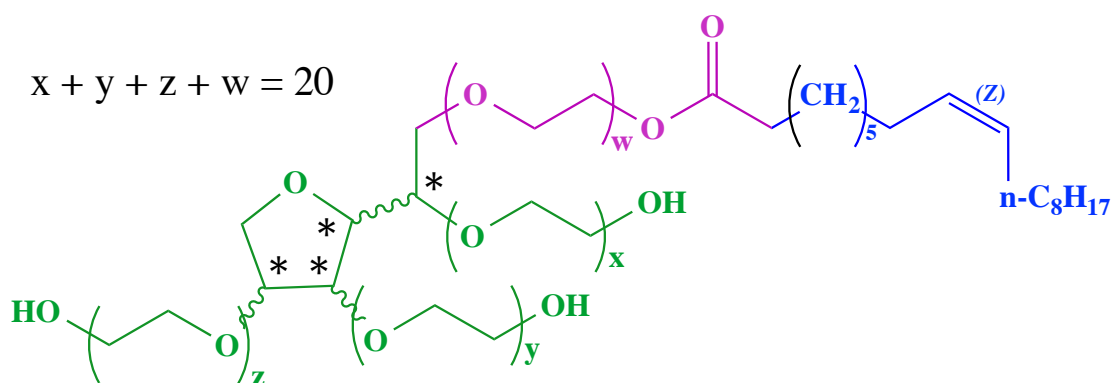


**Figure 3.1** Canonical structure of Tween 80 molecule with X, Y, and Z head groups (green), W headgroup (purple) containing x, y, z, and w number of ethylene oxide (EO) units respectively, and tail (blue). Chiral carbons are marked by “\*”. The “Z” labeling the double bond means that the isomer has the two high-priority (i.e., high atomic number) substituents of the double bond on the same side of the bond, i.e., in the cis configuration.

The “typical” structure of Tween 80 is shown in Figure 3.1:<sup>138,148,149</sup> the four hydrophilic poly(ethylene oxide) (PEO) head groups of Tween 80 are attached to sorbitan with one PEO chain, the “W” chain, connected at its other end via an ester group to an oleate tail, which contains a single unsaturated bond. The four head groups are named the W, X, Y,



and Z heads containing x, y, z, and w number of EO units respectively, and the sum of x, y, z, and w averages 20. While this “typical” structure already allows for a wide range of isomers in which the W, X, Y, and Z groups can vary in length, this does not fully account for the variability in the chemical structures in Tween 80, which is in fact not fully defined. Tween 80 is synthesized by ethoxylation of dehydrated sorbitol followed by oleic acid esterification. Besides forming polyoxyethylene sorbate or polysorbate during ethoxylation, polyisorbide and polysorbitol are other possible intermediates.<sup>148,149</sup> In addition, the position of esterification by oleic acid could be nonselective with respect to the four PEG chains. The final Tween 80 product is probably a mixture of various polysorbates, polyisorbates, and polysorbitols with a distribution of polyethylene glycol chain lengths, numbers and lengths of oleate tail(s), distributions of stereoisomers and constitutional isomers, and unreacted or partially reacted materials as well. Recently, components contained in Tween 80 were identified by several groups using liquid chromatography techniques combined with mass spectrometry, which confirmed its heterogeneous composition.<sup>51,148–150</sup>

MD simulation of all constitutional isomers of Tween 80 is too expensive, not even counting the 16 possible stereoisomers for each constitutional isomer resulting from the four chiral carbons in each molecule. Constitutional isomers have the same molecular formula but different interatomic bonds, while stereoisomers also have the same interatomic bonds but different chirality of one or more of the four chiral carbons. The four chiral carbons are identified by asterisks, and the connections to side chains of the three chiral carbons residing on the ring are marked by wavy bonds in Figure 3.1.

Stereoisomers and constitutional isomers with similar structure are expected to behave similarly at interfaces and in micelles, and thus, a study of representative structures, individually and collectively, is likely to provide a reasonable understanding of Tween 80 behavior.

In the simplest representative structure studied here, the numbers of EO units,  $x$ ,  $y$ ,  $z$ , and  $w$  in each of the four head groups, X, Y, Z, and W, were taken to be equal to  $20/4 = 5$ . In earlier work, the interactions of one Tween 80 molecule with this same structure and polymers hydroxypropyl methylcellulose or Pullulan on a surface of a crystal of the drug fenofibrate were studied using the COMPASS force field in the Materials Studio simulation engine.<sup>151</sup> In addition, the strengths of interaction of this Tween 80 isomer with crystal surfaces of the drugs nabumetone, carbamazepine, or fluorometholone were carried out using the COMPASS force field and the drugs celecoxib and tamozolomide using the CVFF force field.<sup>50</sup> Amani et al.<sup>145</sup> studied the properties of a micelle of 60 Tween 80 using a modified coarse-grained MARTINI force field, which eliminates the stereogenic centers in Tween 80 by lumping the chiral atoms with nearby carbons.

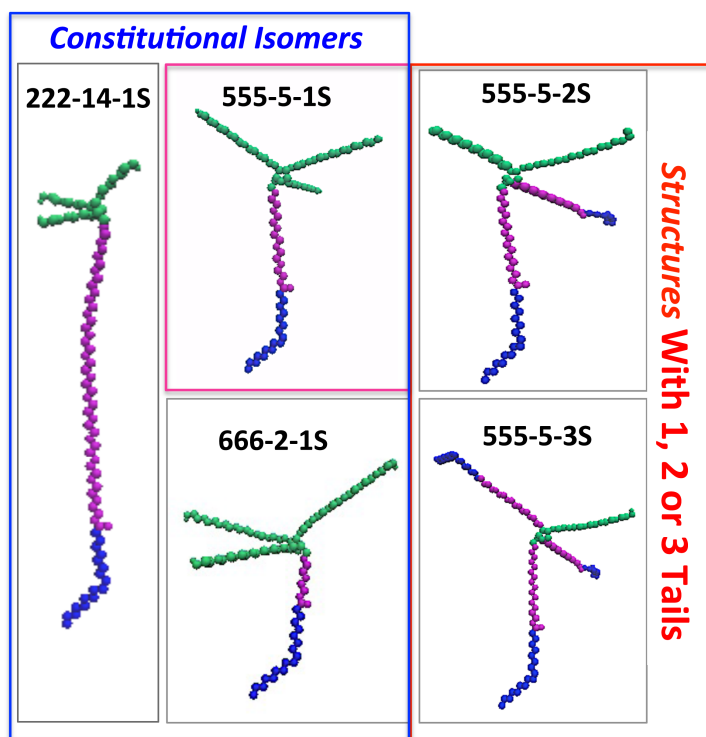


**Figure 3.2** Five different Tween 80 molecules are chosen in this work. The three isomers in the blue frame are constitutional isomers with the same tail but different distributions of headgroup lengths. The three models in the red frame are molecules chosen with the same distributions of the headgroup lengths but different numbers of tails. Shown are tails (blue), W heads (pink), X, Y, and Z heads, the THF ring, and two connected carbons (green).

Thus, earlier MD simulations of Tween 80 have focused on interactions of a single Tween molecule with a polymer or a drug molecule on drug surfaces at an all-atom level, or on micelle properties of a single-component Tween 80 micelle using a coarse-grained model. To our knowledge, the micelle properties of different isomers and variants of Tween 80 have never been studied at an atomistic level. In addition, the behavior of Tween 80 at the air/water and water/oil interfaces, which is critical in the dispersing

process, has not yet been studied computationally. Here, we therefore study the micelle structure and interfacial behavior of the three constitutional isomers and two additional structures of Tween 80 mentioned above. Due to the relatively large size of the Tween 80 molecule, simulation of self-assembly of Tween 80 surfactants into a micelle is not computationally feasible. We therefore simulate preassembled spherical micelles, and preassembled monolayers of Tween 80 at interfaces.

The limitation of using preassembled structures with a fixed aggregation number or surface density is that different components of Tween 80, even if they could be obtained in pure form, are likely to assemble into micelles of different aggregation number and assemble at different densities at interfaces. Simulations that can be meaningfully compared to experimental data, therefore, need to allow self-assembly to create equilibrium micelles and surface layers, preferably containing realistic mixtures of Tween 80 components. While we cannot undertake such simulations at atomistic resolution any time soon, our modeling here should allow at least a qualitative assessment of how differently the various components of Tween 80 behave in micelles and at interfaces, in general. In the future, we also plan to compare the results for preassembled structures presented here with similar results obtained from coarse-grained models, in order to validate the coarse-grained models, in preparation for much larger scale simulations of Tween 80 self-assembly.

The rest of this article is structured as follows: section 3.2 lists the computational models and simulation methods, section 3.3 contains the results, and section 3.4 summarizes the conclusions.

## 3.2. Computational Models and Simulation Methods

### 3.2.1 GROMOS53A6<sub>OXY+D</sub> Force Field

The GROMACS 4.5.5 simulation engine is used with the GROMOS united atom (UA) force field. Compared with all atom (AA) force fields, a UA force field accelerates MD simulations by grouping each carbon with its bonded hydrogen atoms into a pseudo or united atom to reduce the number of atoms in each Tween 80 molecule from 214 to 93, and by applying a larger time step size. A UA force field provides a reasonable resolution and speeds up the simulation to up to 3-fold compared with an AA force field.

The GROMOS53A6 force field is generally known to be problematic for oxygen-containing compounds.<sup>39,48,87</sup> In the past, to use a GROMOS force field to model molecules containing PEO, alcohol, and/or ether groups accurately, researchers typically adjusted either the Lennard-Jones (L-J) potential of the oxygen parameters, the partial charges, or a combination of both, specifically for the oxygen-containing compounds studied.<sup>48,152</sup> Recently, van Gunsteren et al.<sup>87</sup> systematically adjusted potentials of oxygen-containing compounds for alcohols, ethers, ketones, aldehydes, carboxylic acids, and esters, yielding the GROMOS53A6<sub>OXY</sub> extension of the GROMOS53A6 force field, with improved pure-liquid and solvation properties. As a further extension of this, Fuchs et al.<sup>39</sup> developed GROMOS53A6<sub>OXY+D</sub> to fit torsional-energy parameters for the vicinal OCCO and CCOC diether bonds in 1,2-dimethoxyethane to quantum-mechanical (QM) rotational energy profiles of these bonds in a vacuum. This extended force field was then validated against experimental conformer populations of OCCO and CCOC in pure liquid and in aqueous mixtures of 1,2-dimethoxyethane, and its predictions of the radius of

gyration and persistence length of polyethers (PEG and PEO) are in agreement with both experimental data and previous simulations using the CHARMM C35 and C35r force fields.<sup>153,154</sup> The new GROMOS53A6<sub>OXY+D</sub> force field is able to generate an experimentally accurate “gauche effect” (i.e., an unusually high percentage of gauche configurations) for the vicinal diether functions in molecules containing PEO or PEG units. Here we compare the micelle structure of a “canonical” Tween 80 molecule with equal lengths of all four PEG head groups and one tail in water using both GROMOS53A6, which gives an  $R_g$  value of 2.5 nm, and GROMOS53A6<sub>OXY+D</sub>, which gives an  $R_g$  value of 2.7 nm. We find that the latter is closer to the experimental result,  $R_g = 2.72$  nm,<sup>147</sup> and has a denser hydrocarbon core (Figure B.1) than the former. GROMOS53A6<sub>OXY+D</sub> is therefore chosen for all simulations including those used for both the bulk and the interfacial phenomena. The topology, mdp, and trajectory files were uploaded to <https://data.gulfresearchinitiative.org/data/R1.x141.064:0057>.

### 3.2.2 Partial Charges and Topology

The coordinate pdb files for Tween 80 and squalane were generated using Materials Studio followed by nonpolar hydrogen removal. Initial configurations of preassembled spherical micelles and monolayers were generated using PACKMOL software.<sup>114,115</sup> Topology files were generated using the PRODRG server followed by manual adjustments.<sup>99,100</sup> For squalane, the topology file was adopted from the PRODRG server directly except that all the partial charges were adjusted to zero. For the Tween 80 molecule, based on the transferable property for the empirical force field,<sup>27,100</sup> partial

charges and atom assignments, if available, are adopted from the GROMOS force field; otherwise, they are obtained through QM calculations using Gaussian 09 software.<sup>122</sup> The “atom assignments” mentioned above refer to the intramolecular and L-J intermolecular parameters. Specifically, the parameters of the hydrocarbon tail group of Tween 80 were adopted from the Ryckaert—Bellemans (R—B) potential<sup>101</sup> except for the double bond, which was adopted from the tail group of phosphatidylcholine containing a double bond given by Poger et al.;<sup>36</sup> the ester group parameters were adopted directly from the GROMOS53A6<sub>OXY</sub> force field;<sup>87</sup> and parameters for PEO and PEG chains were adopted from the GROMOS53A6<sub>OXY+D</sub> force field.<sup>39</sup> For the tetramethyl sorbitan group, a substituted tetrahydrofuran (THF) structure shown in Figure 3.3, the atomic assignments were adopted from van Gunsteren et al.,<sup>155</sup> and the partial charges were estimated by fitting point charges to electrostatic potential using Gaussian 09 software,<sup>122</sup> with density functional theory at B3LYP/6-31G(d,p) level averaged over 27 conformational isomers.

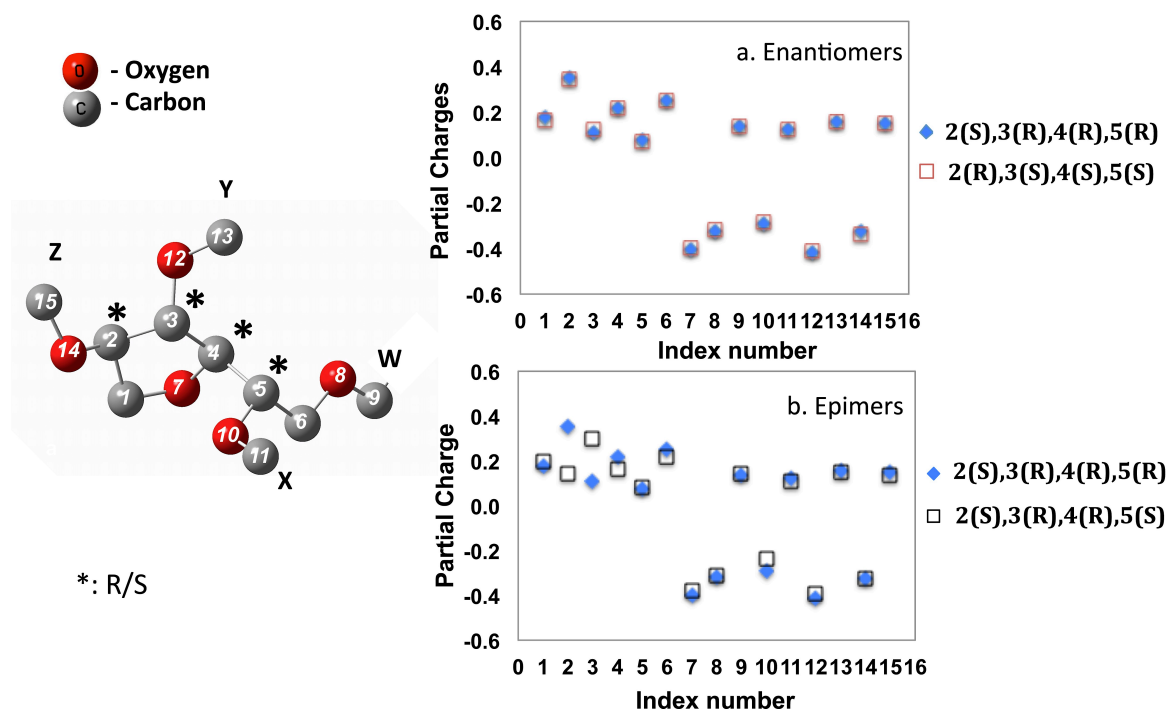


**Figure 3.3** Tetramethyl sorbitan used in quantum mechanical calculations. (a) Comparison of partial charges between two enantiomers that have opposite chirality for all four chiral carbons. (b) Comparison of partial charges between two epimers that have opposite chirality for only the stereogenic center at position 5, and with the same chiralities at the other three carbons.

The four chiral carbons in tetramethyl sorbitan can form 16 possible stereoisomers. These can be grouped as eight pairs of enantiomers, where the two molecules in each pair have completely opposite chirality, i.e., mirror-symmetry. Since other molecules with which they interact are achiral, the mirror-symmetric enantiomers, and their interactions with other molecules, behave identically. Other pairs, called diastereomers, have at least one carbon with the same chirality, of which epimers have all but one carbon with the same chirality, and these can have different physical properties. Here, we designate the particular stereoisomer of tetramethyl sorbitan using the index number and chirality of



the stereogenic center. A pair of enantiomers, namely, 2(S),3(R),4(R),5(R) and 2(R),3(S),4(S),5(S), and a pair of diastereomers (specifically epimers), namely, 2(S),3(R),4(R),5(R) and 2(S),3(R),4(R),5(S), are chosen here for comparison of optimized partial charges obtained from the QM calculations described above. To sample over different conformers in a reasonable computational time, 27 conformers are sampled manually for each isomer. Specifically, we generate three conformers by rotating the bond between atoms 4 and 5 by 120° three times. For each of these three conformers, we rotate the bond between atoms 5 and 10 by 40° 9 times and thereby generate 27 conformers in total. The energy difference among the 27 conformers of the 2(S),3(R),4(R),5(S) is as much as 15 k<sub>B</sub>T (data not shown). The final partial charges used in the MD simulations are assigned by Boltzmann-weighted energy averaging over the partial charges of all 27 conformers. As shown in Figure 3.3a, the partial charges of the two mirror-image enantiomers are almost identical as expected, while the partial charges of the two epimers in Figure 3.3b are slightly different. We found through MD simulations that the micellar structures formed by the two epimers are almost the same, as expected. Hence, for the rest of our simulations, we use 2(S),3(R),4(R),5(S) as a representative stereoisomer.

### 3.2.3 Five Representative Molecules in Tween 80

As shown in Figure 3.2, we built five molecules representing components of Tween 80, including the isomer that had been studied previously in MD simulations, two more constitutional isomers, and two more molecules of Tween 80 with two and three tails instead of only one. The colors used to denote different groups of atoms in Tween 80 are shown in Figures 3.1 and 3.2: The tail in blue is composed of the oleate group without the hydrophilic ester group; the W head in pink, between the tail and the THF ring, is composed of the PEO and the ester group; and the remainder of the molecule in green includes the X, Y, and Z PEG head groups, the THF ring, and the connected carbons. Constitutional isomers having the same molecular formula but different distributions of headgroup lengths over the four heads were chosen. Two more models of Tween 80 were chosen with the same distributions of the head groups but having either two tails, one each connected to the W and X heads, or three tails, one each connected to the W, X, and Y heads. Tween 80 molecules will here be named according to the numbers of EO units in the X, Y, Z, and W head groups (in that order), the numbers of tails, and the chirality of atom 5 (Figure 3.3). For example, “555-5-1S” has five EO units in each head, one tail, with the chiral carbon 5 (the one not on the ring) having the “S” chirality. Of the two additional constitutional isomers, 666-2-1S has a shorter W head with two EO units and 222-14-1S has an extended W head with 14 EO units. 555-5-2S and 555-5-3S have two and three tails, respectively, but the same headgroup lengths. We connected the one (or two) additional tails to the X (or X and Y) head groups, although the oleate tail groups can connect to any of the head groups.<sup>156</sup> 555-5-3S is listed as the “typical” structure for

Tween 85 (polyoxyethylene (20) sorbitan trioleate), which is another one of the nonionic surfactants of Corexit 9500.<sup>128,156</sup>

### 3.2.4 MD Simulations

United atom (UA) molecular dynamic (MD) simulations of mixtures of Tween 80, squalane (oil), and water were carried out. A preassembled spherical micelle composed of 60 surfactants was initially centered in a periodic cubic box with dimension 12 nm, yielding a total surfactant concentration of 58 mM. This was then solvated with SPC<sup>33</sup> water molecules outside of the micelle, followed by energy minimization. For preassembled monolayers, we first varied the number of surfactants 555-5-1S in a simulation box of  $6 \times 6 \times 18 \text{ nm}^3$  and the number of surfactants 555-5-3S in a simulation box of  $8 \times 8 \times 24 \text{ nm}^3$ , to generate a range of surfactant surface densities from about 1 to  $4.5 \text{ nm}^2/\text{molecule}$ , where the long dimension of the box was perpendicular to the interface. The tails of the surfactants were placed in the oil, and the head groups in the water as shown in Figure 3.4. Next, at a surface coverage of  $1.3 \text{ nm}^2/\text{molecule}$  or 98 surfactants total, one of the three constitutional isomers, or one of the two additional structures that have two or three tails, was packed at air–water or oil–water interfaces, 49 molecules at each of the two interfaces, in a simulation box of  $8 \times 8 \times 24 \text{ nm}^3$ . Temperature was controlled using the stochastic velocity rescale method at 300 K ( $\tau_T = 0.1 \text{ ps}$ ), where  $\tau_T$  is the temperature time constant. Pressure control was applied isotropically at 1 bar using the Berendsen weak-coupling method for micelle simulations, with a pressure time constant of  $\tau_p = 1.0 \text{ ps}$ . An NVT ensemble was used to study the air–water interfacial

behavior with the Berendsen weak-coupling method for pressure control and an NAPzT ensemble with the Parrinello—Rahman pressure coupling for the z-axis only for the oil—water interfacial tension estimation. A cutoff scheme was used for short-range nonbonded interactions (van der Waals, 1.4 nm; real-space Coulomb, 0.9 nm), and long-range electrostatic interaction was computed using the particle mesh Ewald (PME) technique (grid spacing set to the default value of 0.12 nm). A time step of 2 fs was used with a neighbor list update every 10 time steps. Bond lengths were constrained using LINCS; SHAKE was used for all bonds containing hydrogen, while the water geometry was constrained using SETTLE. After water was added, energy minimization was performed until the maximum force on any atom dropped below  $1000 \text{ kJ mol}^{-1}\text{nm}^{-1}$ . Further position restraints were employed for an additional 1 ns by harmonically restraining the tail beads with a force constant of  $1000 \text{ kJ mol}^{-1}\text{nm}^{-1}$  to allow water molecules to relax around the micelle or around surfactants at interfaces. The full MD simulation lasted 30 ns or longer for micelle simulations, and the last 5 ns were used for analysis during which the potential energy, radius of gyration ( $R_g$ ), and radial distribution functions (RDFs) of different groups about the micelle center of mass (COM) remained stable. For surface tension investigations, 100 ns MD simulations were carried out using an NVT ensemble to study air—water interfaces and 240 ns MD simulations using an NAPzT ensemble for oil—water interfaces, respectively. All trajectories were visualized with VMD 1.9.1.

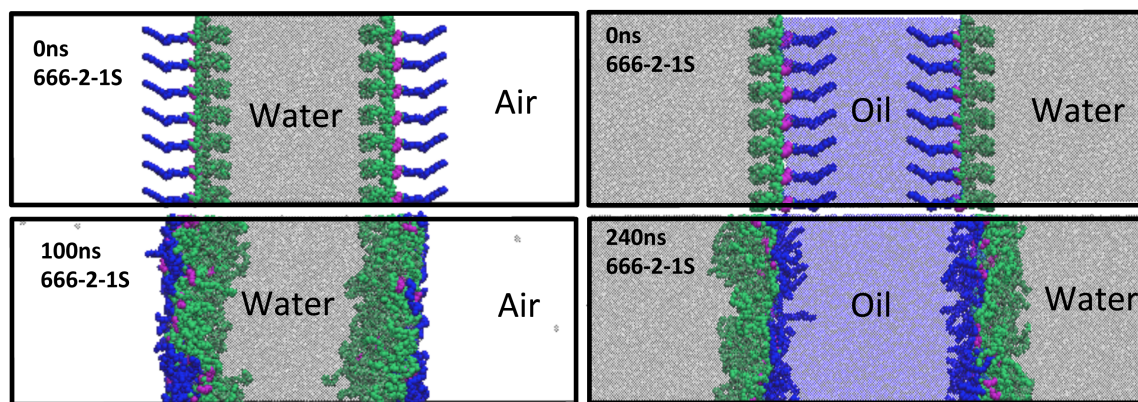


**Figure 3.4** Snapshots of initial (top) and final (bottom) states of air—water and oil—water interfaces in simulations with isomer 666-2-1S. The black frame is the simulation box. Shown are tails (blue), W heads (purple), X, Y, and Z heads, the THF ring, and two connected carbons (green).

### 3.3. Results and Discussion

Table 3.1 lists the radius of gyration ( $R_g$ ) and solvent accessible surface area (SAS) for single molecules and micelles and radial positions of the micelle headgroup RDF peak and shape eccentricity of the micelle with aggregation number 60. Here the SAS is the surface area of a micelle that is accessible to a solvent. In brief, a probe of spherical “water” molecule of radius 1.4 Å is rolled over the rough surface of the micelle to measure the hydrophobic, hydrophilic, and total surface areas of the micelle. The hydrophilic% of SAS is the ratio of the hydrophilic surface area to the total surface area of a micelle. The eccentricity “ $e$ ” is calculated using  $e = \sqrt{1 - c^2/a^2}$ , where  $c$  is the shortest semiaxis of the micelle obtained from the time-average of the smallest instantaneous principal value of the radius of gyration tensor and  $a$  is the corresponding

time-average of the longest semiaxis. The estimated eccentricity “e” of the micellar hydrophobic core containing tail beads only shows a more distorted shape than that for the micelle as a whole, using all surfactant beads, especially for micelles composed of mixtures of 555-5-1S and 555-5-1R, and for micelles containing multitailed surfactants 555-5-2S and 555-5-3S. Since the hydrophobic cores are covered with thick headgroup layers, the resulting final shapes of the micelles are only slightly ellipsoidal for all surfactants, and thus we also present the eccentricities of the hydrophobic cores, which show a more pronounced dependence on surfactant structure. The  $R_g$  and SAS values of different individual surfactant molecules in water are similar; however, a micelle of 222-14-1S shows the highest  $R_g$  and SAS, and a micelle of 555-5-3S shows the second-highest  $R_g$  but lowest SAS. Micellar sizes estimated from the radii at the peak of the headgroup RDF are similar for all single-tailed surfactants and increase significantly when the number of tails is increased. In general, greater differences are found among constitutional isomers and components of Tween 80 with different numbers of tails than between stereoisomers.

**Table 3.1.** Properties of Two Stereoisomers, Two Additional Constitutional Isomers, and Two Component of Tween 80 with Two, and Three tails of Isolated Surfactants and of Spherical Micelles Composed of Those Isomers in Water.

properties in water		222-14-1S	555-5-1S	555-5-1R	Half		666-2-1S	555-5-1S	555-5-2S	555-5-3S
					555-5-1S	Half 555-5-1R				
single surfactant	Rg(nm)	0.83±0.10	0.81±0.08	0.81±0.06			0.85±0.07	0.81±0.08	0.82±0.05	0.79±0.06
	SAS(nm <sup>2</sup> )	17.4±1.5	17.2±1.3	17.5±1.1			17.7±1.1	17.2±1.3	18.6±1.1	19.1±1.1
micelles of 60 Tween 80 molecules	Rg(nm)	2.96±0.02	2.74±0.03	2.78±0.02	2.78±0.02		2.71±0.02	2.74±0.03	2.85±0.01	2.93±0.01
	head RDF peak radius	2.2	2.2	2.3	2.3		2.3	2.2	2.8	3.2
	SAS/Surf. (nm <sup>2</sup> )	10.5±0.1	9.0±0.2	9.3±0.2	9.5±0.2		9.3±0.2	9.0±0.2	9.1±0.2	8.7±0.2
	hydrophilic%	87.9±1.6%	87.6±2.2%	88.6±2.1%	88.3±2.0%		90.0±2.6%	87.6±2.2%	84.2±2.0%	79.6±2.1%
	principal Rg (nm)	1.9:1.7:1.5	1.8:1.6:1.4	1.7:1.6:1.5	1.8:1.6:1.5		1.7:1.6:1.4	1.8:1.6:1.4	1.8:1.6:1.4	1.9:1.7:1.5
	eccentricity- whole micelle	0.58±0.02	0.63±0.04	0.51±0.04	0.58±0.05		0.50±0.04	0.63±0.04	0.60±0.02	0.60±0.03
eccentricity – micelle core	0.59±0.05	0.63±0.06	0.65±0.09	0.75±0.03		0.64±0.03	0.68±0.04	0.72±0.06	0.74±0.03	

### 3.3.1 Micellar Composition Profiles of Isomers and Multitailed Surfactants

Equilibration of self-assembly was impeded by the low diffusivities of small clusters formed during the simulations. We therefore preassembled 60 Tween 80 molecules into a spherical micelle and simulated this in water for 30 ns for isomers 555-5-1S and 666-2-1S and 100 ns for isomers 222-14-1S, 555-5-2S, and 555-5-3S; the longer runs for the latter were due to the slower convergence of their properties. The RDFs of various atomic groups relative to the micelle COM for isomer 555-5-1S averaged over the last 5 ns of two independent simulations show good agreement (Figure B.2). This suggests that the simulations are reproducible and the structure of the micelle, at least with fixed aggregation number, reaches equilibrium in our simulations. Although the aggregation

number of Tween 80 has a large variation experimentally, a fixed aggregation number of 60 was chosen for the purpose of comparisons of micelle profiles among the five components of Tween 80.

The nearly identical partial charges of the two enantiomers of Tween 80 (Figure 3.3a) imply that their micelle structures will also be nearly identical; the slightly different partial charges of the two epimers (Figure 3.3b) show only minor differences in micelle behavior (Figure B.3). Therefore, it seems to be safe to use one stereoisomer to represent any of the 16 stereoisomers. In the following, we therefore use the same chirality of the four chiral carbons as that in 555-5-1S for further studies of the three constitutional isomers and the two molecules with different numbers of tails.

The three constitutional isomers of Tween 80 that we have selected, with EO units divided in three different ways among the four head groups, demonstrate significant property differences. Figure 3.5a shows the RDFs of heads, tails, and waters around the micelle COM for the three chosen constitutional isomers, and Figure 3.5b shows the corresponding distributions of single-surfactant  $R_g$  values within the micelle. The micelles have dry hydrocarbon cores and very thick hydrated coronas, or “water sponges”.<sup>39</sup> Although the RDFs of the tails are the same for the constitutional isomers, the RDFs of heads and waters differ somewhat. Isomer 666-2-1S, with a shorter W headgroup, has the least water penetration into the micelle, the narrowest headgroup RDF (Figure 3.5e), the largest RDF headgroup peak radius and the smallest  $R_g$ . The largest RDF headgroup peak radius for isomer 666-2-1S corresponds to the narrowest headgroup RDF. On the other hand, isomer 222-14-1S has the greatest water penetration into the



micelle, the broadest headgroup RDF (Figure 3.5e), and the largest micelle  $R_g$  and micelle SAS (Table 3.1). The single-surfactant  $R_g$  distribution in Figure 3.5b shows this trend more clearly: isomer 666-2-1S packs more densely due to the shorter W head than the other two. Isomer 222-14-1S has the broadest peak in the  $R_g$  distribution, evidently due to the extremely long W head, which can either bend back inward or extend outward from the micelles. Notice in Figure 3.5a that the headgroup distributions are different within the hydration layer but overlap within the hydrocarbon core.

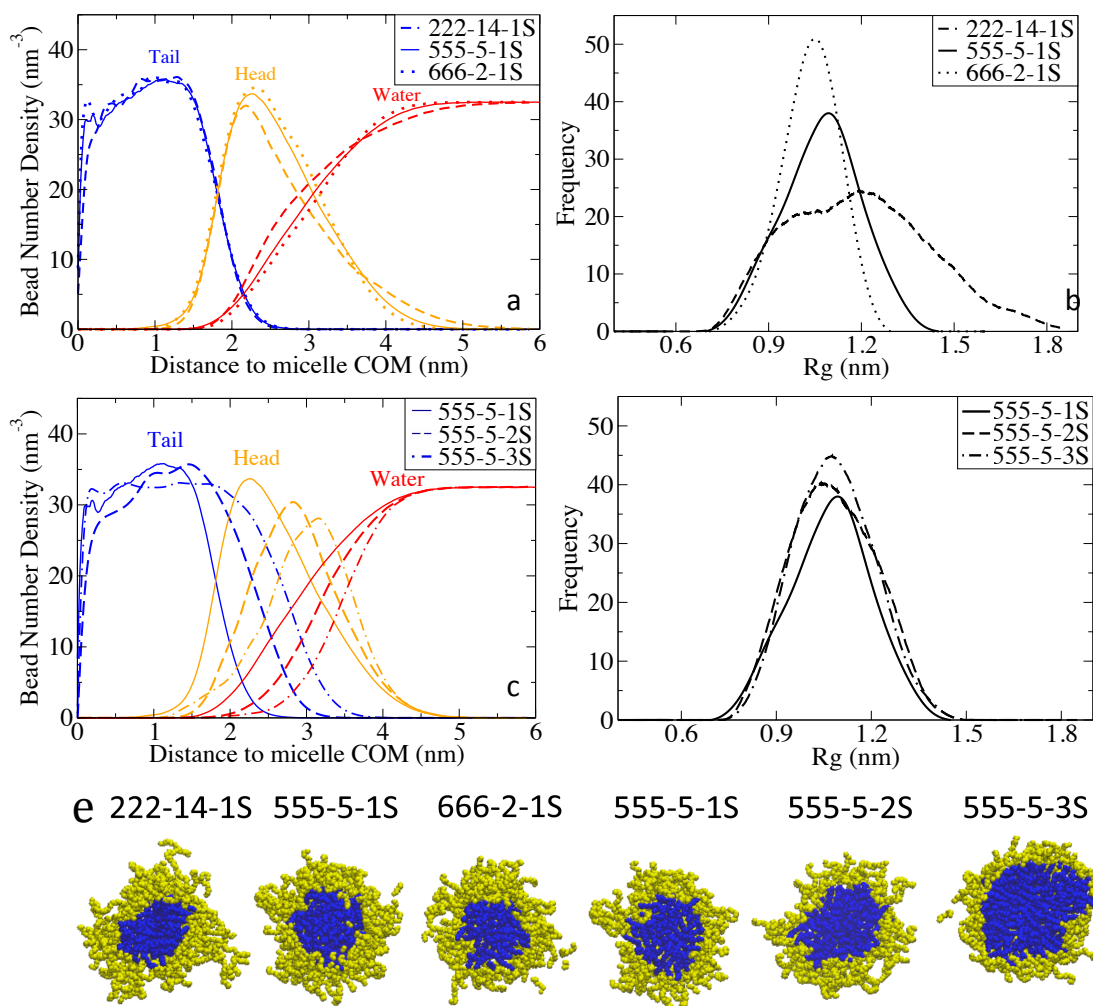


**Figure 3.5** Comparison of properties of three constitutional isomers and three components of Tween 80 with one, two, and three tails: Radial distribution functions (RDFs) of tails, heads, and waters relative to micelle center of mass (COM) of (a) three constitutional isomers and (c) Tween 80 with one, two, and three tails. Distributions of single-surfactant  $R_g$  values within the micelle of (b) three constitutional isomers and (d) Tween 80 with one, two, and three tails, (e) snapshots of micelle cross-section halved through the micelle center of mass. Shown as blue (tail), yellow (head). Water is omitted for clarity.

Generally, Tween 80 surfactants point radially outward, with atoms that are chemically farthest from the tail group in terms of numbers of intervening chemical bonds also lying farthest in physical distance from the micelle COM. Thus, as one moves outward from the tail group, one expects to find the ester group, the W headgroup, the THF ring, and then X, Y, and Z head groups, in that order. For example, the RDFs of tail carbons relative to the micelle COM shift outward as one moves from terminal tail carbon toward the W head (data not shown). The different micellar sizes resulting from the structural differences in the three chosen isomers of Tween 80 suggest that the length of the W headgroup is critical in surfactant packing. To evaluate the effect of the W head length, we show in Figure 3.6 the RDFs of the oxygen atoms in the W head relative to the micelle COM for isomer 222-14-1S. The three snapshots of individual 222-14-1S surfactants within the translucent micelle show the typical conformations of surfactants at each of the three distances to the micelle COM for the WO14 oxygen. The systematic outward shift in oxygen RDFs from the first to ninth oxygen, with little change in peak

width, shows that the W head extends more or less straight outward radially from the first to the ninth EO group. From the 10th to 14th EO group, the RDFs broaden and eventually develop two peaks. This shows that the end of the W headgroup is sometimes curled up (snapshot on the left of Figure 3.6) and sometimes extends outward (snapshot on the right of Figure 3.6).

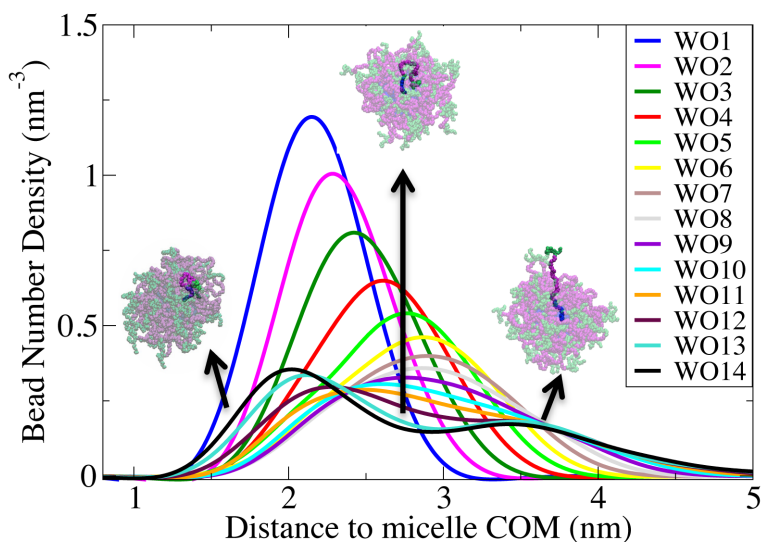


**Figure 3.6** RDFs of oxygens of the W headgroup of isomer 222-14-1S, numbered starting from the attachment point to the THF ring and increasing outward. Shown also are three typical conformations of individual 222-14-1S surfactants within the micelle at each of three distances to the micelle COM of the WO14 oxygen, with colors representing: tail (blue), W head (pink), and X, Y, and Z heads (green). To avoid obscuring these typical configurations, the rest of the surfactants are shown using translucent beads.

Micelles of Tween 80 surfactants with one, two, and three tails and equal EO lengths of the four head groups show a slight increase in the micellar sizes (values of  $R_g$  in Table 3.1 and Figure 3.5c) and similar distributions of single-surfactant  $R_g$  values within the

micelle (Figure 3.5d) as the number of tails increases. Although the micellar sizes are very similar, there are significant differences in the radial distributions of tails, heads, and water relative to the micelle COM. As can be seen in Figure 3.5c, the RDF distribution of tails expands significantly as the number of tails is doubled or tripled as expected. Using the method of Millet,<sup>117</sup> the hydrocarbon core becomes oblate as the number of tails increases to 120 for 555-5-2S and to 180 for 555-5-3S (data not shown), although the micelle as a whole, including the head groups covering the tails, becomes either slightly prolate or at least less oblate than the core. Interestingly, the RDF distributions of head and water converge for all three of these molecules at the edge of the micelle, which is ~5 nm from the micelle COM in Figure 3.5c. Thus, increased numbers of tails are accommodated within nearly the same micelle radius by thinning the hydration layer, resulting in narrower headgroup RDF peaks in Figure 3.5e, a steeper water RDF, a lower SAS, and a lower hydrophilic percentage of the SAS.

For a micelle of Tween 80 with three tails, Figure 3.5c shows that the tail group RDF extends out as far as 3 nm, and overlaps the headgroup RDF to a greater extent than for the one-tailed and two-tailed surfactants. For the three one-tail surfactants in Figure 3.5a, the RDFs of the head groups in the micelle nearly overlap each other within the hydrocarbon core. The deeper penetration of hydrophilic head groups into the hydrophobic core for the 555-5-3S micelle is possibly due to the geometric constraint of the three-tailed surfactants with head groups connected to a THF ring.

Summarizing, as the W headgroup length increases from 2 to 14 EO groups, it becomes more flexible and can both extend and bend. The higher flexibility of the long

W head results in a wider distribution of EO groups and less dense packing within the micelle, somewhat higher  $R_g$  (by 0.25 nm), higher SAS, and a thicker hydration layer. As the number of tails increases from one to three, despite the increase in micelle mass, the  $R_g$  of the micelle increases by only 0.15 nm, which is less than the increase produced by the lengthening of the W group discussed above. Thus, components of Tween 80 with two and three tails have similar micellar sizes but larger hydrocarbon cores, and thus thinner hydration layers with more tightly packed head groups, smaller SAS, and lower percentage of hydrophilic SAS. This variation in micelle structure among five components of Tween 80 may contribute to a wider distribution of aggregation numbers than would be present in a compositionally homogeneous surfactant.

### **3.3.2 Interfacial Tensions of Tween 80-Coated Air–Water and Oil–Water Interfaces**

The rate of oil dispersal depends on both the diffusivity of dispersants and their ability to reduce interfacial tension at the interface. Interfacial tensions are caused by cohesive forces among like molecules near the interfaces, including hydrogen bonds between water molecules. In MD simulations, the interfacial tension of a planar interface can be calculated from Kirkwood and Buff's expression,<sup>157,158</sup> given below, where the interface is perpendicular to the z-axis and  $P_{zz}$  is the normal pressure component:

$$\gamma(t) = \frac{L_z}{2} \left( P_{zz}(t) - \frac{P_{xx}(t) + P_{yy}(t)}{2} \right)$$

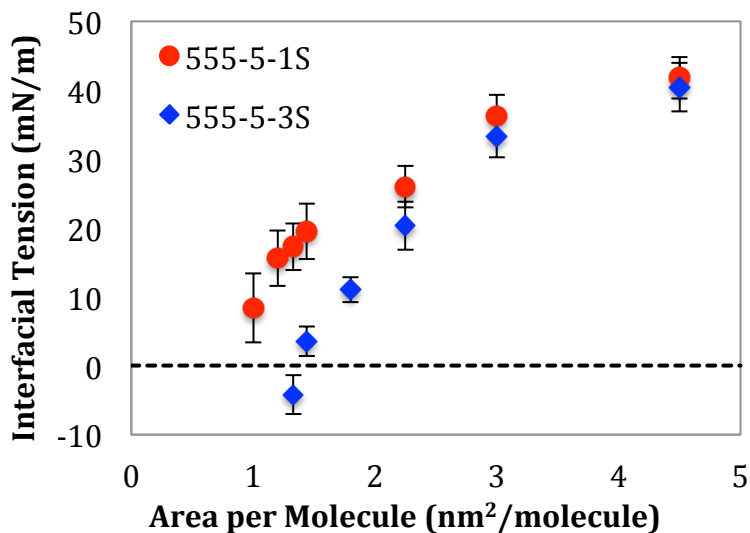


**Figure 3.7** Dependence of interfacial tensions at oil—water interfaces on surfactant surface coverage for surfactants 555-5-1S and 555-5-3S. Standard deviations are calculated from the surface tensions averaged over each of the last seven 20 ns intervals in the time window 100-240 ns after the start of the simulation. The dashed line corresponds to zero interfacial tension.

We first carried out NAPzT simulations at oil—water interfaces with surfactants 555-5-1S and 555-5-3S at different surface coverages. Then, we carried out NVT simulations of air—water interfaces and NAPzT simulations of oil—water interfaces with the five different Tween 80 molecular structures defined in Figure 3.2 at a surface coverage of 1.3 nm<sup>2</sup>/surfactant, which is relatively densely packed. As can be seen in Figure 3.4, the simulations were started with surfactants packed perpendicular to the interfaces with tails in the air or oil, and heads in the water, but by the end of the simulations, the tails of Tween 80 have collapsed onto the interfaces. Density profiles averaged over each 20 ns interval are found to converge after 40 ns of simulations at air—water interfaces and after

100 ns of simulations at oil—water interfaces (Figure B.4) indicating attainment of equilibrium. In Figure 3.7, we plot the interfacial tension of surfactant 555-5-1S and 555-5-3S versus surfactant surface density and the expected inverse relationship between interfacial tension and surfactant surface density is shown. The one-tailed surfactant 555-5-1S shows a steeply decreasing interfacial tension from 41.8 to 8.4 mN/m as the area per surfactant decreases from 4.5 to 1.0 nm<sup>2</sup>/surfactant. For the three-tailed surfactant 555-5-3S, the interfacial tension decreases from 39.0 to -4.2 mN/m as the area per surfactant decreases from 4.5 to 1.3 nm<sup>2</sup>/surfactant. For the three-tailed surfactant 555-5-3S, the negative interfacial tension at high packing density indicates an overly crowded surface. Taking a fixed surface coverage of 1.3 nm<sup>2</sup>/surfactant, we plot in Figure 3.8 the interfacial tensions calculated for the three constitutional isomers 555-5-1S, 666-2-1S, and 222-14-1S and the two multitailed surfactants 555-5-2S and 555-5-3S at both air—water and oil—water interfaces. The surface tension of the air—water interface predicted by the simulations in the absence of Tween 80 is around 52.0 mN/m, which is less than the experimental value because of the inaccuracy of the simple point charged SPC water model<sup>41</sup> that underestimates the vaporization enthalpy of water.<sup>43</sup> Accordingly, we focus more on the comparisons between the surface tensions of various Tween 80 structures at air—water interfaces rather than the absolute values of these surface tensions. The interfacial tension at the squalane-water interface predicted by the simulations in the absence of Tween 80 is around 47.5 N/m, which is close to the experimental value of 55.3 N/m. (The slightly lower interfacial tension obtained from the simulations relative to the experimental value may result from the inaccuracy of the SPC water model, which also

shows a diffusivity that is slightly higher than the experimental value,<sup>41</sup> indicating weaker water-water intermolecular interactions than in real water.) Thus, at oil—water interfaces, both the absolute values of the interfacial tensions and the changes in these values relative to the surfactant-free values are reasonably consistent with experiment. The experimental surface tension for Tween 80 at bulk concentrations greater than 0.1 mM reaches a plateau value of 37.0 mN/m.<sup>11</sup> The experimental interfacial tension for Tween 80 at a squalane—water interface drops to 8.5 mN/m<sup>11</sup> as the bulk concentration of Tween 80 increases to 0.1 mM.<sup>11</sup> Note in Figure 3.8 that isomer 666-2-1S shows the largest oil—water interfacial tension reduction among the one-tailed surfactants, reaching a value as low as 13.3 mN/m. This isomer has the shortest, least flexible W head among all the isomers, and consequently has the thinnest hydration layer and the narrowest head density distribution of the three constitutional isomers, as shown in Figure 3.9a. In addition, the distribution of single-surfactant  $R_g$  values of 666-2-1S at the interface is the narrowest among the three constitutional isomers, as shown in Figure 3.9b. Note the similarity between the single-surfactant  $R_g$  distribution within the micelle (Figure 3.5b) and that at an interface (Figure 3.9b). The narrowest distribution of the head groups and molecular  $R_g$  values for 666-2-1S result in the largest surface tension reduction, presumably because the heads are packed more tightly and closer to the interface than for the other two isomers. As the W head is lengthened to five EO units in 555-5-1S and 14 EO units in 222-14-1S (with a corresponding shortening of the X, Y, and Z groups), the number of EO units packed at the interface decreases, leading to less surface tension reduction. Although not studied here, isomers completely lacking a W head may be most



effective for surface tension reduction, since this will bring all the head units close to the interface. The similar distributions of tails and head groups at air/water and oil/water interfaces in Figs. 3.9a and c show that the interfacial structure is similar for all three constitutional isomers. The experimentally reported surface tension values at an air—water interface in the presence of Tween 80, 37.0 mN/m, and at an oil—water interface in the presence of 0.1 mM Tween 80, 8.5 mN/m,<sup>134</sup> (horizontal lines in Figure 3.8), are lower than those given by any of the three one-tailed isomers in our simulations. Note that the interfacial tension measured experimentally is for a mixture of Tween 80 molecules, while in the simulations the interfacial tensions of single Tween 80 components are reported. The higher interfacial tensions from simulations relative to experiment for one-tail surfactants may suggest the possible importance of multitailed components in Tween 80, as discussed below.

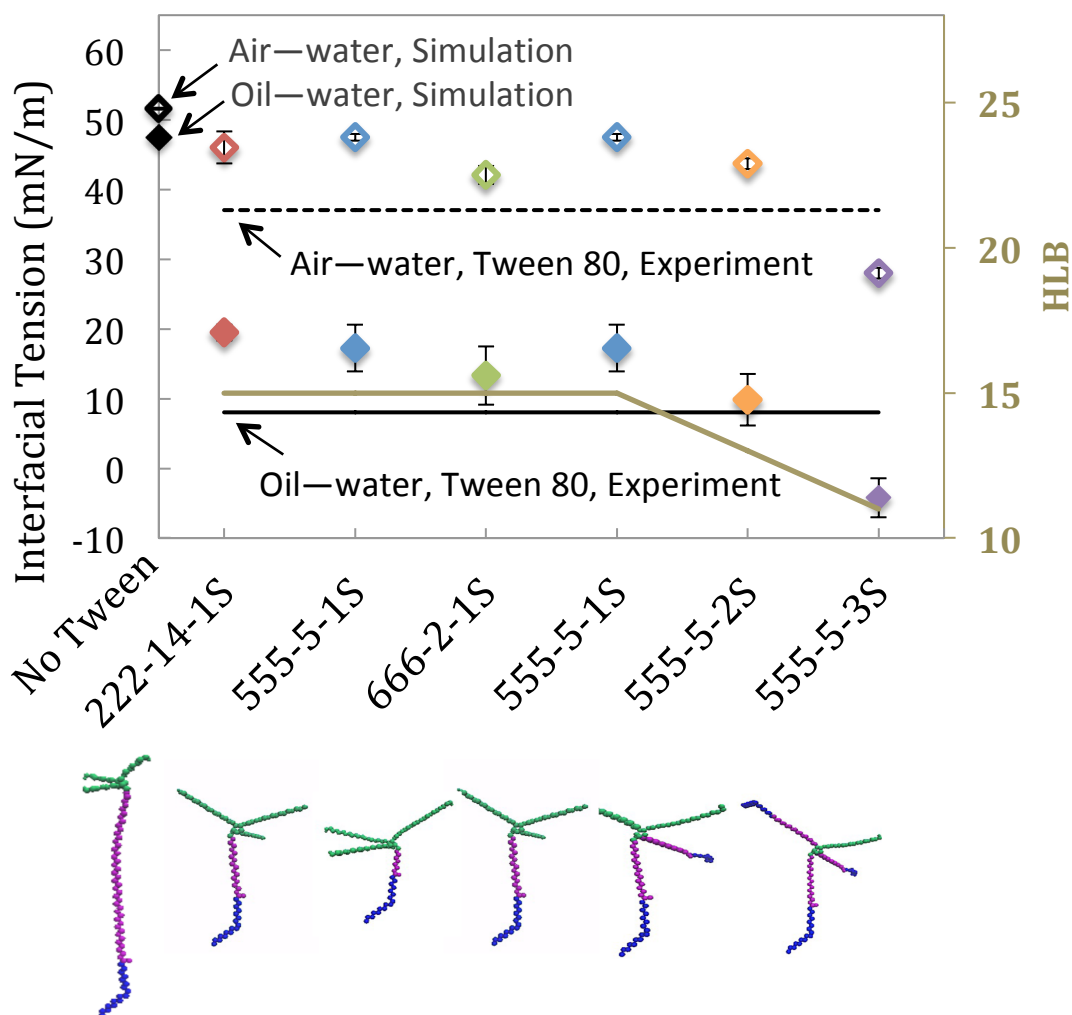


**Figure 3.8** Comparison of interfacial tensions of five Tween 80 molecules at the air–water (open symbols) and oil–water (closed symbols) interfaces. Standard deviations are calculated from the averaged surface tensions over the last three 20 ns intervals from 40 to 100 ns at air–water interfaces and over the last seven 20 ns intervals over 100 to 240 ns at oil–water interfaces. The open and closed black diamonds give the simulated interfacial tensions at air–water and oil–water interfaces, respectively, in the absence of Tween. The dashed and solid horizontal lines give the experimental interfacial tensions at the air–water and oil–water interfaces, respectively, from ref 11. The gold line indicates the HLB values of different Tween 80 molecules.

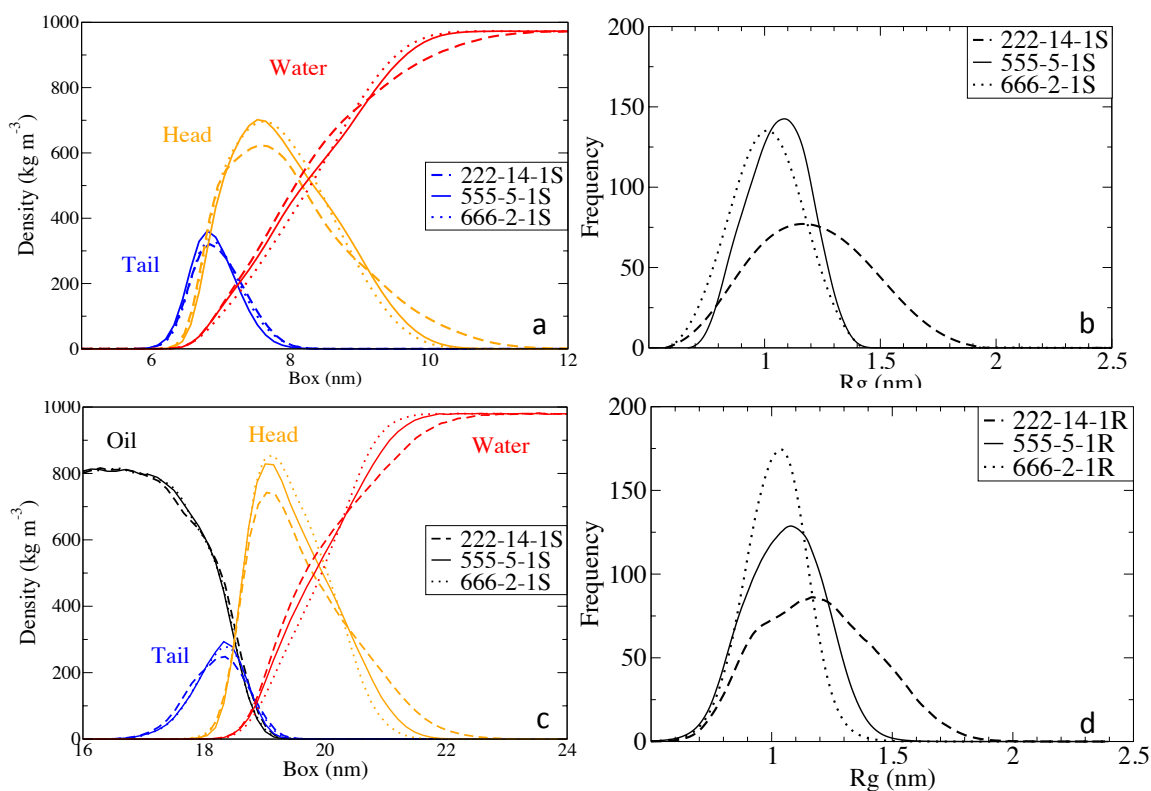


**Figure 3.9** Comparison of properties of three constitutional isomers of Tween 80 surfactant at the air–water (a and b) and oil–water (c and d) interfaces. (a and c) Density distributions of different groups. (b and d) The single-surfactant  $R_g$  distribution.

A more condensed distribution of surfactant at the interface, and a lower interfacial tension, can thus be achieved at a fixed surface density of surfactant by shortening the W head. A lower interfacial tension can also be achieved, in principal, by esterifying more tails onto the surfactant, to decrease the hydrophilic–lipophilic balance (HLB) to a value closer to  $\sim 10$ , where the interfacial tension is theoretically the lowest. The HLB is a measurement of the degree of hydrophilicity or hydrophobicity of the surfactant. Griffin’s method<sup>159</sup> of defining the HLB gives a value of  $20M_h/M$  for nonionic surfactants, where

$M_h$  is the molecular mass of the PEG hydrophilic groups and  $M$  is the total mass. The HLB of the standard Tween 80 structure, shown in Figure 3.1, is thereby calculated to be 15. Constitutional isomers have the same HLB, since they have the same molecular formula. For the two- and three-tailed molecules simulated here, the HLB decreases to 13 for 555-5-2S and to 11 for 555-5-3S, as shown in Figure 3.8. Decreasing the HLB of Tween 80 by increasing the number of hydrophobic tails is thus expected to reduce the surface tension. As can be seen in Figure 3.8, 555-5-2S and 555-5-3S reduce the surface tensions at air–water and oil–water interfaces more than 555-5-1S and 222-14-1S do, but 555-5-2S reduces the surface tension similarly to isomer 666-2-1S, while isomer 555-5-3S reduces it the most.

Just as a lower surface tension is obtained for isomer 666-2-1S with its shorter W head, and its tightly packed head groups within a thinner hydration layer, 555-5-2S also shows a significantly thinner hydration layer and steeper water density distribution than that of 555-5-1S at both the air–water interface in Figure 3.10a and the oil–water interface in Figure 3.10c. The distributions of  $R_g$  values for individual surfactants at the interface are shown in Figure 3.10b at the air–water interface and in 10d at the oil–water interface. There is a slight rightward shift of the peak of single-surfactant  $R_g$  for 555-5-2S and 555-5-3S relative to that of 555-5-1S, which contrasts with the similar distributions of  $R_g$  within the micelles in Figure 3.5d. This difference is possibly due to the additional room for the tails at the air–water and oil–water interfaces than is available within the hydrocarbon core of a spherical micelle.

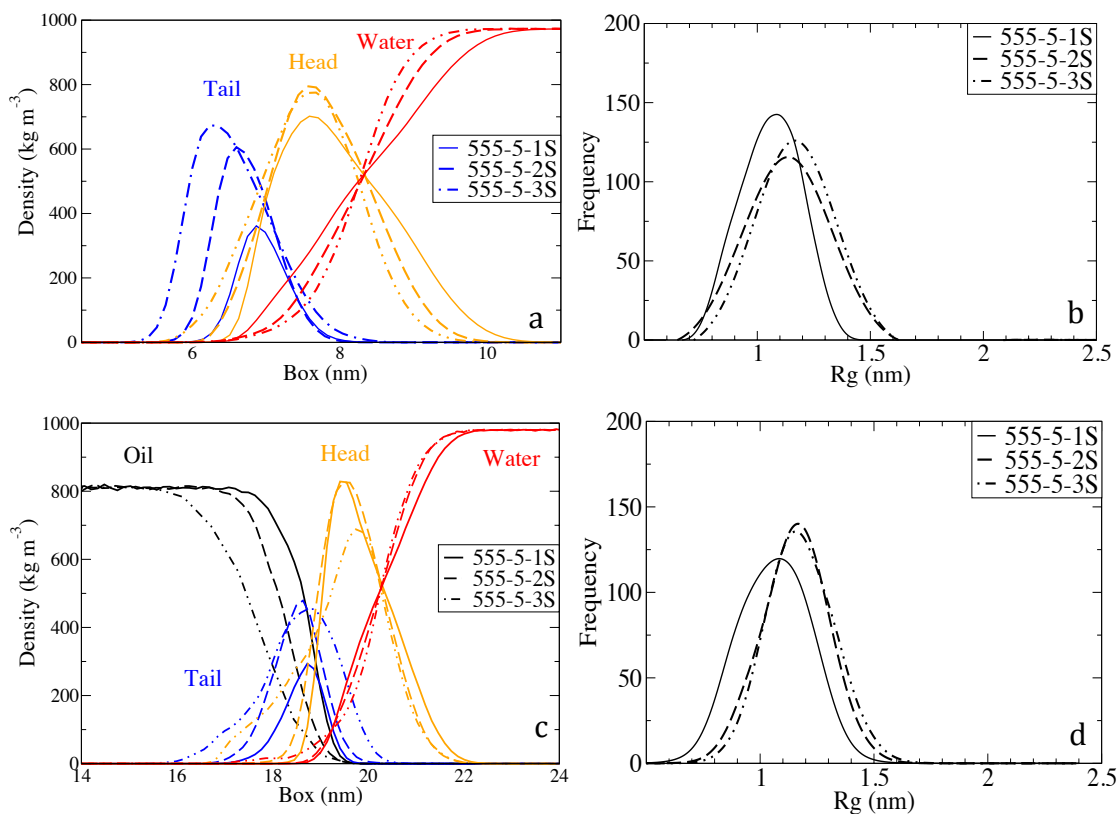


**Figure 3.10** Comparison of properties of three components of Tween 80 with one, two, and three tails at the air–water (a and b) and oil–water (c and d) interfaces. (a and c) The density distributions of different groups. (b and d) The single-surfactant  $R_g$  distribution.

At air–water interfaces, 555-5-3S reduces the surface tension to 28.0 mN/m compared with around 43.7 mN/m for 555-2-1R, where the former has denser headgroup packing and a thinner hydration layer, as shown in Figure 3.10a. At an oil–water interface, 555-5-3S produces a significantly lower interfacial tension than 555-5-2S (–4.2 mN/m versus 9.8 mN/m), but only a slightly different water density distribution. (The negative value of the interfacial tension for 555-5-3S means that the interface is overly crowded with

surfactant, as shown in Figure 3.7, and would lose some surfactant if the simulation could be run long enough.) As shown in Figure 3.10c, the tail density distribution depends significantly on the number of tails. It is apparently difficult to pack the three connections between tails and heads of 555-5-3S at the hydrophobic—hydrophilic interfaces, and a portion of the tails of 555-5-3S penetrates deeply both into the hydrophilic hydration layers and into the hydrophobic oil phase. Interestingly, a small amount of water penetrates deeply into the oil layer, suggesting that 555-5-3S, with an HLB of 11, is near an inversion point where a water-in-oil emulsion might form. Although the tail order parameters increase as the number of tails increases, as shown in Figure B.5, the overall tail order parameters are low due to the very bulky heads and relatively small tails.

The packing densities of different structures of Tween 80 at oil–water interfaces are evaluated by the surfactant density plot as shown in Figure 3.11. Consistent with the results from RDF measurements, while the packing of the tails are the same for the three constitutional isomers with one tail, isomer 666-2-1S (Fig. 3.11c) has the thinnest hydration layer or head group layers within the water phases (in color cyan at the two ends) and the highest surfactant packing density (thicker yellow band and several orange dots). It pushes more water out of the interfaces, reduces the number of hydrogen bonds, and leads to lower interfacial tension comparing with other two constitutional isomers. 555-5-3S (Fig. 11f) shows similar thickness of the surfactant layers as those of 555-5-1S (Fig. 11d and 11e) and 555-5-2S, but higher packing density (thicker yellow bands) at interfaces. It pushes more water as well as oil molecules out of the interface, reduces

attractions of both hydrogen bonds and van der Waals at the interfaces, and leads to the lowest interfacial tension among all the modeled molecules.

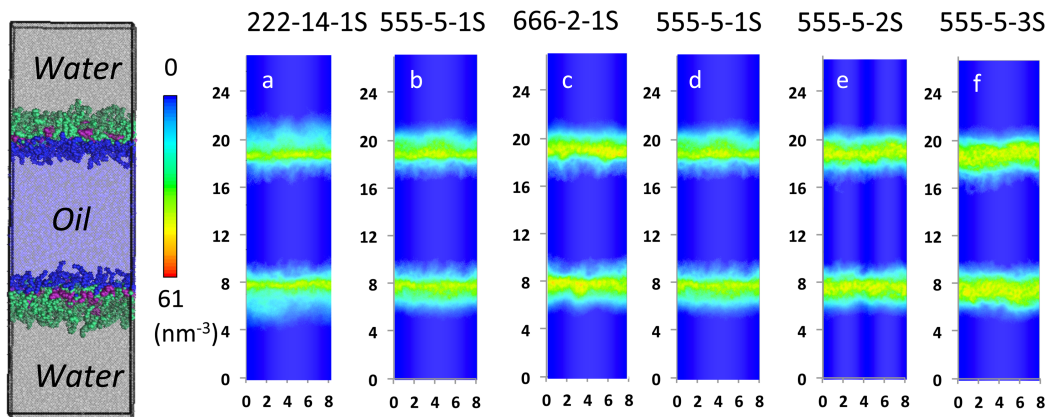


**Figure 3.11** Surfactant density profiles at oil–water interfaces averaged over the axis that is perpendicular to the plane and averaged over time. Water and oil molecules are omitted for clarity. The left snapshot shows the geometry of the simulations.

For these five Tween 80 molecules, the degree of reduction in interfacial tension at the air–water interface parallels the degree of reduction at the oil–water interface. For both interfaces, either decreasing the W headgroup length or increasing the number of tail groups enhances surface tension reduction and presumably also oil dispersing efficiency. This suggests that lower interfacial tensions would be obtained by replacing the predominantly single-tailed Tween 80 entirely with the three-tailed Tween 85, rather than using a mixture of Tween 80 with Tween 85, as is done in the Corexit 9500 formulation. A possible reason this is not done is that the single tail and bulky head groups of Tween 80 favor and stabilize the formation of oil-in-water emulsions, rather than the reverse. Once the HLB decreases to below 11, a water-in-oil emulsion is favored.<sup>159,160</sup>

### 3.4 Conclusions

Micellar and air—water and oil—water interfacial structures of representative Tween 80 molecules were investigated by MD simulations. Two epimers and three constitutional isomers of one-tailed Tween 80 surfactants, as well as two- and three-tailed versions of Tween 80, all with a total of 20 ethoxylate (EO) monomers, were investigated as representative Tween 80 molecules. Pure Tween 80 epimers or mixtures of epimers, when preassemble into spherical micelles of aggregation number 60, result in similar micellar radial distribution functions, while constitutional isomers show significant differences, especially the isomer with a short “W” headgroup connecting the tail group to the THF ring. Longer W head groups favor an expanded micelle corona, a larger micelle  $R_g$ , wider distributions of  $R_g$  values of individual surfactant molecules within the micelle or at interfaces, and less reduction of surface tension. Reducing the hydrophilic/lipophilic balance (HLB) of Tween 80 from 15 to 11 by increasing the number of tails from one to three tails (where the three-tailed Tween corresponds to the average Tween 85 structure) results in the greatest reduction of interfacial tension (to a value of 17.3 mN/m at air—water interfaces and to a small negative value at oil—water interfaces) of all Tween structures investigated here. It will be interesting to investigate synergistic effects of other dispersant components, including AOT and SPAN 80. Investigating the effects of the carbon number of the oil molecule on interfacial tension changes will be interesting as well.



### 3.5 References

- (1) [http://en.wikipedia.org/wiki/Deepwater\\_Horizon\\_oil\\_spill](http://en.wikipedia.org/wiki/Deepwater_Horizon_oil_spill) (last accessed May 20, 2014).
- (2) United States Coast Guard. *On Scene Coordinator Report Deepwater Horizon*. [http://www.uscg.mil/foia/docs/DWH/FOSC\\_DWH\\_Report.pdf](http://www.uscg.mil/foia/docs/DWH/FOSC_DWH_Report.pdf) (last accessed July 23, 2014) 2011.
- (3) Sammalkorpi, M.; Karttunen, M.; Haataja, M. Structural Properties of Ionic Detergent Aggregates: A Large-Scale Molecular Dynamics Study of Sodium Dodecyl Sulfate. *J. Phys. Chem. B* **2007**, *111*, 11722–11733.
- (4) National Research Council. *Oil Spill Dispersants: Efficacy and Effects*. The National Academies Press: Washington, DC, 2005.
- (5) <http://en.wikipedia.org/wiki/Corexit>; <http://saveourgulf.org/updates/corexit-chemical-components-released-public> (last accessed May 20, 2014).
- (6) Canevari, J.; Lindblom, G.; Becker, K.; Bowes, S.; Brown, H.; Cashion, B.; Chen, A.; Clark, J.; Demarco, G.; Fiocco, B. ExxonMobil Oil Spill Dispersant Guidelines; 2008.
- (7) Brochu, C.; Pelletier, E.; Caron, G.; Desnoyers, J. E. Dispersion of Crude Oil in Seawater: The Role of Synthetic Surfactants. *Oil Chem. Pollut.* **1986**, *3*, 257–279.
- (8) Blondina, G. J.; Singer, M. M.; Lee, I.; Ouano, M. T.; Hodgins, M.; Tjeerdema, R. S.; and Sowby, M. L. Influence of Salinity on Petroleum Accommodation by Dispersants. *Spill Sci. Technol. Bull.* **1999**, *5*, 127–134.
- (9) Mahmood, M. E.; Al-koofee, D. A. F. Effect of Temperature Changes on Critical Micelle Concentration for Tween Series Surfactant. *Global. J. Sci. Front. Res. Chem.* **2013**, *13*, 1–7.
- (10) Description of the MC 252 Crude Oil Sample Results from the Deepwater Horizon Crude Oil Spill Show That the Crude Oil Type Can Be Classified as a “light Sweet Crude”. <http://oilspill.fsu.edu/images/pdfs/mc-252crude-oil-desc.pdf>; 2010 (last accessed May 20, 2014).
- (11) Reichert, M. D.; Walker, L. M. Interfacial Tension Dynamics, Interfacial Mechanics, and Response to Rapid Dilution of Bulk Surfactant of a Model Oil—water-Dispersant System. *Langmuir* **2013**, *29*, 1857–1867.

- (12) Kester, D. R.; Duedall, I. W.; Connors, D. N.; Pytkowicz, R. M. Preparation of Artificial Seawater. *Limnol. Oceanogr.* **1967**, *12*, 176–179.
- (13) Reichert, M. D.; Anna, S. L.; Walker, L. M. Tween 80 and Aerosol-OT Adsorption Behavior At An OIL-Aqueous Interface. In ALCHE Annual Meeting, CA, Nov 3–8, 2013; Vol. 17.
- (14) Stephanie, K.; Anna, S. L.; Walker, L. M. Sequential Adsorption Studies of Tween 80 and Aerosol-OT at an Oil/aqueous Interface. In *Gulf of Mexico Oil Spill & Ecosystem Science Conference*, AL, Jan 26–29, 2014.
- (15) [http://en.wikipedia.org/wiki/Polysorbate\\_80](http://en.wikipedia.org/wiki/Polysorbate_80) (last accessed May 20, 2014).
- (16) de Campo, L.; Yaghmur, A.; Garti, N.; Leser, M. E.; Folmer, B.; Glatter, O. Five-Component Food-Grade Microemulsions: Structural Characterization by SANS. *J. Colloid Interface Sci.* **2004**, *274*, 251–267.
- (17) Glenn, K. M.; Moroze, S.; Palepu, R. M. Effect of Ethylene Glycol on the Thermodynamic and Micellar Properties of Tween 40, 60, and 80. *J. Dispersion. Sci. Technol.* **2005**, *26*, 79–86.
- (18) Mahajan, R. K.; Chawla, J.; Bakshi, M. S.; Kaur, G.; Aswal, V. K.; Goyal, P. S. Effect of Adding Glycols to the Micellar Properties of Tween: Small-Angle Neutron Scattering and Turbidity Measurements. *Colloid Polym. Sci.* **2004**, *283*, 164–168.
- (19) Tummino, P. J.; Gafni, A. Determination of the Aggregation Number of Detergent Micelles Using Steady-State Fluorescence Quenching. *Biophys. J.* **1993**, *64*, 1580–1587.
- (20) Haque, M.; Das, A.; Moulik, S. Mixed Micelles of Sodium Deoxycholate and Polyoxyethylene Sorbitan Monooleate (Tween 80). *J. Colloid Interface Sci.* **1999**, *217*, 1–7.
- (21) Lafitte, G.; Thuresson, K.; Jarvoll, P.; Nydén, M. Transport Properties and Aggregation Phenomena of Polyoxyethylene Sorbitane Monooleate (polysorbate 80) in Pig Gastrointestinal Mucin and Mucus. *Langmuir* **2007**, *23*, 10933–10939.
- (22) Amani, A.; York, P.; de Waard, H.; Anwar, J. Molecular Dynamics Simulation of a Polysorbate 80 Micelle in Water. *Soft Matter* **2011**, *7*, 2900–2908.
- (23) <http://www.piercenet.com/product/tween-80-detergent-solution> (last accessed May 20, 2014); <http://www.sigmaaldrich.com/content/dam/sigma->

aldrich/docs/Sigma/Instructions/ detergent\_selection\_table.pdf (last accessed Oct. 28, 2014).

- (24) Kumari, H.; Kline, S. R.; Atwood, J. L. Aqueous Solubilization of Hydrophobic Supramolecular Metal–organic Nanocapsules. *Chem. Sci.* **2014**, *5*, 2554–2559.
- (25) Bendedouch, D.; Chen, S.-H.; Koehler, W. C. Structure of Ionic Micelles From Small Angle Neutron Scattering. *J. Phys. Chem.* **1983**, *87*, 153–159.
- (26) Zhang, R.; Wang, Y.; Tan, L.; Zhang, H. Y.; Yang, M. Analysis of Polysorbate 80 and Its Related Compounds by RP-HPLC with ELSD and MS Detection. *J. Chromatogr. Sci.* **2012**, *50*, 598–607.
- (27) Zhang, R.; Wang, Y.; Ji, Y.; Shi, B.; Zhang, Z.; Zhang, H.; Yang, M.; Wang, Y. Quantitative Analysis of Oleic Acid and Three Types of Polyethers according to the Number of Hydroxy End Groups in Polysorbate 80 by Hydrophilic Interaction Chromatography at Critical Conditions. *J. Chromatogr. A* **2013**, *1272*, 73–80.
- (28) Raith, K.; Schmelzer, C. E. H.; Neubert, R. H. H. Towards a Molecular Characterization of Pharmaceutical Excipients: Mass Spectrometric Studies of Ethoxylated Surfactants. *Int. J. Pharm.* **2006**, *319*, 1–12.
- (29) Ayorinde, F. O.; Gelain, S. V; Johnson, J. H.; Wan, L. W. Analysis of Some Commercial Polysorbate Formulations Using Matrix-Assisted Laser Desorption/ionization Time-of-Flight Mass Spectrometry. *Rapid Commun. Mass Spectrom.* **2000**, *14*, 2116–2124.
- (30) Zhu, W.; Romanski, F. S.; Meng, X.; Mitra, S.; Tomassone, M. S. Atomistic Simulation Study of Surfactant and Polymer Interactions on the Surface of a Fenofibrate Crystal. *Eur. J. Pharm. Sci.* **2011**, *42*, 452–461.
- (31) Konkel, J. T.; Myerson, A. S. Empirical Molecular Modeling of Suspension Stabilisation with Polysorbate 80. *Mol. Simul.* **2008**, *34*, 1353–1357.
- (32) Shang, B. Z.; Wang, Z.; Larson, R. G. Molecular Dynamics Simulation of Interactions between a Sodium Dodecyl Sulfate Micelle and a Poly(ethylene Oxide) Polymer. *J. Phys. Chem. B* **2008**, *112*, 2888–2900.
- (33) Horta, B. A. C.; Fuchs, P. F. J.; van Gunsteren, W. F.; Hünenberger, P. H. New Interaction Parameters for Oxygen Compounds in the GROMOS Force Field : Improved Pure-Liquid and Solvation Properties for Alcohols, Ethers, Aldehydes, Ketones, Carboxylic Acids, and Esters. *J. Chem. Theory Comput.* **2011**, *7*, 1016–1031.

- (34) Fuchs, P. F. J.; Hansen, H. S.; Hünenberger, P. H.; Horta, B. A. C. A GROMOS Parameter Set for Vicinal Diether Functions : Properties of Polyethyleneoxide and Polyethyleneglycol. *J. Chem. Theory Comput.* **2012**, *8*, 3943–3963.
- (35) Hansen, H. S.; Hünenberger, P. H. A Reoptimized GROMOS Force Field for Hexopyranose-Based Carbohydrates Accounting for the Relative Free Energies of Ring Conformers , Anomers , Epimers , Hydroxymethyl Rotamers , and Glycosidic Linkage Conformers. *J. Comput. Chem.* **2011**, *32*, 998–1032.
- (36) Lee, H.; Venable, R. M.; Mackerell Jr, A. D.; Pastor, R. W. Molecular Dynamics Studies of Polyethylene Oxide and Polyethylene Glycol: Hydrodynamic Radius and Shape Anisotropy. *Biophys. J.* **2008**, *95*, 1590–1599.
- (37) Vorobyov, I.; Anisimov, V. M.; Greene, S.; Venable, R. M.; Moser, A.; Pastor, R. W.; MacKerell, J. A. D. Additive and Classical Drude Polarizable Force Fields for Linear and Cyclic Ethers. *J. Chem. Theory Comput.* **2007**, *3*, 1120–1133.
- (38) Martínez, L.; Andrade, R.; Birgin, E. G.; Martínez, J. M. Software News and Update Packmol : A Package for Building Initial Configurations. *J. Comput. Chem.* **2009**, *30*, 2157–2164.
- (39) Martinez, J. M.; Martinez, L. Packing Optimization for Automated Generation of Complex System ' S Initial Configurations for Molecular Dynamics and Docking. *J. Comput. Chem.* **2003**, *24*, 819–825.
- (40) Lemkul, J. A.; Allen, W. J.; Bevan, D. R. Practical Considerations for Building GROMOS-Compatible Small-Molecule Topologies. *J. Chem. Inf. Model.* **2010**, *50*, 2221–2235.
- (41) Schüttelkopf, A. W.; van Aalten, D. M. F. PRODRG: A Tool for High-Throughput Crystallography of Protein-Ligand Complexes. *Acta Crystallogr. Sect. D. Biol. Crystallogr.* **2004**, *D60*, 1355–1363.
- (42) MacKerell Jr., A. D. Empirical Force Fields for Biological Macromolecules: Overview and Issues. *J. Comput. Chem.* **2004**, *25*, 1584–1604.
- (43) Frisch, M. J.; Trucks, G. W.; Schlegel, H. B.; Scuseria, G. E.; Robb, M. A.; Cheeseman, J. R.; Scalmani, G.; Barone, V.; Mennucci, B.; Petersson G. A.; et al. Gaussian 09, revision D.01; Gaussian, Inc.; Wallingford, CT, 2009.
- (44) Ryckaert, J.-P.; Bellemans, A. Molecular Dynamics of Liquid Alkanes. *Faraday Discuss. Chem. Soc.* **1978**, *66*, 95–106.

- (45) Poger, D.; Gunsteren, W. F. V. A. N.; Mark, A. E. A New Force Field for Simulating Phosphatidylcholine Bilayers. *J. Comput. Chem.* **2010**, *31*, 1117–1125.
- (46) Baron, R.; Bakowies, D.; van Gunsteren, W. F. Principles of Carbopeptoid Folding: A Molecular Dynamics Simulation Study. *J. Pept. Sci.* **2005**, *11*, 74–84.
- (47) Erdem, N. S.; Alawani, N.; Wesdemiotis, C. Analytica Chimica Acta Characterization of Polysorbate 85 , a Nonionic Surfactant , by Liquid Chromatography vs . Ion Mobility Separation Coupled with Tandem Mass Spectrometry. *Anal. Chim. Acta* **2014**, *808*, 83–93.
- (48) Berendsen, H. J. C.; Postma, J. P. M.; van Gunsteren, W. F.; Hermans, J. In *Intermolecular Forces*; Pullman, B., Ed.; Reidel: Dordrecht, The Netherlands, 1981; pp 331–338.
- (49) Rawdon, E. J.; Kern, J. C.; Piatek, M.; Plunkett, P.; Stasiak, A.; Millett, K. C. Effect of Knotting on the Shape of Polymers. *Macromolecules* **2008**, *41*, 8281–8287.
- (50) Kirkwood, J. G.; Buff, F. P. The Statistical Mechanical Theory of Surface Tension. *J. Chem. Phys.* **1949**, *17*, 338–343.
- (51) Buff, F. P. Some Considerations of Surface Tension. *Z. Electrochem.* **1952**, *56*, 311–313.
- (52) Mark, P.; Nilsson, L. Structure and Dynamics of the TIP3P, SPC, and SPC/E Water Models at 298 K. *J. Phys. Chem. A* **2001**, *105*, 9954–9960.
- (53) Vega, C.; de Miguel, E. Surface Tension of the Most Popular Models of Water by Using the Test-Area Simulation Method. *J. Chem. Phys.* **2007**, *126*, 154707.
- (54) Griffin, W. C. Calculation of HLB Values of Non-Ionic Surfactants. *J. Soc. Cosmet. Chem.* **1954**, *5*, 249–256.
- (55) Bourrel, M.; Graciaa, A.; Schechter, R. S.; Wade, W. H. The Relation of Emulsion Stability to Phase Behavior and Interfacial Tension of Surfactant Systems. *J. Colloid Interface Sci.* **1979**, *72*, 161–163.

## Chapter 4

### Multi-Scale Modeling and Rheological Approaches Understanding the Structure-Property Relationships of Two-Modeled Body Washes, the Effect of Salt and Perfume Raw Materials (PRMs)

The work in Chapter 4 has been collaborated with Peter H. Koenig, Shawn D. McConaughy, and Mike R. Weaver at Procter and Gamble Company.

#### 4.1 Introduction

Surfactants have been widely used in consumer products including detergents, health and personal care products, and foodstuffs, and in industrial applications including oil recovery and drug delivery industries.<sup>1-7</sup> Many of these surfactant solutions contain elongated micelles and are viscoelastic, which are of great importance, especially in design of consumer products such as shampoos and body washes. Extensive studies of the rheology of micellar solutions have been carried out over the past three decades, both to satisfy scientific interest and in hopes of improving their design for applications. Many studies have focused on relatively simple experimental systems containing a single species of surfactant along with one species of anionic hydrotrope or inorganic salt. For example, rheological properties of cationic surfactants such as cetyltrimethylammonium

bromide (CTAB), cetyltrimethylammonium chloride (CTAC), cetylpyridinium chloride (CPyCl), and erucylbis(hydroxyethyl)methyl-ammonium chloride (EHAC/KCl) mixed with hydrotropes such as salicylate ions or simple inorganic salts such as sodium chloride, sodium bromide, and sodium chlorate, have been investigated extensively.<sup>1,2,8-19</sup> In addition, the microstructures of these surfactant solutions have been analyzed by techniques such as static and dynamic light scattering (SLS and DLS), small-angle neutron scattering (SANS), small-angle x-ray scattering (SAXS), flow birefringence, diffusive wave spectrometry (DWS), neutron spin echo spectroscopy, cryogenic transmission electron microscopy (cryo-TEM). Cationic surfactants are widely used in a range of applications but anionic surfactants are better suited for cleaning soils from consumer relevant substrates which typically bear negative surface charges in aqueous environments.

Instead, anionic surfactants are mainly used in consumer products. The simplest representative anionic surfactant, sodium dodecyl sulfate (SDS) has been investigated extensively in the concentration range between the first critical micelle concentration (CMC) at 0.008 M and the second CMC at 0.069 M, over which concentration range the majority of the micelles are small spheres or ellipsoids.<sup>20-22</sup> Wormlike micelle solutions composed of anionic surfactants at concentrations far above the 2<sup>nd</sup> CMC are studied less frequently, even though those concentration ranges are more relevant to practical applications, for example, exhibiting viscoelastic properties.

In practical applications, mixed surfactants are usually used because of their lower cost and improved performance over that of the single-surfactant solutions.<sup>23</sup> For example,

typically instead of SDS, sodium lauryl sulfate (SLnS) features an “n” distribution of different hydrophobic tail lengths and n is in the range of 10 to 16. In addition to lower cost, such mixtures feature lower freezing points allowing for wider application ranges. The addition of the ionic surfactant sodium lauryl ether sulfate (SLES) to an SDS solution enhances the viscosity of the mixture at low total surfactant concentration.<sup>24</sup> Superior interfacial tension reduction is obtained upon addition of the zwitterionic surfactant cocoamidopropyl betain (CAPB) to an SDS solution.<sup>25–28</sup> Sharp drops of both the 1<sup>st</sup> and 2<sup>nd</sup> CMC is obtained in mixtures of CAPB and SLES having one to three ethylene oxide (EO) over that seen in each of the individual surfactant components, as determined through experimental measurements using rheometry and SAXS.<sup>29–31</sup> Here the EO groups connect the alkane tails to the negatively charged sulfate head groups within an SLES molecule. Although the addition of cationic surfactant to anionic surfactants boost viscosity enormously at low surfactant concentrations, the formation of an insoluble complex can limit the range of practicable formulations.<sup>23,32</sup>

Earlier studies of simple surfactant solutions containing at most two species of surfactants have provided insights into the structure-property relationships of wormlike micelle solutions. However, such systems are oversimplified relative to commercial surfactant mixtures, which contain many species. For example, the commercial body washes are complex mixtures of anionic surfactants of SLEnS (n is the number of EOs in SLEnS surfactants and varies from 0 to 10), CAPB, unreacted alcohols, perfumes, and salts. The alkyl tails of SLEnS and CAPB, and the numbers of EOs within the head groups of a given SLEnS all have distributions. In addition, perfumes used in commercial



mixtures contain some tens of distinct small organic molecules, named perfume raw materials (PRMs). One of the main challenges in applications of complex fluids such as surfactant solutions is to accurately measure their microstructure at the molecular scale so that these microstructures can be designed for optimal performance of the product. To address this issue and accelerate formulation development, we here report our efforts at multiscale modeling and its use in the prediction of rheological properties of two commercial body wash formulations. Specifically, here we systematically study the effects of salts and PRMs on the viscoelastic properties of body washes, and estimate the corresponding micellar properties through application of the Cates model<sup>13,33</sup> for the rheology of threadlike micelles, and through molecular modeling techniques, and application of the packing parameter concept of Israelachvili.<sup>34</sup> By connecting the surfactant packing at the molecular scale, to micellar properties at the mesoscale, and these, in turn, to the rheological properties at the macroscopic scale, we develop an approach for achieving fundamental understanding of the structure-property relationships of commercial surfactant solutions.

## **4.2 Theory for Predicting Micellar Microstructures**

### **4.2.1 Packing Argument**

At concentrations above the 1<sup>st</sup> CMC in solution, surfactants self-assemble into diverse structures including spherical, global, and cylindrical micelles as well as ordered phases like lamellar, cubic, hexagonal, and exotic bicontinuous phases<sup>2,8,19,34,35</sup>. The size and shape of surfactant aggregates depend on the concentration and chemical structures of the

surfactants, the nature of the counter ions, the presence of salts and/or other surfactants, pH, temperature and pressure<sup>2,19</sup>. Israelachvili proposed a packing argument based on a dimensionless shape parameter  $p$ , defined as  $p = V/l_c a_0$ , to predict the shape of the micelles.<sup>34</sup> Here,  $V$  is the occupied volume of the hydrophobic tail,  $l_c$  is the tail length, and  $a_0$  is the area occupied by the hydrophilic heads on the micelle surface. For a saturated hydrocarbon chain of  $n_c$  carbon atoms,  $V$  and  $l_c$  can be estimated as<sup>36</sup>

$$l_c \cong (1.54 + 1.265 n_c) \text{Å}; \quad V \cong (27.4 + 26.9 n_c) \text{Å}^3 \quad (4.1)$$

Generally, the hydrophobic tails are wrapped within the hydrophilic heads giving them limited access to their environment. Therefore the tail volume  $V$  and tail length  $l_c$  are typically taken to be constant, while the head group area  $a_0$  can change. For example, with added salt, more counterions condense on the surface of the micelles, screen the electrostatic repulsions between the surfactant heads thereby reducing their surface area  $a_0$ , resulting in an increase of the packing parameter  $p$  and therefore a transition from spherical to growing threadlike micelles. Thus, it is straightforward to apply the packing parameter  $p$  to explain qualitatively the effects of salts and non-hydrophobic PRMs on the rheological properties of body washes. However, extremely hydrophobic PRMs penetrate the hydrophobic core of the micelle, changing the tail parameters as well as the head parameters, making more complicated the application of the packing argument.

#### 4.2.2 Cates Model

Cryo-TEM measurements of body washes verify the formation of entangled networks of wormlike micelles. The solutions are viscoelastic and their rheology is similar to that

of entangled polymer solutions. One difference is that wormlike micelles break and recombine rapidly. By combining the theories considering polymer reptation and micellar fast reversible scission, Cates developed a reptation-reaction model to estimate linear micellar characteristic time and length parameters.<sup>1,11,13,37,38</sup> The linear rheological moduli predicted by the Cates model in the fast-breakage limit are given by a single-relaxation-time Maxwell model:

$$G'' = \frac{G\omega^2\tau^2}{1 + \omega^2\tau^2}, \quad G' = \frac{G\omega\tau}{1 + \omega^2\tau^2} \quad (4.2)$$

where  $\omega$  is the oscillatory angular frequency,  $\tau$  is the relaxation time,  $G''$  is the loss or viscous modulus that is out of phase with the strain, and  $G'$  is the storage or elastic modulus that is in phase with the strain. Lequeux extended this linear model to branched wormlike micelles by considering the additional relaxation mechanisms of micellar sliding at the branch points.<sup>39</sup> For unbranched micelles, Larson developed an improved method of estimating the average micelle length from the rheology data based on the terminal relaxation time at low frequency.<sup>33</sup>

#### 4.2.2.1 Predicting Micellar Characteristic Times

A mean field treatment predicts an exponential distribution of micelle lengths  $N(L)$ <sup>37</sup>

$$N(L) \propto \exp\left(-\frac{L}{\bar{L}}\right) \quad (4.3)$$

where  $L$  is the micelle contour length,  $N(L)$  is the number fraction of micelles of length  $L$ , and  $\bar{L}$  is the number-average micelle length. The stress in a wormlike micellar solution relaxes similarly to that of polymers. Micelles curvilinearly reptate out of tubes that are

formed by topological constraint with neighboring chains. Unlike ordinary polymers, wormlike micelles are “living polymers” that have additional stress relaxation paths through reversible scission. Assuming that the breakage occurs with equal probability per unit time per unit length of micelle, the characteristic breakage time is inversely proportional to the average micelle length:

$$\tau_{br} = 1/c_1\bar{L} \quad (4.4)$$

If the time for a micelle to break,  $\tau_{br}$ , is longer than the time for it to reptate out of the tube, which is the reptation time  $\tau_{rep}$ , then the stress relaxation is by purely reptation. This is relaxation regime I, which holds for  $\zeta > 1$ , where:

$$\zeta \equiv \tau_{br}/\tau_{rep} \quad (4.5)$$

As the average micelle length increases, the reptation time increases and the breakage time decreases. Once  $\zeta < 1$ , micelles break and recombine with nearby micelles before reptation is complete, and we enter regime II. To define the range of regime II, where relaxation occurs by a combination of reptation and breakage/rejoining, we define a dimensionless parameter  $\alpha$ , as the inverse of the number of entanglements in each micelle:

$$\alpha \equiv l_e/\bar{L} \quad (4.6)$$

Here  $l_e$  is the contour length between two neighboring entanglements. In the range  $\alpha < \zeta < 1$ , the breakage time of the micelle is longer than the reptation time of a chain of length one entanglement. This regime is defined as regime II. Within this regimes, in the “fast breaking” limit when  $\zeta \ll 1$ ,

$$\tau \cong (\tau_{br}\tau_{rep})^{1/2} \quad (4.7)$$

As the breakage time decreases further, so that  $\zeta < \alpha$ , micelles relax by a combination of breakage/rejoining and end fluctuations, rather than reptation. We do not consider this regime here, since stress relaxation of micelles in body washes are generally within regime I (i.e., pure reptation) or regime II (reptation combined with reversible scission). There is a version of the Cates model for each of these regimes.

To apply the Cates model to a set of  $G'$  and  $G''$  data for a wormlike micelle solution, a typical fitting procedure involves fitting a “Cole-Cole” plot of  $G'$  against  $G''$  to a semi-circle to obtain its diameter  $G_{sc}$ . Extrapolation of the Cole-Cole plot at a slope of -1 before its high-frequency up-turn yields an elastic modulus  $G_e$ . The ratio of  $G_{sc}/G_e$ , termed the diameter of the fitted semicircle (DFS), can be related to the ratio of breakage time  $\tau_{br}$  to the terminal relaxation time  $\tau$  according to Turner and Cates’ Monte Carlo simulation work.<sup>40</sup> Then the reptation time  $\tau_{rep}$  can be computed from  $\tau$  or Eq. 4.7 by assuming the relaxation regime iteratively. This procedure is straightforward when there is a clear -1 slope in the Cole-Cole plot before its upturn. Please see the work of Turner and Cates<sup>40</sup> for details.

Depending on the ratios of  $\tau_{br}$  to  $\tau_{rep}$  and to  $\tau_e$  (which is the relaxation time of a short micelle whose length is only long enough to contain one entanglement), the shape of the Cole-Cole plot at its high-frequency side (which is the right side) varies and the slope could become either greater than or less than -1 before turning up. When  $\zeta \sim 1$  especially  $\zeta < 1$  in the reptation regime, there are multiple relaxation times near the terminal

relaxation regime and the deviation of the Cole-Cole plot from semicircular shape is apparent. This leads to an upturn in the Cole-Cole plot at its high-frequency side (which is the right side of the Cole-Cole plot) before the slope reaches -1. When  $\zeta \ll 1$ , on the other hand, a single relaxation time dominates the dynamics and deviation from semicircular shape is minimal. Depending on the ratio of  $\tau_{br}$  to  $\tau_e$ , the slope reaches -1 or even lower before the high frequency upturn. To improve the approximation to  $G_e$ , we sampled more points at high frequencies and interpolated  $G''$  near the slope minimum before the upturn.

#### 4.2.2.2 Predicting Micellar Characteristic Lengths

Three important micellar solution characteristic lengths are related to each other by:

$$l_e \cong \xi^{\frac{5}{3}} / l_p^{\frac{2}{3}} \quad (4.8)$$

Here  $\xi$  is the mesh size, which is the average distance between different micelles,  $l_p$  is the persistence length, and  $l_e$  is the entanglement spacing, which is the average contour distance along a micelle between successive entanglements.

For ionic micelles at low ionic strength, both the natural (or intrinsic) persistence length and electrostatic effects contribute to the overall persistence length.<sup>2</sup> When the ionic strength of solution is high, counterions condense on the surface of the micelles and weaken the contribution of electrostatics to the persistence length by screening the electrostatic repulsions between the surfactant head groups. Above a critical ionic strength, the persistence length is approximately equal to the natural persistence length. In this study, we approximate the persistence length by the natural persistence length

since the concentrations of salts in solutions we consider are high enough to minimize head-head electrostatic interactions.

Methods of estimating  $l_e$  and  $\xi$  depend on the relaxation regime of wormlike micelles, which is itself determined by the ratio of  $l_e$  to  $l_p$ . When  $l_e \gg l_p$ , micelles are said to be “loosely entangled”, and are flexible on the length scale of a single entanglement spacing so that the micelle can curl up on itself within the tube, and the micelle contour length is then longer than the tube. When  $l_p \gg l_e$ , on the other hand, micelles are “tightly entangled”, and their contour length is scarcely longer than the tube length. Within the loosely-entangled regime, the mesh size can be related to  $G_0$ , the plateau modulus, as<sup>41</sup>

$$G_0 \cong 9.75k_B T / \xi^3 = 9.75k_B T / \left( l_e^{3/5} l_p^{2/5} \right) \quad (4.9)$$

$G_0$  is estimated as  $G'$  at the frequency of the local  $G''$  minimum  $G''_{min}$ . Within the tightly-entangled regime, on the other hand,  $l_e$  and  $G_0$  are related as below:<sup>42</sup>

$$G_0 = \frac{7}{5} \rho k_B T / l_e \quad (4.10)$$

where  $k_B$  is Boltzmann’s constant and  $T$  is the absolute temperature. For the micelles in body washes considered in this study,  $10l_p > l_e > l_p$  which is in the cross-over between tight and loose entanglements. We therefore use a cross-over formula to interpolate between Eqs. (9) and (10) using:

$$G_0 = \frac{9.75k_B T}{\left( l_e^{3/5} l_p^{2/5} \right)} \left( \frac{(l_e/l_p)^n}{n + (l_e/l_p)^n} \right) + \frac{7}{5} \rho k_B T / l_e \left( 1 - \frac{(l_e/l_p)^n}{n + (l_e/l_p)^n} \right) \quad (4.11)$$

where we take  $n = 3$ , and solve for  $l_e$  iteratively from pre-determined values of  $G_0$  and  $l_p$ .

We then use the value of  $l_e$  to obtain the average micelle length, as discussed next.

In the Cates model the average micelle length  $\bar{L}$  is estimated at high frequency as:

$$G_{min}''/G_0 \approx l_e/\bar{L} \quad (4.12)$$

Granek refined this estimate of the relationship between  $l_e/\bar{L}$  and  $G_{min}''$  and obtained<sup>43</sup>

$$G_{min}''/G_0 \approx (l_e/\bar{L})^{0.8} \quad (4.13)$$

Contour lengths calculated from either formula are only several hundred nanometers, which is inconsistent with the high value of the solution viscosity.<sup>33</sup> In fact, the length of the micelle has its strongest effects on micellar relaxation at low frequency, rather than at high frequencies near the  $G_{min}''$ . Based on a Rouse reorientation time and the Batchelor formula for the drag coefficient of a cylinder, Larson developed a new method to estimate  $\bar{L}$ :<sup>33</sup>

$$\bar{L} = \left( \frac{\tau_{rep} \pi l_e \ln(\xi/d) k_B T}{4 \eta_s l_p} \right)^{1/3} \quad (4.14)$$

This formula gives an estimated average micelle length that is several times higher than that of Eqs. 4.12 or 4.13, and is consistent with the magnitude of the solution viscosity. Therefore we adopt Eq. 4.14 in our model calculations. We assume that the diameter of the micelles is 5 nm and the persistence length is 30 nm, based on former wormlike micelle studies and molecular modeling.

Once the average micelle length is estimated appropriately, the scission free energy can be estimated from Boltzmann dependence of this average micelle length on temperature.



This “scission energy”  $E_{\text{scission}}$  is the free energy of creating two additional end caps. The micellar length depends exponentially on its value as<sup>10,13</sup>

$$\bar{L} \sim \varphi^{-1.85} \exp\left(\frac{E_{\text{scission}}}{2k_B T}\right) \quad (4.15)$$

Here, the dependence on  $\varphi$ , the volume fraction of solution occupied by the micelles, arises because the breakage/rejoining reaction is “bi-molecular” transforming two micelles into one, and the factor of two in the exponent also arises for this reason. To avoid significant changes in the packing of micellar head groups, which would invalidate Eq. 4.15, we apply the above equation only over a set of four temperatures separated by intervals of 1 or 2 degrees within a narrow range from 17.5 to 25.0 °C.

Similar to the scission free energy, we express the temperature dependence of  $\tau/\eta_{s0}$  and  $\eta/\eta_{s0}$  in Arrhenius forms involving activation energies, where here  $\eta_{s0}$  is solvent viscosity at the reference temperatures:<sup>13</sup>

$$\tau \sim \eta_{s0} \exp\left(\frac{E_{\text{terminal relaxation}}}{k_B T}\right), \quad \eta \sim \eta_{s0} \exp\left(\frac{E_{\text{viscosity}}}{k_B T}\right) \quad (4.16)$$

In what follows, the above activation energies for terminal relaxation time of micelles and viscosity are extracted from the corresponding semi-log plots.

Applying these micellar models to rheological data can connect surfactant microstructures to the continuum viscoelastic properties. Specifically, we relate viscosity to the micellar characteristic length and elasticity to the micellar characteristic time constants in what follows. We also analyze the behavior of the micelles at molecular scales using molecular simulations to help link molecular-level information to rheological properties.

### 4.2.3 Octanol/Water Partition Coefficient $\log P_{ow}$

Perfumes are essential components in body washes to meet consumers' fragrance preferences. They are typically mixtures of some tens to a hundred or so small organic molecules, named as perfume raw materials (PRMs). Before studying the synergistic effects of mixtures of PRMs on viscoelastic properties of surfactant solutions, the effects of a single PRM are often studied and correlated with the value of its octanol/water partition coefficient,  $\log P_{ow}$ .<sup>44-51</sup>  $\log P_{ow}$  is defined as the logarithm of the concentration ratio of the PRM in hydrophobic octanol to the hydrophilic water phase, and used as a hydrophobicity parameter. The hydrophobic octanol phase approximates the hydrophobic environment of the surfactant tail region within micelles, and the hydrophilic water phase approximates the hydrophilic surfactant head region and the water phase outside the micelles, as shown in Eq. 4.17:

$$\begin{aligned} \log P_{ow} &= \log \left( \frac{[PRM]_{Octanol}}{[PRM]_{Water}} \right) \\ &\cong \log \left( \frac{[PRM]_{Surfactant\ tail\ region\ within\ micelles}}{[PRM]_{Surfactant\ head\ region\ within\ micelles} + [PRM]_{Water}} \right) \end{aligned} \quad (4.17)$$

This approximation neglects geometric constraints, especially in the tightly packed surfactant tail regions, which might restrict access of PRMs to the micelle core or cause a major change of the surfactant packing within micelles. To understanding how different PRMs modify the packing of the cylindrical micelles and resulted in the changes of the rheological properties of surfactant solutions, 15 PRMs with a broad distribution of  $\log P_{ow}$  were added separately to the BW-1EO formulation. PRMs having similar values

of  $\log P_{ow}$  but different chemical structures were also chosen to help compare the resulted viscoelastic properties of BW-1EO.

#### 4.2.4. Dissipative Particle Dynamic (DPD) Simulations

Although molecular dynamics simulations of small cylindrical micelles containing less than four hundred molecules of sodium dodecyl sulfate surfactants have been carried out using a united atom force field,<sup>52</sup> investigating cylindrical micelles containing tens of different surfactant species and over one thousand surfactant molecules using MD simulations is still too expensive to be routinely carried out. To describe accurately the relevant hydrodynamic behavior and rheological properties of cylindrical micelles in a computationally more efficient way, coarse-grained dissipative particle dynamics (DPD) simulations using a soft repulsive potential are here applied.<sup>53,54</sup> In DPD, three to five heavy atoms are lumped into one quasi-particle or bead, which interacts with other beads via pairwise forces, and obeys Newton's equations of motion. The interparticle force is separated into pairwise contributions of three parts,

$$f_i = \sum_{j \neq i} (F_{ij}^C + F_{ij}^D + F_{ij}^R) \quad (4.18)$$

where  $F_{ij}^C$  is a conservative force defined by a purely repulsive (harmonic) soft-core potential based on chemical identity,  $F_{ij}^D$  is a dissipative force and  $F_{ij}^R$  is a random force. The latter two forces take into account the fluctuation and dissipation of energy and serve as the Langevin thermostat. The conservative force determines the thermodynamics of the DPD system and the soft potential allows for larger time steps of picoseconds instead of the femtosecond timesteps used in traditional MD simulations. Since its introduction

by Hoogerbrugge and Koelman in 1992,<sup>55</sup> DPD has been improved significantly by Español and Warren<sup>53</sup> and then by Groot and Warren.<sup>54</sup> Recently, to differentiate the type of interactions between beads representing different properties, Travis<sup>56</sup> et al. demonstrated the use of the Hildebrandt solubility parameters for DPD parametrization, along with variable bead sizes. Siepmann<sup>57</sup> et. al applied COSMOtherm software<sup>58,59</sup> to compute the infinite-dilution transfer free energy of alkane molecules into acetic anhydride for molecular volume estimation. This refined model considers the importance of different bead volumes to reflect the impact of different molecular shapes and sizes of surfactants packing in micelles (see packing parameter discussion above). We applied the refined DPD model in canonical ensembles of constant pressure and constant temperature with semi-isotropic pressure coupling to study the effects on micelle properties of salts in the two formulas BW-1EO and BW-3EO and the effects of four PRMs in BW-1EO. Detailed DPD parameters and molecular mapping were listed in Table C.1 and C.2 in Supplementary Material. Using a combination of the Cates micellar model and the DPD molecular model, we seek to predict the rheological property changes at macroscopic scales that result from the addition of salts and PRMs and thereby build a fundamental understanding of the structure-property relationships of surfactant formulations.

Experimentally, the effects of different concentrations of salt (NaCl) on the rheological properties of BW-1EO and BW-3EO were determined as well as the effects on BW-1EO of separate addition of 15 PRMs having a wide distribution of values of  $\log P_{ow}$  varying from -0.61 to 6.44. In addition, the effect of linalool on the rheological properties of BW-3EO was also measured for comparison against its effect on BW-1EO. By applying the

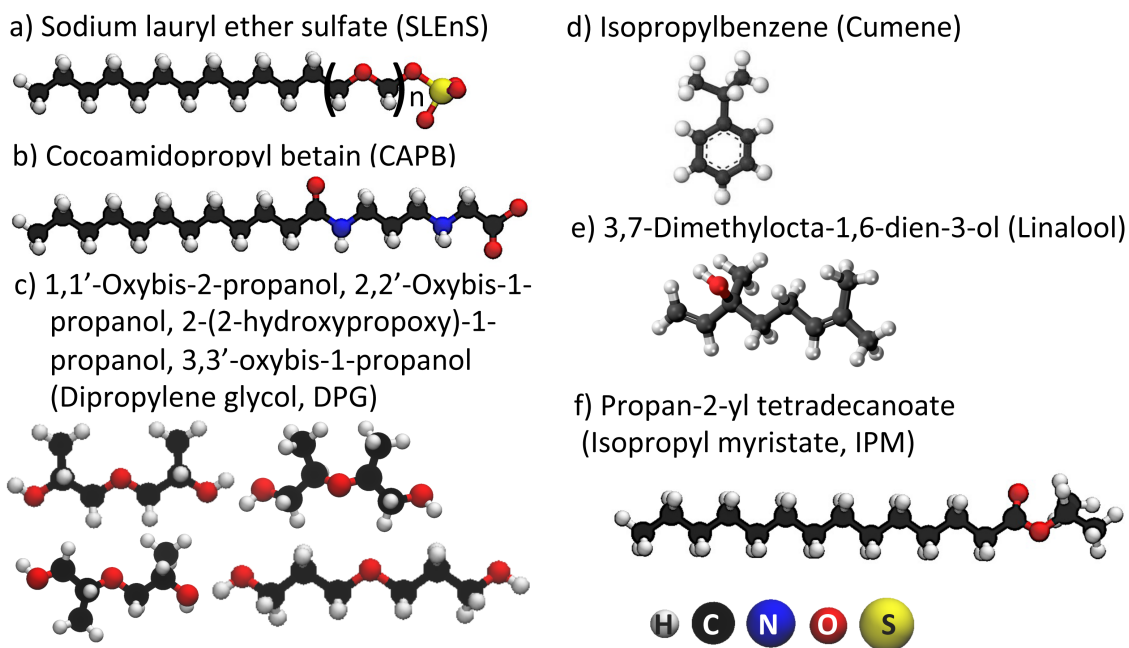
Cates model to estimate micellar scale parameters, and performing DPD simulations at the molecular scale to estimate surfactant packing, we develop a more fundamental understanding of how the rheological behavior of body washes is affected by the addition of salts and PRMs.

## **4.3 Materials and Methods**

### **4.3.1 Rheological Experimental Set Up**

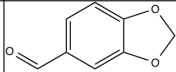
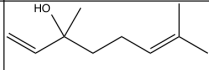
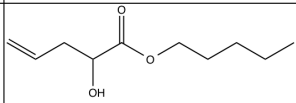
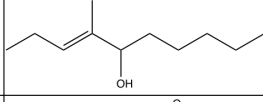
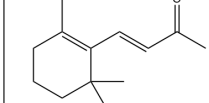
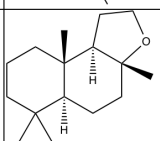
Raw industrial grade surfactants, analytical grade salts and PRMs, and Milli-Q water were used in all experiments. Due to the complexity of the industrial raw materials, weight percentage (wt.) instead of molar concentration was used to define concentrations of surfactants, ACCORD, and salts. Molar concentration is used when defining the addition of one additional species of PRM to body washes to study the effects of different individual PRMs on viscoelastic properties. Two body wash formulations, “BW-1EO” and “BW-3EO” with a simple salt (sodium chloride, NaCl), were tested. The BW-1EO formulation is a mixture of SLE1nS (9.85%), CAPB (1.15%), and 1wt.% ACCORD, where SLE1nS (Fig. 4.1a) has on average one EO group but a distribution of EOs ranging from 0 to 10, and CAPB (Fig. 1b) is a zwitterionic co-surfactant. The BW-3EO formulation is similar to that of BW-1EO formulation except that the formula has on average three EOs and the ratio of surfactants are different: SLE3nS (6.95%), SLS (2.90%), CAPB (1.15%), and 1% ACCORD. The 1% ACCORD is added to mimic the impact of a perfume on the micellar structure and the viscoelastic properties. In the past,

studies have focused on the impact of single compounds on micellar structure and rheology. Screening experiments and the results presented here suggest that the impact of a single compound may not translate in a simple linear and additive fashion to mixtures of additives. The ACCORD is a mixture of six small organic perfume molecules as listed in Table 4.1. In addition, four PRMs (Schemes 1c, 1d, 1e, and 1f) were chosen for DPD simulations including dipropylene glycol (a mixture of four isomers: a. CAS number 110-98-5, 1,1'-Oxybis-2-propanol; b. CAS number 108-61-2, 2,2'-Oxybis-1-propanol; c. CAS number 106-62-7, 2-(2-hydroxypropoxy)-1-propanol; d. CAS number 2396-61-4, 3,3'-oxybis-1-propanol, abbreviated as DPG), isopropylbenzene (CAS number: 98-82-8, common name cumene), 3,7-dimethylocta-1,6-dien-3ol (CAS number: 78-70-6, common name linalool), and propan-2-yl-tetradecanoate (CAS number: 110-27-0, common name isopropyl myristate, abbreviated as IPM). Components added together in the following order: concentrated surfactant paste, ACCORD, water, PRMs (if added), and salts. Samples were well mixed and centrifuged at least an hour for degassing prior to measurements.



**Figure 4.1 Figure 1** Structures of surfactants and perfume raw materials (PRM) used in this study: a). sodium lauryl ether sulfate (SLEnS) number of ethylene oxide groups varying from  $n = 0$  to 10; b). cocoamidopropyl betain (CAPB); c). dipropylene glycol modeled as a mixture of 1,1'-Oxybis-2-propanol, 2,2'-Oxybis-1-propanol, 2-(2-hydroxypropoxy)-1-propanol, 3,3'-oxybis-1-propanol, and is abbreviated as DPG; d). isopropylbenzene with common name cumene; e). 3,7-dimethylocta-1,6-dien-3-ol with common name linalool; f). propan-2-yl-tetradecanoate with common name isopropyl myristate and abbreviated as IPM.

**Table 4.1.** Composition of ACCORD and each PRM's properties, including CAS number, IUPAC name, common name, chemical structure, octanol/water partition coefficient, molecular weight, and its weight percentage.

CAS Number	IUPAC name	Common Name	Chemical Structure	Octanol/Water Partition Coefficient LogPow	Molecular Weight	Weight %
120-57-0	1,3-Benzodioxole-5-carbaldehyde	Heliotropin		1.43	150.13	15.4
78-70-6	3,7-dimethylocta-1,6-dien-3-ol	Linalool		2.44	154.25	23.3
67634-00-8	prop-2-enyl 2-(3-methylbutoxy)acetate	Allyl amyl glycolate		2.81	186.25	13.5
81782-77-6	4-methyl-3-decen-5-ol	Undecavertol		3.06	170.29	25.6
14901-07-6	(3E)-4-(2,6,6-Trimethylcyclohex-1-en-1-yl)but-3-en-2-one	beta-Ionone		4.02	192.3	11.5
6790-58-5	Naphtho[2,1-b]furan,dodecahydro-3a,6,6,9a-tetramethyl-,	synambran		4.58	236.4	10.7

An AR-G2 rotational rheometer with cone and plate geometry made of acrylic was used to measure the zero shear viscosity at constant shear rate, and rheological moduli of constant shear stress but varying frequency. We sampled 25 data points per decade at high frequency and 10 data points per decade at low frequency to obtain enough information for model fitting in a reasonable time. Samples were freshly loaded each time and a solvent trap was used to prevent sample evaporation near the edge. Randomly selected samples were re-measured and the standard deviation of rheological measurements was found to be less than 3%.



### 4.3.2 DPD Simulation Set Up and Analysis

Initial periodic cylindrical micelles were packed straightly along the z direction of the simulation box and the heads of surfactants within the micelles enclosed the tails. The simulation box has a size of  $10.6 \times 11.4 \times 62.3 \text{ nm}^3$ . All surfactants, ACCORDS, and additional PRM if added, were packed randomly into the periodic micelle close to a common axis at the beginning of the simulations. The tail beads of the micelle were first constrained in an NVT ensemble briefly to equilibrate the surfactants with water. Then simulations in an NPT ensemble were carried out by minimizing the difference between the pressure along the normal (z, or micelle) axis and the average over the x and y axes. The wormlike micelles were maintained in a tensionless state throughout the remainder of each simulation.

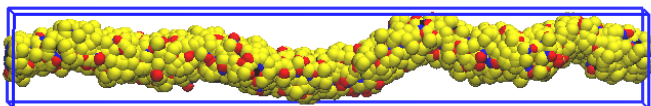


**Figure 4.2** Snapshot of an equilibrated periodic wormlike micelle. Salt and water are omitted for clarity. Shown are sulfate (yellow) and other head groups including ethylene oxide, amide, tetramethyl ammonium, and acetate (red), ACCORD (black), and alkyl carbon tail beads (blue). ACCORD and tail beads are nearly covered by head beads.

The equilibrated periodic wormlike micelles were then analyzed by slicing the simulation box along the micelle direction z and averaging the values per segment over all the slices and over time as shown in Fig. 4.2. The number of beads in each slice was counted within a narrow shell of 1.6 nm centered at a given radial distance with respect to the center of the spherical micelle (COM) or with respect to the core of the cylindrical

micelle and was averaged over time. The packing distance is defined as the ratio of micelle spine length to the number of surfactant molecules within the micelle. The spine length is computed as the sum of the lengths of the segments connecting the micelle COMs of neighboring slices.

## **4.4 Results and Discussion. I. Salt Effects**

### **4.4.1 Salt Effects on Rheology Measurements**

#### **4.4.1.1 Salt Curves and Impact of ACCORD Addition**

The zero shear viscosity vs. the concentration (wt.%) of sodium chloride (NaCl), or “salt curves,” are shown in Fig. 4.3 for the 11% BW-1EO (diamonds) and BW-3EO (triangles) containing 1% ACCORD (solid lines) and in the absence (dashed lines) of ACCORD. The salt curve for 9.5% BW-3EO (circles) containing 1% ACCORD is also shown. With increasing salt concentration, the zero shear viscosity, called simply “viscosity” in the following, increases and, when ACCORD is present, reaches a maximum, and then decreases. The dashed lines, for which ACCORD is absent, are also expected to eventually show a maximum if the salt concentration were increased further. In each formulation, the concentration of SDS on its own is already higher than its 2<sup>nd</sup> CMC, which is the concentration at which the majority of the micelles change from spheres to elongated rods and are polydisperse.<sup>20,21,60</sup> Previous studies have indicated that addition of SLEnS and/or CAPB to SDS solutions lowers the CMC or promotes longer micelles especially for longer EO lengths in SLEnS.<sup>24–29, 61</sup> Therefore, even in the absence of salts, the majority of the micelles in body washes are already expected to be

cylindrical, although the zero shear viscosities are still low. In the presence of 1% ACCORD the viscosity is higher (to the left of its maximum) the micelles are presumably longer, and the salt curve is shifted to the left relative to that in the absence of ACCORD. Since the viscosity maximum is attributed to formation of micellar branches, the reduced viscosity maximum in the presence of ACCORD suggests easier branch formation. Since actual body wash formulations have rheological properties similar to those of 11% BW-1EO and 11% BW-3EO formulations containing ACCORD, we will discuss those formulations in detail in the following. In the following, the terminology “BW-1EO” and “BW-3EO” refer to the 11% solutions containing the ACCORD PRMs.

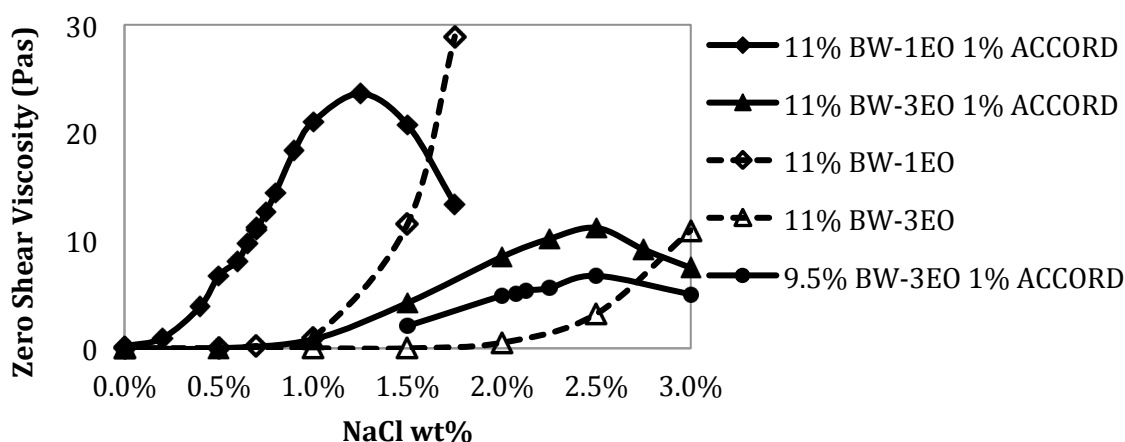


**Figure 4.3** Salt curves for 11% and 9.5% formulations containing 1% ACCORD (solid lines) and without ACCORD (dashed lines): diamonds - 11% BW-1EO formulation, triangles - 11% BW-3EO formulation, and circles - 9.5% BW-3EO formulation.

The addition of salt screens the electrostatic repulsion between the surfactant head groups, which increases the value of the packing parameter  $p$ , and lengthens the micelles, leading to a viscosity increase. The 11% BW-1EO and BW-3EO formulations containing

1% ACCORD (solid line with filled symbols) show initially nearly exponential increases in viscosity at low salt concentration, which changes to a linear dependence, and finally a concave shape near the maximum. A critical micellar length, needed for the micelle to entangle with other micelles, is proposed to explain the nonlinearity of the viscosity increase at the beginning of the salt curve. The micelles in body washes are polydisperse and their length distribution ranges from short rods to long worms. At the beginning of the salt curve, only the growth of the micelles above the critical length contributes significantly to the viscosity. The growth of the short rods with lengths below that necessary to entangle, does not contribute to the viscosity increase. As the salt concentration increases, however, a larger fraction of the micelles are above the critical micellar length and contribute to the viscosity increase, leading to an exponential increase of viscosity near the beginning of the salt curve. Once all micelles exceed the critical lengths, further micelle growth contributes only linearly to the viscosity increase.

At high salt concentration near the viscosity maximum, the further addition of salts screening the electrostatic repulsions between the surfactant head groups may lead to branch or planar structures that reduce the viscosity. The relatively short micelles still lengthen, however, and the competition between these two effects reaches a balance at the viscosity maximum, where on the left side of the salt curve the growth in micellar length dominates branch formation, and on the right side the reverse occurs. Some branch formation on the left side of the viscosity maximum has in fact been observed in cryo-TEM studies.<sup>2,62</sup>

The salt curve for BW-3EO containing ACCORD, in which EOs are longer, shows a slower viscosity increase upon addition of salt, a lower viscosity maximum, and a broader regime of linear viscosity increase for BW-1EO with ACCORD. Consistent with the packing parameter argument, the longer EOs of SLE3nS make the area per head group larger, which decreases the packing parameter  $p$ , and thereby shortens the micelles relative to SLE1nS. The longer electrostatically neutral EOs also likely makes SLE3nS less sensitive to the addition of salt. This leads to a slower increase of packing parameter on addition of salt, a lower rate of viscosity increase, and a rightward shift of the salt curve, relative to BW-1EO containing ACCORD. Interestingly, reducing the total concentration of surfactants in BW-3EO from 11% to 9.5% results in the reduction in the viscosity without shifting of the viscosity maximum, according to Fig. 4.3.

In short, increasing the concentration of salts or surfactants, or adding ACCORD, boosts the viscosity of body washes. Formula BW-1EO having surfactants of shorter EOs builds up viscosity faster with increasing salt and to a higher viscosity magnitude.

#### **4.4.1.2 Frequency Sweeps**

Fig. 4.4 shows the loss and storage moduli vs. frequency for BW-1EO (a-c) and BW-3EO (a'-c') at various salt concentrations. As the salt concentration increases, the storage moduli shift upward and leftward monotonically up to the maximum in the salt peak, with the greatest differences at the lower frequencies. The loss moduli also shift upward and leftward at low frequencies, but shift downward monotonically at high frequencies at the two sides of the intersection point. Interestingly, Figs. 4.5c and 4.5c' show common

intersection points of loss moduli for data on the left side of the linear salt curves for BW-1EO and BW-3EO, respectively. The physical meaning of the intersection point is still unclear.

The plateau modulus, viscosity, elasticity, and average micelle length can be obtained directly from the frequency sweeps. Here, and elsewhere, we quantify “elasticity” by the ratio of the loss to the storage modulus at high frequency of 100 rad/s. Thus, “elasticity” is here taken to be the inverse of the loss tangent  $\tan\delta$  at high frequency 100 rad/s. As the salt concentration increases in Figs. 4.5a and 4.5a’, the plateau in the high-frequency storage moduli increase monotonically. In Figs. 4.5b and 4.5b’, the viscosities increase monotonically as the loss moduli shift upward at low frequency, until the salt peak is reached. The elasticities increase monotonically before hitting the salt peak since the ratios of loss moduli to storage moduli decrease at frequency 100 rad/s. The terminal relaxation time, which can be approximated by inverse of the the crossover frequency of loss and storage moduli (data not shown), increases with increasing salt concentration on the left side of the salt curve, which indicates that micelles are lengthened before reaching the salt peak. Once the concentration of salt passes the viscosity maximum (at 1.25% for BW-1EO and 2.5% for BW-3EO), the dependences of viscosity and elasticity on salt concentration reverse direction and decrease with increasing salt, but the plateau moduli continue to increase. BW-3EO with longer EO groups shows less sensitivity to salt concentration than does BW-1EO, since the magnitude of changes in the rheological curves with salt are smaller for for BW-3EO. These observations are consistent with the packing argument.

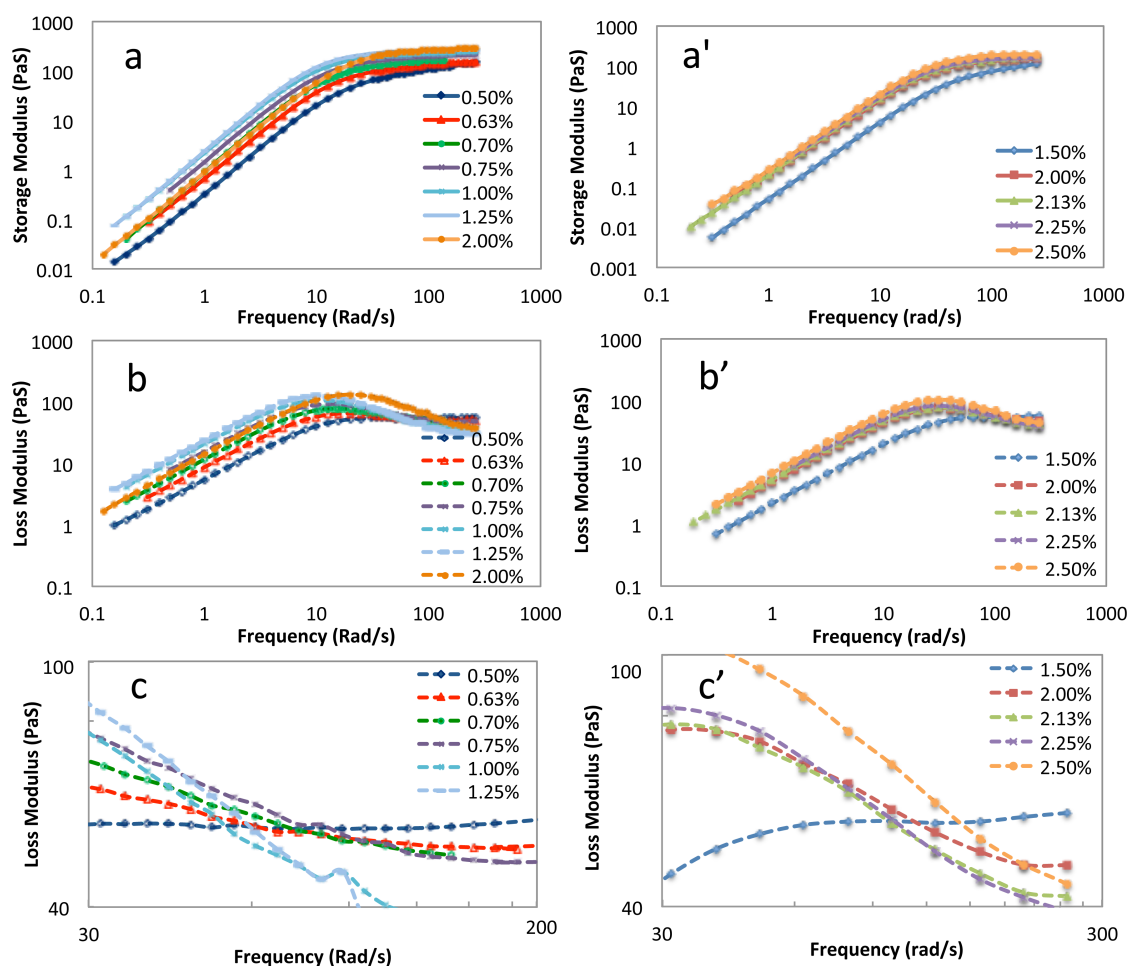


**Figure 4.4** Storage and loss moduli for BW-1EO (a, b) and BW-3EO (a', b') at different salt weight percentages, given in the legends. Loss moduli pass a common point at different salt concentrations before branch formation in BW-1EO (c) and BW-3EO (c').

#### 4.4.1.3 Cole-Cole Plots

Plotting the loss modulus  $G''$  vs. the storage modulus  $G'$  gives the Cole-Cole plots for BW-1EO (Fig. 4.5a) and BW-3EO (Fig. 4.5a'). The diameters of the approximate semi-circles increase monotonically with salt concentration, and the shapes change. By normalizing the curves with respect to the loss modulus maximum  $G''_{maximum}$  in Figs.

Fig. 4.5b and Fig. 4.5b'. the deviations from perfect semi-circles (dashed lines) decrease as the salt concentrations increase, until the peak in the salt curve is passed, and then the deviations increase again (gray curve in Fig. 4.5b). The deviations of the Cole-Cole plot from semi-circular shape at low salt concentrations are greatest to the right of the loss modulus. At low salt concentrations, the solutions contain shorter micelles and the micellar relaxation mechanisms are dominated by reptation in relaxation regime I. The wide distribution of reptation times resulting from the distribution of micellar lengths leads to the observed deviation of the Cole-Cole plot from a semi-circular shape which corresponds to a single or very narrow distribution of relaxation times.<sup>10</sup> As the salt concentration increases, micelles lengthen and the relaxation mechanisms become dominated by the combination of reptation and reversible scission. The Cole-Cole plots then become closer to a semi-circular shape especially at high salt concentrations, before the peak in the salt curve is reached. The up-turns of the Cole-Cole plot at the right side of the Cole-Cole plot where  $G'/G''_{maximum}$  exceeds 2 is due to the contributions of Rouse modes at high frequencies. At these high frequencies the relaxation of short portions of chain between neighboring entanglements dominates and produces the upturn. Beyond the viscosity maximum in the salt curve, increasing deviation in the Cole-Cole plot from a semi-circular shape is due to the end fluctuations of the increasing numbers of branches. Although BW-1EO at 0.7% NaCl and BW-3EO at 2.125% NaCl have the same zero-shear viscosity of ~11 PaS, the Cole-Cole plot of BW-1EO deviates more from a semi-circular shape than does that of BW-3EO, possibly because the BW-1EO



formulation is farther from the maximum in the salt curve than is the BW-3EO formulation at this fixed viscosity.

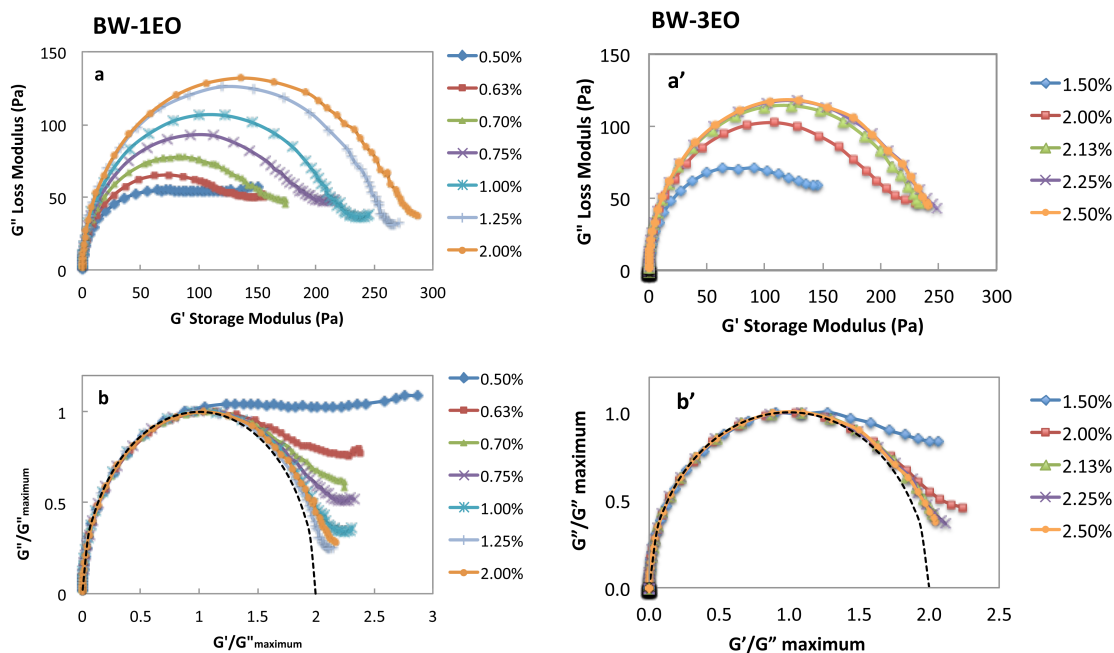


**Figure 4.5** Cole-Cole plots and normalized Cole-Cole plots for BW-1EO (a, b) and BW-3EO (a', b').

#### 4.4.1.4 Time-Temperature Superposition

Next we evaluate the time-temperature superposition (TTS) principal for BW-1EO. Shifting the  $G'$  and  $G''$  curves for temperatures ranging from 20.0 to 25.0 °C as shown in Fig 4.6, the storage moduli approximately overlap over the entire frequency domain as predicted by TTS. However, at low salt concentrations before the salt peak, the loss moduli fail to superpose at the highest frequencies (Figs. 4.6a and 4.6b). Interestingly, after passing the salt peak in the highly branched micelle region, as shown in Fig 4.6c, loss moduli do superpose. The convergence of the loss moduli in the region dominated by

branched micelles suggests the relaxation mechanisms dominated by end fluctuations of the increasing numbers of branches are not temperature sensitive.

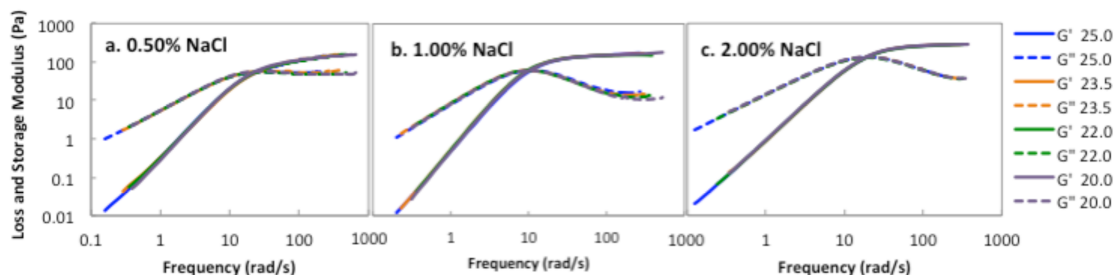


**Figure 4.6** Master curves of frequency dependent moduli obtained by time-temperature superposition (TTS) at salt concentrations of 0.50% (a), 1.00% (b), and 2.00%(c) NaCl for BW-1EO. Shift factor  $\alpha_T \equiv \eta_T/\eta_{T0}$ . Here  $\eta_T$  is the viscosity of solution at temperature T and  $\eta_{T0}$  at 25.0 °C. At 0.50% NaCl the shift factors are inconsistent with the dependence of viscosity on temperature and we use empirical shift factors 1.5 at 23.5 °C, 1.8 at 22.0 °C and 2.5 at 20.0 °C. At 1.00% NaCl and 2.00% NaCl, the shift factors are consistent with the dependence of viscosity. The values of the shift factors are 1.1, 1.4 and 2.0 at 1.00% NaCl and 1.1, 1.2, and 1.4 at 2.00% NaCl at 23.5 °C, 22.0 °C and 20.0 °C, respectively.

#### 4.4.2 Salt Effects on Micellar Lengths and Time Scales Obtained From the Cates Model

##### 4.4.2.1. Micelle Characteristic Lengths and Times for BW-1EO at Different Temperatures

The viscoelastic properties of surfactant solutions are sensitive to the addition of salts and ACCORD, and to the temperature as well. Fig 4.7a shows the salt curves of BW-1EO at different temperatures. Figs. 4.7b and 4.7c show the corresponding micelle average lengths and reptation times estimated from the Cates model, as described above in

Sections 2.2.1 and 2.2.2. As the temperature decreases, the viscosity and the average micelle length of BW-1EO increase rapidly.<sup>13,62</sup> The viscosity maximum occurs at a salt concentration of around 1.25% at 25.0 °C, but shifts to a lower concentration of between 1.00 and 1.25% at 23.5 °C, and around 1.00% at the other two temperatures. Changes in the average micelle length, micellar reptation time and elasticity (data not shown) are consistent with that of the viscosity. When branches are present, stress relaxation occurs by sliding of micellar material through the branch points, and the speed of this process increases the more branch points there are even if the branched micelles become larger. Hence, the average apparent “micellar length” estimated using Eq. 4.14 from data on the right side of the salt peak are is actually an estimate of the average contour length between branch points, rather than an estimate of the true micellar length. On the right side of the salt curve, the contour length between branch points decreases with increasing salt concentration, because of the increasing prevalence of branches. Thus, while the actual contour length of the micelle continues to increase with increasing salt on the right side of the salt curve<sup>39</sup> branch formation dominates over micellar length growth, and the contour lengths between the adjacent branch points decreases rapidly with increasing salt, and results in a sharp drop in viscosity and in apparent “micellar length,” inferred from Eq. 4.14, which is based on linear, unbranched micelles..

The entanglement length, mesh size (data not shown), and breakage time decrease monotonically (Figs. 4.7d-e), and the plateau modulus increases monotonically (Figs. 4.7f) as the salt concentration increases. The rate of change slows once the salt concentration passes the viscosity maximum. In the highly branched region at 2.00%

NaCl concentration, the differences in temperature dependence of these properties are very small. This suggests that the properties of branched micellar solutions are less sensitive to temperature than is the case for linear micelles.

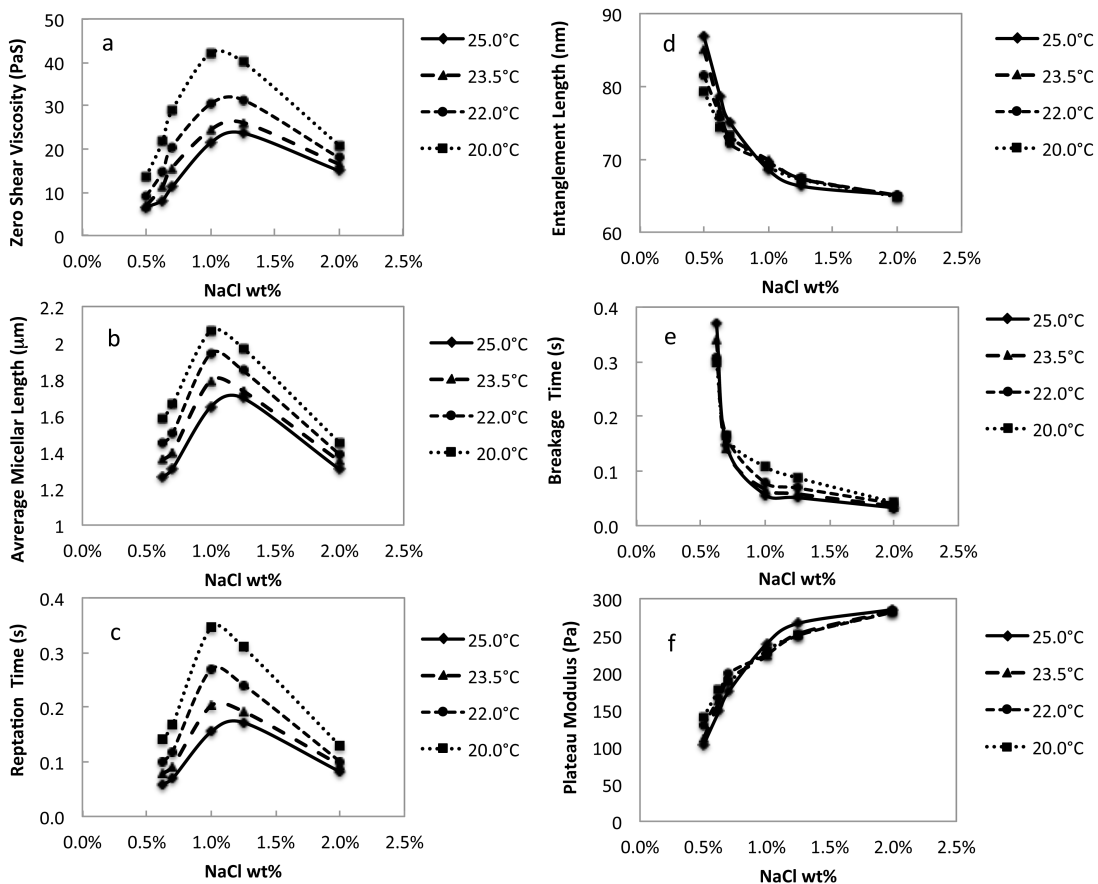


**Figure 4.7** Viscosity (a) vs. salt concentration at 20.0, 22.0, 23.5, and 25.0°C, and the computed micellar characteristic lengths and times, including average micelle length (b), reptation time (c), micellar entanglement length (d) breakage time (e), and plateau modulus (f) of BW-1EO.

The Boltzmann law, Equation (15), predicts a linear dependence of the natural logarithm of the average micelle length,  $\ln(\bar{L})$ , on  $1/T$  at various surfactant

concentrations as is in fact shown in Fig 4.8 and is used to compute the scission free energies  $E_{scission}$  at around 25.0 °C. The scission energies are expected to increase as the viscosity and average micelle length increase until the salt peak is reached, and then the apparent scission energy should decrease when the formation of branches becomes dominant. In the branched micellar regime, the “scission energy” must be re-interpreted as an apparent scission energy, because the decrease in apparent “micellar length” is not due to a decrease in actual micelle length, but due to a proliferation of branches, creating shorter segments between branch points, as discussed above. The Boltzmann temperature dependence fits the data well at NaCl concentrations of 0.63, 0.70, and 2.00% when the data for all temperatures at each of these salt concentrations all fall on the same side of the salt peak (Fig 4.7a) at all four temperatures. For example, micelle lengthening dominates at the left of the salt peaks (0.63% and 0.70%) and branch formation dominates at the right side of the salt peak (2.00%) at all four temperatures. The data at these salt concentrations are nearly perfectly linear with squared correlation coefficient of  $R^2 > 0.998$ . However the data at NaCl concentrations of 1.00% and 1.25% are on the left side of the salt curve only at the highest temperature (25.0°C), but are on the right side of the salt curve at the lowest temperature (20.0°C). For 1.0% salt, only the data point at the lowest temperature (20.0°C) is on the right side of the salt curve, while for 1.25% salt, only the data point at the highest temperature (25.0°C) is on the left side of the salt curve. This means that for both 1.00% and 1.25% salt, we have three data points that do not cross the salt curve maximum, and one point that is on the opposite side of the salt curve, that we mark in Fig 4.8 with an open symbol. Excluding the single temperature for

which the sample has traversed the maximum in the salt curve, in each case, the three remaining data points for 1.00% and 1.25% salt are linear with high  $R^2$ . The estimated “scission energies” for all salt concentrations are then plotted as open circles in Fig 4.8b. These free energies presumably represent a combination of free energies of scission and free energies of branch point formation. For salt concentrations up to 1.00%, the free energy is presumably dominated by scission, but for higher salt concentration it represents predominantly branch point formation. Thus, the decrease of the free energy observed on increasing salt concentration from 1.00% to 1.25% NaCl is presumably due to the switch from predominant influence of micelle breakage to formation of branch points. As the salt concentration increases, we expect the free energy cost for breaking a micelle to increase, consistent with what we see on the left side Fig 4.8b for salt concentrations of 1.00% or lower. With increasing salt, the free energy for micelle breakage should continue to increase, but no longer dominates the rheology, which is more affected by branch formation, and its free energy, which is expected to decrease with increasing salt concentration, giving rise to the maximum in the free energy plotted as circles in Fig 4.8b.

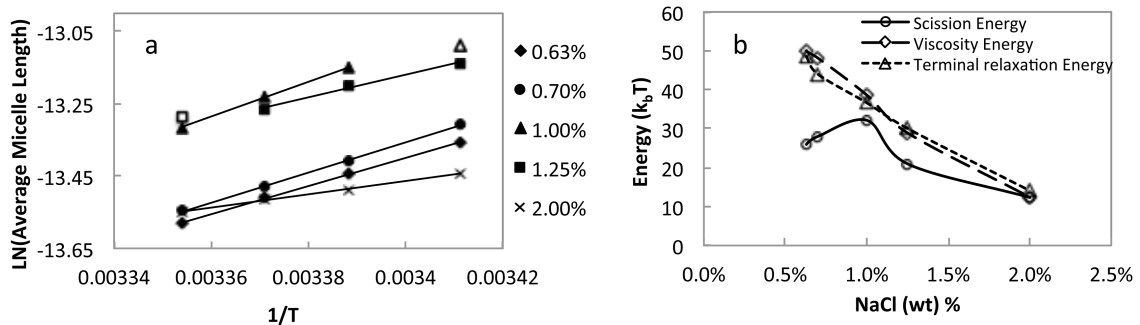


**Figure 4.8** a). Boltzmann behavior of average micelle length vs.  $1/T$  at various salt concentrations for BW-1EO. The open square and open triangle are excluded from calculations of free energy as explained in the text. b) Scission/branch formation free energy, viscosity activation energy, and terminal relaxation time activation energy from Arrhenius laws converge at high salt concentrations. The lines connecting the symbols are guides to the eye.

The viscosity and terminal relaxation time activation energies from equation (16) are also plotted in Fig 4.8b. Not surprisingly, the activation energies for viscosity and relaxation time are nearly the same over the whole range of salt concentration. Interestingly these activation energies decrease with increasing salt concentration and converge to the free energy for branch formation at 2.00% salt in the branch-dominant region. The reason for the decrease in activation energies and the significance, if any, of the convergence to the value of the free energy for branch formation at high salt, is not clear.

#### **4.4.2.2 Comparison of Micellar Properties of BW-1EO and BW-3EO**

BW-1EO, which as noted earlier has surfactants with shorter EOs, is more sensitive to the addition of salt and has longer micelles and higher scission energies than BW-3EO, as shown in Fig 4.9. On addition of salt, the properties of BW-1EO can be tuned while the properties of BW-3EO are less sensitive to salt concentration. The viscosity of BW-1EO at 0.70% NaCl is similar to that BW-3EO at 2.13%, although 0.70% BW-1EO has longer micelles and higher scission energy than BW-3EO at 2.13% NaCl.

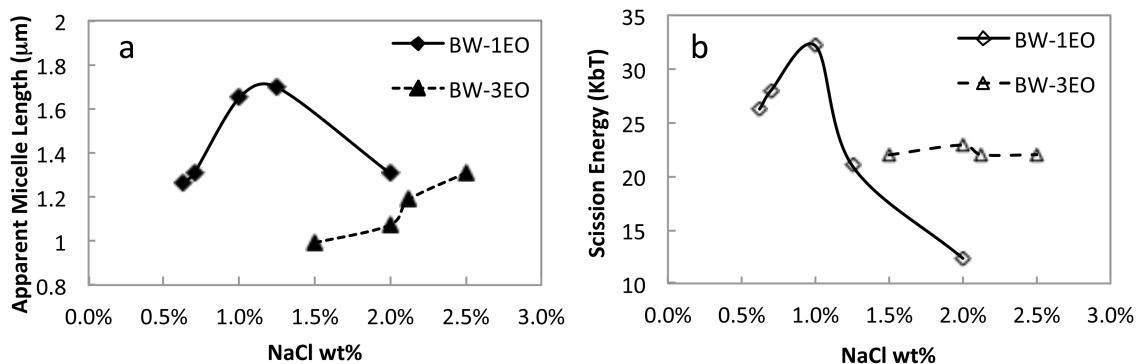


**Figure 4.9** Comparison of average micelle length (filled symbols) (a) and scission energy (open symbols) (b) for BW-1EO (diamonds) and formular BW-3EO (triangles). The lines connecting the symbols are guides to the eye.

#### 4.4.3 Salt Effects on Rheological Properties and Surfactant Packing at Molecular Scale using DPD Modeling

Surfactant packing at the molecular scale determines the micellar-scale properties, and, through this, the rheological properties at the macroscopic scale. Here we investigate surfactant packing through DPD simulations of preassembled periodic cylindrical micelles at various concentrations of surfactant, salt, and PRMs. The snapshot of one periodic cylindrical micelle at equilibrium is shown in Fig 4.2. Figs. 4.10a-c compares the bead number density distribution of surfactant tail, head and water within a shell at the radial distance with respect to the core of the cylindrical micelles for 11.0% BW-1EO at concentrations of NaCl ranging from 0.70% to 1.75%, for surfactant concentrations ranging from 8.0 to 11.0% at 0.70% NaCl, and for 11.0% surfactant concentration of BW-1EO and BW-3EO. Fig 4.10d shows the corresponding surfactant packing distances.



Salts screen the electrostatic repulsions between the surfactant charged head groups, reduce the surfactant head group surface area  $a_0$ , while keeping  $l_c$  and  $V$  constant, and thereby increase the packing parameter  $p$ , resulting in longer micelles and higher viscosity and elasticity. The decreased surface area per surfactant is revealed in the decreased packing distance at higher salt concentration in Fig 4.10d. Nevertheless, the RDF of surfactants with respect to the core of the micelles remains nearly constant with increased salt, as shown in Fig 4.10a, although at a high salt concentration of 1.75%, where branch formation is dominant, slight outward shifts of the RDFs are observed.

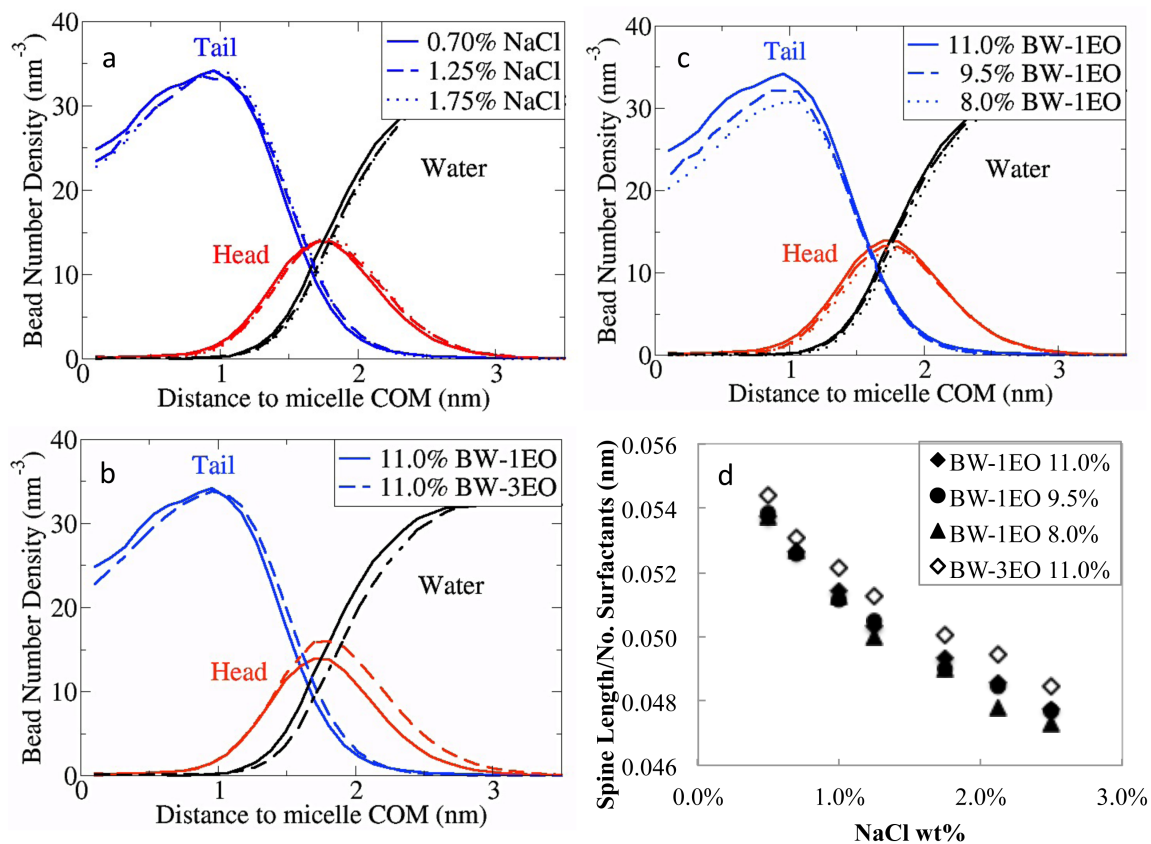


**Figure 4.10** Bead number density distribution of head, tail, and water within a shell at the radial distance with respect to the core of the cylindrical micelles a) for solutions

containing 11% BW-1EO at salt concentrations spanning the peak of the salt curve; b) for 11.0% BW-1EO at 0.70% NaCl and 11.0% BW-3EO at 2.13% NaCl, which have the same experimental viscosity of 11.0 Pas; and c) for BW-1EO solutions of three different surfactant concentrations at 0.7% NaCl. d) Surfactant packing distance defined as the ratio of the micelle spine length to the number of surfactants in the micelle in all of the above systems.

As shown in Fig 4.10b, BW-3EO, which has surfactants with longer EOs and has a thicker head layer than does BW-1EO. The thicker EO layer is less sensitive to the addition of salts and leads to slower viscoelasticity changes on addition of salt. The longer EOs in BW-3EO has two effects on surfactant packing: it leads to a greater packing distance due to bulkier head groups; it also lead to a decrease of the packing distance due to the increases of the cross-section radius of tails and heads as shown in Fig 4.10b. The net effect of the two leads to longer surfactant packing distances within BW-3EO as shown in Fig 4.10d. This indicates more space in the core of the micelles in BW-3EO than in BW-1EO due to the increase of the packing distance and the cross-section radius of the tail beads. The shift in the radial distribution is only about 1 Angstrom, however, and would be difficult to quantify experimentally, even though it may be enough to produce differences in rheological properties. This illustrates the importance of supplementing experimental characterization of micellar solutions with simulation data.

These DPD results are thus consistent with traditional packing arguments and with rheological measurements, as interpreted by the Cates micellar model. Although not compared to rheological measurements, DPD simulations of 11.0%, 9.5% and 8.0% BW-1EO at 0.70% NaCl, show that a lower concentration of surfactants produces slightly

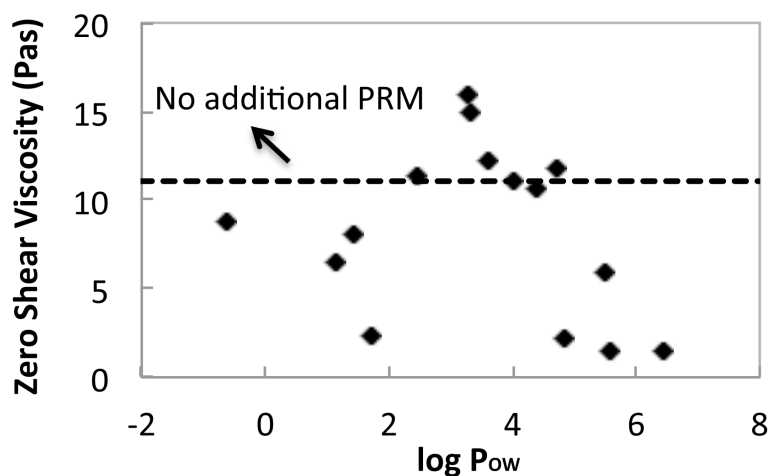
larger RDFs and slightly smaller packing distances due to the increase of the cross section radius, as shown in Fig 4.10c.

## **4.5. Results and Discussion. II. PRM Effects**

### **4.5.1 PRM Effects on Viscosity for BW-1EO Correlated With $\log P_{ow}$**

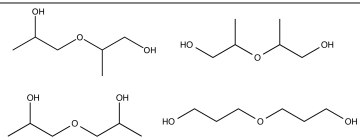
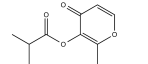
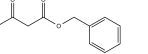
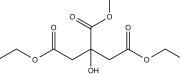
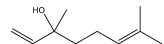
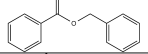
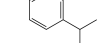
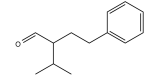
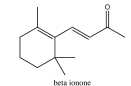
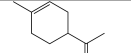
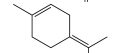
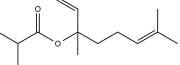
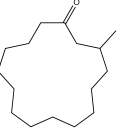
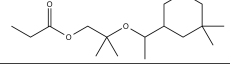
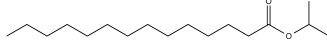
Here we characterize PRMs by their  $\log P_{ow}$  values and their chemical structures.<sup>63</sup> Fig 4.11 plots the zero shear viscosities of BW-1EO upon addition of each of 15 PRMs at a concentration of 15 mM vs. the  $\log P_{ow}$  of those PRMs. The dashed line is the reference viscosity of BW-1EO without the additional PRM, but containing ACCORD, which is a mixture of six PRMs. Table 4.2 lists the names of the additional PRMs, values of their  $\log P_{ow}$ , chemical structures, and the resulting viscosities plotted in Fig 4.11. Spanning a broad distribution of  $\log P_{ow}$  values from -0.61 to 6.44, the plot shows a local maximum in the vicinity of  $\log P_{ow}$  around 2-4, similar to Fischer's report of an envelop shape of equivalent radius of micelle vs.  $\log P_{ow}$  for 22 PRMs, where the increases of micellar radius suggest a viscosity increase.<sup>63</sup> PRMs of very low or very high values of  $\log P_{ow}$  reduce the viscosity significantly, and PRMs having intermediate values of  $\log P_{ow}$  modify the viscosity only slightly, among which only a few PRMs increase the viscosity. The PRMs having a value of  $\log P_{ow}$  between 1 and 2 are methyl isobutyrate, benzyl acetoacetate, and triethyl citrate, among which triethyl citrate has the least compact structure and reduces the viscosity the most, possibly due to a sharp increase of surfactant head group surface area when it enters the micelle. The other two PRMs in this range of  $\log P_{ow}$  have relatively more compact structures and fewer branches and reduce the

viscosity only moderately. Among the eight PRMs of higher value of  $\log P_{ow}$  between 2 to 5, are linalool, d-limonene, terpinolene, and cumene, among which the latter three have very similar structures. The highly branched terpene alcohol linalool, and structural isomers d-limonene and terpinolene, modify the viscoelastic properties insignificantly based on viscosity and rheological measurements. On the other hand, cumene has a benzene ring in a planar structure and increases the viscosity by around 40%. For PRMs with  $\log P_{ow}$  above 4.7 and having bulky and/or long structures, the viscosity is reduced significantly possibly due to the penetration of PRMs into the core of the cylindrical micelle, resulted in a greatly increase of the cross-section radius, and reducing the scission energy enormously.



**Figure 4.11** Viscosities of BW-1EO on addition of 15 PRMs at 15 mM plotted against  $\log P_{ow}$ , of the PRM. The dashed line shows the viscosity of BW-1EO without any additional PRM beyond the six ACCORD components. Some data, if not available at 15 mM, are computed from the best linear or polynomial fit of the viscosities of BW-1EO vs. PRMs at different concentrations.

**Table 4.2.** 15 PRMs added separately to BW-1EO at 15 mM. The corresponding values of  $\log P_{ow}$ , the molecular structures, and resulting zero-shear viscosities (in Pas) are tabulated. Some data, if not available at 15 mM, are computed from the best linear or polynomial fit of the viscosities of BW-1EO vs. PRMs at different concentrations.

Name of PRMs	LogPow	Structures	Viscosity
No PRM			11.06
Dipropylene Glycol	-0.61		8.72
Maltyl isobutyrate	1.16		6.44
Benzyl acetoacetate	1.43		7.99
Triethyl citrate	1.73		2.33
Linalool	2.44		11.41
Benzyl benzoate	3.29		15.87
Cumene	3.30		14.95
Florhydral	3.59		12.20
beta-Ionone	4.02		11.04
d-Limonene	4.38		10.62
Terpinolene	4.71		11.84
Linalyl isobutyrate	4.82		2.22
Muscone	5.48		5.86
Helvetolide	5.56		1.43
Isopropyl myristate	6.44		1.41

## 4.5.2 PRM Effects on Micellar Properties Based on the Cates Model

To understand the relationships between viscoelastic properties and micellar structures, we choose four PRMs among the 15 for detailed study. In addition, we add linalool to BW-3EO for examination of the effect EO length on micellar properties.

### 4.5.2.1 Comparison of the Effects of PRMs, Dipropylene Glycol, Linalool, Cumene, and Isopropyl Myristate on Rheological and Micellar Properties of BW-1EO

The structures of the four PRMs spanning a broad range of  $\log P_{ow}$  from -0.61 (for DPG) to 6.44 (for IPM) are shown in Scheme 1. The viscosities as a function of concentration of each of these four PRMs added to BW-1EO are shown in Fig 4.12a. As can be seen, DPG with the lowest value of  $\log P_{ow}$  decreases the viscosity of BW-1EO roughly linearly; linalool with a moderately low value of  $\log P_{ow}$  reduces the viscosity only marginally; cumene with a higher value of  $\log P_{ow}$  increases the viscosity; and IPM with the highest value of  $\log P_{ow}$  reduces viscosity rapidly.

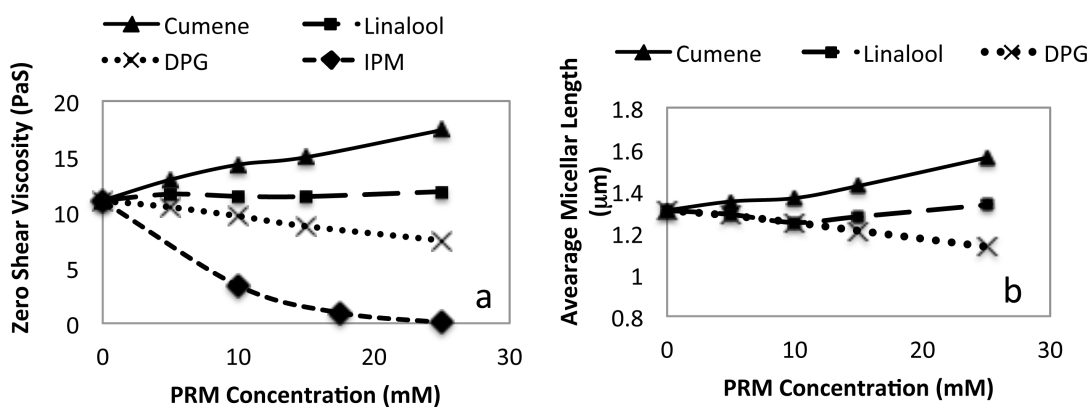


**Figure 4.12** a) Dependence of viscosity on concentration of dipropylene glycol (DPG), cumene, linalool, and isopropyl myristate (IPM) in BW-1EO containing ACCORD. b). Average micelle length vs. PRM concentration, computed from the Cates model. The

average micelle length of IPM is too short to be modeled. The lines connecting the symbols are guides to the eye.

We fit the Cates model, using the equations in Section 2.2.2 to the rheological data to obtain micelle lengths shown in Fig 4.12b. Since DPG has an extremely low value of  $\log P_{ow}$ , the average micelle length decreases slowly with added PRM. Other micellar characteristic lengths and time constants, including mesh size and entanglement length, breakage time, and plateau modulus remain nearly constant (data not shown), possibly due to the weak partitioning of DPG into the micelles, leading to at most minor changes in the micelle structures. For linalool and cumene with intermediate values of  $\log P_{ow}$ , the average micelle lengths remain nearly constant or increase slightly. Other micellar characteristic length and time constants, including mesh size and entanglement length, as well as breakage time, decrease. The plateau modulus remains nearly constant with added cumene, while with added linalool it increases monotonically. In the following, we compare the rheological properties upon linalool addition to BW-1EO and BW-3EO. Linalool is chosen since its effects have been modeled before<sup>63,64</sup> and the changes of the micellar properties, except for the average micelle length and viscosity, are monotonic.

#### **4.5.2.2 Effect of Linalool Rheology of BW-1EO and BW-3EO**

Adding the same amount of linalool to BW-1EO and BW-3EO results in very different changes in viscoelastic properties as shown in Fig 4.13. The addition of linalool modifies the viscosity of BW-1EO only slightly, as shown by the near overlap of loss moduli at low frequency in Fig 4.13a. On the other hand, addition of linalool to BW-3EO decreases

the viscosity significantly, as shown by the monotonic downward shift of loss moduli Fig 4.13a'. Although the viscosities of BW-1EO are almost constant, storage modulus does shifts monotonically over all frequencies, and the loss modulus shifts monotonically at high frequencies. The magnitude of the modulus shifts in BW-3EO is considerably higher than for BW-1EO. Elasticities decrease in Fig 4.13a and increases in 14a'. The plateau moduli, which are proportional to the diameters of the semi-circles in 14b and 14b', increase monotonically with added linalool. The Cole-Cole plot normalized with respect to the  $G_{maximum}''$  shows significant changes in shape and therefore in relaxation regimes for micelles in BW-1EO in 14c but not for micelles in BW-3EO formulation in 14c'.



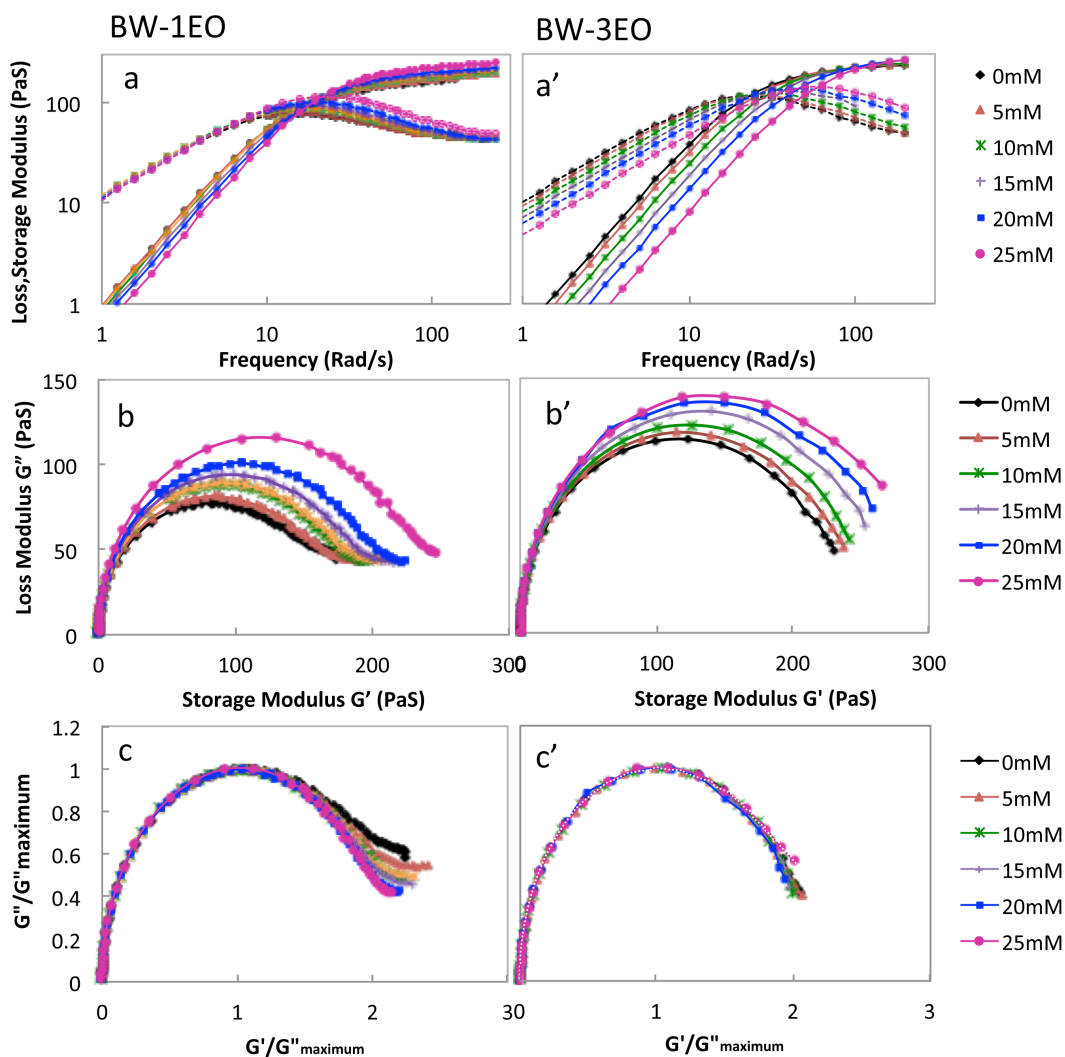


**Figure 4.13** (a) Loss (dashed lines) and storage modulus (solid lines) vs. frequency, (b) Cole-Cole plot, and (c) normalized Cole-Cole plot at various linalool concentrations in BW-1EO; and the same in BW-3EO are presented in a'), b') and c').

Next we quantify the micellar characteristic times and length constants by fitting the Cates model to rheological data as described in Sections 2.2.1 and 2.2.2 (data are not shown). BW-1EO shows nearly constant viscosity and increasing elasticity as the concentration of linalool increases. The changes in estimated average micelle length

(shown in Fig 4.12b) and reptation time are slight and consistent with the changes in viscosity. The micellar mesh size and entanglement length decrease monotonically but slightly. The breakage time decreases significantly and is related to the decrease of elasticity. Addition of linalool to BW-3EO reduces the viscosity and increases the elasticity significantly. The estimated average micelle length, mesh size, entanglement length, reptation time, and breakage time all decrease monotonically and more significantly than in BW-1EO (data not shown).

We find that a plot of  $\tan\delta$  against the ratio of breakage time to reptation time squared is linear at various temperatures and concentrations of linalool in BW-3EO as shown in Fig 4.14, if we exclude two data points of 25 mM linalool at 25.0 °C ( $\tau_{br}/\tau_{rep}^2=34.4$ ,  $\tan\delta=0.9$ , data not shown) and 22.5 °C (open square). The two points have very low viscosities that cannot be modeled well enough to give accurate breakage time estimates. The linear relationship between  $\tan\delta$  and the ratio of breakage time to the reptation time of the power law exponent 3 were found upon addition of several PRMs to BW-1EO when viscosity changes are linear on addition of PRM. The slopes of the linear fitting depend on the particular PRM.

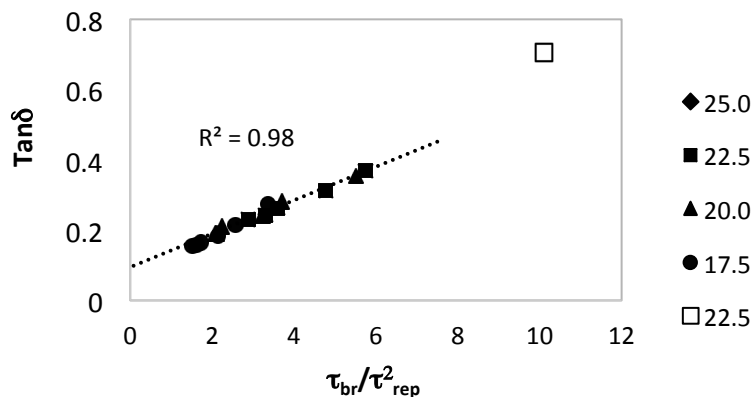


**Figure 4.14** Plot of  $\tan\delta$  (at 100 rad/s) vs. ratio of breakage time to reptation time squared at various temperatures and concentrations of linalool in BW-3EO.

Changes in micellar properties upon addition of four different PRMs to BW-1EO, and addition of linalool to BW-3EO, presumably result from different PRM partitioning within the micelles. Next we relate the viscoelastic properties to micellar properties, and to molecular-scale surfactant packing using DPD modeling.

### 4.5.3 PRM Effects on Surfactant Packing Using DPD Simulations

#### 4.5.3.1 Addition of Dipropylene Glycol, Linalool, Cumene, and Isopropyl Myristate to BW-1EO

To further study the relationship between surfactant packing and rheological properties, we carried out DPD simulations of 11% BW-1EO in the presence of the four PRMs with a broad distribution of  $\log P_{ow}$ . Fig 4.15 shows the zero shear viscosities (colored filled diamonds) and surfactant packing distances (colored open triangles) upon addition of 15 mM PRM to BW-1EO vs. their values of  $\log P_{ow}$ .

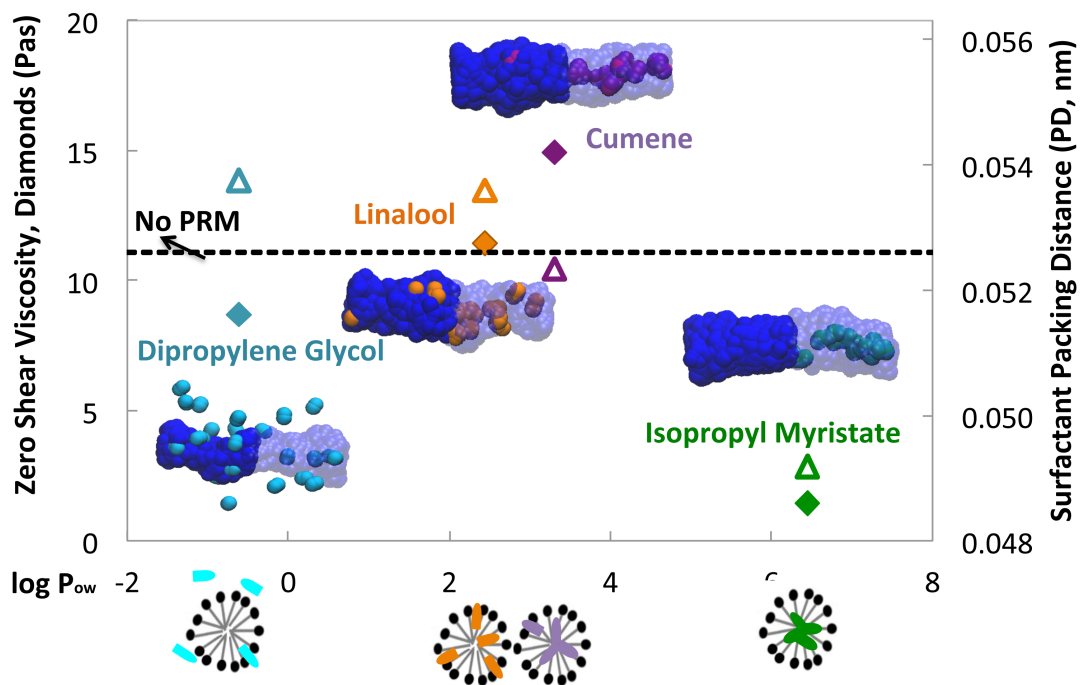


**Figure 4.15** Plot of zero shear viscosity (colored filled diamonds) and surfactant packing distances (colored open triangles) for BW-1EO upon addition of 15 mM dipropylene glycol (DPG), cumene, linalool, and isopropyl myristate (IPM) vs. their  $\log P_{ow}$ . The dashed line is the viscosity (left y-axis) and surfactant packing distance (right y-axis) of BW-1EO in the absence of PRM. Each of the four PRMs is given a color used consistently in symbols and text, as well as in the PRM molecules contained in snapshots of 15 nm slices of the periodic cylindrical micelles. The snapshots of cylindrical periodic micelles show the tail beads in blue and PRM beads in their respective colors. On the right side of each micelle, the blue tail beads are rendered translucent to show the positioning of PRMs within the micelles. Head and water beads are omitted for clarity. The schematic cartoons below the y-axis show the location of the PRMs (colored bulletin) in the cross section of the cylindrical micelles at the corresponding  $\log P_{ow}$  range.

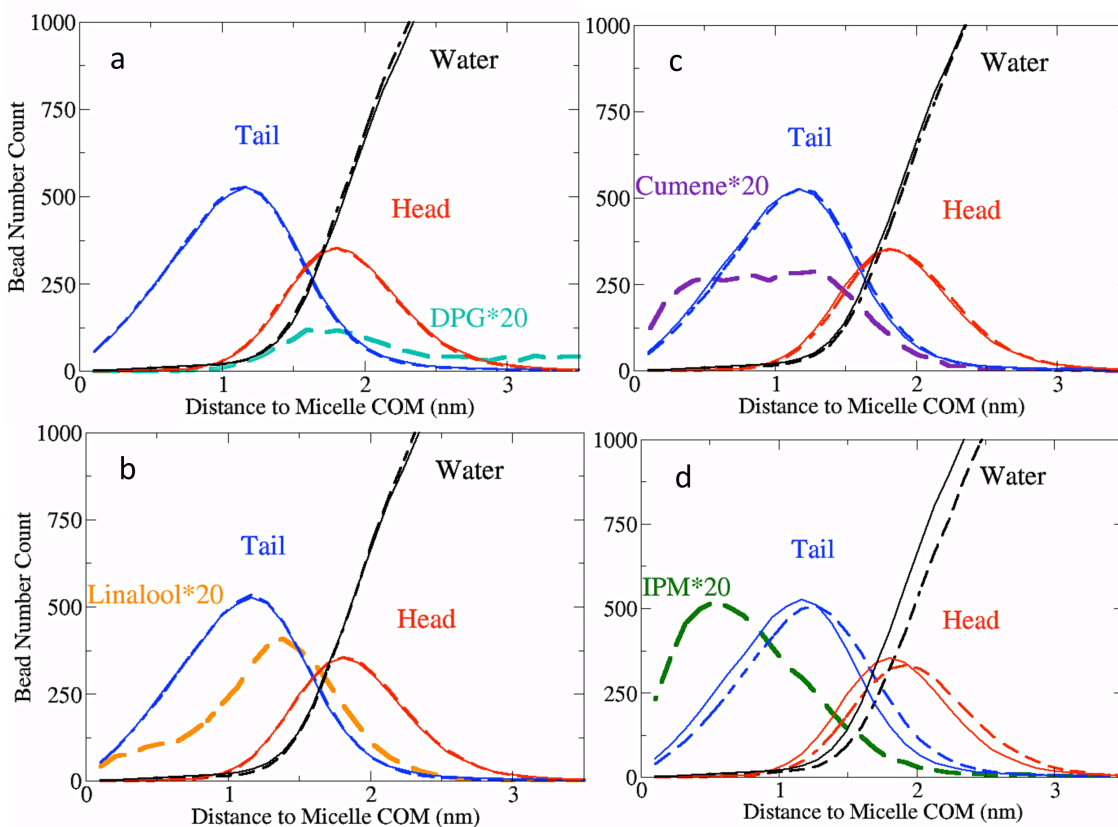


**Figure 4.16** Bead number count of tail, head, water and an additional PRM, namely a). DPG, b). linalool, c). cumene, and d). IPM within a shell of 1.3 nm width at a radial distance with respect to the core of the cylindrical micelles. The dashed lines represent distribution of BW-1EO in the presence of 15 mM of the added PRM and the solid lines represent the RDFs in the absence of the added PRM. In all solutions, with or without the single added PRM, the six ACCORD PRMs were present.

We expect dipropylene glycol (DPG) with its extremely low value of  $\log P_{ow}$  to partition mainly into water and to some extent into the surfactant head group region, as is in fact seen in the first cartoon below the y-axis and the left snapshot in Fig 4.15. This is consistent also with the corresponding bead number distribution in Fig 4.16. The near-perfect overlap of tail, head, and water distribution with those in the absence of DPG

indicates that the partitioning of DPG does not modify the radius of the cylindrical micelle cross section, and that there is some geometric crowding within the head group region produced by the DPG. This is consistent with the minor modification of the micellar characteristic lengths and times calculated for this PRM (see Fig 4.12b, for example). In principle, the partition of DPG into the head group region should increase the surfactant head group surface area  $a_0$ . At constant surfactant tail length  $l_c$  and tail volume  $V$ , the increase of  $a_0$  leads to a decrease of packing parameter  $p$ , shorter micelles, and a lower zero shear viscosity (as shown by the filled cyan diamond in Fig 4.15, and in Fig 4.12). Due to increase of  $a_0$  and constant tail parameters, the surfactant packing distance increases (open cyan triangle). The bulkier PRMs with low value  $\log P_{ow}$  reduce the viscosity further through greater increases in  $a_0$  (Fig 4.11).

Linalool, with a moderate value of  $\log P_{ow}$  partitions in both the tail region and in the interface between the surfactant tail and the head group region as shown in the second cartoon below the y-axis and the snapshot having orange beads of linalool in Fig 4.15. Addition of linalool leads to near overlaps of the distributions of tail, head, and water distribution with those in the absence of linalool as shown in Fig. 4.16. This indicates a constant micelle radius and  $l$ . However, the highly branched linalool partitions in both the tail region and the interface between the tail and head group regions, and results in increased packing distances and increased  $V$  and  $a_0$ . Interestingly, the changes of  $V$  and  $a_0$  are cancelled out on the effects of packing parameter  $p$ . This leads to no significant change in viscosity and micelle length. The partition of linalool into both the

tail and head group regions modifies the micellar breakage time, and results in an increased elasticity.

Cumene, with a moderately high  $\log P_{ow}$ , partitions mainly within the surfactant tail region in the micelle core, while only a small amount enters the interface between tail and head groups as shown in the third cartoon below the y-axis. This is consistent with the snapshots showing many fewer purple dots than orange linalool dots in the micelle images in Fig 4.15. Due to geometric constraints within the tightly packed surfactant tail region, the planar structure of linalool, despite its small size, pushes surfactants radially outward and pushes tails away. As shown in Fig. 4.16, the nearly perfect overlaps of the distributions of tail, head, and water distribution with those in the absence of cumene indicates the effects of pushing surfactant radially outward is minor and the micelle radius is constant. However, the packing distance decreases. This suggests the planar structure of cumene both pushes tails away and condenses head groups so that the micelle radius has no significant net change. Thus cumene decreases  $a_0$  and increases  $p$ . This leads to longer micelles and higher viscosity. Due to the partitioning of cumene within the micelle, elasticity is modified as well.

IPM has a very high  $\log P_{ow}$ , and therefore partitions predominantly within the surfactant tail region as shown in the last cartoon below the y-axis. Although the molecule is large in size, it buries itself almost completely within the tail region. This pushes surfactants outward radially. Although it is unclear from this information alone how the simultaneous modifications to  $a_0$ ,  $l_c$ , and  $V$  might affect the packing parameter  $p$ , DPD simulations at a higher concentration of 100 mM IPM, show that the periodic

cylindrical micelles start to break into rodlike micelles, which suggests a significant decrease in the packing parameter  $p$  and shortening of the micelles.

#### 4.5.3.2 Linalool Addition to BW-1EO and BW-3EO

In contrast to the changes in RDFs upon linalool addition to BW-1EO, addition of linalool to BW-3EO increases the radius of the micelle slightly but does not change the surfactant packing distance (data not shown). The tail region within micelles of BW-3EO is larger than that of BW-1EO (Fig 4.10b), and this geometrically should favor the partition of linalool into the core area in addition to partitioning to the interface between heads and tails as shown in Fig 4.1. More linalool in BW-3EO than in BW-1EO enters the core of the micelle and pushes surfactants radial outward slightly. Interestingly, this does not shorten the micellar packing distance (data not shown), which can only be realized by increasing the surfactant surface area  $a_0$ . The partitioning of linalool into the core of BW-3EO micelles leads to a decrease in packing parameter  $p$ , shorter micelles, and lower viscosity in contrast to its more negligible effect on BW-1EO.

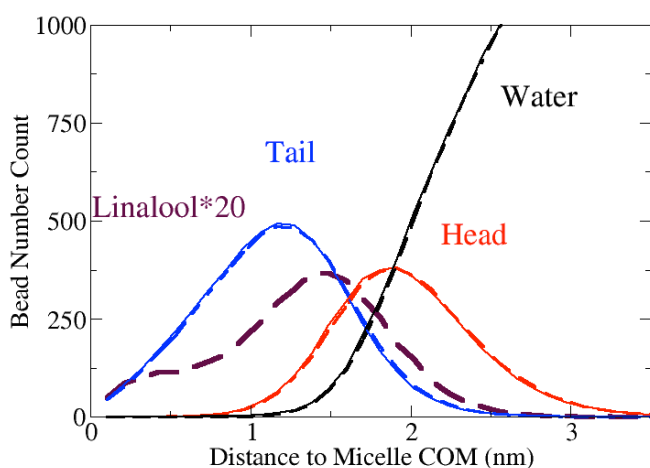




**Figure 4.17** Comparison of the bead number count within a shell at a radial distance from the center of a periodic cylindrical micelle of BW-3EO containing 1% ACCORD in the presence (dashed line) and in the absence (solid line) of 15 mM linalool.

In short, we find that PRMs having a very low or a very high  $\log P_{ow}$  reduce the viscosity significantly. PRMs with low values of  $\log P_{ow}$  mainly partition within the head group region of the micelle, increase the head group surface area  $a_0$  at constant micellar radius, decrease the packing parameter  $p$  and result in shorter micelles and lower viscosity. PRMs with higher  $\log P_{ow}$  mainly partition within the core of the micelle, pushing surfactant radial outwards and favoring shorter micelles. PRMs with medium  $\log P_{ow}$  values either do not change the viscosity of the solutions much or at most increase the viscosity slightly. Partitioning of PRMs into micelles especially in the tail region modifies the elasticity of the micelle significantly. Partitioning of PRMs depends on the compositions of the surfactant solutions as well as on the PRM.

#### **4.6. Conclusions and Future Work**

We have combined rheology and multiscale modeling, to connect macroscopic viscoelastic properties to surfactant packing structures at the molecular scale. Specifically, we studied the rheological property changes in two modeled body wash formulations, namely BW-1EO and BW-3EO, upon addition of salts and PRMs at various concentrations and temperatures. We computed the corresponding micellar properties by applying the Cates model, and determined the surfactant packing structure at the molecular scale using DPD simulations and traditional packing arguments.

Upon addition of salt to a body wash the viscosity at first increases, reaches a maximum, and then decreases, forming the so-called “salt curve.” At the molecular scale, counterions from salts condense at the charged surface of the cylindrical micelle, screen the electrostatic repulsion between the surfactant head groups, reduce both the surfactant surface area  $a_0$  and surfactant packing distances. If the radius of the cylindrical micelle remains constant, this results in higher packing parameter  $p$  and longer micelles, and shorter micellar breakage time, all of which we infer quantitatively from application of the Cates model to linear viscoelastic data. The viscosity is most closely connected to the average micelle length, and elasticity to the ratio of micellar breakage time and the reptation time, where “elasticity” here refers to the high frequency ratio of storage modulus  $G'$  to loss modulus  $G''$ .

PRMs modify the viscoelastic properties of body washes by partitioning within the micelles at different locations according to their values of  $\log P_{ow}$  and their chemical structures. Dipropylene glycol (DPG), with a low value of  $\log P_{ow}$ , partitions to the interface of surfactant head groups and the water phase, increases surfactant head group surface area  $a_0$ , maintains constant radius of the cylindrical micelles, increases surfactant packing distances, reduces packing parameter  $p$ , and results in shorter micelles and lower viscosity. Linalool, with a moderate value of  $\log P_{ow}$ , partitions both into the surfactant tail region and the interface between the surfactant head and tail regions, maintains the same radius of the cylindrical micelles and surfactant packing distance apparently due to its relatively small size, leading to little change in the viscosity and an increase of the elasticity due to its partitioning into the micelles. Cumene, with a moderately high value

of  $\log P_{ow}$ , partitions mainly in the surfactant tail region, pushes surfactants radial outward slightly, reduces the surfactant packing distance apparently due to its planar structure which condenses surfactants, lowers  $a_0$  and increases  $P$ , and results in longer micelles, and higher viscosity and elasticity. Isopropyl myristate (IPM), with a very higher value of  $\log P_{ow}$ , partitions within the core of the cylindrical micelles and pushes surfactant out, leading to shorter micelles at high IPM concentration. The rheological responses of addition of the same PRM (linalool) to two different formulations are different due to the different packing of the surfactants within the two formulations.

In summary, multiscale modeling and rheological measurements were used to determine the structure-property relationships of surfactant formulations. Consistent results were obtained at different length scales, from molecular, to micellar, to bulk rheological. The methods used here can be applied to other complex fluids to determine structure-property relationships. The development of molecular parameters for more complex PRMs, for use in DPD and molecular dynamics simulations are needed, and application of similar methods to determine the synergistic effects of two or more PRMs are also needed. Experimental measurement of the persistence length and radius of the micelle, and applying rheometry or diffusive wave spectrometry at higher frequencies will improve the accuracy and usefulness of the modeling.

#### **4.7. References:**

- (1) Cates, M. E.; Fielding, S. M. Rheology of Giant Micelles. In *Advances in Physics*; 2006; pp. 799–879.

- (2) Zana, R.; Kaler, E. W. *Giant Micelles: Properties and Applications*; v140 ed.; CRC Press: Surfactant Science Series, 2007.
- (3) Rehage, H.; Hoffmann, H. Rheological Properties of Viscoelastic Surfactant Systems. *J. Phys. Chem.* **1988**, *92*, 4712–4719.
- (4) Rhein, L. D. ; Schlossman, M.; O’Lenick, A.; Somasundaran, P. . *Surfactants in Personal Care Products and Decorative Cosmetics*; Third.; CRC Press: Surfactant Science Series, 2006; Vol. 40.
- (5) Kralova, I.; Sjoblom, J. Surfactants Used in Food Industry : A Review. *J. Dispers. Sci. Technol.* **2009**, *30*, 1363–1383.
- (6) Maitland, G. . Oil and Gas Production. *Curr. Opin. Colloid Interface Sci.* **2000**, *5*, 301–311.
- (7) Lawrence, M. J. Surfactant Systems: Their Use in Drug Delivery. *Chem. Soc. Rev.* **1994**.
- (8) Imae, T.; Kamiya, R.; Ikeda, S. Formation of Spherical and Rod-like Micelles of Cetyltrimethylammonium Bromide in Aqueous NaBr Solutions. *J. Colloid Interface Sci.* **1985**, *108*, 215–225.
- (9) Imae, T.; Ikeda, S. Characteristics of Rodlike Micelles of Cetyltrimethylammonium Chloride in Aqueous NaCl Solutions : Their Flexibility and the Scaling Laws in Dilute and Semidilute Regimes. **1987**, *1098*, 1090–1098.
- (10) Kern, F.; Zana, R.; Candau, S. J. Rheological Properties of Semidilute and Concentrated Aqueous Solutions of Cetyltrimethylammonium Chloride in the Presence of Sodium Salicylate and Sodium Chloride. *Langmuir* **1991**, *7*, 1344–1351.
- (11) Khatory, A.; Lequeux, F.; Kern, F.; Candau, S. J. Linear and Nonlinear Viscoelasticity of Semidilute Solutions of Wormlike Micelles at High Salt Content. *Langmuir* **1993**, *9*, 1456–1464.
- (12) Candau, S. J.; Hirsch, E.; Zana, R.; Delsanti, M. Rheological Properties of Semidilute and Concentrated Aqueous Solutions of Cetyltrimethylammonium Bromide in the Presence of Potassium Bromide. *Langmuir* **1989**, *5*, 1225–1229.
- (13) Cates, M. E.; Candau, S. J. Statics and Dynamics of Worm-like Surfactant Micelles. *J. Phys. Condens. Matter* **1990**, *2*, 6869–6892.
- (14) Cappelaere, E.; Cressely, R.; Makhoulfi, R.; Decruppe, J. P. Temperature and Flow-Induced Viscosity Transitions for CTAB Surfactant Solutions. *Rheol. Acta* **1994**, *437*, 431–437.

- (15) Wheeler, E. K.; Izu, P.; Fuller, G. G. Structure and Rheology of Wormlike Micelles. *Rheol. Acta* **1996**, *35*, 139–149.
- (16) Croce, V.; Cosgrove, T.; Maitland, G.; Hughes, T.; Karlsson, G. Rheology, Cryogenic Transmission Electron Spectroscopy, and Small-Angle Neutron Scattering of Highly Viscoelastic Wormlike Micellar Solutions. *Langmuir* **2003**, *19*, 8536–8541.
- (17) Nettesheim, F.; Wagner, N. J. Fast Dynamics of Wormlike Micellar Solutions. *Langmuir* **2007**, *23*, 5267–5269.
- (18) Oelschlaeger, C.; Waton, G.; Candau, S. J. Rheological Behavior of Locally Cylindrical Micelles in Relation to Their Overall Morphology. *Langmuir* **2003**, *19*, 10495–10500.
- (19) Larson, R. G. *The Structure and Rheology of Complex Fluids*; Oxford University Press, New York, USA, 1999; pp. 551–593.
- (20) Kodama, M.; Kubota, Y.; Miura, M. The Second CMC of the Aqueous Solution of Sodium Dodecyl Sulfate. III. Light-Scattering. *Bull. Chem. Soc. Jpn.* **1972**, *45*, 2953–2955.
- (21) Ma, C.; Li, G.; Xu, Y.; Wang, H.; Ye, X. Determination of the First and Second CMCs of Surfactants by Adsorptive Voltammetry. *Colloids Surfaces A Physicochem. Eng. Asp.* **1998**, *143*, 89–94.
- (22) Yasunaga, T.; Oguri, H.; Miura, M. Acoustic Study on the Kinetics for the Dissociation-Recombination Reaction between Micelle and Counterion in Sodium Dodecyl Sulfate Solution. *J. Colloid Interface Sci.* **1967**, *23*, 352–357.
- (23) Scamehorn, J. F. An Overview of Phenomena Involving Surfactant Mixtures. In *Phenomena in Mixed Surfactant Systems*; 1986; Vol. 311, pp. 1–27.
- (24) Acharya, D. P.; Sato, T.; Kaneko, M.; Singh, Y.; Kunieda, H. Effect of Added Poly(oxyethylene)dodecyl Ether on the Phase and Rheological Behavior of Wormlike Micelles in Aqueous SDS Solutions. *J. Phys. Chem. B* **2006**, *110*, 754–760.
- (25) Sarmiento-Gomez, E.; Lopez-Diaz, D.; Castillo, R. Microrheology and Characteristic Lengths in Wormlike Micelles Made of a Zwitterionic Surfactant and SDS in Brine. *J. Phys. Chem. B* **2010**, *114*, 12193–12202.
- (26) Galvan-Miyoshi, J.; Delgado, J.; Castillo, R. Diffusing Wave Spectroscopy in Maxwellian Fluids. *Eur. Phys. J. E. Soft Matter* **2008**, *26*, 369–377.
- (27) Danov, K. D.; Kralchevska, S. D.; Kralchevsky, P. A.; Ananthapadmanabhan, K. P.; Lips, A. Mixed Solutions of Anionic and Zwitterionic Surfactant ( Betaine ): Surface-Tension Isotherms , Adsorption , and Relaxation Kinetics. *Langmuir* **2004**, *20*, 5445–5453.

- (28) Hines, J. D.; Thomas, R. K.; Garrett, P. R.; Rennie, G. K.; Penfold, J. Investigation of Mixing in Binary Surfactant Solutions by Surface Tension and Neutron Reflection: Anionic/Nonionic and Zwitterionic/Nonionic Mixtures. *J. Phys. Chem. B* **1998**, *102*, 8834–8846.
- (29) Christov, N. C.; Denkov, N. D.; Kralchevsky, P. A.; Ananthapadmanabhan, K. P.; Lips, A. Synergistic Sphere-to-Rod Micelle Transition in Mixed Solutions of Sodium Dodecyl Sulfate and Cocoamidopropyl Betaine. *Langmuir* **2004**, *20*, 565–571.
- (30) Eguchi, K.; Kaneda, I.; Hiwatari, Y.; Masunaga, H.; Sakurai, K. Salt-Concentration Dependence of the Structure and Form Factors for the Wormlike Micelle Made from a Dual Surfactant in Aqueous Solutions. *J. Appl. Crystallogr.* **2007**, *40*, s264–s268.
- (31) Naruse, K.; Eguchi, K.; Akiba, I.; Sakurai, K.; Masunaga, H.; Ogawa, H.; Fossey, J. S. Flexibility and Cross-Sectional Structure of an Anionic Dual-Surfactant Wormlike Micelle Explored with Small-Angle X-Ray Scattering Coupled with Contrast Variation Technique. *J. Phys. Chem. B* **2009**, *113*, 10222–10229.
- (32) Schubert, B. A.; Kaler, E. W.; Wagner, N. J. The Microstructure and Rheology of Mixed Cationic/ Anionic Wormlike Micelles. *Langmuir* **2003**, *19*, 4079–4089.
- (33) Larson, R. G. The Lengths of Thread-like Micelles Inferred from Rheology. *J. Rheol.* **2012**, *56*, 1363–1374.
- (34) Israelachvili, J. N.; Mitchell, D. J.; Ninham, B. W. Theory of Self-Assembly of Hydrocarbon Amphiphiles into Micelles and Bilayers. *J. Chem. Soc. Faraday Trans. 2 Mol. Chem. Phys.* **1975**, *72*, 1525–1568.
- (35) Kekicheff, P. Phase Diagram of Sodium Dodecyl Sulfate-Water System 2. Complementary Isoplethal and Isothermal Phase Studies. *J. Colloid Interface Sci.* **1989**, *131*, 133–152.
- (36) Tanford, C. *The Hydrophobic Effect: Formation of Micelles and Biological Membranes*; 1980; Vol. 124, p. 127.
- (37) Cates, M. E. Reptation of Living Polymers: Dynamics of Entangled Polymers in the Presence of Reversible Chain-Scission Reactions. *Macromolecules* **1987**, *20*, 2289–2296.
- (38) Granek, R.; Cates, M. E. Stress Relaxation in Living Polymers: Results From a Poisson Renewal Model. *J. Chem. Phys.* **1992**, *96*, 4758–4767.
- (39) Lequeux, F. Reptation of Connected Wormlike Micelles. *Europhys. Lett.* **1992**, *19*, 675–681.
- (40) Turner, M. S.; Cates, M. E. Linear Viscoelasticity of Living Polymers: A Quantitative Probe of Chemical Relaxation Time. *Langmuir* **1991**, *7*, 1590–1594.

- (41) Zou, W.; Larson, R. G. A Mesoscopic Simulation Method for Predicting the Rheology of Semi-Dilute Wormlike Micellar Solutions. *J. Rheol.* **2014**, *58*, 681–721.
- (42) Morse, D. C. Viscoelasticity of Concentrated Isotropic Solutions of Semiflexible Polymers. 1. Model and Stress Tensor. *Macromolecules* **1998**, *31*, 7030–7043.
- (43) Granek, R. Dip in  $G''(\omega)$  of Polymer Melts and Semidilute Solutions. *Langmuir* **1994**, *10*, 1627–1629.
- (44) Bradbury, R.; Penfold, J.; Thomas, R. K.; Tucker, I. M.; Petkov, J. T.; Jones, C.; Grillo, I. Impact of Model Perfume Molecules on the Self-Assembly of Anionic Surfactant Sodium Dodecyl 6-Benzene Sulfonate. *Langmuir* **2013**, *29*, 3234–3245.
- (45) Bradbury, R.; Penfold, J.; Thomas, R. K.; Tucker, I. M.; Petkov, J. T.; Jones, C. Adsorption of Model Perfumes at the Air-Solution Interface by Coadsorption with an Anionic Surfactant. *Langmuir* **2013**, *29*, 3361–3369.
- (46) Bradbury, R.; Penfold, J.; Thomas, R. K.; Tucker, I. M.; Petkov, J. T.; Jones, C. The Impact of Alkyl Sulfate Surfactant Geometry and Electrolyte on the Co-Adsorption of Anionic Surfactants with Model Perfumes at the Air-Solution Interface. *J. Colloid Interface Sci.* **2013**, *403*, 84–90.
- (47) Saito, Y.; Hashizaki, K.; Taguchi, H.; Ogawa, N. Solubilization of (+)-Limonene by Anionic/cationic Mixed Surfactant Systems. *Drug Dev. Ind. Pharm.* **2003**, *29*, 345–348.
- (48) Zhou, W.; Zhu, L. Solubilization of Polycyclic Aromatic Hydrocarbons by Anionic-Nonionic Mixed Surfactant. *Colloids Surfaces A Physicochem. Eng. Asp.* **2005**, *255*, 145–152.
- (49) Tokuoka, Y.; Uchiyama, H.; Abe, M. Solubilization of Some Synthetic Perfumes by Anionic-Nonionic Mixed Surfactant Systems. 2. *J. Phys. Chem.* **1994**, *98*, 6167–6171.
- (50) Suratkar, V.; Mahapatra, S. Solubilization Site of Organic Perfume Molecules in Sodium Dodecyl Sulfate Micelles: New Insights from Proton NMR Studies. *J. Colloid Interface Sci.* **2000**, *225*, 32–38.
- (51) Penfold, J.; Tucker, I.; Green, a.; Grainger, D.; Jones, C.; Ford, G.; Roberts, C.; Hubbard, J.; Petkov, J.; Thomas, R. K.; et al. Impact of Model Perfumes on Surfactant and Mixed Surfactant Self-Assembly. *Langmuir* **2008**, *24*, 12209–12220.
- (52) Tang, X.; Koenig, P. H.; Larson, R. G. Molecular Dynamics Simulations of Sodium Dodecyl Sulfate Micelles in Water-the Effect of the Force Field. *J. Phys. Chem. B* **2014**, *118*, 3864–3880.
- (53) Espanol, P.; Warren, P.; Road, M.; Sunlight, P.; East, Q. R. Statistical Mechanics of Dissipative Particle Dynamics. *EPL (Europhysics Lett.)* **1995**, *30*, 191–196.

- (54) Groot, R. D.; Warren, P. B. Dissipative Particle Dynamics: Bridging the Gap between Atomistic and Mesoscopic Simulation. *J. Chem. Phys.* **1997**, *107*, 4423–4435.
- (55) Hoogerbrugge, P. J.; Koelman, J. M. V. a. Simulating Microscopic Hydrodynamic Phenomena with Dissipative Particle Dynamics. *Europhys. Lett.* **2007**, *19*, 155–160.
- (56) Travis, K. P.; Bankhead, M.; Good, K.; Owens, S. L. New Parametrization Method for Dissipative Particle Dynamics. *J. Chem. Phys.* **2007**, *127*, 014109–1 – 12.
- (57) Liyana-arachchi, T. P.; Jamadagni, S. N.; Eike, D.; Koenig, P. H.; Siepmann, J. I.; Liquid – Liquid Equilibria for Soft-Repulsive Particles : Improved Equation of State and Methodology for Representing Molecules of Different Sizes and Chemistry in Dissipative Particle Dynamics. *Imp. J. Chem. Phys.* **2015**, *142*, 044902–1 – 13.
- (58) Klamt, A.; Eckert, F.; Arlt, W. COSMO-RS: An Alternative to Simulation for Calculating Thermodynamic Properties of Liquid Mixtures. *Annu. Rev. Chem. Biomol. Eng.* **2010**, *1*, 101–122.
- (59) Klamt, A. The COSMO and COSMO-RS Solvation Models. *John Wiley Sons, New York* **2011**, *1*, 699–709.
- (60) Mazer, N. A.; Benedek, G. B.; Carey, M. C. An Investigation of the Micellar Phase of Sodium Dodecyl Sulfate in Aqueous Sodium Chloride Solutions Using Quasielastic Light Scattering Spectroscopy. *J. Phys. Chem.* **1976**, *80*, 1075–1085.
- (61) Mukerjee, P.; Mysels, K. *Critical Micelle Concentrations of Aqueous Surfactant Systems*; NSRDS-NBS.; US. Government Printing Office: Washington D.C., 1971; pp. 1–21.
- (62) Helgeson, M. E.; Hodgdon, T. K.; Kaler, E. W.; Wagner, N. J. A Systematic Study of Equilibrium Structure, Thermodynamics, and Rheology of Aqueous CTAB/NaNO<sub>3</sub> Wormlike Micelles. *J. Colloid Interface Sci.* **2010**, *349*, 1–12.
- (63) Fischer, E.; Fieber, W.; Navarro, C.; Sommer, H.; Benczédi, D.; Velazco, M. I.; Schönhoff, M. Partitioning and Localization of Fragrances in Surfactant Mixed Micelles. *J. Surfactants Deterg.* **2008**, *12*, 73–84.
- (64) Parker, A.; Fieber, W. Viscoelasticity of Anionic Wormlike Micelles: Effects of Ionic Strength and Small Hydrophobic Molecules. *Soft Matter* **2013**, *9*, 1203–1213.



## **Chapter 5**

### Conclusions and Future Work

#### **5.1 Summary**

The properties of complex fluids containing surfactants at the continuum scale are determined by the microstructures assembled by surfactants at the molecular scale. The microstructures are correlated to the structures and properties of the surfactants and the surrounding environments in a systematic way. The challenges of quantifying these microstructures experimentally motivate the applications of computational modeling, especially in those days as the computational power and algorithm are improved to a new era. Applications of the computational models at multi-scales accurately and efficiently, in combination with the corresponding experimental measurements, help to determine the structure-property relationships of surfactant solutions or other complex fluids, and accelerate the formulation developments and assist the design of novel products in practical applications.

In this dissertation, we have systematically investigated the force field effects on surfactant micelle properties of simple surfactant SDS in water. Based on the learning from this fundamental study, we developed several models of Tween 80 representing its

commercial mixtures understanding the structure-property relationships Tween 80 in water and at interfaces. To further connect to practical applications, we used multiscale modeling and rheological measurements to determine the structure-property relationships of surfactant formulations upon addition of salts and perfume raw materials. Consistent results were obtained at different length scales, from molecular, to micellar, to bulk rheological. In sum, for the first time we applied the method of using multiscale modeling and experimental techniques to connect the microstructure of surfactant packing at molecular mesoscale scale, to micellar scale, and to practical applications at continuum scale as shown in Fig. 5.1. The method used here can be applied to other complex fluids to determine structure-property relationships for property predictions.

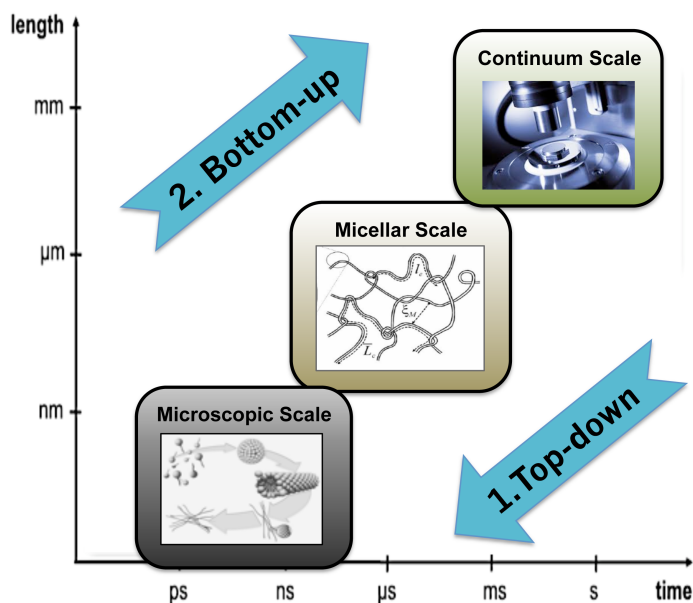


**Figure 5.1.** Developing the structure-property relationship of surfactant formulations using multi-scale modeling and experimental techniques. The picture in the microscopic scale is adopted from <http://www.ifnh.ethz.ch/vt/research/projects/vivianel>.

The key findings in this dissertation can be summarized as follows:

I. MD simulations of SDS micelles in water: key parameters that control the larger micellar shapes are obtained, and more stringent method for force field validation is defined.

- a. L-J parameters of sodium ions and ionic oxygen in SDS head groups, and the water model that solvate the ions, determine the equilibrium micellar structure in MD simulations. Stronger L-J interactions between sodium and ionic oxygen, or weaker binding of water to sodium, lead to sodium ions screen the electrostatic repulsion more effectively, reduce SDS surface area more, resulting in bicelle formations in large aggregates.
- b. The number of sodium ions within the first shell, rather than the total number of sodium ions condensed within the first two shells, determines the structure of large micelles;
- c. The radial distribution function (RDF) of sodium to ionic oxygen can be used as a quantitative metric to determine the larger micellar shapes at lower aggregation number.

II. MD simulations of Tween 80: developed six models to represent Tween 80 commercial mixtures, and developed the structure-property relationships of Tween 80 in water and at interfaces.

- a. Preassembled micelles are similar in sizes and different in head group packing. The constitutional isomer with a shorter W head group and for

Tween 80 isomers with more than one tail groups have efficient packing of head groups;

- b. At the air-water and oil-water interfaces, the molecules with a shorter W head group and with more than one tail group have efficient packing of head groups and reduce surface tension more;
- c. Structure without W head group is expected to reduce surface tension the most among one-tailed Tween 80.

III. Multiscale modeling and rheological measurements were used to determine the structure-property relationships of surfactant formulations. Consistent results were obtained at different length scales, from molecular, to micellar, to bulk rheological. The methods used here can be applied to other complex fluids to determine structure-property relationships:

- a. Salts modify the rheology by condensing at the charged surface of the cylindrical micelle, screening the electrostatic repulsion between the surfactant head groups, reducing both the surfactant surface area  $a_0$  and surfactant packing distances, and maintaining the radius of the cylindrical micelle constant. This results in higher packing parameter  $p$  and longer micelles, and shorter micellar breakage time.
- b. The viscosity is most closely connected to the average micelle length, and elasticity to the ratio of micellar breakage time and the reptation time, where “elasticity” here refers to  $G''/G'$  at 100 rad/s.

- c. PRMs modify the viscoelastic properties of body washes by partitioning within the micelles at different locations according to their values of  $\log P_{ow}$  and their chemical structures, possibly changing the surfactant head group surface area  $a_0$ , surfactant packing distances, and the radius of the cylindrical micelles, and these changes modify the micellar length and viscoelasticity.
- d. The rheological responses of addition of the same PRM (linalool) to two different formulations are different due to the different packing of the surfactants within the two formulations.

## 5.2 Future Directions

The results in this dissertation lay the groundwork for a good understanding of structure-property relationships of surfactant solutions. There are some extensions to this work that would help expand its applications.

In chapter 2 we found the L-J parameters of sodium and ionic oxygen, together with the water model, determine the shape of the SDS micelles at higher aggregation numbers. This result indicate that optimization of the force field parameters for ionic surfactants can be simplified to optimize the L-J parameters of the counterions and charged atoms in surfactants in the presence of water to any physical-chemical properties related to the interaction of these two groups. The micellar distribution profile can be used to develop coarse-grained (CG) models of SDS surfactants.

In Chapter 3 we studied the micellar property of Tween 80 at an aggregation number of 60. The aggregation number of Tween 80 reported in experiments varies from 22 to 350.

Predicting the aggregation number of Tween 80 through self-assembly in MD simulations is still too expensive at atomistic level. Developing CG models of Tween 80 by validating the model against micelle RDF profiles at atomistic level, and studying the self-assembly behavior of Tween 80 can provide information of micellar size distributions. In addition, components other than Tween 80 within corexit 9500, including SPAN 80, Aerosol OT, and solvent molecules, should also be considered in studying the oil dispersion, either at atomistic or CG level. Understanding the effects of each component and the synergistic effects of the mixtures will provide useful information for formulation optimization.

In Chapter 4, testing more PRMs in rheological measurements and molecular modeling can build the statistical quantitative structure-property relationship models to accelerate product designs. Applying similar methods to determine the synergistic effects of two or more PRMs is more relevant to practical applications. Modeling the length of the micelle in molecular simulations, for example, by computing the potential of mean force of cylindrical micelles, and comparing results to modeling or experimental data is also helpful to connect the surfactant packing structures to viscoelastic properties of solutions. In addition, computing the persistence length and radius of the micelle, either from micellar models or molecular models, or using diffusive wave spectrometry or flow birefringence will improve the accuracy and usefulness of the modeling.

## **APPENDIX A**

### Supplementary Information for Chapter 2

Hydration numbers, solvent accessible surface areas, intra and intermolecular parameters of SDS using OPLS-UA and GROMOS45A3, RDF's of sodium to ionic oxygen using different sodium ion/water models for micelles at aggregation number of 60, principal moments versus time for micelles of 382 SDS in 2% NaCl, RDF's of sulfur to sulfur and RDF's of sodium to ionic oxygen using GROMOS53A6 and GROMOS54A8 force fields are listed.

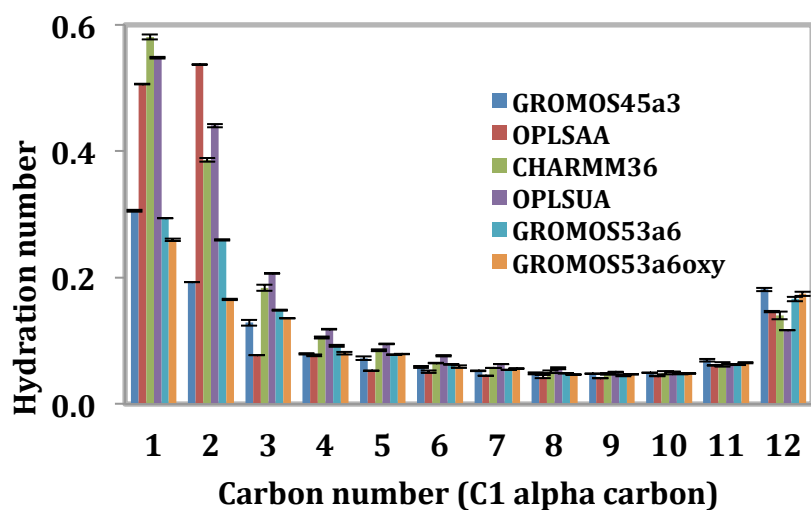


**Figure A.1** Hydration number for methylene hydrocarbons of SDS micelle in the small box estimated as the average number of water oxygens within 0.35 nm of the center of mass of the corresponding methylene. Carbon number 1 represents the alpha carbon and 12 the terminal methyl carbon.

**Table A.1** Hydrophilic and total surface areas of SDS micelles at an aggregation number of 60.

Force Field Measurements	12.65*12.65*12.65 nm <sup>3</sup> (0.05M)		5*5*5 nm <sup>3</sup> (0.80 M)			
	Total SASA	Hydrophilic Percentage	Total SASA		Hydrophilic Percentage	
GROMOS45A3	99.6	50.4%	97	± 0.1*	50.2%	± 0.0%
OPLS-AA	104.7	50.4%	103.8	± 1.0	50.5%	± 0.1%
CHARMM	113.3	63.1%	111.9	± 0.2	62.6%	± 0.2%
OPLS-UA	116.8	48.9%	112.1	± 1.4	49.6%	± 0.0%
GROMOS53A6	107.4	51.6%	105.2	± 0.1	52.0%	± 0.0%
GROMOS53A6OXY	105.0	51.6%	102.3	± 0.2	58.3%	± 0.1%

\*All standard deviations were calculated using two sets of simulations with different initial configurations.



**Table A.2** Intramolecular parameters of SDS in GROMOS45A3<sup>48</sup> and OPLS-UA force fields.

Intermolecular parameters	GROMOS45A3		OPLS-UA		
	$K_{str}$ (kJ mol <sup>-1</sup> nm <sup>-4</sup> )	$b_0$ (nm)	$K_{str}$ (kJ mol <sup>-1</sup> nm <sup>-2</sup> )	$b_0$ (nm)	
C-C	7.2E+06	0.153	3.4E+05	0.153	
C-O(ester)	8.2E+06	0.143	2.7E+05	0.141	
O(ester)-S	8.4E+06	0.150	2.7E+05	0.158	
S-O	8.4E+06	0.150	3.8E+05	0.146	
Angle	$K_{bend}$ (kJ mol <sup>-1</sup> )	$\theta_0$ (deg)	$K_{bend}$ (kJ mol <sup>-1</sup> rad <sup>-2</sup> )	$\theta_0$ (deg)	
C-C-C	520.0	109.5	460.2	111.0	
C-C-O(ester)	520.0	109.5	460.2	111.0	
C-O (ester)-S	530.0	120.0	460.2	112.6	
O(ester)-S-O	520.0	109.5	460.2	102.6	
O-S-O	520.0	109.5	460.2	115.4	
Torsion	$\phi_{tors}$ (deg) $K_{tors}$ (kJ mol <sup>-1</sup> ) multiplicity			$\phi_{tors}$ (deg) $K_{tors}$ (kJ mol <sup>-1</sup> ) multiplicity	
C-C-C-C*	9.28 12.16 -13.12 -3.06 26.24 -31.50			9.28 12.16 -13.12 -3.06 26.24 -31.50	
C-C-C-O(ester)*	0.0 5.9 3			7.00 17.74 0.89 -25.60 0.00 0.00	
C-C-O-S	0.0 1.3 3			0.0 3.03 3	
C-O-S-O	0.0 1.3 3			0.0 1.046 3	

Intramolecular parameters for C-C-C-C\* and C-C-C-O\* in OPLS-UA are for the R-B potential.

**Table A.3** Simulations with 382 surfactant molecules using different combinations of intramolecular parameters and the resulting micelle shape.

Intramolecular parameters							Intermolecular parameters	Equilibrium micelle shapes
S-O head		S-O-ester		H-C tail		Dihedrals, Improper dihedrals		
Bond Length	Bond Angle	Bond Length	Bond Angle	Bond Length	Bond Angle		L-J of Water, ions, and SDS	
GROMOS45A3	GROMOS45A3	GROMOS45A3	GROMOS45A3	GROMOS45A3	GROMOS45A3	GROMOS45A3	GROMOS45A3	Bicelle
OPLS-UA	GROMOS45A3	OPLS-UA	GROMOS45A3	OPLS-UA	GROMOS45A3	GROMOS45A3	GROMOS45A3	Bicelle
GROMOS45A3	OPLS-UA	GROMOS45A3	OPLS-UA	GROMOS45A3	OPLS-UA	GROMOS45A3	GROMOS45A3	Bicelle
OPLS-UA	OPLS-UA	OPLS-UA	OPLS-UA	OPLS-UA	OPLS-UA	GROMOS45A3	GROMOS45A3	Bicelle
OPLS-UA	OPLS-UA	OPLS-UA	OPLS-UA	OPLS-UA	OPLS-UA	OPLS-UA	GROMOS45A3	Bicelle
OPLS-UA	OPLS-UA	OPLS-UA	OPLS-UA	OPLS-UA	OPLS-UA	OPLS-UA	OPLS-UA	Cylinder

**Table A.4** Intermolecular parameters for two force fields.

Functional groups		GROMOS45A3		OPLS-UA	
L-J Parameters		$\sigma$ (nm)	$\epsilon$ (kJ/mol)	$\sigma$ (nm)	$\epsilon$ (kJ/mol)
Tail	CH3	0.375	0.867	0.396	0.570
	CH2 (internal)	0.407	0.411	0.396	0.380
Head	CH2 (attached to O)	0.407	0.411	0.395**	0.382**
	O (ester)	0.295	0.850	0.280**	0.457**
	S	0.331	1.906	0.355*	1.046*
	O (SO3)	0.295 <sup>1</sup>	0.850 <sup>1</sup>	0.315*	0.837*
	O (SO3)	0.263 <sup>2</sup>	1.725 <sup>2</sup>	0.315*	0.837*
Counterions	Na <sup>+</sup>	0.258	0.062	0.333	0.012
Others	Cl <sup>-</sup>	0.445	0.446	0.442	0.493
	OW	0.317	0.650	0.317	0.650
Special cross term	O (ester)- O (SO3)			0.277	1.35

The parameters for GROMOS45A3 were converted from C6 and C12 coefficients to  $\epsilon$  and  $\sigma$  to allow comparison with the OPLS-UA values. Cross-terms were created using the normal rules, respectively, for GROMOS45A3 and OPLS-UA, except for the ester oxygen-water oxygen cross terms in OPLS-UA, which were obtained as described in the text and listed in the last row of the table.

<sup>1</sup>These L-J parameters were taken from Shang et al.<sup>1</sup> and converted from the L-J C6 and C12 parameters to  $\epsilon$  and  $\sigma$ . They correspond to GROMOS45A3 parameters for hydroxyl oxygen, and were used for one of the three ionic oxygens in the sulfate group, as in Shang et al.<sup>1</sup>

<sup>2</sup>These L-J parameters were taken from Shang et al.<sup>1</sup> and converted from the L-J C6 and C12 parameters to  $\epsilon$  and  $\sigma$ . They correspond to GROMOS45A3 parameters for carbonyl oxygen, and were used for one of two of the three ionic oxygens in the sulfate group, as in Shang et al.<sup>1</sup>

\* Adopted from Berkowitz's group<sup>45,46</sup>

\*\* Adopted from Stubbs et al.<sup>93</sup>

**Table A.5** List of cross terms of the L-J parameters for sodium ion and oxygen tested in this study within the OPLS-AA force field.

Water Model	Sodium Ion Force Field	Na O (SO3)		Na OW	
		$\sigma$ (nm)	$\epsilon$ (kJ/mol)	$\sigma$ (nm)	$\epsilon$ (kJ/mol)
TIP4P	Jorgensen <sup>72</sup>	0.245	2.371	0.245	2.088
SPC/E	Joung and Cheatham <sup>111</sup>	0.276	1.111	0.277	0.979
TIP4P <sub>EW</sub>	Joung and Cheatham <sup>111</sup>	0.278	0.768	0.278	0.693
TIP3P	Joung and Cheatham <sup>111</sup>	0.296	0.553	0.296	0.482
SPC/E	Dang <sup>110</sup>	0.301	0.661	0.302	0.583
SPC/ TIP3P	Aqvist <sup>109</sup>	0.324	0.096	0.325	0.085
TIP4P	Jensen and Jorgensen <sup>112</sup>	0.358	0.042	0.358	0.037

Here “O” stands for an ionic oxygen in the head group while “OW” stands for an oxygen in water.

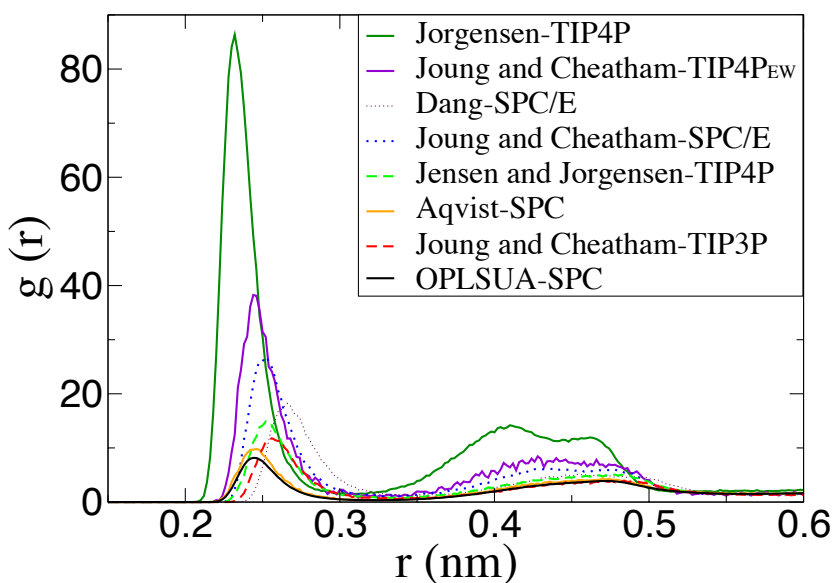


**Figure A.2** (a) RDF of sodium to ionic oxygens in SDS head group in a simulation of box of size 5\*5\*5 nm<sup>3</sup> with a micelle having an aggregation number of 60 and different Na<sup>+</sup>/water models and Aqvist<sup>5</sup> sodium ion within OPLS-AA.

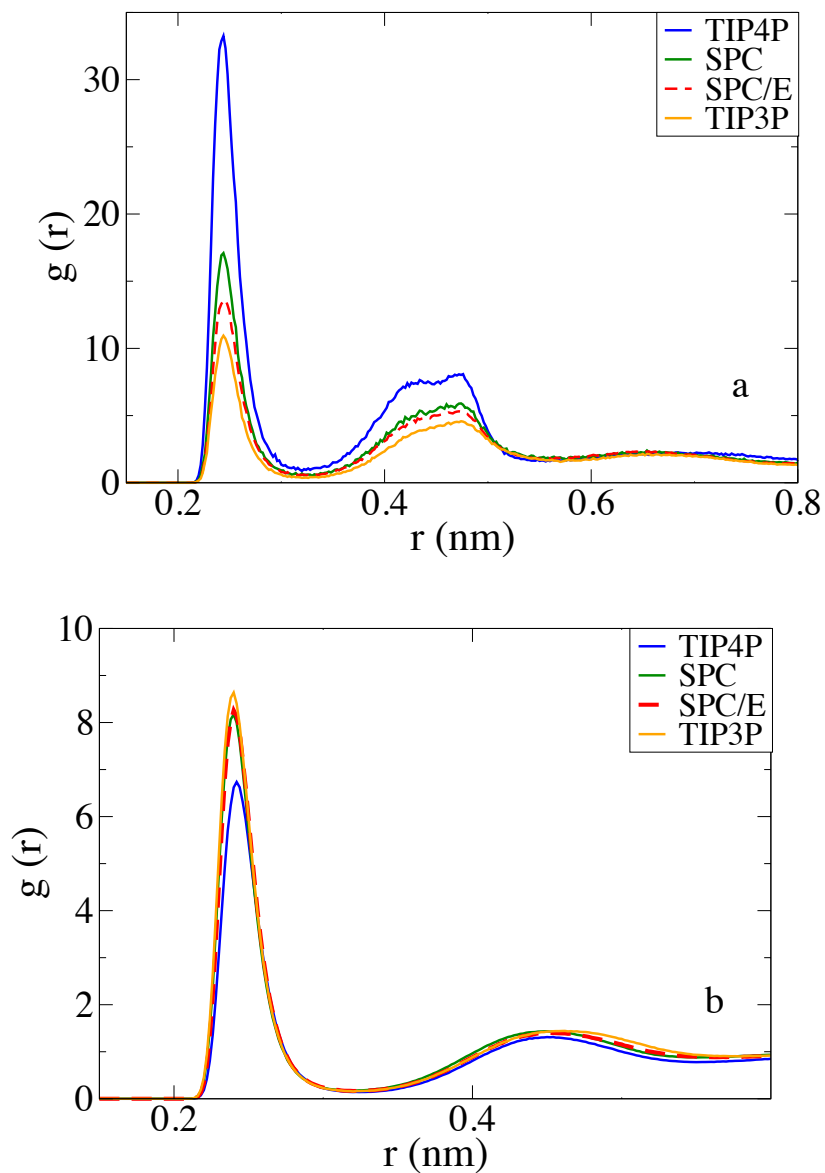


**Figure A.3** a). RDF of sodium to ionic oxygens and b). sodium to water oxygens in SDS head group in a simulation of box of size  $6 \times 6 \times 6 \text{ nm}^3$  with a micelle having an aggregation number of 100 and Aqvist<sup>5</sup>  $\text{Na}^+$ /different water model within OPLS-AA.

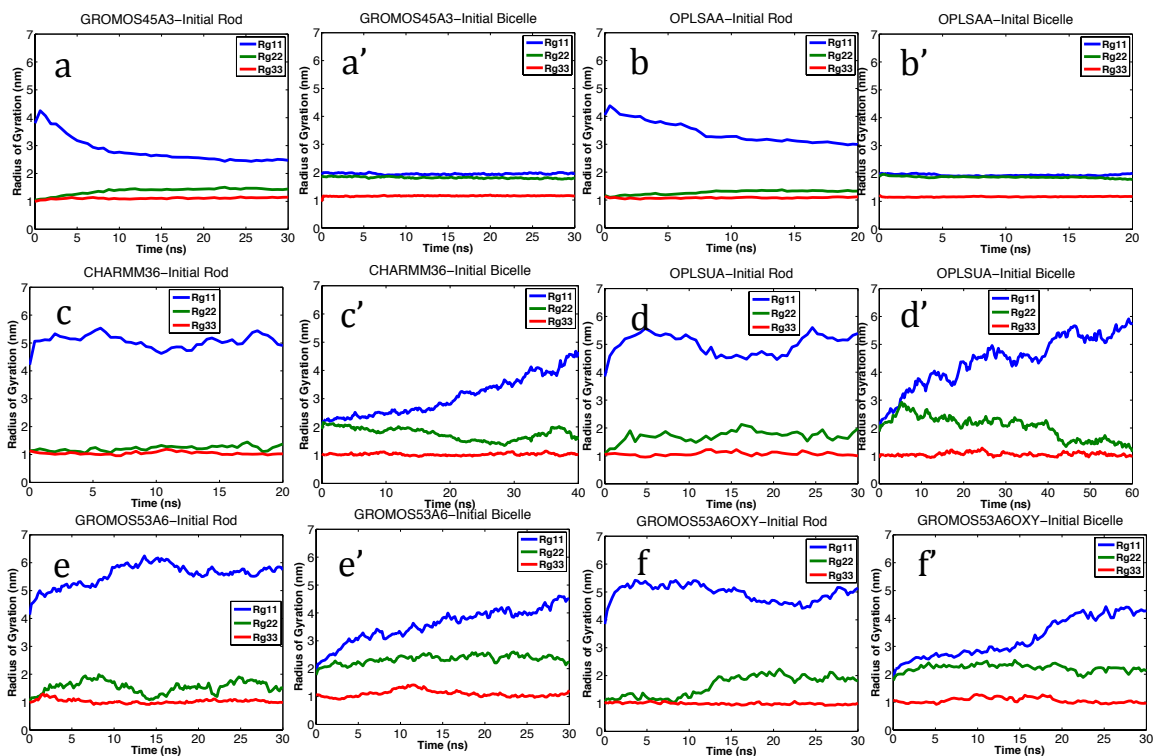


**Figure A.4** Square root of principal radii of gyration vs. time for preassembled rod-like micelles (a-f) and preassembled bicelles (a'-f') of 382 SDS molecules in 2% NaCl for six force fields.

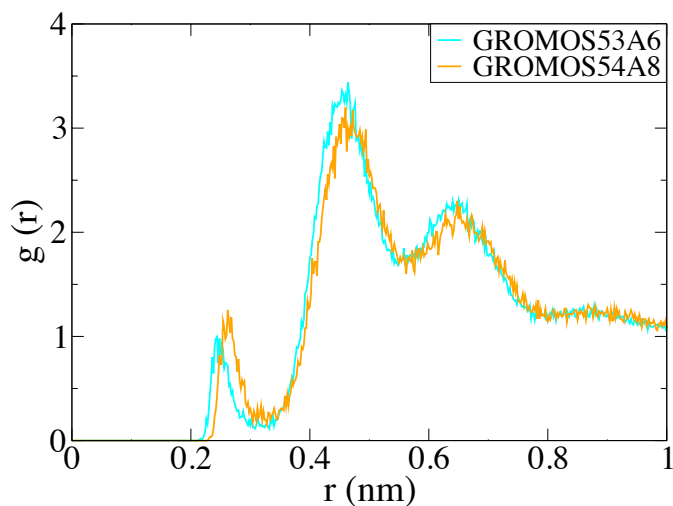


**Figure A.5** RDF of sodium with respect to ionic oxygen atoms in the micelle head group for an SDS micelle with aggregation number 60 using GROMOS53A6<sup>86</sup> and GROMOS54A8<sup>95</sup> force fields.

#### A.6 References:

1. Shang, B. Z.; Wang, Z.; Larson, R. G. Molecular Dynamics Simulation of Interactions Between a Sodium Dodecyl Sulfate Micelle and a Poly(ethylene Oxide) Polymer. *J. Phys. Chem. B* **2008**, *112*, 2888–2900.
2. Schweighofer, K. J.; Essmann, U.; Berkowitz, M. Simulation of Sodium Dodecyl Sulfate at the Water-Vapor and Water-Carbon Tetrachloride Interfaces at Low Surface Coverage. *J. Phys. Chem. B* **1997**, *101*, 3793–3799.
3. Dominguez, H.; Berkowitz, M. L. Computer Simulations of Sodium Dodecyl Sulfate at Liquid/Liquid and Liquid/Vapor Interfaces. *J. Phys. Chem. B* **2000**, *104*, 5302–5308.
4. Stubbs, J. M.; Potoff, J. J.; Siepmann, J. I. Transferable Potentials for Phase Equilibria. 6. United-Atom Description for Ethers, Glycols, Ketones, and Aldehydes. *J. Phys. Chem. B* **2004**, *108*, 17596–17605.
5. Jorgensen, W. L. Intermolecular Potential Functions and Monte Carlo Simulations for Liquid Sulfur Compounds. *J. Phys. Chem.* **1986**, *90*, 6379–6388.

6. Joung, I. S.; Cheatham, T. E. Determination of Alkali and Halide Monovalent Ion Parameters for Use in Explicitly Solvated Biomolecular Simulations. *J. Phys. Chem. B* **2008**, *112*, 9020–9041.
7. Dang, L. X. Mechanism and Thermodynamics of Ion Selectivity in Aqueous Solutions of 18-Crown-6 Ether : A Molecular Dynamics Study. *J. Am. Chem. Soc.* **1995**, *117*, 6954–6960.
8. Aqvist, J. Ion-Water Interaction Potentials Derived From Free Energy Perturbation Simulations. *J. Phys. Chem.* **1990**, *94*, 8021–8024.
9. Jensen, K. P.; Jorgensen, W. L. Halide, Ammonium, and Alkali Metal Ion Parameters for Modeling Aqueous Solutions. *J. Chem. Theory Comput.* **2006**, *2*, 1499–1509.
10. Oostenbrink, C.; Villa, A.; Mark, A. E.; van Gunsteren, W. F. A Biomolecular Force Field Based on the Free Enthalpy of Hydration and Solvation: The GROMOS Force-Field Parameter Sets 53A5 and 53A6. *J. Comput. Chem.* **2004**, *25*, 1656–1676.
11. Reif, M. M.; Winger, M.; Oostenbrink, C. Testing of the GROMOS Force-Field Parameter Set 54A8: Structural Properties of Electrolyte Solutions, Lipid Bilayers, and Proteins. *J. Chem. Theory Comput.* **2013**, *9*, 1247–1264.

## APPENDIX B

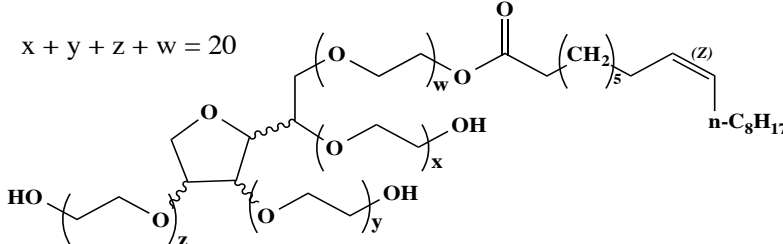
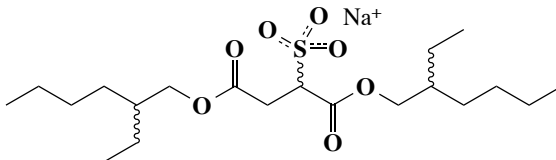
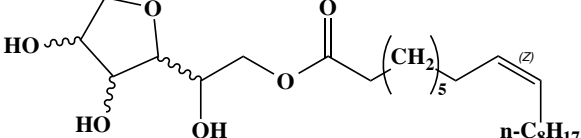
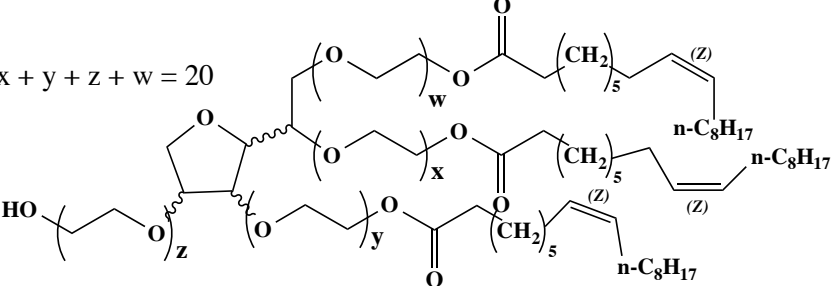
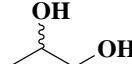
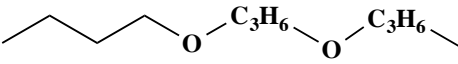
### Supplementary Information for Chapter 3

The comparison of micelle properties using the GROMOS53A6 and GROMOS53A6<sub>OXY+D</sub> force fields, validation of simulation reproducibility, comparison of micelle RDF profiles of two epimers of Tween 80, density distributions of Tween 80 at air–water and oil–water interfaces, and tail order parameters are listed.

The deuterium order parameters of the five Tween 80 molecules were estimated using the formula:  $S_{CD} = \left\langle \frac{3\cos^2\theta - 1}{2} \right\rangle$ , where  $\theta$  is the time-dependent angle between the C-D bond vector and the monolayer normal after the positions of the deuterium atoms were reconstructed from the united atom model. The angular brackets denote a time and ensemble average. All order parameters are estimated using g\_order code in GROMACS simulation engine with the consideration of the double bond as well.



**Table B.1** Main components of Corexit 9500 released by Nalco Holding Company.

Name (CAS number)	Chemical Structure
Tween 80 (Polysorbate 80) (CAS 9005-65-6)	$x + y + z + w = 20$ 
Dioctyl sodium sulfosuccinate (DOSS, AOT) (CAS 577-11-7)	
Span 80 (CAS 1338-43-8)	
Tween 85 (CAS 9005-70-3)	$x + y + z + w = 20$ 
Propylene glycol (CAS 57-55-6)	
Butoxypolypropylene glycol (CAS 29911-28-2)	
Distillates (petroleum), hydrotreated light (CAS 64742-47-8)	

Chiral carbons are connected with wavy bonds. Double bonds are assigned to (Z) configurations. (I.e., based on the Cahn–Ingold–Prelog priority rules, in the Z configuration, the two groups of higher priority or higher atomic numbers are on the same side of the double bond; i.e., in the *cis* configuration.)

**Table B.2** Partial charges of tetramethyl sorbitan calculated using Gaussian 09, with density functional theory method at B3LYP/6-31G(d,p) level averaged over 27 conformational isomers.

Index	Atom Name	2(S),3(R),4(R),5(R)	2(R),3(S),4(S),5(S)	2(S),3(R),4(R),5(S)
1	FC1	0.179	0.163	0.200
2	FC5	0.352	0.349	0.144
3	FC4	0.111	0.127	0.296
4	FC3	0.220	0.221	0.166
5	CX0	0.077	0.069	0.082
6	CWE	0.249	0.250	0.217
7	FO2	-0.401	-0.396	-0.380
8	WO1	-0.320	-0.317	-0.314
9	WC2	0.138	0.136	0.142
10	XO1	-0.290	-0.284	-0.234
11	XC2	0.123	0.123	0.112
12	YO1	-0.415	-0.413	-0.393
13	YC2	0.156	0.157	0.149
14	ZO1	-0.326	-0.334	-0.322
15	ZC2	0.149	0.150	0.136

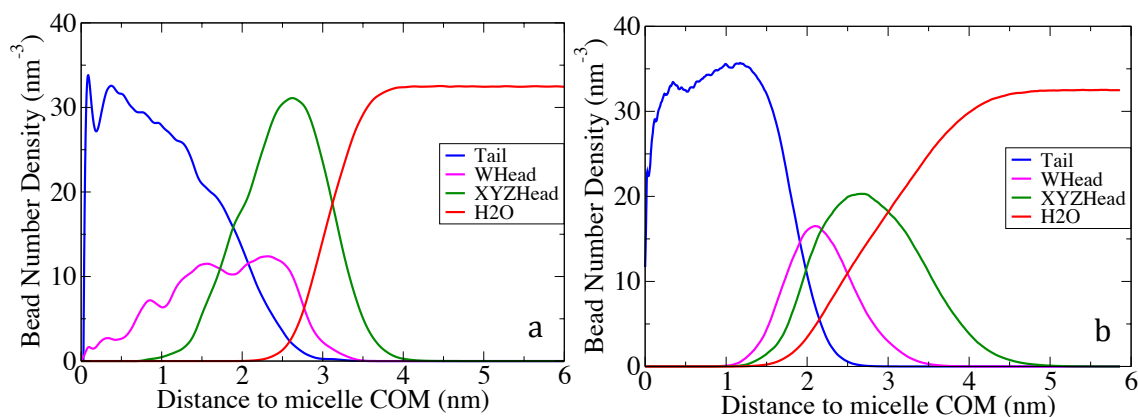


**Figure B.1** RDF distributions of tail, W head, X, Y, Z head, and water for a micelle of Tween 80 composed of 60 surfactants using (a) the GROMOS53A6 force field, and (b) the GROMOS53A6<sub>OXY+D</sub> force field.

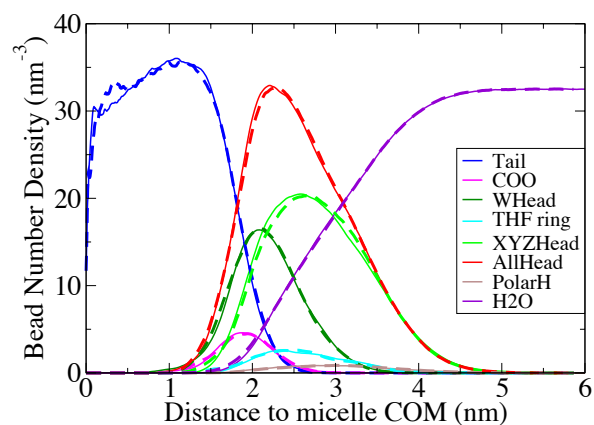


**Figure B.2** Comparison of radial distribution functions (RDFs) of various atom groups of Tween 80 isomer 555-5-1S with respect to the micelle center of mass (COM) from two independent runs, as shown by solid and dashed lines. The atom groups are specified in the legend, where “PolarH” consists of the polar hydrogen atoms located at the ends of the X, Y, and Z head groups.

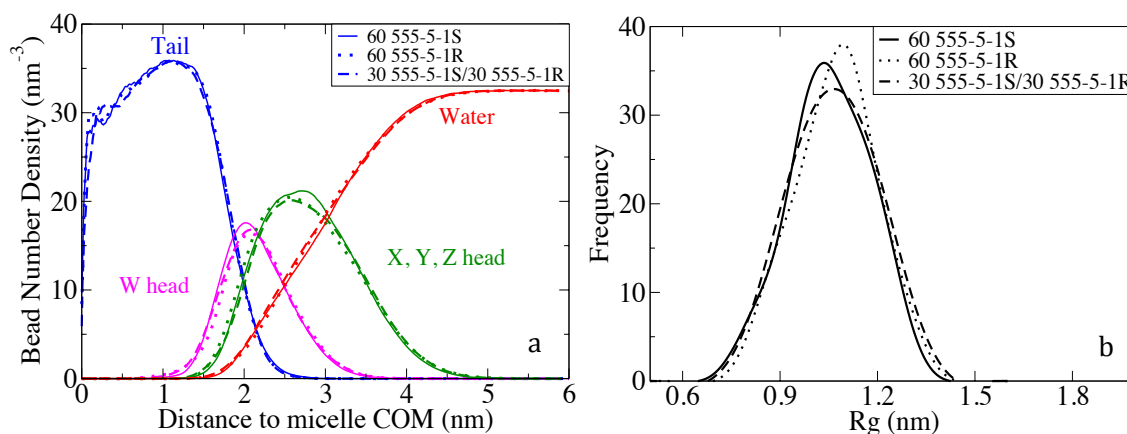


**Figure B.3** Comparison of micelle properties of two epimers of Tween 80: (a) Radial distribution functions (RDFs) of different groups with respect to the micelle center of mass (COM); (b) The distributions of single-surfactant  $R_g$  values for surfactants within the micelle.

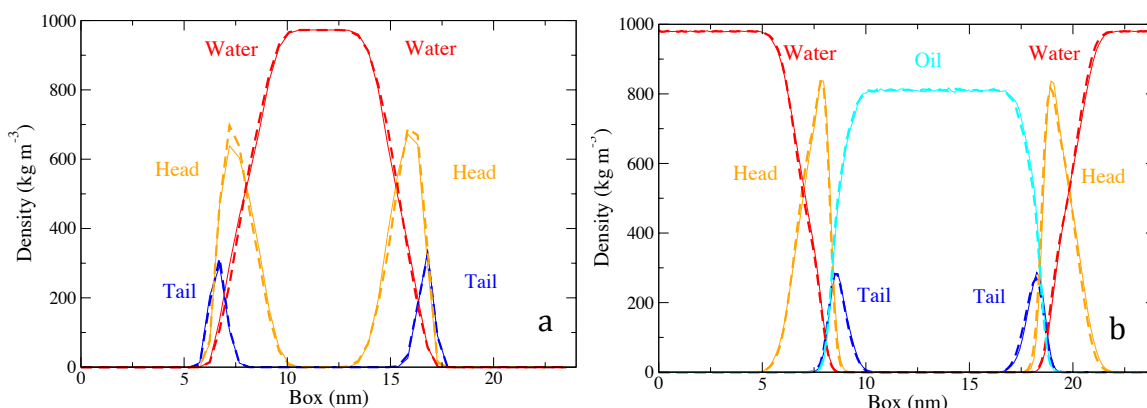


**Figure B.4** Densities of water, head, tail, and oil atoms of isomer 555-5-1S, at (a) an air–water interface, averaged over both 40 to 50 ns (solid lines) and 90 to 100 ns (dashed lines) after the start of the simulation; and at (b) an oil–water interface, averaged over both 100 to 120 ns (solid lines) and 220 to 240 ns (dashed lines).

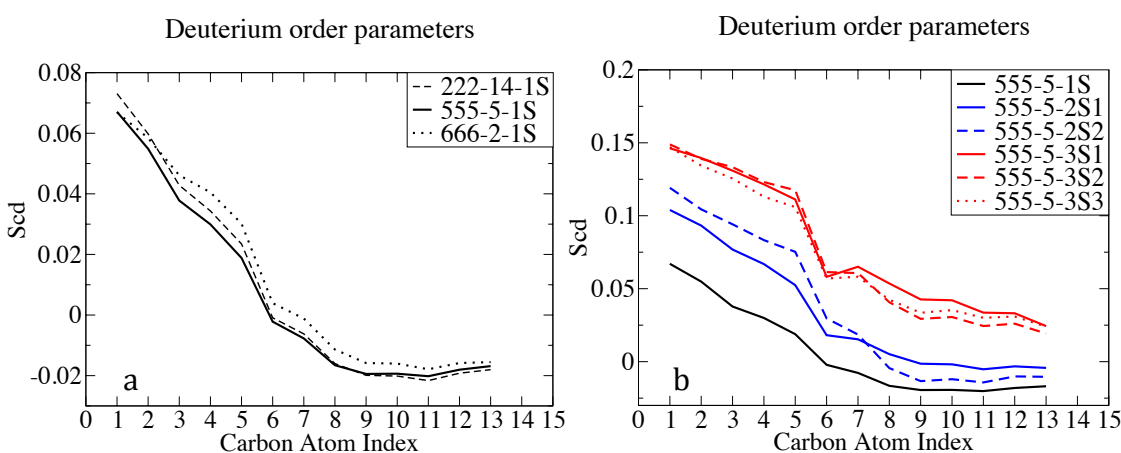


**Figure B.5** Comparison of oleate tail order parameters of (a) three one-tailed structure isomers of Tween 80 and (b) one, two, and three-tail Tween 80 molecules. For 555-5-2S and 555-5-3S, the tail order parameters of the different tails are plotted separately. The carbon atom index number starts from the second carbon connected to the ester carbonyl carbon.

## APPENDIX C

### Supplementary Information for Chapter 4

Table C.1 Coarse-grained DPD molecular mapping of surfactants and PRMs.

Common Name	Chemical Structure	Common Name	Chemical Structure
Dodecyl Sulfate (C3T)(C3)(C3)(C3)(SO4)		Heliotropin (CDO)(O2rC)	
Lauryl Ether Sulfate (C3T)(C3)(C3)(C3) -(EO)n(SO4)		Linalool (BTNL)(CCD)(CDC1)	
Cocamidopropyl Betain (C3T)(C3)(C3)(C2P)(C3tq) -(NC2)(ACE)		Allyl Amyl Glycolate (PPT)(COSR)(iPT)	
Cumene (TLB)(TLA)(iPBb)		Undecavertol (DCCT)(PPL2)(C4T)	
Isopropyl Myristate (C3T)(C4)(C4)(iPBc)(iPBb)		beta-Ionone (CDMC)(C3DM)(P3O)	
Dipropylene Glycol (DPGA)(DPGB)(DPGC)		Synambran (CDMC)(CTMC) (CrDM)(OCCr)	

Table C.2 DPD force field parameters, including bead densities, bond equilibrium distances and spring constants, and chi parameters. All parameters are in DPD units.

Bead Name	Bead Density	Bond	Equilibrium Distance	Spring Constant
C3T	0.394	("C3","SO4")	0.55	400.0
C3	0.512	("C3","EO")	0.42	513.0
C4	0.513	("EO","SO4")	0.46	400.0
C4T	0.417	("C2P","C3tq")	0.46	400.0
SO4	1.454	("C3tq","NC2")	0.38	400.0
EO	0.756	("C3T","C4")	0.54	292.6
NC2	0.535	("C3","C3T")	0.47	397.0
C2P	0.947	("C3","C3")	0.46	275.4
C3tq	0.512	("C3","C3T")	0.47	397.0
ACE	0.870	("C4","C4T")	0.60	188.6
TLA	0.655	("C4","iPBc")	0.61	132.4
TLB	0.601	("CDO","O2rC")	0.48	192.7
iPBb	0.395	("BTNL","CCD")	0.41	400.0
iPBc	0.874	("CCD","CDC1")	0.39	400.0
DPGA	0.619	("COSR","iPT")	0.61	258.2
DPGB	0.624	("DCCT","PPL2")	0.47	400.0
DPGC	0.639	("CTMC","CrDM")	0.31	400.0
CDO	0.696	("CTMC","OCCr")	0.27	400.0
O2rC	0.869	("C2P","C3")	0.54	172.1
BTNL	0.594	("C2P","C3tq")	0.46	400.0
CCD	0.527	("ACE","NC2")	0.36	213.2
CDC1	0.411	("TLA","TLB")	0.24	400.0
PPT	0.419	("iPBb","iPBc")	0.44	400.4
COSR	0.970	("COSR","PPT")	0.51	400.4
iPT	0.471	("C4T","PPL2")	0.59	327.1
DCCT	0.408	("C3DM","CDMC")	0.34	400.4
PPL2	0.719			
CDMC	0.520			
C3DM	0.591			
P3O	0.629			
CTMC	0.680			
CrDM	0.615			
OCCr	0.611			

### Chi Parameter List

chi[('C3T', 'C3T')] = 0.00	chi[('ACE', 'NC2')] = 0.0	chi[('C3T', 'iPBb')] = 0.02
chi[('C3', 'C3T')] = -0.0	chi[('DPGA', 'NC2')] = 1.73	chi[('C3', 'iPBb')] = 0.03
chi[('C2P', 'C3T')] = 4.45	chi[('DPGB', 'NC2')] = 1.92	chi[('C4', 'iPBb')] = 0.04
chi[('ACE', 'C3T')] = 10.87	chi[('DPGC', 'NC2')] = 1.17	chi[('C4T', 'iPBb')] = 0.02
chi[('BTNL', 'C3T')] = 1.7	chi[('CDO', 'NC2')] = 2.23	chi[('SO4', 'iPBb')] = 10.18
chi[('C3DM', 'C3T')] = 0.03	chi[('BTNL', 'NC2')] = 2.45	chi[('EO', 'iPBb')] = 0.4
chi[('C3', 'C3')] = 0.00	chi[('CCD', 'NC2')] = 7.11	chi[('NC2', 'iPBb')] = 10.18
chi[('C2P', 'C3')] = 3.87	chi[('CDC1', 'NC2')] = 9.82	chi[('C2P', 'iPBb')] = 3.82
chi[('ACE', 'C3')] = 8.93	chi[('COSR', 'NC2')] = 0.98	chi[('C3tq', 'iPBb')] = 1.92
chi[('BTNL', 'C3')] = 1.54	chi[('DCCT', 'NC2')] = 9.97	chi[('ACE', 'iPBb')] = 10.18
chi[('C3T', 'C4')] = 0.0	chi[('CDMC', 'NC2')] = 12.51	chi[('TLA', 'iPBb')] = 0.2
chi[('C3', 'C4')] = -0.02	chi[('C3DM', 'NC2')] = 10.03	chi[('TLB', 'iPBb')] = 0.28
chi[('C4', 'C4')] = 0.00	chi[('CTMC', 'NC2')] = 7.91	chi[('iPBb', 'iPBb')] = 0.00
chi[('C2P', 'C4')] = 4.54	chi[('CrDM', 'NC2')] = 10.16	chi[('DPGA', 'iPBb')] = 1.65
chi[('C3tq', 'C4')] = 2.46	chi[('C2P', 'C2P')] = 0.00	chi[('DPGB', 'iPBb')] = 3.23
chi[('ACE', 'C4')] = 10.92	chi[('ACE', 'C2P')] = -1.13	chi[('DPGC', 'iPBb')] = 1.75
chi[('BTNL', 'C4')] = 1.79	chi[('BTNL', 'C2P')] = -0.22	chi[('CDO', 'iPBb')] = 1.14
chi[('C3DM', 'C4')] = 0.07	chi[('C3T', 'C3tq')] = 2.41	chi[('O2rC', 'iPBb')] = 0.95
chi[('C3T', 'C4T')] = -0.01	chi[('C3', 'C3tq')] = 2.14	chi[('BTNL', 'iPBb')] = 1.42
chi[('C3', 'C4T')] = -0.04	chi[('C2P', 'C3tq')] = 0.88	chi[('CCD', 'iPBb')] = -0.01
chi[('C4', 'C4T')] = 0.0	chi[('C3tq', 'C3tq')] = 0.00	chi[('CDC1', 'iPBb')] = 0.0
chi[('C4T', 'C4T')] = 0.00	chi[('ACE', 'C3tq')] = 3.62	chi[('PPT', 'iPBb')] = 0.06
chi[('C2P', 'C4T')] = 5.14	chi[('BTNL', 'C3tq')] = 1.22	chi[('COSR', 'iPBb')] = 4.66
chi[('C3tq', 'C4T')] = 2.73	chi[('C3DM', 'C3tq')] = 1.94	chi[('DCCT', 'iPBb')] = 0.0
chi[('ACE', 'C4T')] = 12.91	chi[('ACE', 'ACE')] = 0.00	chi[('PPL2', 'iPBb')] = 1.79
chi[('BTNL', 'C4T')] = 1.95	chi[('C3T', 'TLA')] = 0.35	chi[('CDMC', 'iPBb')] = -0.01
chi[('C3DM', 'C4T')] = 0.04	chi[('C3', 'TLA')] = 0.38	chi[('C3DM', 'iPBb')] = -0.0
chi[('C3T', 'SO4')] = 10.87	chi[('C4', 'TLA')] = 0.4	chi[('P3O', 'iPBb')] = 1.14
chi[('C3', 'SO4')] = 8.93	chi[('C4T', 'TLA')] = 0.36	chi[('CTMC', 'iPBb')] = -0.0
chi[('C4', 'SO4')] = 10.92	chi[('SO4', 'TLA')] = 5.8	chi[('CrDM', 'iPBb')] = 0.02
chi[('C4T', 'SO4')] = 12.91	chi[('EO', 'TLA')] = 0.05	chi[('OCCr', 'iPBb')] = 0.33
chi[('SO4', 'SO4')] = 0.00	chi[('NC2', 'TLA')] = 5.8	chi[('C3T', 'iPBc')] = 1.52
chi[('EO', 'SO4')] = 0.44	chi[('C2P', 'TLA')] = 2.05	chi[('C3', 'iPBc')] = 1.36
chi[('NC2', 'SO4')] = 0.0	chi[('C3tq', 'TLA')] = 0.98	chi[('C4', 'iPBc')] = 1.6
chi[('C2P', 'SO4')] = -1.13	chi[('ACE', 'TLA')] = 5.8	chi[('C4T', 'iPBc')] = 1.75
chi[('C3tq', 'SO4')] = 3.62	chi[('TLA', 'TLA')] = 0.00	chi[('SO4', 'iPBc')] = 1.78
chi[('ACE', 'SO4')] = 0.0	chi[('DPGA', 'TLA')] = 1.0	chi[('EO', 'iPBc')] = -0.01
chi[('DPGA', 'SO4')] = 1.73	chi[('DPGB', 'TLA')] = 2.1	chi[('NC2', 'iPBc')] = 1.78
chi[('DPGB', 'SO4')] = 1.92	chi[('DPGC', 'TLA')] = 1.01	chi[('C2P', 'iPBc')] = 0.87
chi[('DPGC', 'SO4')] = 1.17	chi[('CDO', 'TLA')] = 0.05	chi[('C3tq', 'iPBc')] = -0.2
chi[('CDO', 'SO4')] = 2.23	chi[('O2rC', 'TLA')] = 0.02	chi[('ACE', 'iPBc')] = 1.78

chi[('O2rC','SO4')] = 6.57  
 chi[('BTNL','SO4')] = 2.45  
 chi[('CCD','SO4')] = 7.11  
 chi[('CDC1','SO4')] = 9.82  
 chi[('PPT','SO4')] = 8.53  
 chi[('COSR','SO4')] = 0.98  
 chi[('DCCT','SO4')] = 9.97  
 chi[('PPL2','SO4')] = 1.43  
 chi[('CDMC','SO4')] = 12.51  
 chi[('C3DM','SO4')] = 10.03  
 chi[('P3O','SO4')] = 0.16  
 chi[('CTMC','SO4')] = 7.91  
 chi[('CrDM','SO4')] = 10.16  
 chi[('OCCr','SO4')] = -0.37  
 chi[('C3T','EO')] = 0.73  
 chi[('C3','EO')] = 0.67  
 chi[('C4','EO')] = 0.75  
 chi[('C4T','EO')] = 0.81  
 chi[('EO','EO')] = 0.00  
 chi[('C2P','EO')] = 0.36  
 chi[('C3tq','EO')] = -0.07  
 chi[('ACE','EO')] = 0.44  
 chi[('DPGA','EO')] = -0.78  
 chi[('DPGB','EO')] = -1.94  
 chi[('DPGC','EO')] = -0.41  
 chi[('CDO','EO')] = 0.12  
 chi[('BTNL','EO')] = -0.84  
 chi[('CCD','EO')] = 0.21  
 chi[('CDC1','EO')] = 0.5  
 chi[('COSR','EO')] = 0.9  
 chi[('DCCT','EO')] = 0.57  
 chi[('CDMC','EO')] = 0.67  
 chi[('C3DM','EO')] = 0.43  
 chi[('CTMC','EO')] = 0.39  
 chi[('CrDM','EO')] = 0.61  
 chi[('C3T','NC2')] = 10.87  
 chi[('C3','NC2')] = 8.93  
 chi[('C4','NC2')] = 10.92  
 chi[('C4T','NC2')] = 12.91  
 chi[('EO','NC2')] = 0.44  
 chi[('NC2','NC2')] = 0.00  
 chi[('C2P','NC2')] = -1.13

chi[('BTNL','TLA')] = 0.75  
 chi[('CCD','TLA')] = 0.16  
 chi[('CDC1','TLA')] = 0.17  
 chi[('PPT','TLA')] = 0.02  
 chi[('COSR','TLA')] = 2.2  
 chi[('DCCT','TLA')] = 0.22  
 chi[('PPL2','TLA')] = 1.13  
 chi[('CDMC','TLA')] = 0.28  
 chi[('C3DM','TLA')] = 0.11  
 chi[('P3O','TLA')] = 0.1  
 chi[('CTMC','TLA')] = 0.25  
 chi[('CrDM','TLA')] = 0.31  
 chi[('OCCr','TLA')] = -0.02  
 chi[('C3T','TLB')] = 0.47  
 chi[('C3','TLB')] = 0.48  
 chi[('C4','TLB')] = 0.54  
 chi[('C4T','TLB')] = 0.52  
 chi[('SO4','TLB')] = 6.48  
 chi[('EO','TLB')] = 0.06  
 chi[('NC2','TLB')] = 6.48  
 chi[('C2P','TLB')] = 2.27  
 chi[('C3tq','TLB')] = 1.11  
 chi[('ACE','TLB')] = 6.48  
 chi[('TLA','TLB')] = -0.01  
 chi[('TLB','TLB')] = 0.00  
 chi[('DPGA','TLB')] = 1.18  
 chi[('DPGB','TLB')] = 2.33  
 chi[('DPGC','TLB')] = 1.19  
 chi[('CDO','TLB')] = 0.11  
 chi[('O2rC','TLB')] = 0.07  
 chi[('BTNL','TLB')] = 0.91  
 chi[('CCD','TLB')] = 0.2  
 chi[('CDC1','TLB')] = 0.25  
 chi[('PPT','TLB')] = 0.07  
 chi[('COSR','TLB')] = 2.5  
 chi[('DCCT','TLB')] = 0.3  
 chi[('PPL2','TLB')] = 1.31  
 chi[('CDMC','TLB')] = 0.44  
 chi[('C3DM','TLB')] = 0.2  
 chi[('P3O','TLB')] = 0.13  
 chi[('CTMC','TLB')] = 0.32  
 chi[('CrDM','TLB')] = 0.43

chi[('TLA','iPBc')] = 0.16  
 chi[('TLB','iPBc')] = 0.2  
 chi[('iPBb','iPBc')] = 1.0  
 chi[('iPBc','iPBc')] = 0.00  
 chi[('DPGA','iPBc')] = 0.18  
 chi[('DPGB','iPBc')] = -0.58  
 chi[('DPGC','iPBc')] = 0.47  
 chi[('CDO','iPBc')] = 0.09  
 chi[('O2rC','iPBc')] = -0.72  
 chi[('BTNL','iPBc')] = 0.04  
 chi[('CCD','iPBc')] = 0.59  
 chi[('CDC1','iPBc')] = 1.11  
 chi[('PPT','iPBc')] = 0.56  
 chi[('COSR','iPBc')] = 0.7  
 chi[('DCCT','iPBc')] = 1.23  
 chi[('PPL2','iPBc')] = 0.4  
 chi[('CDMC','iPBc')] = 1.57  
 chi[('C3DM','iPBc')] = 1.05  
 chi[('P3O','iPBc')] = 0.01  
 chi[('CTMC','iPBc')] = 0.92  
 chi[('CrDM','iPBc')] = 1.35  
 chi[('OCCr','iPBc')] = -0.03  
 chi[('C3T','DPGA')] = 1.93  
 chi[('C3','DPGA')] = 1.72  
 chi[('C4','DPGA')] = 1.99  
 chi[('C4T','DPGA')] = 2.19  
 chi[('C2P','DPGA')] = -0.43  
 chi[('C3tq','DPGA')] = 1.16  
 chi[('ACE','DPGA')] = 1.73  
 chi[('DPGA','DPGA')] = 0.00  
 chi[('CDO','DPGA')] = 0.36  
 chi[('BTNL','DPGA')] = 0.03  
 chi[('CCD','DPGA')] = 1.15  
 chi[('CDC1','DPGA')] = 1.67  
 chi[('COSR','DPGA')] = 2.23  
 chi[('DCCT','DPGA')] = 1.72  
 chi[('CDMC','DPGA')] = 2.09  
 chi[('C3DM','DPGA')] = 1.64  
 chi[('CTMC','DPGA')] = 1.41  
 chi[('CrDM','DPGA')] = 1.75  
 chi[('C3T','DPGB')] = 3.53  
 chi[('C3','DPGB')] = 3.12



chi[('C4T', 'DPGB')] = 3.99  
 chi[('C2P', 'DPGB')] = -2.48  
 chi[('C3tq', 'DPGB')] = 1.88  
 chi[('ACE', 'DPGB')] = 1.92  
 chi[('DPGA', 'DPGB')] = -0.06  
 chi[('DPGB', 'DPGB')] = 0.00  
 chi[('CDO', 'DPGB')] = -0.31  
 chi[('BTNL', 'DPGB')] = 0.45  
 chi[('CCD', 'DPGB')] = 2.41  
 chi[('CDC1', 'DPGB')] = 3.17  
 chi[('COSR', 'DPGB')] = 1.31  
 chi[('DCCT', 'DPGB')] = 3.22  
 chi[('CDMC', 'DPGB')] = 3.88  
 chi[('C3DM', 'DPGB')] = 3.2  
 chi[('CTMC', 'DPGB')] = 2.77  
 chi[('CrDM', 'DPGB')] = 3.33  
 chi[('C3T', 'DPGC')] = 2.08  
 chi[('C3', 'DPGC')] = 1.85  
 chi[('C4', 'DPGC')] = 2.14  
 chi[('C4T', 'DPGC')] = 2.36  
 chi[('C2P', 'DPGC')] = -0.14  
 chi[('C3tq', 'DPGC')] = 1.14  
 chi[('ACE', 'DPGC')] = 1.17  
 chi[('DPGA', 'DPGC')] = -0.06  
 chi[('DPGB', 'DPGC')] = -0.65  
 chi[('DPGC', 'DPGC')] = 0.00  
 chi[('CDO', 'DPGC')] = 0.65  
 chi[('BTNL', 'DPGC')] = -0.04  
 chi[('CCD', 'DPGC')] = 1.23  
 chi[('CDC1', 'DPGC')] = 1.78  
 chi[('COSR', 'DPGC')] = 2.27  
 chi[('DCCT', 'DPGC')] = 1.84  
 chi[('CDMC', 'DPGC')] = 2.24  
 chi[('C3DM', 'DPGC')] = 1.74  
 chi[('CTMC', 'DPGC')] = 1.51  
 chi[('CrDM', 'DPGC')] = 1.88  
 chi[('C3T', 'CDO')] = 1.64  
 chi[('C3', 'CDO')] = 1.54  
 chi[('C4', 'CDO')] = 1.8  
 chi[('C4T', 'CDO')] = 1.89  
 chi[('C2P', 'CDO')] = 1.01  
 chi[('C3tq', 'CDO')] = 0.1

chi[('C3T', 'CDC1')] = 0.03  
 chi[('C3', 'CDC1')] = 0.05  
 chi[('C4', 'CDC1')] = 0.06  
 chi[('C4T', 'CDC1')] = 0.03  
 chi[('C2P', 'CDC1')] = 3.84  
 chi[('C3tq', 'CDC1')] = 2.04  
 chi[('ACE', 'CDC1')] = 9.82  
 chi[('BTNL', 'CDC1')] = 1.42  
 chi[('CCD', 'CDC1')] = 0.02  
 chi[('CDC1', 'CDC1')] = 0.00  
 chi[('C3DM', 'CDC1')] = -0.01  
 chi[('C3T', 'PPT')] = 0.17  
 chi[('C3', 'PPT')] = 0.19  
 chi[('C4', 'PPT')] = 0.21  
 chi[('C4T', 'PPT')] = 0.18  
 chi[('EO', 'PPT')] = 0.18  
 chi[('NC2', 'PPT')] = 8.53  
 chi[('C2P', 'PPT')] = 3.05  
 chi[('C3tq', 'PPT')] = 1.49  
 chi[('ACE', 'PPT')] = 8.53  
 chi[('DPGA', 'PPT')] = 1.35  
 chi[('DPGB', 'PPT')] = 2.71  
 chi[('DPGC', 'PPT')] = 1.42  
 chi[('CDO', 'PPT')] = 0.55  
 chi[('O2rC', 'PPT')] = 0.35  
 chi[('BTNL', 'PPT')] = 1.09  
 chi[('CCD', 'PPT')] = 0.03  
 chi[('CDC1', 'PPT')] = 0.06  
 chi[('PPT', 'PPT')] = 0.00  
 chi[('COSR', 'PPT')] = 3.48  
 chi[('DCCT', 'PPT')] = 0.08  
 chi[('PPL2', 'PPT')] = 1.49  
 chi[('CDMC', 'PPT')] = 0.13  
 chi[('C3DM', 'PPT')] = 0.03  
 chi[('P3O', 'PPT')] = 0.59  
 chi[('CTMC', 'PPT')] = 0.09  
 chi[('CrDM', 'PPT')] = 0.16  
 chi[('OCCr', 'PPT')] = 0.13  
 chi[('C3T', 'COSR')] = 5.5  
 chi[('C3', 'COSR')] = 4.88  
 chi[('C4', 'COSR')] = 5.68  
 chi[('C4T', 'COSR')] = 6.33

chi[('OCCr', 'iPT')] = 0.49  
 chi[('C3T', 'DCCT')] = 0.01  
 chi[('C3', 'DCCT')] = 0.03  
 chi[('C4', 'DCCT')] = 0.03  
 chi[('C4T', 'DCCT')] = 0.0  
 chi[('C2P', 'DCCT')] = 3.99  
 chi[('C3tq', 'DCCT')] = 2.12  
 chi[('ACE', 'DCCT')] = 9.97  
 chi[('CDO', 'DCCT')] = 1.26  
 chi[('BTNL', 'DCCT')] = 1.48  
 chi[('CCD', 'DCCT')] = 0.02  
 chi[('CDC1', 'DCCT')] = 0.0  
 chi[('COSR', 'DCCT')] = 4.82  
 chi[('DCCT', 'DCCT')] = 0.00  
 chi[('CDMC', 'DCCT')] = -0.02  
 chi[('C3DM', 'DCCT')] = -0.01  
 chi[('CTMC', 'DCCT')] = 0.01  
 chi[('CrDM', 'DCCT')] = 0.02  
 chi[('C3T', 'PPL2')] = 2.05  
 chi[('C3', 'PPL2')] = 1.81  
 chi[('C4', 'PPL2')] = 2.11  
 chi[('C4T', 'PPL2')] = 2.34  
 chi[('EO', 'PPL2')] = -0.46  
 chi[('NC2', 'PPL2')] = 1.43  
 chi[('C2P', 'PPL2')] = -0.16  
 chi[('C3tq', 'PPL2')] = 1.29  
 chi[('ACE', 'PPL2')] = 1.43  
 chi[('DPGA', 'PPL2')] = -0.0  
 chi[('DPGB', 'PPL2')] = 0.06  
 chi[('DPGC', 'PPL2')] = -0.0  
 chi[('CDO', 'PPL2')] = 0.53  
 chi[('O2rC', 'PPL2')] = 1.19  
 chi[('BTNL', 'PPL2')] = 0.04  
 chi[('CCD', 'PPL2')] = 1.27  
 chi[('CDC1', 'PPL2')] = 1.8  
 chi[('COSR', 'PPL2')] = 2.32  
 chi[('DCCT', 'PPL2')] = 1.84  
 chi[('PPL2', 'PPL2')] = 0.00  
 chi[('CDMC', 'PPL2')] = 2.25  
 chi[('C3DM', 'PPL2')] = 1.79  
 chi[('P3O', 'PPL2')] = -0.16  
 chi[('CTMC', 'PPL2')] = 1.52

chi[('ACE','CDO')] = 2.23  
 chi[('CDO','CDO')] = 0.00  
 chi[('BTNL','CDO')] = 0.07  
 chi[('CCD','CDO')] = 0.71  
 chi[('CDC1','CDO')] = 1.13  
 chi[('CDMC','CDO')] = 1.73  
 chi[('C3DM','CDO')] = 1.04  
 chi[('C3T','O2rC')] = 1.31  
 chi[('C3','O2rC')] = 1.23  
 chi[('C4','O2rC')] = 1.45  
 chi[('C4T','O2rC')] = 1.52  
 chi[('EO','O2rC')] = -0.79  
 chi[('NC2','O2rC')] = 6.57  
 chi[('C2P','O2rC')] = 1.01  
 chi[('C3tq','O2rC')] = 0.08  
 chi[('ACE','O2rC')] = 6.57  
 chi[('DPGA','O2rC')] = 0.96  
 chi[('DPGB','O2rC')] = 2.29  
 chi[('DPGC','O2rC')] = 0.81  
 chi[('CDO','O2rC')] = -0.67  
 chi[('O2rC','O2rC')] = 0.00  
 chi[('BTNL','O2rC')] = 0.78  
 chi[('CCD','O2rC')] = 0.52  
 chi[('CDC1','O2rC')] = 0.88  
 chi[('COSR','O2rC')] = 1.46  
 chi[('DCCT','O2rC')] = 0.98  
 chi[('CDMC','O2rC')] = 1.41  
 chi[('C3DM','O2rC')] = 0.82  
 chi[('CTMC','O2rC')] = 0.88  
 chi[('CrDM','O2rC')] = 1.15  
 chi[('ACE','BTNL')] = 2.45  
 chi[('BTNL','BTNL')] = 0.00  
 chi[('C3T','CCD')] = 0.03  
 chi[('C3','CCD')] = 0.05  
 chi[('C4','CCD')] = 0.02  
 chi[('C4T','CCD')] = -0.01  
 chi[('C2P','CCD')] = 2.73  
 chi[('C3tq','CCD')] = 1.3  
 chi[('ACE','CCD')] = 7.11  
 chi[('BTNL','CCD')] = 0.97  
 chi[('CCD','CCD')] = 0.00  
 chi[('CrDM','P3O')] = 1.56

chi[('C2P','COSR')] = 0.89  
 chi[('C3tq','COSR')] = -0.89  
 chi[('ACE','COSR')] = 0.98  
 chi[('CDO','COSR')] = 1.16  
 chi[('BTNL','COSR')] = 2.32  
 chi[('CCD','COSR')] = 3.18  
 chi[('CDC1','COSR')] = 4.65  
 chi[('COSR','COSR')] = 0.00  
 chi[('CDMC','COSR')] = 6.05  
 chi[('C3DM','COSR')] = 4.48  
 chi[('C3T','iPT')] = -0.04  
 chi[('C3','iPT')] = -0.07  
 chi[('C4','iPT')] = -0.0  
 chi[('C4T','iPT')] = 0.0  
 chi[('SO4','iPT')] = 13.34  
 chi[('EO','iPT')] = 0.56  
 chi[('NC2','iPT')] = 13.34  
 chi[('C2P','iPT')] = 5.01  
 chi[('C3tq','iPT')] = 2.52  
 chi[('ACE','iPT')] = 13.34  
 chi[('TLA','iPT')] = 0.21  
 chi[('TLB','iPT')] = 0.38  
 chi[('iPBb','iPT')] = -0.04  
 chi[('iPBc','iPT')] = 1.47  
 chi[('DPGA','iPT')] = 2.1  
 chi[('DPGB','iPT')] = 4.0  
 chi[('DPGC','iPT')] = 2.26  
 chi[('CDO','iPT')] = 1.67  
 chi[('O2rC','iPT')] = 1.36  
 chi[('BTNL','iPT')] = 1.85  
 chi[('CCD','iPT')] = -0.1  
 chi[('CDC1','iPT')] = -0.03  
 chi[('PPT','iPT')] = 0.08  
 chi[('COSR','iPT')] = 6.17  
 chi[('iPT','iPT')] = 0.00  
 chi[('DCCT','iPT')] = -0.05  
 chi[('PPL2','iPT')] = 2.28  
 chi[('CDMC','iPT')] = 0.0  
 chi[('C3DM','iPT')] = -0.0  
 chi[('P3O','iPT')] = 1.69  
 chi[('CTMC','iPT')] = -0.08  
 chi[('C3tq','CrDM')] = 2.09

chi[('CrDM','PPL2')] = 1.89  
 chi[('OCCr','PPL2')] = -0.81  
 chi[('C3T','CDMC')] = -0.03  
 chi[('C3','CDMC')] = -0.06  
 chi[('C4','CDMC')] = -0.0  
 chi[('C4T','CDMC')] = -0.0  
 chi[('C2P','CDMC')] = 4.9  
 chi[('C3tq','CDMC')] = 2.55  
 chi[('ACE','CDMC')] = 12.51  
 chi[('BTNL','CDMC')] = 1.86  
 chi[('CCD','CDMC')] = -0.05  
 chi[('CDC1','CDMC')] = -0.0  
 chi[('CDMC','CDMC')] = 0.00  
 chi[('C3DM','CDMC')] = 0.02  
 chi[('C3','C3DM')] = 0.04  
 chi[('C2P','C3DM')] = 3.88  
 chi[('ACE','C3DM')] = 10.03  
 chi[('BTNL','C3DM')] = 1.4  
 chi[('C3DM','C3DM')] = 0.00  
 chi[('C3T','P3O')] = 1.73  
 chi[('C3','P3O')] = 1.58  
 chi[('C4','P3O')] = 1.84  
 chi[('C4T','P3O')] = 1.99  
 chi[('EO','P3O')] = 0.1  
 chi[('NC2','P3O')] = 0.16  
 chi[('C2P','P3O')] = 0.51  
 chi[('C3tq','P3O')] = -0.37  
 chi[('ACE','P3O')] = 0.16  
 chi[('DPGA','P3O')] = -0.53  
 chi[('DPGB','P3O')] = -2.18  
 chi[('DPGC','P3O')] = -0.09  
 chi[('CDO','P3O')] = -0.03  
 chi[('O2rC','P3O')] = -1.1  
 chi[('BTNL','P3O')] = -0.64  
 chi[('CCD','P3O')] = 0.71  
 chi[('CDC1','P3O')] = 1.22  
 chi[('COSR','P3O')] = 0.3  
 chi[('DCCT','P3O')] = 1.38  
 chi[('CDMC','P3O')] = 1.78  
 chi[('C3DM','P3O')] = 1.16  
 chi[('P3O','P3O')] = 0.00  
 chi[('DPGC','OCCr')] = -0.82

chi[('OCCr','P3O')] = 0.08	chi[('ACE','CrDM')] = 10.16	chi[('CDO','OCCr')] = 0.02
chi[('C3T','CTMC')] = 0.0	chi[('CDO','CrDM')] = 1.46	chi[('O2rC','OCCr')] = -1.01
chi[('C3','CTMC')] = 0.01	chi[('BTNL','CrDM')] = 1.57	chi[('BTNL','OCCr')] = -1.22
chi[('C4','CTMC')] = -0.01	chi[('CCD','CrDM')] = 0.01	chi[('CCD','OCCr')] = 0.17
chi[('C4T','CTMC')] = -0.03	chi[('CDC1','CrDM')] = 0.04	chi[('CDC1','OCCr')] = 0.45
chi[('C2P','CTMC')] = 3.25	chi[('COSR','CrDM')] = 4.84	chi[('COSR','OCCr')] = 0.62
chi[('C3tq','CTMC')] = 1.64	chi[('CDMC','CrDM')] = -0.02	chi[('DCCT','OCCr')] = 0.53
chi[('ACE','CTMC')] = 7.91	chi[('C3DM','CrDM')] = 0.05	chi[('CDMC','OCCr')] = 0.61
chi[('CDO','CTMC')] = 1.1	chi[('CTMC','CrDM')] = -0.01	chi[('C3DM','OCCr')] = 0.38
chi[('BTNL','CTMC')] = 1.24	chi[('CrDM','CrDM')] = 0.00	chi[('CTMC','OCCr')] = 0.35
chi[('CCD','CTMC')] = 0.01	chi[('C3T','OCCr')] = 0.69	chi[('CrDM','OCCr')] = 0.58
chi[('CDC1','CTMC')] = 0.02	chi[('C3','OCCr')] = 0.64	chi[('OCCr','OCCr')] = 0.00
chi[('COSR','CTMC')] = 3.91	chi[('C4','OCCr')] = 0.71	chi[('C3tq','NC2')] = 3.62
chi[('CDMC','CTMC')] = -0.06	chi[('C4T','OCCr')] = 0.76	chi[('OCCr','TLB')] = -0.02
chi[('C3DM','CTMC')] = 0.01	chi[('EO','OCCr')] = -0.01	chi[('C4','DPGB')] = 3.59
chi[('CTMC','CTMC')] = 0.00	chi[('NC2','OCCr')] = -0.37	chi[('C3DM','CCD')] = -0.01
chi[('C3T','CrDM')] = -0.01	chi[('C2P','OCCr')] = 0.11	chi[('CrDM','IPT')] = -0.03
chi[('C3','CrDM')] = -0.02	chi[('C3tq','OCCr')] = -0.22	chi[('CTMC','P3O')] = 1.09
chi[('C4','CrDM')] = -0.01	chi[('ACE','OCCr')] = -0.37	chi[('C2P','CrDM')] = 4.19
chi[('C4T','CrDM')] = -0.01	chi[('DPGA','OCCr')] = -1.26	chi[('DPGB','OCCr')] = -2.58